Assessing spring phenology of a temperate woodland: a multiscale comparison of ground, Unmanned Aerial Vehicle and Landsat satellite observations

Newcastle University

Elias Fernando Berra

Thesis submitted for the degree of Doctor of Philosophy

School of Engineering

Newcastle University

August 2017

Abstract

Vegetation phenology is the study of plant natural life cycle stages. Plant phenological events are related to carbon, energy and water cycles within terrestrial ecosystems, operating from local to global scales. As plant phenology events are highly sensitive to climate fluctuations, the timing of these events has been used as an independent indicator of climate change. The monitoring of forest phenology in a cost-effective manner, at a fine spatial scale and over relatively large areas remains a significant challenge. To address this issue, unmanned aerial vehicles (UAVs) appear to be a potential new platform for forest phenology monitoring. The aim of this research is to assess the potential of UAV data to track the temporal dynamics of spring phenology, from the individual tree to woodland scale, and to cross-compare UAV results against ground and satellite observations, in order to better understand characteristics of UAV data and assess potential for use in validation of satellite-derived phenology. A time series of UAV data were acquired in tandem with an intensive ground campaign during the spring season of 2015, over Hanging Leaves Wood, Northumberland, UK. The radiometric quality of the UAV imagery acquired by two consumer-grade cameras was assessed, in terms of the ability to retrieve reflectance and Normalised Difference Vegetation Index (NDVI), and successfully validated against ground $(0.84{\leq}R^2{\geq}0.96)$ and Landsat $(0.73{\leq}R^2{\geq}0.89)$ measurements, but only NDVI resulted in stable time series. The start (SOS), middle (MOS) and end (EOS) of spring season dates were estimated at an individual tree-level using UAV time series of NDVI and Green Chromatic Coordinate (GCC), with GCC resulting in a clearer and stronger seasonal signal at a tree crown scale. UAV-derived SOS could be predicted more accurately than MOS and EOS, with an accuracy of less than 1 week for deciduous woodland and within 2 weeks for evergreen. The UAV data were used to map phenological events for individual trees across the whole woodland, demonstrating that contrasting canopy phenological events can occur within the extent of a single Landsat pixel. This accounted for the poor relationships found between UAV- and Landsat-derived phenometrics $(R^2{<}0.45)$ in this study. An opportunity is now available to track very fine scale land surface changes over contiguous vegetation communities, information which could improve characterization of vegetation phenology at multiple scales.

Acknowledgments

I would like to thank:

Table of Contents

List of Tables

List of Figures

UAV VIs were compared against the structural variables of each plot. Std. = Standard deviation. No significant relationships were found (*p*<0.05). 90

List of Abbreviations

2D	Two Dimensions
3D	Three Dimensions
AVHRR	Advanced Very High Resolution Radiometer
CAA	Civil Aviation Authority
COTS	Commercial Off-The-Shelf
DBH	Diameter at Breast Height
DGPS	Differential Global Positioning System
DHP	Digital Hemispherical Photography
DMA	Delayed Moving Window
DN	Digital Number
DOY	Day Of Year
EOF	End Of Fall season
EOS	End Of Spring season
EVI	Enhanced Vegetation Index
FFT	Fast Fourier Transform
FOV	Field Of View
GCC	Green Chromatic Coordinate
GCP	Ground Control Point
GCT	Ground Calibration Target
GNSS	Global Navigation Satellite System
GPP	Gross Primary Productivity
LAI	Leaf Area Index
Lidar	Ligth Detection and Ranging
LiDAR	Light Detection And Ranging
LSP	Land Surface Phenology
MOD	NIR-MODified RGB camera
MODIS	Moderate Resolution Imaging Spectroradiometer
MOS	Middle Of Spring season
NDVI	Normalized Difference Vegetation Index
NDWI	Normalized Difference Water Index
NIR	Near Infra-Red
NOAA	National Oceanic and Atmospheric Administration
PAI	Plant Area Index
RGB	Red Green Blue
RMA	Reduced Major Axis
RMSE	Root Mean Sqaure Error
ROI	Region Of Interest
RSR	Relative Spectral Response
RTK	Real Time Kinematic
SAR	Synthetic Aperture Radar
SOF	Start Of Fall season
SOS	Start Of Spring season
SPOT	Satellite Pour l` Observation de la Terre

TLS	Terrestrial Laser Scanner
UAV	Unmanned Aerial Vehicle
VI	Vegetation Index
VIS	VISible RGB camera
VOD	Vegetation Optical Depth

Chapter 1. Introduction

1.1 Research context

Vegetation phenology is the study of plant natural life cycle stages (Schwartz 2013) or the annual timing of development events (Polgar and Primack, 2011), such as the date and duration of budburst, flowering, leaf-out and autumn leaf-fall. Such phenological events are related to carbon, energy and water cycles within terrestrial ecosystems (Garrity *et al.*, 2011; Mizunuma *et al.*, 2013), operating from local to global scales, as around 55% of the Earth`s land surface is covered by grasslands, shrub lands and forests (Bartholomé and Belward, 2005). As plant phenology events are highly sensitive to climate fluctuations, the timing of these events has been used as an independent indicator of climate change (Thackeray et al. 2010; Menzel et al. 2006), mainly in temperate environments with deciduous species (Fisher and Mustard 2007). In Europe, advancing leaf unfolding, flowering and fruiting at a rate of 2.5 days decade^{-1} has been reported (Menzel et al. 2006). In the UK context, Thackeray et al. (2010) show warming trends of 0.04-0.05 °C^{-1} year^{-1} between 1976-2005 that lead to an earlier flowering of plants at a rate of 0.57 days year^{-1}, accelerating to a rate of 1.75 days year^{-1} earlier during 1996-2005. Therefore, a changing climate can drive shifts in plant phenology (e.g. timing and length of growing season), with potential impacts on ecosystem services, ecosystem dynamics, plant-based economies, trophic interactions and species ranges (Morisette *et al.*, 2009; White *et al.*, 2009; Campoy *et al.*, 2011; Sparks, 2014). Assessing and monitoring phenological dynamics are therefore key requirements to improve understanding of how plants respond to a changing world and how this influences forest ecosystems (Morisette *et al.*, 2009; Moore *et al.*, 2016).

Remote sensing techniques have been used to monitor vegetation phenology to complement traditional ground based manual measurements (Polgar and Primack, 2013). Currently, vegetation phenology monitoring by remote sensing is effectively performed at two contrasting scales: by ground and near-surface remote sensing or by coarse spatial resolution satellite sensors. The great advantage of satellite sensors is the capability to detect continuous patterns of vegetation changes across the land surface (Eastman *et al.*, 2013; Rodriguez-Galiano *et al.*, 2015). However, the estimation of phenological metrics (the timing of the phenology events, for example, the day of the year (DOY) of greening onset) has many uncertainties, mainly due the absence of validation data and the relatively coarse spatial resolution of many satellite remote sensing instruments, which often integrate the spectral

response of many species (Eastman *et al.*, 2013; Hmimina *et al.*, 2013), each with a particular phenology (Polgar and Primack, 2011; Melaas *et al.*, 2013), therefore limiting the phenological representativeness at ecosystem or species-level (Delbart *et al.*, 2005). Some of these scale-based limitations could be addressed by using medium spatial resolution satellites[1], but image availability can be significantly reduced due to cloud contamination, reducing the dataset temporal resolution and increasing prediction uncertainties (Melaas *et al.*, 2013; White *et al.*, 2014). Combining imagery from multiple sensors such as Landsat and Sentinel-2 (launched in 2015) (Wang *et al.*, 2017) could improve the quality of observations at this scale. However, even with an appropriate temporal resolution dataset, mixed vegetation composition is still an issue at a 30 m spatial resolution (Fisher *et al.*, 2006; Liu *et al.*, 2017).

On the other hand, ground and near-surface sensors have the ability to observe individual plants (or specific regions of interest), detecting very subtle variation in vegetation, which in turn makes it possible to accurately estimate phenological metrics (Ryu *et al.*, 2012; Zhao *et al.*, 2012). In a forest environment, the amount of trees being analysed varies from tens (Ryu *et al.*, 2012) to hundreds (Richardson *et al.*, 2009), depending on the sensor position and arrangement, which may constraint such analysis to small areas. Nevertheless, ecosystem representativeness can potentially be increased by phenological networks (Nasahara and Nagai, 2015) and the derived data set can allow more objective and direct comparisons with spaceborne measures (Baumann *et al.*, 2017) than is possible with traditional ground based manual measurements. Despite these advantages, there are still issues related to viewing angle and areal representativeness, which can confound the comparisons (Hufkens *et al.*, 2012; Hmimina *et al.*, 2013). While satellite sensors have synoptic views (Liu *et al.*, 2017), near-surface sensors are often close to the horizontal (Liu *et al.*, 2017), which may result in near-surface sensors receiving a smaller contribution from the background cover (Hufkens *et al.*, 2012; Mizunuma *et al.*, 2013; Liu *et al.*, 2017). Secondly, because ground/near-surface data are usually not georeferenced, it is necessary to assume that such data are representative of the satellite pixel(s) area (Zhang *et al.*, 2017).

An intermediate level of observation, between ground/near-surface and spaceborne data, can be achieved by airborne sensors. For example, Higgins et al. (2011) used a multichannel camera mounted on a helicopter to differentiate phenological behaviour of African savanna trees and grasses. Such imaging platforms allow data to be obtained that is almost as spatially detailed as cameras fixed to a tower, but over a much larger spatial extent. However, an evident constraint is the use of manned aircraft, which implies high

---

[1]Commercial satellites can provide high spatial resolutions, but time series data are prohibitively costly.

2

operational/logistical costs (Hill *et al.*, 2010; Anderson and Gaston, 2013), which make it difficult to perform frequent flights. There may also be difficulties in undertaking long-term airborne observations due to sensor availability (Lucas *et al.*, 2008). For this reason, is not usual to use airborne data for vegetation phenological event date estimation, although it is more widely used to obtain other types of information, such as tree species composition (Boschetti *et al.*, 2007; Hill *et al.*, 2010).

The monitoring of vegetation phenology in a cost-effective manner, at a fine spatial scale and over relatively large areas therefore remains a significant challenge (Hufkens *et al.*, 2012; Morris *et al.*, 2013). To address this issue, unmanned aerial vehicles (UAVs) appear as a potential new option for vegetation phenology monitoring (Dandois and Ellis, 2013; Berra *et al.*, 2016; Burkart *et al.*, 2017), and this assumption is under test in this research. A new era of fine-scale remote sensing has emerged with the arrival of UAVs (Berni *et al.*, 2009; Sharma *et al.*, 2013), which have the advantages of being lightweight, low-cost and operationally easy to deploy as safe remote sensing acquisition platforms (Anderson and Gaston, 2013; Torresan *et al.*, 2017). Additionally, UAVs can be particularly helpful for surveying optical time-series data in regions that experience frequent cloud cover, such as Great Britain (Armitage *et al.*, 2013).

UAVs offer scientists new opportunities for scale-appropriate measurement of ecological phenomena, delivering fine spatial resolution data at user-controlled revisit periods (Anderson and Gaston, 2013). In terms of vegetation phenology studies, these characteristics can be of great importance, as some phenological events occur faster than others (Polgar and Primack, 2011). In a forest environment, for example, budburst occurs quicker than autumn leaf-fall, meaning that the frequency of observation to detect budburst needs to be higher than the frequency of observation to detect autumn leaf-fall. Therefore, convenient temporal resolutions can be planned with UAVs (Chabot and Bird, 2013) in order to provide appropriate time-series required to monitor phenological changes. Furthermore, a temporal series of fine spatial imagery can be useful to spatially resolve individual plants and consequently, to allow phenology monitoring by species, as phenological events may occur at different times for each species (Soudani *et al.*, 2008; Polgar and Primack, 2011). Finally, the intermediate level of observation, between ground/near-surface and spaceborne data, achieved by UAVs, can be useful to validate satellite-based phenological products.

However, some limitations of UAVs are also recognised. These include relatively small area coverage, that flights cannot be performed in high winds and during precipitation,

significant investment in training, fixed-wing UAVs requiring flat terrain for landing, the limited payload constraints on sensor types and the mission endurance (Berni *et al.*, 2009; Anderson and Gaston, 2013; Chabot and Bird, 2013; Dandois and Ellis, 2013). There are also flight restrictions imposed by civil and federal aviation laws (Torresan *et al.*, 2017). For example, within the UK, UAVs can operate up to 500 m horizontally and 400 ft vertically from the pilot (www.caa.co.uk). There are also remaining technical challenges in dealing with very high spatial resolution data, such as influence of viewing geometry (Sharma *et al.*, 2013), radiometric calibration and atmospheric correction (Berni *et al.*, 2009) and georeferencing and mosaicking the large amount of images typically acquired (McGwire *et al.*, 2013). These factors can diminish the capability to generate accurate quantitative information (Kelcey and Lucieer, 2012), which is critical in applications such as quantification of land surface parameters or time series analysis (Lebourgeois *et al.*, 2008).

Despite multi-temporal UAV datasets having been successfully acquired and applied across a number of different disciplines (Lisein *et al.*, 2013; Vega *et al.*, 2015; van Iersel *et al.*, 2016), the potential for forest phenology monitoring has yet to be tested. In one study, Dandois and Ellis (2013) showed that UAV time series data can detect the seasonal profile of deciduous forests in a manner similar to satellite sensors (R^2=0.87); nevertheless, no further phenological investigation was carried out as the authors focused on 3D measurements of forest attributes. In another study, Burkart *et al.* (2017) employed UAV time series data for phenological analysis of experimental plots of barley, with an emphasis on precision agriculture. Therefore, there is an open opportunity to employ UAVs in forest phenology studies, technology which has been recognized to play an important role in future vegetation phenology monitoring (Cole *et al.*, 2015; Brown *et al.*, 2016). Using observations at multiple scales acquired by different sensors is key to improve our understand of vegetation phenology (Hufkens *et al.*, 2012; Henebry and de Beurs, 2013; Nagai *et al.*, 2015; Brown *et al.*, 2016).

1.2 Aim of research

The aim of this research is to assess the potential of UAV data to track the temporal dynamics of spring phenology, from the individual tree to woodland scale, and to cross-compare UAV results against ground and satellite observations, in order to better understand characteristics of UAV data and assess potential for use in validation of satellite-derived phenology. Because Consumer-Off-the-Shelf (COTS) cameras were utilized onboard the

UAV in this study, a comprehensive radiometric calibration and validation of spectral products is carried out, as there is a need for a better understanding of the quality and consistencies of spectral data retrieved from these commonly used sensors (Zaman *et al.*, 2014; von Bueren *et al.*, 2015). A multi-scale characterization of forest phenology, from single species to ecosystem, is then derived from the UAV data set, information which is linked with ground and satellite observations. The challenge of accurately monitoring the phenological behaviour of individual organisms over contiguous vegetation communities (Hufkens *et al.*, 2012; Morris *et al.*, 2013; Tang *et al.*, 2016) is addressed, which can provide novel insights into species phenology and a better understanding of relationships between ecosystem processes (as observed with satellite sensors) and species-specific phenological events (as observed on the ground and by near-surface sensors).

1.2.1 Research questions

A number of specific research questions are addressed in this research:

1. Can consumer-grade cameras on-board UAVs be used for consistent and quantitative multispectral remote sensing of vegetated land surfaces?
2. Can an UAV time series of imagery resolve tree species specific phenological behaviour and therefore detect the differences in timing of phenological events over the woodland canopy?
3. Can UAV time series imagery differentiate between the effects of understorey and overstorey development?
4. What is the accuracy and the biophysical meaning of key phenological metrics derived from UAV data?
5. How can observations of plant phenology measured by cameras on-board an UAV be associated with the overall phenological dynamics recorded by orbital sensors? Therefore, do UAVs provide a basis for validating satellite-derived land surface phenology products?

1.2.2 Objectives

1) To identify strengths and weaknesses of current methods used to monitor vegetation phenology, whilst setting the theoretical background for this research.
2) To retrieve reflectance and vegetation indices from consumer-grade cameras on-board UAVs, for use in vegetation monitoring.

3) To track tree species-specific spring seasonal changes in a mixed woodland ecosystem, which can provide novel insights into the timing of phenology events between and within tree species.

4) To examine the spatial and temporal characteristics of canopy phenology across an entire woodland at a fine-scale perspective. This could allow investigation of the variability in phenology within tree species and with tree species composition.

5) To assess and better understand the fine-scale spatial variability in phenology events occurring at a sub-pixel level for widely-used satellite data sets.

1.3 Structure of thesis

Besides this introductory chapter, this thesis has 6 more chapters addressing the aim and objectives, as stated in Section 1.2. Chapter 2 reviews relevant literature in the field of forest phenology monitoring, defining key concepts and discussing the main remote sensing techniques and datasets used for this purpose. Chapter 3 presents a description of the study area and the ground data collected for validation purposes. The ability of two consumer-grade cameras on-board a UAV to generate consistent time series of reflectance and vegetation indices is tested in Chapter 4. The potential of UAV time series data for forest phenology monitoring, at a tree- and plot-level, is tested and validated in Chapter 5. Chapter 6 then expands the UAV individual tree-level phenology detection to the entire woodland, providing the opportunity to cross-compare UAV and Landsat (7 and 8) results. Finally, Chapter 7 presents a general discussion and conclusion, highlighting key findings and their contributions to forest phenology monitoring.

Chapter 2. Remote Sensing of Vegetation Phenology

2.1 Introduction

The aim of this chapter is to critically examine key studies related to remote sensing of vegetation phenology, with a special focus on temperate forests. This chapter addresses therefore the Objective 1 of this research as presented in Chapter 1: "To identify strengths and weaknesses of current methods used to monitor vegetation phenology, whilst setting the theoretical background for this research."

Firstly, the importance of studying vegetation phenology is addressed followed by the biophysical and physiological processes behind plant phenology. Afterwards, relevant approaches for measuring phenology (or specific phenological events) with aid of time series of remote sensing data at ground, near-surface and orbital level are discussed, helping to define relevant terms and setting a framework for this research. Throughout the text, challenges from current data sets and techniques used to monitor phenology are outlined, highlighting opportunities for new remote sensing platforms such as UAVs.

2.2 Importance of vegetation phenology

Vegetation phenology is the study of plant natural life cycle stages (Schwartz 2013) or the annual timing of development events (Polgar and Primack, 2011), such as the date and duration of budburst, flowering, leaf-out and autumn leaf-fall. Such phenological events are related to carbon, energy and water cycles within terrestrial ecosystems (Garrity *et al.*, 2011; Mizunuma *et al.*, 2013), operating from local to global scales, as around 55% of the Earth`s land surface is covered by grasslands, shrub lands and forests (Bartholomé and Belward, 2005). These phenological events are also related to many other processes occurring iteratively in the biosphere-atmosphere layer (Richardson *et al.*, 2013a), as schematized in Figure 2-1.

For example, phenology controls the development and senescence of foliage, which then controls the physiological activity of the canopy (Figure 2-1). The latter influences carbon, water and energy fluxes, and emissions of volatile organic compounds (VOC). All these processes (along with surface roughness length and albedo, Figure 2-1) influence the atmosphere structure and composition, which in turn influences the climate system.

Therefore, many important feedbacks to the climate system are affected by the seasonality of vegetation.
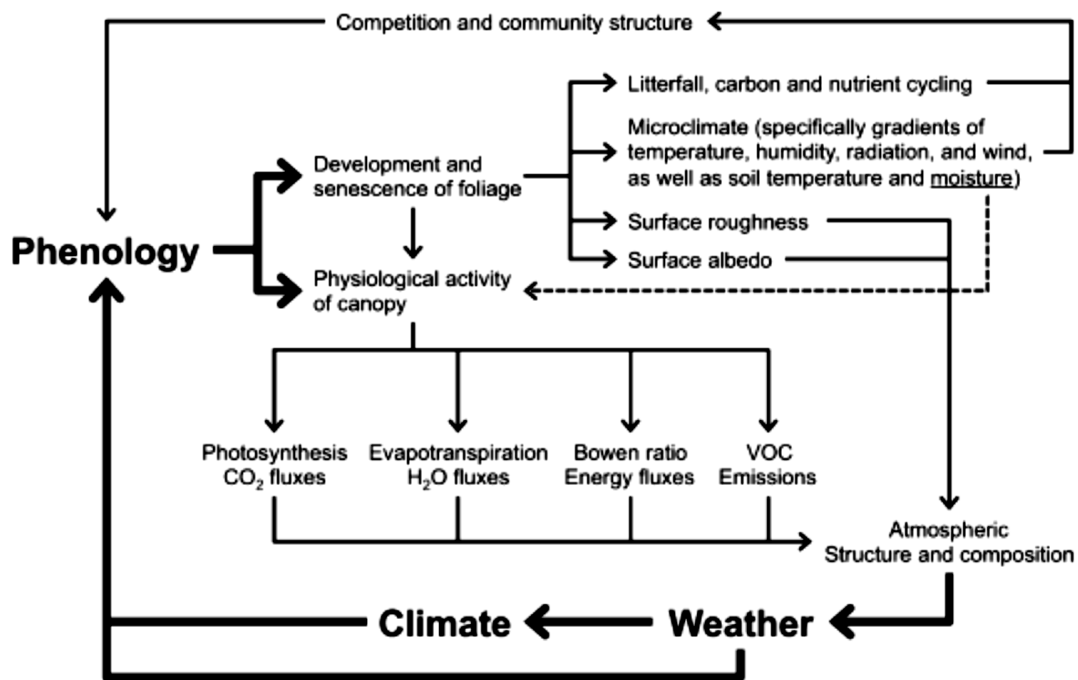
Figure 2-1. "*Conceptual model illustrating the primary feedbacks between vegetation and the climate system that are influenced by vegetation phenology*" (Richardson *et al.*, 2013a). Credits[2].

As plant phenology events are highly sensitive to climate fluctuations, the timing of these events has been used as an independent indicator of climate change (Menzel *et al.*, 2006; Thackeray *et al.*, 2010) mainly in temperate environments with deciduous species (Fisher and Mustard 2007). Many studies have reported shifts in plant phenology as a likely response to climate change. In England, records of tree-leaf out from temperate forests (1772 to 2006) have detected phenological advances of 3-8 days per 1°C increase in temperature (Thompson and Clark, 2008). In Europe, for the period 1971-2000, an increase of 1°C was reported to cause an overall advancement of 2.5 days in spring phenology and a delay of autumn phenology of 1 day (Menzel *et al.*, 2006). In Japan, tree phenological observations from 1953 to 2005 revealed that, on average, plant phenological events in spring occurred 0-8 days earlier and in autumn 4-5 days later, for each degree Celsius increase in temperature (Ibáñez *et al.*, 2010). These studies report therefore that, overall, warming temperatures are related to earlier spring and later autumn phenology. In temperate zones, if trends of risings in air temperature continue to occur over the next decades (Christensen *et al.*, 2007), earlier

---

[2] Reprinted from Richardson *et al.* (2013a), with permission from Elsevier.

spring leaf-out (0.7 days per decade) (Lebourgeois *et al.*, 2010) and later senescence (1.4 to 2.3 days per decade) (Vitasse *et al.*, 2011) are predicted to occur, which will lead to consequent longer growing seasons. However, despite this broad pattern observed in mid and high latitudes, not all species are responding similarly, and there is significant variability even within species (Thompson and Clark, 2008; Vitasse *et al.*, 2009; Ibáñez *et al.*, 2010), a fact which can add uncertainties in models forecasting phenology under climate change scenarios. There are also uncertainties coming from the different climate changes scenarios available to feed the models (Christensen *et al.*, 2007), and uncertainties due to different models (Migliavacca *et al.*, 2012; Richardson *et al.*, 2013a).

Therefore, a changing climate can drive shifts in plant phenology (e.g. timing and length of growing season), with potential impacts on ecosystem services, ecosystem dynamics, plant-based economies, trophic interactions and species ranges (Morisette *et al.*, 2009; White *et al.*, 2009; Campoy *et al.*, 2011; Sparks, 2014). Assessing and monitoring phenological dynamics are therefore key requirements to improve understanding of how plants respond to a changing world and how this influences forest ecosystems (Morisette *et al.*, 2009; Moore *et al.*, 2016).

2.3 Definition of tree phenology and how it is traditionally observed

Deciduous trees have been the main focus of phenology studies (Menzel *et al.*, 2006; Polgar and Primack, 2011) as their phenological events are more pronounced and evident than with evergreen species (Hmimina *et al.*, 2013). Field-based ecological studies have shown that deciduous tree species have a well-characterized annual temporal pattern. After the period of dormancy and leafless (or no green leaves) phase over winter, the bud-break (when the tip of the leaf is visible) on deciduous trees signals the transition between winter and spring, an event which marks the onset of the growing season (Polgar and Primack, 2011; Polgar and Primack, 2013) and consequent beginning of the photosynthetically active period (Garrity *et al.*, 2011; Hmimina *et al.*, 2013).

The bud-break and consequent emergence of leaves in deciduous temperate species is controlled by a combination of three main factors: warming in the spring, winter chilling and photoperiod (Hunter and Lechowicz, 1992; Polgar and Primack, 2013); but there might have been an influence of site-specific factors too, such as precipitation and soil conditions (Ibáñez *et al.*, 2010). After bud-break, the leaf emerges and it grows relatively rapidly (green-up) until

its adult size (Zhao *et al.*, 2012; Klosterman *et al.*, 2014). Internally the leaf accumulates chlorophyll as it grows in size and it keeps accumulating pigments after the leaf reaches adult size, until reaching physiological maturity. After that, a relatively stable period of maximum leaf area occurs (over summer) (Zhang *et al.*, 2003; Ryu *et al.*, 2012). The end of growing season and consequent end of the photosynthetically active period is characterized by depigmentation, leaf yellowing and then leaf fall under the control of abscission processes (Hmimina *et al.*, 2013). This process is relatively slower than leafing-out (Zhao *et al.*, 2012; Klosterman *et al.*, 2014). Over winter the tree returns to a no-green leaf phase when its physiological activity becomes near zero (Zhang *et al.*, 2003), closing/restarting its annual life cycle.

Similar processes also occur in evergreen temperate species. Young leaves appear during the spring season, reaching adult size towards the beginning of summer (Kimball *et al.*, 2004; Zhao *et al.*, 2012). However, adult leaves have a longer life span than deciduous leaves without a specific senescence period (Kimball *et al.*, 2004; Zhao *et al.*, 2012). Old leaves shed gradually in temperate forests (Givnish, 2002). Photosynthetic rates are also influenced by the seasons (with a dormancy period in winter), but a longer photosynthetic period (longer growing season) is observed, due to the evergreen plants ability to break dormancy earlier in the spring and enter dormancy later in autumn (Givnish, 2002; Toomey *et al.*, 2015).

Traditionally, the monitoring of phenological changes has been by direct observations of plants, with phenological records dating back the 9th century (e.g. of Japanese cherry tree) (Richardson *et al.*, 2013a). Visual assessments are usually carried out by scientists (Menzel *et al.*, 2006; Liang *et al.*, 2011; Schwartz, 2013), but also by people interested in nature (Beck *et al.*, 2007; Jorde, 2016; National Science Foundation, 2016; Universität Bern, 2016; Woodland Trust, 2016). This consists of observing the tree and recording its phenological phase (discrete observation) according to a defined protocol, as exemplified in Table 2-1. For example, a scientist performs recurrent visits to a same plant in order to observe and record the date when the first flower (or first bud) appears.

Visual observations are relatively easy to be made, as the method only demands a person to observe and record the phenological phase of interest. Additionally, visual observations are considered to be an accurate method to monitor phenology of individuals due to its explicit biophysical meaning (Liang *et al.*, 2011; Liu *et al.*, 2015). However, observations can be time consuming and labour intensive, hampering the acquisition of a

large volume of good quality data, facts which often constrain studies to small areas and to a few species. Furthermore, there is a degree of subjectivity involved, as the assessment of a plant phenological status depends on the observer experience, and usually the quality (or uncertainty) of such observations cannot be evaluated (unless multiple observers assess a same plant, which is difficult due to time constraints).

To measure phenological events on a larger scale, remote sensing has emerged as valuable new tool (Polgar and Primack, 2013). Over the last three decades, remote sensing techniques have largely been used to monitor vegetation phenology to complement traditional ground based manual measurements (Liang *et al.*, 2011; Polgar and Primack, 2013). Currently, vegetation phenology monitoring by remote sensing is effectively performed at two contrasting scales: by sensors very close to the plant (ground and near-surface remote sensing) or by sensors very distant (satellite sensors). These topics are discussed in the next sections.

Table 2-1. Examples of phenological phases observed from the ground. The phenophases are usually recorded as occurring in a specific day of year (DOY).

Season	Phenophases	Author
Spring	-Leaf unfolding; Full flowering; Needle appearance.	Studer *et al.* (2007)
Spring	-First leaves.	Delbart *et al.* (2005)
Spring	- Buds open/leaf visible (<10%; 10-50%; 50-90%; >90%); - Leaf out/not fully unfolded (<10%; 10-50%; 50-90%; >90%); - Full leaf unfolded (<10%; 10-50%; 50-90%; >90%); - Leaf expansion (Size <25% of full; 25-50%; 50 -75%; > 75% of full; full).	Schwartz *et al.* (2013)
Autumn	-Leaf colouration (10%; 10–50%; 50–90%; 90–100%); -Leaf fall (10%; 10–50%; 50–90%; 90–100%);	Liu *et al.* (2015)
Autumn	-Beginning of leafing colouring.	Delbart *et al.* (2005)

2.4 Satellite-derived phenology

The development of geospatial technologies in 1970`s has allowed monitoring of aggregated effects of leaf phenology from local to global extents with the aid of data from satellite sensors (Henebry and de Beurs, 2013). While visual observations of tree phenology offer an explicit biophysical meaning for specific organisms (Table 2-1), phenology derived from a satellite is distinct from plant phenology because the satellite sensor integrates a mixture of signals coming not only from trees but also from all the objects visible in the

background within the pixel`s instantaneous field of view, such as soil and rivers (Friedl *et al.*, 2006). For this reason satellite-based phenology is often called land surface phenology (LSP) and can be defined as *"the seasonal pattern of variation in vegetated land surfaces observed from remote sensing"* (Henebry and de Beurs, 2013) and, complementarily, as the *"spatio-temporal development of the vegetated land surface as revealed by synoptic spaceborne sensors"* (White *et al.*, 2009).

The majority of studies investigating LSP have used time series of optical imagery (but see Kimball *et al.* (2004) for radar data), exploiting the exclusive and well-known spectral characteristics of green healthy leaves over the 400-2600 nm wavelengths (Jensen, 2007), which have low spectral reflectance in the visible and middle-infrared wavelengths and high reflectance in the near-infrared (NIR) wavelengths (Gates, 1970). This behaviour results in a spectral contrast which makes the basis for many vegetation indices (VI) (Table 2-2). VIs are robust satellite products (Jackson and Huete, 1991) defined as optical measures of canopy "greenness", a composite property of leaf chlorophyll content, green leaf area, canopy cover and structure (Glenn *et al.*, 2008). Therefore, satellite-derived VIs can allow tracking of the spatio-temporal patterns of the photosynthetic activity of the vegetation (Franklin, 1986; Baret and Guyot, 1991; Jackson and Huete, 1991; Zhang *et al.*, 2003; Glenn *et al.*, 2008).

Time series of satellite-derived VIs can therefore be used to identify seasonal transitions in vegetation activity, where significant changes in VI values over time can potentially be associated with the biophysical/physiological phenomena occurring on the ground (Zhang *et al.*, 2003; Henebry and de Beurs, 2013). Various methods have been developed to estimate timing of key phenological transitions from a time series of VIs (as discussed on section 2.4). These methods are used to derive phenological metrics (phenometrics), which are defined as occurring on a particular day-of-year (DOY) (Fisher *et al.*, 2006). In an annual cycle, the primary phenometric of interest has been the start of growing season, also referred to as start of spring season (SOS) (White *et al.*, 2009; Liang *et al.*, 2011), due to its importance within the context of climate change (Menzel, 2002; Polgar and Primack, 2013) and relationship with key transition dates of carbon and energy seasonal cycles (Toomey *et al.*, 2015). SOS can be defined as a rapid sustained increase in greenness (green-up) after the annual period of photosynthetic senescence, as a result of increases in chlorophyll and leaf area (White *et al.*, 2009; Garrity *et al.*, 2011). The end of growing season, or end of fall season (EOF), is another phenometric with great value for phenology studies as it allows estimation of the length of the growing season (Garrity *et al.*, 2011; Liu *et al.*, 2015), which can be characterized by a decrease in greenness (relatively slower than SOS)

after a period of constant chlorophyll content and leaf area (Garrity *et al.*, 2011; Liu *et al.*, 2015).

Table 2-2. Vegetation indices derived from optical satellite imagery often used in vegetation phenology studies: Normalized Difference Vegetation Index (NDVI), Enhanced Vegetation Index (EVI), Soil Adjusted Vegetation Index (SAVI), Green Normalized Difference Vegetation Index (GNDVI), Normalized Difference Water Index (NDWI) and Excess Green Index (ExG).

Vegetation index	Formula	Reference
NDVI	$\dfrac{\rho_{NIR} - \rho_{red}}{\rho_{NIR} + \rho_{red}}$	Tucker (1979)
EVI	$G \dfrac{\rho_{NIR} - \rho_{red}}{\rho_{NIR} + C_1 \times \rho_{red} - C_2 \times \rho_{blue} + L}$	Huete *et al.* (2002)
SAVI	$\dfrac{\rho_{NIR} - \rho_{red}}{\rho_{NIR} + \rho_{red} + L} \times (1 + L)$	Huete (1988)
GNDVI	$\dfrac{\rho_{NIR} - \rho_{green}}{\rho_{NIR} + \rho_{green}}$	Gitelson *et al.* (1996)
NDWI	$\dfrac{\rho_{NIR} - \rho_{MIR}}{\rho_{NIR} + \rho_{MIR}}$	Delbart *et al.* (2005)
ExG	$2*\rho_{green} - (\rho_{blue} + \rho_{red})$	Hufkens *et al.* (2012)

Note: ρ_{blue} = Spectral reflectance in the blue wavelength; ρ_{green}= Spectral reflectance in the green wavelength; ρ_{red}= Spectral reflectance in the red wavelength; ρ_{NIR}= Spectral reflectance in the near-infrared wavelength; ρ_{MIR} = Spectral reflectance in the middle-infrared wavelength; L = Factor to account for background effects; C_1 and C_2 = Factor to correct for aerosol influences; G = Gain factor.

Besides these two main phenometrics, Reed *et al.* (1994) showed that it might be possible to derive 10 more phenometrics from a complete annual time series of VI, which were divided in three groups (Table 2-3): (1) temporal: refers to times (DOY) marking the beginning, end and duration of growing season (referred to as time of greenness) and peak of the growing season (referred to as maximum NDVI value); (2) VI-based: the VI value at which events occur in the first group; and (3) derived metrics which can be extracted based on the data points corresponding to beginning, peak and end of growing season, such as the area under the VI time series curve (time-integrated NDVI). Each phenometric is accompanied by a phenological interpretation, where both the time and value of greenness are related to

photosynthetic activity of vegetation. The original interpretation of Reed *et al.* (1994) (Table 2-3) is modified to include an interpretation in terms of leaf area index (LAI), since VIs are expected respond to chlorophyll content and to the amount of green leaf material (Myneni *et al.*, 2002; Zhang *et al.*, 2003; Ryan *et al.*, 2012), which is in agreement with other studies deriving phenometrics from VI time series (Zhang *et al.*, 2003; Garrity *et al.*, 2011; Liang *et al.*, 2011; Polgar and Primack, 2011; Hufkens *et al.*, 2012; Hmimina *et al.*, 2013; Melaas *et al.*, 2013; Liu *et al.*, 2015).

However, there remains a significant challenge to associate LSP-derived metrics (Table 2-3) with the biophysical measures coming from ground-based phenology (Table 2-1), as these metrics may not necessarily correspond directly to phenological events as observed on ground, but provide indicators of ecosystem dynamics (Reed *et al.*, 1994; Henebry and de Beurs, 2013). This fact can be attributed to the limited capacity of satellite remote sensing data to monitor species-specific phenology, mainly due to the underlying spatial complexity/heterogeneity of the objects which might be present within the resolved scene (White *et al.*, 2009).

Another major challenge is to define what accuracy is necessary from these metrics in order to allow a consistent monitoring of possible shifts expected to occur due to climate change (Richardson *et al.*, 2012). This is critically important if these metrics are to be used as an indicator of climate change by the public and scientific community (IPCC, 2014). Recent figures for observed phenology shifts were presented in section 2.2 and the accuracy of estimated phenological events from time series of remote sensing data is presented in section 2.6.

Table 2-3. 12 phenological metrics derived from an annual satellite-based NDVI time series and their phenological interpretation, as suggested by Reed *et al.* (1994) (Credits[3]). A complementary interpretation (Zhang *et al.*, 2003) was added in between brackets.

Metric	Phenological interpretation
Temporal NDVI metric	
Time of onset of greenness (green-up)	Beginning of measurable photosynthesis (onset of photosynthetic activity)
Time of end of greenness (senescence)	Cessation of measurable photosynthesis (photosynthetic activity and LAI begin to rapidly decrease)
Duration of greenness	Duration of photosynthetic activity
Time of maximum NDVI (maturity)	Time of maximum measurable photosynthesis (LAI is maximum)
NDVI-value metric	
Value of onset of greenness	Level of photosynthetic activity at beginning of growing season
Value of end of greenness	Level of photosynthetic activity at end of growing season
Value of maximum NDVI	Maximum measurable level of photosynthetic activity
Range of NDVI	Range of measurable photosynthetic activity
Derived metrics	
Time-integrated NDVI	Net primary production
Rate of greenup	Acceleration of photosynthesis
Rate of senescence	Deceleration of photosynthesis
Modality	Periodicity of photosynthetic activity

2.4.1 LSP with microwave satellite data

The seasonal life-cycle events of vegetated surfaces have been also investigated with the aid of microwave satellite data, although to significantly less of an extent than with optical-NIR data. Microwave data has the advantage of being less (or not) affected by factors commonly hampering the data acquisition of high quality optical-NIR data: darkness, atmospheric composition, clouds, and off-nadir viewing angles (but depending on surface roughness) (Ryan *et al.*, 2012; Lu *et al.*, 2013a). Nevertheless, the two data sources are sensitive to different characteristics of the land surface: microwave remote sensing data are likely to respond to vegetation structure and moisture content (including soil moisture) (Jones

---

[3] Retyped from Reed *et al.* (1994), with permission from John Wiley and Sons. ©IAVS; Opulus Press Uppsala. Printed in Sweden.

et al., 2011; Ryan *et al.*, 2012), whereas optical VIs are a composite property of leaf chlorophyll content, green leaf area, canopy cover and structure (Glenn *et al.*, 2008). For this reason, microwave LSP metrics are usually considered a complement to the optical-NIR LSP metrics, potentially providing a more comprehensive assessment of LSP (Jones *et al.*, 2011; Ryan *et al.*, 2012).

For the first time, Ryan *et al.* (2012) investigated the relationship between SOS derived from ground-based measurements, optical-NIR and microwave satellite data over a tropical forest in Mozambique. The experiment contained 14 plots (1 ha) spread over an area of 20 km x 30 km. Within each plot, monthly digital hemispherical photography (DHP) were taken over four years to estimate PAI, time series from which SOS was derived and used as reference data. Nine 16-day composite MODIS/EVI pixels (~5.6 km spatial resolution) covering the study area and the Ku-band data (2.1 cm wavelength) from SeaWinds-on-QuikSCAT at 4-day composite and ~5.5 km spatial resolution were obtained. Three different methods were tested to estimate SOS, resulting in differences in estimated SOS dates < 19 days among the methods. PAI was highly correlated with EVI (r=0.94) and scatterometry (r=0.90), and EVI and scatterometry were correlated by r=0.94. SOS derived from EVI and scatterometry had a mean difference < 10 days compared to PAI derived SOS, indicating the potential of scatterometry data to complement optical LSP. An immediate constraint of their methodology is the acquisition of validation data at a monthly frequency, which is likely to not be tracking the rapid changes occurring in the canopy structure during the growing season. As the main limitation, the authors noted the scatterometry data detecting SOS significantly earlier (>45 days) than EVI across areas with low tree cover (<25%). However, a clear advantage of microwave satellite data is that a consistent temporal resolution can be achieved, avoiding the data gaps in the time series (a common problem with optical-NIR time series data).

Other studies have also used scatterometry data to monitor forest seasonality. Frolking *et al.* (2006) demonstrated that the Ku-band backscatter measurements from the SeaWinds-on-QuikSCAT scatterometer could monitor canopy phenology and vegetation seasonal dynamics at a continental scale (Northern America). Time series of SeaWinds and MODIS LAI were compared resulting in good agreements (generally R^2>0.5) but the SeaWinds series detected SOS earlier than MODIS LAI, mirroring results of Ryan *et al.* (2012) (above) and Lu *et al.* (2013b) (same sensor but across China). The usually large spatial resolution of scatterometer data (~25 km) means that this kind of microwave remote sensing data is more suited to continental/global scale than local scale studies (Steele-Dunne *et al.*, 2017).

A few studies have tested the potential of multi-temporal synthetic aperture radar (SAR) data for forest phenology monitoring. Rüetschi *et al.* (2018) demonstrated the potential of using multi-temporal Sentinel-1 C-band (24 days temporal resolution, 10 m spatial resolution) for monitoring phenology of mixed temperate forests in northern Switzerland. Deciduous covers followed distinctive seasonal backscatter patterns (at vertical-horizontal (VH) polarization, with higher backscatter values in winter and lower in summer), which was associated with that forest seasonal cycle (evergreen covers presented only weak seasonality). Volunteered phenological observations were gathered (dates of leaf emergence and leaf fall) for two study sites (within 25 km) to validate the timing of the change in forest backscatter (breakpoints in spring and fall season); the differences between the SAR phenometrics and ground observations were <12 days, but no consistent bias was observed in between the two years analysed. Although these are promising results, a more robust validation approach is needed to increase the confidence and understanding of SAR-derived phenometric dates. Dostalova *et al.* (2016) also analysed the seasonal variability of Sentinel-1 C-Band SAR backscatter but over an Austrian mixed temperate forest (during one year) and found results mirroring Rüetschi *et al.* (2018). An early study of Proisy *et al.* (2000) analysed time series of Environmental Research Satellite (ERS)-1/2 C-Band (1994 to 1997) Vertical-Vertical (VV) backscatter of a mixed temperate forest in France and noted a weak dependency of the backscatter on foliage (also noted by Rüetschi *et al.* (2018)), fact which might represent a major challenge to conciliate SAR and optical VIs phenology. Despite these few studies, the recent availability of Sentinel-1 C-Band SAR data (and future RADARSAT constellation) offers an unprecedented temporal resolution of SAR observations (Canisius *et al.*, 2017; Steele-Dunne *et al.*, 2017), data set which can open new opportunities for a better understanding of SAR phenology over forested areas.

Unlike for forest phenology, there have been a number of studies of microwave data for crop phenology, primarily exploiting SAR spaceborne, as it can present a spatial resolution high enough to resolve the crop fields (Canisius *et al.*, 2017; Steele-Dunne *et al.*, 2017). Data from polarimetric SAR has been used to map and detect phenological stages of rice (Lopez-Sanchez *et al.*, 2011; Yuzugullu *et al.*, 2015), canola and wheat (Canisius *et al.*, 2017), corn and soybean (McNairn *et al.*, 2014), onion fields (Mascolo *et al.*, 2015) and other crops (Steele-Dunne *et al.*, 2017). Information on crop phenology derived from multi-temporal polarimetric SAR parameters can be used as a proxy for crop production surveillance, yield prediction (Canisius *et al.*, 2017) and classifying the different crop types (Steele-Dunne *et al.*, 2017). Despite a consistent temporal resolution can be achieved with

SAR data sets, as they are less influenced by weather conditions, a high temporal resolution may be difficult to be achieved when the sensors have a high spatial resolution (spatial-for-temporal trade-off); nevertheless, as discussed previously, combining Sentinel-1 and RADARSAT missions can allow a finer temporal scale, at a relatively high spatial resolution, to be achieved in the near future (Rüetschi *et al.*, 2018).

Jones *et al.* (2011) evaluated the potential of satellite passive microwave remote sensing based Vegetation Optical Depth (VOD) (~25 km spatial resolution) for global LSP monitoring over a six year period. Correlations between VOD and MODIS VIs were generally strong (R>0.5), but the VOD phenology curves were generally phase shifted to the VI curves, resulting in significant lags between phenometrics derived from VOD and VIs. Jones *et al.* (2011) also found reduced correspondence between MODIS VIs and microwave data at higher biomass levels (0.03<R<0.51). This is likely to reflect the different biophysical parameters that the microwave and optical-infrared instruments are sensitive to.

2.5 Methodologies to derive phenological markers from satellite imagery

The first efforts to observe the dynamic cycles of the vegetated land surface began with the Landsat era in the 1970s (Tucker, 1979), when, in the subsequent years, many studies focused on the monitoring of crop phenology in agriculture (Kanemasu, 1974; Heilman *et al.*, 1977; Badhwar, 1984). Despite the relatively high spatial resolution of Landsat data (<60 m), a key limitation was the long return interval relative to vegetation dynamics (Henebry and de Beurs, 2013). The launch of the Advanced Very High Resolution Radiometer (AVHRR) sensor in the 1980`s brought, in contrast, much finer temporal resolution (sub-daily) data at the cost of much coarser (1-4 km) spatial resolution (Yates *et al.*, 1986). This spatial-for-temporal trade-off made it possible to capture seasonal vegetation dynamics at the continental scale (Henebry and de Beurs, 2013).

Currently at spaceborne level, the Landsat series is still one of the highest spatial resolution data (30 m) at which phenology studies can be cost-effectively carried out (Isaacson *et al.*, 2012; Melaas *et al.*, 2013; Baumann *et al.*, 2017) (the Sentinel-2 mission, with the first satellite launched in June 2015, records data with spatial resolutions as fine as 10 m, and offers now opportunities for detailed observations of land surface phenology). However, as frequent observations are necessary (Zhao *et al.*, 2012; Miao *et al.*, 2013), the less frequent temporal acquisition of images (16-day) and missing data due cloud cover/cloud

shadow and sensor technical problems significantly reduces the number of suitable images per year (Isaacson *et al.*, 2012; Melaas *et al.*, 2013), consequently making it difficult to use the Landsat series for phenology purposes (Fisher *et al.*, 2006). Nevertheless, motivated by the high spatial resolution and long-term data offered by the Landsat series, approaches were developed to overcome the temporal resolution limitation, such as fusion with higher temporal resolution data (Walker *et al.*, 2012; Walker *et al.*, 2014), merging multi-year time series of images into a single one (Melaas *et al.*, 2013) and re-ordering (in time) Landsat images based on denser time series from a different sensor (Isaacson *et al.*, 2012; Baumann *et al.*, 2017). However, the accuracy of the phenometrics derived from the reconstructed Landsat series can be affected by land cover changes (natural and anthropogenic disturbances), land cover heterogeneity within the coarser spatial resolution data (used as reference) (Fisher *et al.*, 2006) and uncertainties introduced by the applied algorithm.

Therefore, at spaceborne level, phenology studies are commonly made using sensors with higher temporal resolution, but with coarser spatial resolution (> 250 m), such as the Advanced Very High Resolution Radiometer (AVHRR), Moderate Resolution Imaging Spectroradiometer (MODIS) and Satellite Pour l` Observation de la Terre (SPOT, VEGETATION programme) (Miao *et al.*, 2013). Although these satellites have a potential daily temporal resolution (the ideal scenario for vegetation phenology studies), in practice overcast conditions can significantly reduce this (Armitage *et al.*, 2013), potentially causing large gaps in the time-series (Soudani *et al.*, 2008). As some phenological events (e.g. leafing-out and leaf expansion) can happen relatively quickly (Polgar and Primack, 2011; Polgar and Primack, 2013), it is necessary to reconstruct a daily time series of satellite data in order to extract phenometrics of interest (Cong *et al.*, 2012).

Many approaches have been developed and modified to extract phenological markers from a time series of satellite data. These approaches usually follow two steps (Cong *et al.*, 2012; Wang *et al.*, 2014). In the first step, vegetation indices (e.g. NDVI and EVI), or other products derived from VIs (e.g. LAI and cover fraction), usually acquired on a weekly or biweekly basis, are reconstructed to a daily series, after having had noisy and spurious points filtered out, based on curve fitting approaches, such as Fourier filter (Roerink *et al.*, 2000; Studer *et al.*, 2007), Gaussian filter (Jonsson and Eklundh, 2002), Savitzky-Golay filter (Chen *et al.*, 2004), spline filter (White *et al.*, 2009), polynomial function (Piao *et al.*, 2006) or piecewise logistic functions (Zhang *et al.*, 2003). In the next step, critical thresholds are derived from the reconstructed daily time series in order to determine the timing (DOY) of vegetation changes, such as onset of greenup and senescence. This threshold is therefore

defined as a phenological marker since it is assumed to mark a specific phenological event (Reed *et al.*, 1994; Soudani *et al.*, 2008).

Different methods have been developed for calculating phenological markers from time series of data (Soudani *et al.*, 2008), and the most common may be sorted into two categories (White *et al.*, 2014; Filippa *et al.*, 2016): (1) Establishing either a local or global user-defined threshold, conceptualized as being able to represent key phenological changes (White *et al.*, 1997; Schwartz *et al.*, 2002; Chen *et al.*, 2004; Delbart *et al.*, 2005; White and Nemani, 2006; Studer *et al.*, 2007; Delbart *et al.*, 2015), and (2) Fitting a function and calculating markers from the curve properties (Zhang *et al.*, 2003; Fisher *et al.*, 2006; Beck *et al.*, 2007; Fisher and Mustard, 2007; Soudani *et al.*, 2008; Garrity *et al.*, 2011).

Exemplifying the first category (1), Studer *et al.* (2007) used an approach named "threshold method" to calculate SOS from NDVI acquired by AVHRR instrument onboard the National Oceanic and Atmospheric Administration`s (NOAA) Polar Orbiting Environmental Satellites at 10-day interval and 0.1° spatial resolution. In a full year reconstructed time series (via a Gaussian filter), a threshold was defined for each pixel as the midpoint between the minimum and maximum NDVI value. The DOY when the vegetation index value crosses this threshold marks the SOS for that pixel. In another example, Delbart *et al.* (2005) reconstructed an annual times series of Normalized Difference Water Index (NDWI), obtained with the sensor VEGETATION onboard SPOT, and defined an optimal threshold value to mark SOS as being 20% of the NDWI amplitude.

Rate of change of curvature exemplify the second category of methods used to define phenological markers. Zhang *et al.* (2003) were one of the first to use MODIS time series (1 km spatial resolution) to monitor vegetation phenology. EVI time-series were fitted by a series of piecewise logistic functions of time to characterize four key phenological transitions dates (phenometrics) at pixel level: green-up, maturity (growth period), senescence and dormancy (senescence period). For each growth and senescence period, the EVI time series was modelled using a sigmoid-based function of the form (Eq. (2-1)):

$$y(t) = \frac{c}{1 + e^{a+bt}} + d \qquad (2\text{-}1)$$

where *t* is time in days, *y(t)* is the VI value at time *t*, *a* and *b* control the timing and rate of increase, respectively, *c* + *d* is the maximum VI value, and *d* is the initial background VI value.

The phenological transition dates correspond to the times at which the rate of change in curvature in the vegetation index data exhibits local minima or maxima (second derivative), as shown schematically in Figure 2-2a, with results presented in Figure 2-2b for a mixed forest pixel. This study found that the phenological transition dates were "realistically" detected as the EVI returned a seasonal pattern linked with the annual life cycle of that forest (Figure 2-2b).

Thresholding methods, despite having been able to detect the general expected seasonal cycles of deciduous vegetated surfaces (Delbart *et al.*, 2005; Studer *et al.*, 2007), need an arbitrary threshold to be defined which in turn may not be applicable to all vegetated surfaces (Zhang *et al.*, 2006). This fact means that they might be not flexible enough to track complex spatio-temporal changes in phenology resulting from wider areas, due to variations in forest types, micro and regional climate regimes, topography, soils and land management (Zhang *et al.*, 2003; Fisher and Mustard, 2007; Bradley and Mustard, 2008). On the other hand, methods based on function proprieties are more flexible since each pixel will have its own fitting parameters to track changing phenology, i.e. each pixel`s trend is compared to itself instead of a threshold (Zhang *et al.*, 2006). This flexibility may justify the preference of the scientific community for deriving phenological markers using methods based on functions in the last 15 years (Fisher *et al.*, 2006; Fisher and Mustard, 2007; Soudani *et al.*, 2008; Richardson *et al.*, 2009; Liang *et al.*, 2011; Hufkens *et al.*, 2012; Polgar *et al.*, 2013; White *et al.*, 2014; Liu *et al.*, 2015; Baumann *et al.*, 2017). Among them, Zhang *et al.* (2003)`s logistic function itself or its modifications (Fisher *et al.*, 2006; Elmore *et al.*, 2012) seems to be the most used as some studies indicated that logistic-based functions can successfully monitor vegetation phenology from local to regional scales (Zhang *et al.*, 2003; Fisher *et al.*, 2006; Garrity *et al.*, 2011; Zhu *et al.*, 2012; Polgar *et al.*, 2013).
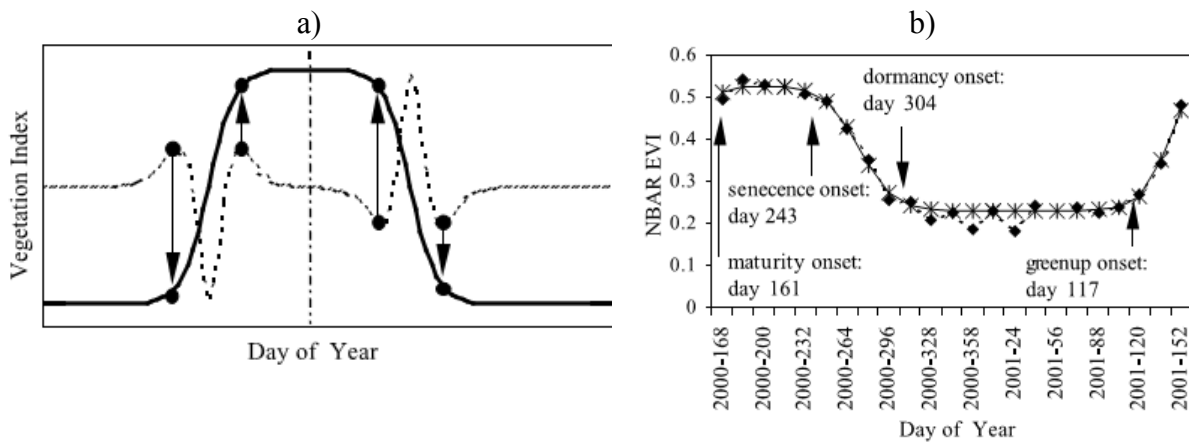
Figure 2-2: The method of rate of change in curvature is used to estimate phenological transition dates in a simulated (a) and a MODIS EVI time series of data (b). In a) the solid line represents the idealized time series and the dashed line its rate of change, whereas the closed circles mark the DOY of significant changes. Credits[4].

It has been proven that phenological markers derived from different methods can result in very different results (Reed *et al.*, 2009; White *et al.*, 2009; Wang *et al.*, 2014). In one study, White *et al.* (2009) conducted a comprehensive intercomparison of ten methods to derive SOS from satellite imagery time series (Table 2-4). The methods ranged from simple empirical approaches to more complex mathematical models. AVHRR NDVI data was used to estimate SOS over North America between 1982 and 2006 and it was found that the relative differences between the individual methods were up to ± 60 days and standard deviations up to ± 20 days. The ordinal ranking of the SOS methods was found to vary geographically, indicating that none of the SOS methods performed uniformly well, which echoes with study of Bradley and Mustard (2008). Similarly, but over East China, Wang *et al.* (2014) employed five methods to estimate SOS also from AVHRR NDVI and found the methods differing relatively each other by more than 100 days for some pixels.

---

[4] Reprinted from Zhang *et al.* (2003), with permission from Elsevier.

Table 2-4. Methods tested by White *et al.* (2009) to derive SOS from satellite imagery time series. The methods are grouped in three categories, from which the main advantages and limitations are presented.

Method	Category	Advantages	Limitations
Quadratic DMA HANTS-FFT Timesat	Conceptual-Mathematical	• The phenological development can be represented by functions; • It detects the period showing significant and rapid increase in VI time-series using numerical procedures (except Timesat); • They can be easily generalized, as each pixel`s trend is compared to itself instead of a threshold; • The Quadratic model allows other variables than spectral to be added to the model (e.g. temperature);	▪ The functions can have many parameters, making interpretations more difficult. HANTS, in particular, may be difficult understand, as the algorithm uses series of Fourier transform coefficients; ▪ DMA needs a user-defined time window size; ▪ In Timesat, SOS is defined as an arbitrary threshold; ▪ The algorithm can be computationally expensive, depending on the number of parameters;
NDVI 0.2 NDVI 0.3	Global threshold	• Simplest of methods, as a single threshold is fixed for a study area or ecoregion;	▪ Needs an arbitrary user-defined threshold, the value of which may not be optimal across different study areas;
Gausian	Hybrid	• The phenological development can be represented by functions; • A single threshold is fixed for a study area or ecoregion;	▪ Needs an arbitrary user-defined threshold, the value of which may not be optimal across different study areas;
Midpoint$_{pixel}$ PAT Midpoint$_{cluster}$	Local threshold	• Simple method. Compared to global threshold, a locally tuned threshold can be defined based on, for example, similar biological characteristics;	▪ It is necessary to define the extent and meaning of "local"; ▪ Needs an arbitrary user-defined threshold, the value of which may not be optimal across different study areas;

DMA = Delayed Moving Window; HANTS-FFT = Harmonic Analysis of NDVI Time Series - Fast Fourier Transform; PAT = Percentage Above Threshold;

Therefore, the works from White *et al.* (2009) and Wang *et al.* (2014) suggest that it might be necessary to test more than one method over a study area to assess the most precise one. Besides that, it has been shown that LSP monitoring can be also sensitive to the choice of

VIs (Reed *et al.*, 2009; White *et al.*, 2009; Garrity *et al.*, 2011; Hufkens *et al.*, 2012; Nagai *et al.*, 2014).

While the effectiveness of VIs can vary with environmental conditions (e.g. local climate, soil) and aim of the research (Rondeaux *et al.*, 1996; Hufkens *et al.*, 2012; White *et al.*, 2014), phenological studies have most commonly employed NDVI and EVI (Zhang *et al.*, 2003; Liang *et al.*, 2011; Liu *et al.*, 2015). Generally, EVI has been shown to be more appropriate than NDVI to track forest phenology (Liang *et al.*, 2011; Klosterman *et al.*, 2014; White *et al.*, 2014; D'Odorico *et al.*, 2015; Baumann *et al.*, 2017), which can be due to the EVI ability to remain sensitive to canopy changes at higher biomass (high LAI) (Huete *et al.*, 2002; Reed *et al.*, 2009). However, in some studies, EVI performed worse than NDVI (Hufkens *et al.*, 2012). Furthermore, mid-infrared based VIs (e.g. NDWI) have shown to be effective in detecting seasonal patterns of vegetation in regions of high snowfall (Delbart *et al.*, 2005; Delbart *et al.*, 2015).

Therefore, when different study areas are analysed or when different sensors are employed, different combinations of methods and VIs might need to be tested in order to assess the most suitable combination for phenology monitoring (Klosterman *et al.*, 2014; Filippa *et al.*, 2016). This can be determined by comparing the derived phenometrics against reference observations, i.e., validating the phenometrics, a subject which is discussed next.

2.6 Validation of phenological metrics derived from satellite imagery

It has been discussed that the multiple methodologies available to derive LSP phenometrics can give very different results (White *et al.*, 2009; Wang *et al.*, 2014). Validation of LSP phenometrics requires therefore a comparison with independent data, typically ground observations of species- or community-specific phenology (Liang *et al.*, 2011; Delbart *et al.*, 2015). Often, the most accurate methods to monitor tree phenology phases are through visual assessments of tree canopy development phases, which can be achieved by recording a phase when observing the plant (traditional method) (Liang *et al.*, 2011) and, more recently, interpreting phenophases from red-green-blue (RGB) cameras positioned either over (most common) (Hufkens *et al.*, 2012) or under the canopy (Fisher *et al.*, 2006). However, this approach is not free of uncertainties and some studies have reported differences of up to 7 days among different observers (Schaber, 2002; Klosterman *et al.*,

2014), which is due to the degree of subjectivity involved when visually assessing a canopy (Table 2-1).

Nevertheless, these data are considered ideal given their explicit biophysical meaning (Schwartz *et al.*, 2002; Liu *et al.*, 2015), but might lack landscape representativeness. On the other hand, satellite imagery has the potential to track phenology patterns over continental scales but might have large uncertainties (Fisher and Mustard, 2007; White *et al.*, 2009). In this sense, many studies have been devoted efforts to developing approaches to consistently validate LSP metrics based on ground observations.

LSP metrics have been derived at various scales, ranging from (infrequently) a few dozens of metres (e.g. using Landsat, Fisher *et al.* (2006)), a few hundreds of metres (using MODIS, Liang *et al.* (2011)), to kilometres (using MODIS, Zhang *et al.* (2003), AVHRR, White *et al.* (2009) and the SPOT`s VEGETATION S10, Delbart *et al.* (2015)). At any of these scales, one of the biggest challenges for validating LSP metrics is to have ground phenology data which are representative of the variability in phenology events occurring within the whole pixel area (Delbart *et al.*, 2005; Liang *et al.*, 2011). Over forests, this variability mainly arises from heterogeneity in tree species composition and heterogeneity in timing of phenological events, since phenology events can vary among species (interspecific variations) and within species (intraspecific variations) (Delbart *et al.*, 2005; Fisher *et al.*, 2006; Polgar and Primack, 2011). Validation studies conducted over more homogeneous deciduous forests, such as taiga in Siberia (Delbart *et al.*, 2005), tundra in low-arctic ecosystem (Delbart and Picard, 2007) and taiga in boreal Eurasia (Delbart *et al.*, 2008), have shown that even a low density of ground plots (in relation to the pixel area) might achieve accurate results.

In one study, NDVI and NDWI from SPOT`s VEGETATION S10 10-day composite at ~1 km spatial resolution were used to estimate SOS and Start Of Fall (SOF) by Delbart *et al.* (2005). SOS and SOF were determined by testing different methods (user-defined thresholds and functions). *In situ* phenological observations of 3 tree species from ten taiga sites were used to validate the LSP metrics. In each site the mean DOY for first leaf appearance and the mean DOY for beginning of leaf colouring was calculated. SOS and SOF from pixels surrounding each *in situ* measurement point (pixels with large proportions of deciduous trees) were compared to *in situ* phenology. For SOS, the best results were obtained with NDWI (RMSE=8.7 days; R^2=0.75) using a user-defined threshold method. For SOF, the estimations with the best results were obtained using NDVI (RMSE=16 days; R^2=0.01) and a

different user-defined threshold method. For the SOS estimate, a RMSE of 8.7 days can be considered a good result given that each point measurement (*in situ* data) was compared to LSP within a 26 km^2 area (~26 pixels) surrounding the site. This result can be explained by a combination of: 1) low tree species diversity; 2) large deciduous forest fractional cover (agreeing with Klosterman *et al.* (2014)), and 3) observed leaf appearance dates being highly uniform for the different deciduous species assessed, with average time difference between species of <3 days (SD = 4.7 days). In contrast, the observed DOY of beginning of leaf senescence differed up to 40 days among species, which might explain the poor agreement with SOF or, it might indicate that the method was inappropriate for autumnal events comparisons. It can be also noted that the best combination of "method + VI" for estimating leaf appearance was not the same as for detecting autumn events, suggesting that both methods and data inputs for detecting phenometrics might be sensitive to the season being monitored, in agreement with other studies (Zhao *et al.*, 2012; Klosterman *et al.*, 2014).

However, even when forests with low species diversity are analysed, if the ground data is not able to adequately sample all species present, the uncertainties can increase. For example, Beck *et al.* (2007) used a six year time series of 16-day composite MODIS NDVI (250 m) to map LSP in Fennoscandia and the Kola peninsula. A double sigmoid model fitted the time series from which both the DOY of SOS and EOF (End Of Fall) were estimated and compared with ground observations of the date of onset of leafing and the date of end of leaf fall in birch (the most common deciduous tree species), respectively. The ground phenology (data points) were compared with metrics from 5 x 5 km windows centred over the ground observations locations, yielding a R^2=0.48 and RMSE=12 days (*n*=108) for SOS and R^2=0.44 and RMSE=10 days (*n*=26) for EOF. Even though they managed to validate the MODIS-derived SOS and EOF over many sites spread over larger areas, they achieved only a moderate correlation. The authors commented that although the ground observations came from dominant tree species, their abundance varied among sites, meaning that other non-observed species were present, for which phenology was not considered. Besides this, the authors used ground observations surveyed by citizens interested in nature (Jorde, 2016), which has the potential to provide ground observations spread over wider regions, increasing the sample size, but it is often not possible to check the quality of these volunteered data, a difficulty also reported in other studies (Delbart *et al.*, 2015; Mehdipoor *et al.*, 2015).

Ideally, comparing ground phenology observations of trees to LSP-derived phenometrics entails the observed trees being representative of the trees species within the pixel area and observations made at an appropriate frequency (Liang *et al.*, 2011; Delbart *et*

al., 2015). This might be challenging when the following factors are present alone or combined: different land cover types, accentuated slope terrains, high plant species diversity and pronounced heterogeneity in timing of phenological events (Fisher *et al.*, 2006; Polgar and Primack, 2011; Delbart *et al.*, 2015). Some methods have been suggested to tackle such challenges, which include using high medium resolution imagery (Fisher *et al.*, 2006; Melaas *et al.*, 2013; White *et al.*, 2014), cross-comparing results obtained at different spatial resolution (Fisher and Mustard, 2007), using ground and near-surface sensors (Hufkens *et al.*, 2012; Hmimina *et al.*, 2013) or increasing the intensity of ground observations within the pixel (Liang *et al.*, 2011; Liu *et al.*, 2015). These methods are presented in the following sub-sections, where advantages and limitations are discussed.

2.6.1 Using high spatial resolution imagery and ground data with high representativeness

As discussed previously, Landsat is the satellite data with the finest spatial resolution used in phenology studies. For this reason, this sub-section presents studies which have investigated the potential of Landsat for monitoring of local/regional scale LSP and also its potential to understand variability in phenology within coarser spatial resolution sensors (e.g. MODIS). Finally, a few studies using a high intensity of ground data to validate LSP are discussed.

In 32 plots spread over mixed and homogeneous stands, trees located within 20 m of the plot centre had their spring phenology phases (from no buds to leaves fully expanded) visually ranked by White *et al.* (2014). To scale from tree to plot level, they calculated a plot average rank (PR) based on a species average weighted by its plot percent basal area. NDVI and EVI time series from 12 Landsat images (30 m spatial resolution) were fitted by five different sigmoidal models in order to test the best combination of "VI + method" for estimating SOS. For this, the mean absolute difference between PR and Landsat-derived SOS was calculated, averaged across all plots. SOS derived from EVI time series, fitted with the sigmoid model described by Zhang *et al.* (2003), compared best to full leaf out date achieving a $R^2 = 0.95$ and a mean absolute error for all plots types equal to 11 days. The authors noted that the tested methods and VIs were not accurate to detect bud-break (green tip of leaf showing) and the first unfolded leaves, suggesting that the reflectance signal of these events are not strong enough to significantly alter the reflectance signal within the pixel, which is in accordance with other authors (Fisher *et al.*, 2006; Liang *et al.*, 2011; Henebry and de Beurs, 2013).

However, White *et al.* (2014) noted VIs increasing slowly from the winter baseline prior to leaf development, which could be a clue of the first development of bud burst, but it was inferred to be more likely due to the greening up of understorey vegetation, which is expected to occur earlier than for the forest canopy (Ahl *et al.*, 2006; Richardson and O'Keefe, 2009; Calders *et al.*, 2015; Pisek *et al.*, 2015). The above findings demonstrate therefore that the start of growing season estimated from LSP (which was associated with the DOY of full leaf out) is highly likely to be different from the start of growing season as observed from dominant trees (e.g. DOY of bud-break), a fact which is expected in LSP studies as satellites integrate ecosystem processes rather than species-specific events (Garrity *et al.*, 2011; Polgar and Primack, 2011; Henebry and de Beurs, 2013). Finally, White *et al.* (2014) investigated effects of heterogeneity and found that when the analysis was restricted to only homogeneous stands the accuracy improved from 11 to 7 days mean absolute error. This latter result suggests that even at Landsat 30 m spatial resolution, mixed composition is still an issue, most likely due to interspecies differences (Lechowicz, 1984; Rötzer *et al.*, 2004).

White *et al.* (2014) were able to monitor phenology of a spring season with Landsat images mainly because they concentrated their study area within overlapping paths, which in turn allowed them to have a relatively high temporal resolution of (partially) cloud-free images (~3 images per month). However, in non-overlapping areas and places with frequent cloud cover, the temporal resolution of useful Landsat images can drop to a few per year (Fisher *et al.*, 2006), making their use in phenology studies very difficult. Aware of this problem, Fisher et al. (2006) developed an approach which consists of compositing multi-years of (partially) cloud-free images into a single year of observations in order to increase Landsat temporal resolution.

The method of Fisher et al. (2006) consists of applying weights for each pixel based on greenness fraction (GF) and thermal data (Landsat band 6). Pixels containing temporal anomalies in temperature (e.g. due to clouds) and GF with high RMSE values are down-weighted during the curve fit. To account for interannual variability, all scenes from a given year are phase shifted from a global mean. The GF pixel values were fitted by logistic functions in order to estimate the DOY of SOS. On the ground, spring-time observations were conducted on deciduous forest plots in southern New England; for each plot multiple photographs were taken and used to later on visually rank the phenological development phases from dormancy to full canopy. The ground-observed dates of leaf onset were compared to SOS from coincident pixels, yielding a strong relationship ($R^2 = 0.91$). Although the approach was effective in scaling from plot to Landsat scale, the analysis was constrained

to homogenous stands of deciduous forests. It was also observed that the date of leaf onset was negatively dependent of elevation (R^2 = 0.82), in agreement with more recent observations (Vitasse *et al.*, 2009; Klosterman *et al.*, 2014; White *et al.*, 2014), a fact which is reflected in Landsat-derived SOS varying consistently by over 2 weeks within <1 km in forested areas with accentuated differences in elevation. This fact highlights the challenges of scaling-up phenological field-observations to regional and global scales using coarser spatial resolution satellites, due to spatial heterogeneity in timing of phenology events (Fisher and Mustard, 2007). It can be noted that perhaps the main difficulty in replicating Fisher *et al.* (2006)`s approach is to ensure that the forest under analysis doesn`t suffer any human or natural disturbance (e.g. changes in land use or ecological succession) throughout the multiple years of interest which are merged into a single 'average' year. Besides that, multi-year analysis is prevented as the output is a single year time series.

Fisher and Mustard (2007) expanded their previous work (Fisher *et al.*, 2006) by comparing both ground-based phenology and Landsat-based phenology (30 m) to MODIS-based phenology (500 m). Eighteen years of Landsat imagery and six years of MODIS imagery were compressed into a single year, from which time series the SOS was calculated similarly to Fisher *et al.* (2006). Firstly, the Landsat-derived estimates were aggregated up to MODIS scale and comparisons were made only in deciduous dominated MODIS pixels (Landsat-derived vegetation maps were used to isolate the MODIS pixels with at least ~50% of deciduous vegetation). The SOSs estimated by Landsat and MODIS resulted in a moderate relationship (R^2 = 0.60) with a mean Landsat variance within a MODIS pixel of ±5.7 days. This variance indicates how much of the fine-grain spatial variability of vegetation phenology cannot be captured within a 500 m pixel and is therefore lost at coarser scales. In the second step, MODIS-based estimates from 10 selected pixels were validated against ground observations of deciduous forests from two experimental forests in New England, in a six year comparison. Within each forest boundary, the ground-based date of onset (average/year) was compared against the MODIS-based estimate (average/year). MODIS followed the general interannual phenological patterns as observed in the field, predicting 86% of the variance in one forest and 70% on the other. The latter result was attributed to a more heterogeneous topography on that site, agreeing with Fisher *et al.* (2006).

Aware of the significant spatiotemporal scale mismatch between LSP and ground phenology, Liang *et al.* (2011) developed a step-wise landscape scaling approach to validate MODIS-derived phenology through the use of intensive ground observations and high spatial resolution imagery. 288 ground plots were sampled within two 625 x 625 m study areas

(mixed seasonal forest), which yielded ~23 plots within a MODIS pixel area (250 m spatial resolution). Percentages of phenology phases, varying from buds starting to appear to leaves fully expanded, were recorded at a bi-daily frequency. The methodology consists of two main steps: upscaling individual phenology observations to landscape phenology (LP) and adjusting MODIS pixels values. In the first step, *in situ* phenology observations were averaged to generate population phenology. Afterwards, high spatial resolution images (IKONOS 1 m and QuickBird 4 m) were used to delineate forest community's boundaries and also to estimate proportions of deciduous and conifer cover, the results of which were used as input to generate community phenology patterns. Finally, these patterns were related/regressed to ground observations to generate maps of the so-called landscape phenology (LP) indices over the whole study area, with values used as validation data for MODIS-derived SOS. The LP map is therefore spatially continuous information derived/extrapolated from visual observations of canopy phenology.

In the second step of Liang *et al.* (2011)'s methodology, a QuickBird-based NDVI change map was applied to weight MODIS NDVI and EVI time series, from which the DOY of SOS was estimated. For deciduous cover, EVI-based SOS achieved a mean absolute error <3 three days compared to the LP (full bud burst dates), but for NDVI the differences were up to 15 days. In a subsequent work, Liu *et al.* (2015) tracked temporal dynamics of autumn (instead of spring) phenology over the same area and using the same method described by Liang *et al.* (2011). Liu *et al.* (2015) found that MODIS-based EOF differed from LP (full leaf coloration date) by 5 days on average (ranging from 0 to 12 days).

These two studies (Liang *et al.*, 2011; Liu *et al.*, 2015) indicate that, if the ground data set is able to account for the spatial heterogeneity in timing of phenological events and heterogeneity in species composition within a pixel area (spatio-temporal variability), then the uncertainties in the estimated phenodates can be diminished, in accordance with suggestions from others studies (Polgar *et al.*, 2013; Wang *et al.*, 2014; Delbart *et al.*, 2015). However, such highly intense ground campaigns can be time consuming and labour intensive, which might constrain multi-year monitoring and replication in different study areas. This also demands high resolution images from at least two different dates in order to delineate and differentiate deciduous communities, which are generally not freely available.

2.6.2 Ground and near-surface remote sensing of phenology
Ground-based and near-surface sensors have been increasingly used to collect data for LSP validation purposes (among other purposes) in substitution or in complement to

traditional ground observation (Ryu *et al.*, 2012; Zhao *et al.*, 2012; Nagai *et al.*, 2014; Nagai *et al.*, 2015). Imaging and radiometric sensors are used to automatically collect very high temporal resolution of phenological time series (daily or sub-daily), providing species-specific and/or ground LSP observations (Hmimina *et al.*, 2013; Klosterman *et al.*, 2014).

Consumer-grade cameras are usually employed as imaging sensors and the aim is to monitor changes in canopy colour associated with the different plant development stages (Moore *et al.*, 2016). Because the RGB DN values stored across the multiple scenes can be strongly affected by the varying illumination conditions (Woebbecke *et al.*, 1995; Richardson *et al.*, 2007), colour indices are calculated in order to diminish this effect and allow consistent time series to be generated (Sonnentag *et al.*, 2012). The Green Chromatic Coordinate (GCC, Eq. (2-2)) has been successfully used to track green leaf phenology (Sonnentag *et al.*, 2012; Klosterman *et al.*, 2014; Moore *et al.*, 2016), but a variety of other indices can potentially be formulated (Mizunuma *et al.*, 2014), dependent upon the objective of the study (Zhao *et al.*, 2012).

$$GCC = \frac{G}{G + R + B} \qquad (2\text{-}2)$$

where *R*, *G* and *B* are DNs values in the red, green and blue channels.

Because a quantitative time series of data is generated, the series can be processed similarly to satellite time series, i.e., phenometrics can be automatically calculated (Filippa *et al.*, 2016), allowing a more direct comparison (in relation to visual assessments) with orbital-derived phenology (Hufkens *et al.*, 2012). In this section, some examples of ground and near-surface remote sensing data are presented in more detail, with comparisons with visual assessments presented first, followed by comparisons with satellite measurements.

(a)

(b)

(c)
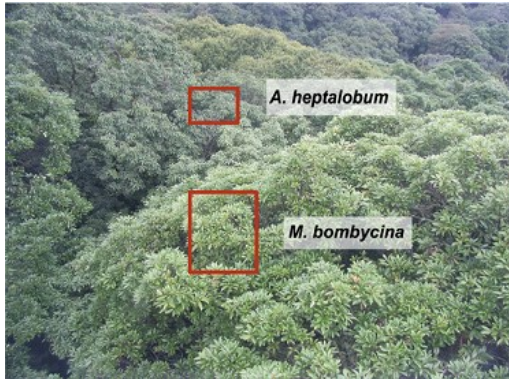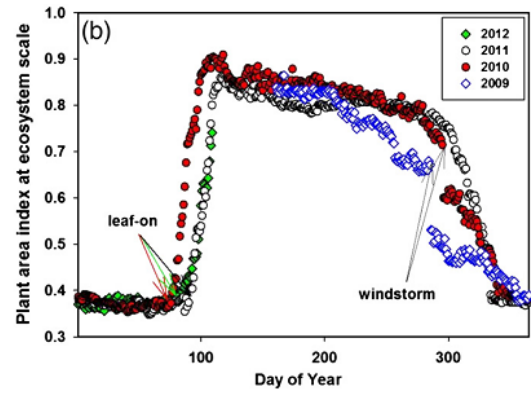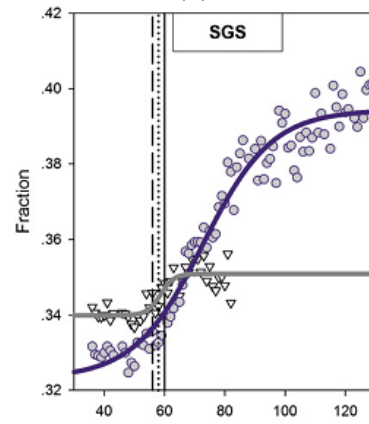
(d)

Figure 2-3: (a) Sample image from an upward-pointing digital camera; (b) Plant area index (PAI) derived from (a) and used to estimate leaf-out and leaf-senescence dates in an open canopy savannah; (c) Sample image (tower-based camera) showing the area of interest monitored for *Acer heptalobum* and *Machilus bombycina*; (d) Sigmoid regressions fitted with colour indices (RF: red fraction, GF: green fraction) for estimating the time of phenological event in *A. heptalobum* (SGS: start of growing season). [5]Credits for (a) and (b); [6]Credits for (c) and (d).

Ryu *et al.* (2012) used three upward viewing cameras (50 m apart) to monitor an open canopy savannah (Figure 2-3a) over 4 years, with daily Plant Area Index (PAI) estimated (Figure 2-3b). Zhang *et al.* (2003)`s method was applied in order to estimate SOS (related to leaf-out date) and EOF (related to leaf-senescence date); comparison with *in situ* observations gave a mean bias of 5 days and RMSE of 5.4 days for leaf-out and a mean bias of 2 days and RMSE of 4.8 days for leaf-senescence. Zhao *et al.* (2012) also used Zhang *et al.* (2003)`s method to fit daily colour indices (Figure 2-3d) from two digital cameras at 30 m height (Figure 2-3c) to estimate SOS (leaves begin to appear), Start of Fall (SOF, start of leaf senescence, i.e. leaves begin to change colour) and EOF (end of leaf senescence, i.e., tree become leafless) dates for three tree species (at different sites). They found differences

---

between observed (by visual assessment of the original images) and estimated phenological dates ranging from -4 to 1 days.

A similar mean absolute error for start of growing season (4 days) was found by Bater *et al.* (2011), who compared phenometrics from near-surface digital cameras to field-based observations of phenological phases at seven sites. Klosterman *et al.* (2014) found higher uncertainties between near-surface remote sensing-derived phenometrics and visual assessments (RMSE = 7 days for start of spring and RMSE = 22 days for start of fall). Generally, spring phenology is predicted more consistently than autumn phenology (Bater *et al.*, 2011; Zhao *et al.*, 2012; Klosterman *et al.*, 2014).

Therefore, even using fine detail data (in both spatial and temporal resolution), uncertainties exist and can be substantial dependent upon the data, method and phenological season being evaluated. Nevertheless, because the visual assessments also contain uncertainties (Schaber, 2002; Klosterman *et al.*, 2014), ground and near-surface estimates are expected to have higher accuracy than the comparisons with visually assessed dates (Klosterman *et al.*, 2014). For this reason, and because they can allow more objective and direct comparisons with spaceborne measures to be undertaken, ground and near-surface remote sensing using RGB cameras to monitor tree phenology have been increasingly used as an option for validating LSP (Richardson *et al.*, 2007; Hufkens *et al.*, 2012; Sonnentag *et al.*, 2012; Brown *et al.*, 2016).

Hufkens *et al.* (2012) compared near-surface (RGB cameras) and satellite (MODIS) remote sensing-based observations of vegetation phenology in four deciduous broadleaf forest sites; one camera was installed in each site. MODIS data (EVI, NDVI and ExG) were extracted for 5 x 5 pixel (~2.3 x 2.3 km) regions centred over the location of each camera site. ExG was calculated from daily RGB images. A logistic model (Zhang *et al.*, 2003) was used to fit both the MODIS and RGB camera VI time series and to estimate phenological metrics related to the dates of onset of green-up and senescence. In terms of seasonal trends, both RGB cameras and MODIS returned a similar pattern. However, differences arose when phenological metric dates were compared, with mean absolute errors ranging from 3 to 67 days, depending upon the MODIS data, metric and site analysed. Therefore, this study suggests that near-surface sensors have potential to be used as validation data for satellite estimates; however, such approaches have a number of common limitations.

Firstly, dependent upon the sensor location, only a small area and reduced number of trees can be observed per sensor (Ryu *et al.*, 2012; Zhao *et al.*, 2012), which is a constraint in

obtaining a conclusive result about the phenology of some species, since phenology events can vary among species (interspecific variations) and within species (intraspecific variations) (Polgar and Primack, 2011). Moreover, this constrains the ability to compare the results with satellite data as satellite sensors` pixel area is generally much larger than the area viewed by these *in situ* sensors (Hufkens *et al.*, 2012; Richardson *et al.*, 2013b; Klosterman *et al.*, 2014); Secondly, issues of calibration and long-term stability of the imaging sensors are not yet fully addressed (Henebry and de Beurs, 2013; Keenan *et al.*, 2014), raising questions about how to use such data for validation purposes and how to compare data between different cameras and different sites; Thirdly, cameras above the canopy are usually inclined at a fixed position (e.g. 45°), meaning that phenocams and satellite may have very different zenith angles when acquiring images; additionally, this oblique angle can impact on data quality as more distant targets will have weaker signals and stronger atmospheric influence (Richardson *et al.*, 2009) and the effective LAI incorporated within a phenocam's FOV can be greater than for the same sensor mounted at a nadir position (Brown *et al.*, 2017). Fourthly, variations in illumination geometry throughout the year can affect the temporal trajectory of derived VIs (Brown *et al.*, 2017). Fifthly, at sites characterised by medium to high satellite VIs, phenocam-derived VIs can saturate asymptotically when compared with satellite-derived VIs, as phenocams usually do not incorporate near-infrared wavelengths resulting in a lower sensitivity to LAI increments than satellite VIs (Brown *et al.*, 2017). Finally, near-surface cameras (although low-cost) are normally installed on tall towers, the construction of which, in forests, can be difficult and expensive (Nagai *et al.*, 2013), consequently making it difficult to sample many locations.

Some of these challenges have been addressed or are subject of on-going research. Calibration issues are minimized by using a same camera model in as many sites as possible, and by adopting standard protocols for data acquisition (Brown *et al.*, 2016). An expansion of camera networks (referred to as phenocams) worldwide allows broad geographic areas and different biomes to be represented (Toomey *et al.*, 2015; Filippa *et al.*, 2016), with efforts being made towards a global phenocam network (Brown *et al.*, 2016). As an example, the PhenoCam network (Richardson *et al.*, 2007) monitors hundreds of sites (mainly in North America); but there are a few more networks fully operational in Europe, Asia and Australia (Moore *et al.*, 2016). Besides this, studies have being investigating the potential of using traffic and security cameras for phenology purposes (Morris *et al.*, 2013; Bothmann *et al.*, 2017), which could increase dramatically the number of sampling locations and diminish

installation costs. Furthermore, additional instrumentation is usually available (e.g. temperature sensors), which can supply with extra ground-truth data (Moore *et al.*, 2016).

Klosterman *et al.* (2014) used near-surface camera (phenocam) observations from 13 sites across US to evaluate MODIS phenology. Phenology transition dates of canopies (up to 100 trees per site) were automatically extracted from the near-surface images (GCC time series). EVI and NDVI median values from a 3 x 3 window centred at the plot centre were calculated from MODIS (500 m spatial resolution). The remote sensing data were fitted by sigmoid-based models. The comparison between MODIS- and phenocam-derived metrics showed various degrees of correspondence (dependent on "method + VI"), ranging from 7 to 18 days (RMSE) for SOS and ranging from 14 to 28 days (RMSE) for SOF, with MODIS EVI better matching near-surface remote sensing. Despite gaining a better understanding of the links between LSP and canopy phenology in different ecosystems, there were still localized discrepancies associated with spatial scale and areal representativeness. Even though phenocams provide a means for direct comparisons with satellites phenometrics, the precise areal representativeness of the phenocam images are usually not known as they are not georeferenced. A defined region of interest within a phenocam image is therefore assumed to represent the satellite pixel(s) area.

In another study, phenocams from eight sites (pure and mixed deciduous forests) across US were used to validate Landsat and MODIS phenology (Baumann *et al.*, 2017). Over these sites, time series of Landsat images were reconstructed/densified based on temporal profiles of MODIS data, which allowed Landsat phenology curves to be extracted from a 12 year period. Phenometrics related to spring and autumn season were extracted from Landsat EVI, MODIS EVI and phenocam ExG via curve fitting. The spring phenometrics (start, middle and end of spring season) were cross-compared for the years when the phenocam data were available and showed an average coefficient of correlation of ($n = 29$): (a) phenocam vs. Landsat (r = 0.85), (b) phenocam vs. MODIS (r = 0.79) and, (c) Landsat vs. MODIS (r = 0.88), with relationships being slightly weaker in autumn. The phenodates of growing season were estimated later by the orbital sensors, in comparison to phenocam (Landsat up to 12 days and MODIS up to 18 days later). The good agreement between phenometrics estimated from the Landsat synthetic series and from the ground data could encourage phenology studies with Landsat data beyond only overlapping scenes (White *et al.*, 2014; Melaas *et al.*, 2016). Nevertheless, uncertainties exist and part of it could be due the algorithm used to reconstruct the Landsat series. Besides that, MODIS and Landsat are not independent observations anymore, which prevent the use of Landsat to validate MODIS.

Finally, this work seems to reflect a current tendency, which is using ground/near-surface remote sensing data for validating LSP rather than visual assessments (Brown *et al.*, 2016; Bothmann *et al.*, 2017).

2.6.3 Spectral radiometers

Although less common, near-surface remote sensing of phenology has also used methods based on spectral radiometers (Jenkins *et al.*, 2007; Eklundh *et al.*, 2011; Hmimina *et al.*, 2013; Nagai *et al.*, 2015). Sensors are usually installed on towers, at a height well above the canopy and inclined towards the target of interest (Eklundh *et al.*, 2011). The reflected radiance of the viewed surface is measured at a high temporal frequency, allowing dense time series of spectral reflectance and vegetation indices to be calculated and used to track vegetation phenology (Hilker *et al.*, 2011; Nagai *et al.*, 2015).

In one study, Hmimina *et al.* (2013) used *in situ* NDVI measurements (daily resolution) from 4 radiometers installed on towers above three different deciduous forests and one evergreen forest for comparison with NDVI from MODIS (250 m spatial resolution, 16-day composite and daily). The *in situ* sensor was inclined 30° looking downward with a field of view (FOV) of 100°, with areal representativeness calculated to be between 80% and 96% for the main tree species within a MODIS pixel, based on basal areas ratios. MODIS-based NDVI time series showed a strong relationship over deciduous forests ($R^2 = 0.92$), but weak relationship ($R^2 = 0.14$) over evergreen forest (which was suggested to be due to low seasonal variation in LAI and leaf chlorophyll content, with this response potentially having the same magnitude as satellite sensor noise). Spring and autumn phenological metrics were thereafter extracted from the *in situ* and orbital NDVI fitted time series, and cross-compared. Spring metrics were better correlated ($0.80 \leq R^2 \leq 0.97$) than autumn metrics ($0.04 \leq R^2 \leq 0.56$). The best agreements were found for the middle of season metrics ($4 \leq RMSE \leq 4.5$ days for spring; $6 \leq RMSE \leq 8$ days for autumn), rather than start of growing season ($3 \leq RMSE \leq 11$ days), start of senescence season ($14 \leq RMSE \leq 14.5$ days) and peak ($14 \leq RMSE \leq 14.5$ days) and end ($10 \leq RMSE \leq 10.5$ days) of growing season ($14 \leq RMSE \leq 22$ days) (results which were dependent upon using either 16-day composite or daily MODIS data).

These best results for middle of season metrics (RMSE < 1 week) were explained to be due to middle of season metrics being less sensitive to data gaps, agreeing with Hufkens *et al.* (2012). Finally, an interesting finding from Hmimina *et al.* (2013)`s work is that while *in*

situ NDVI was able to track the seasonal changes from the evergreen forest, the MODIS sensor was insensitive to the changes, highlighting the need for new sensors or methods to track the less pronounced seasonal changes over evergreen forests (Wu *et al.*, 2017).

The drawback of using non-imaging sensors or not using traditional visual assessment as validation data (Garrity *et al.*, 2011; Soudani *et al.*, 2012; Hmimina *et al.*, 2013) is that it might be difficult to be conclusive about which phenological phase the data actually represent. It can also be problematic because the footprint of the spectroradiometer is often much smaller than that of orbital sensors (Nagai *et al.*, 2014; Nagai *et al.*, 2015), although Hmimina *et al.* (2013) achieved a representativeness of around 90% of the forest within a MODIS pixel. On the other hand, high temporal resolution data (sub-daily) can be acquired (Nagai *et al.*, 2014) and the resulting measurements are analogous to quantities measured by satellites (Richardson *et al.*, 2013b), allowing tracking of the seasonal dynamics of the ecosystem in a manner similar to satellite sensors (Hmimina *et al.*, 2013), if the *in situ* sensor is representative of the area within the pixel.

2.6.4 Carbon dynamics of vegetated surfaces

Carbon fluxes of vegetated surfaces can be estimated by eddy covariance instrumentation (Wu *et al.*, 2017). Once the carbon balance of an ecosystem is calculated, it is possible to characterize whether this system is acting as a sink or source of carbon over time (Wilkinson *et al.*, 2012; Mizunuma *et al.*, 2013). Because digital cameras (phenocam) are usually co-located at these instrumentation sites, the seasonal cycles of canopy photosynthesis (carbon fluxes) can be investigated in terms of camera-derived canopy developments (Toomey *et al.*, 2015), as shown in Figure 2-4. Ultimately, carbon seasonality can be used to understand satellite LSP metrics in terms of physiological processes (Wu *et al.*, 2017).

Moderate to strong correlations between colour indices (near-surface remote sensing) and canopy photosynthesis were found across a variety of plant functional types (Richardson *et al.*, 2007; Richardson *et al.*, 2009; Mizunuma *et al.*, 2013; Toomey *et al.*, 2015). However, relationships generally weakened when ecosystem productivity was compared to satellite-derived land surface phenology (Mizunuma *et al.*, 2013; Wu *et al.*, 2017).

In a comprehensive study, Toomey *et al.* (2015) used data from 17 towers (eddy covariance and phenocam) monitoring deciduous and evergreen forests and crops/grasslands across North America. Time series of Gross Primary Productivity (GPP, in units of grams of carbon per square meter per day) and colour indices were generated for 59 site-years. The

temporal trajectory of colour indices was found to parallel the temporal profile of GPP (Figure 2-4 and also noted by Mizunuma *et al.* (2013), Richardson *et al.* (2009)), with GPP achieving better correlations with canopy greenness at deciduous forests ($0.50 \leq R^2 \geq 0.79$) and grasslands/crops ($0.80 \leq R^2 \geq 0.90$), than at evergreen sites ($0.53 \leq R^2 \geq 0.76$). Relationships between GCC and GPP at evergreen sites were notably phase-shifted, with GCC increasing in value earlier than GPP in spring and decreasing later in autumn (middle graph in Figure 2-4), as also noted by Richardson *et al.* (2009). It is inferred that seasonal changes in leaf pigmentation (chlorophyll content) of existing needles may be driving the temporal pattern depicted by the colour indices rather than the appearance of new needles and shed of old ones (Richardson *et al.*, 2009; Sonnentag *et al.*, 2012; Toomey *et al.*, 2015).
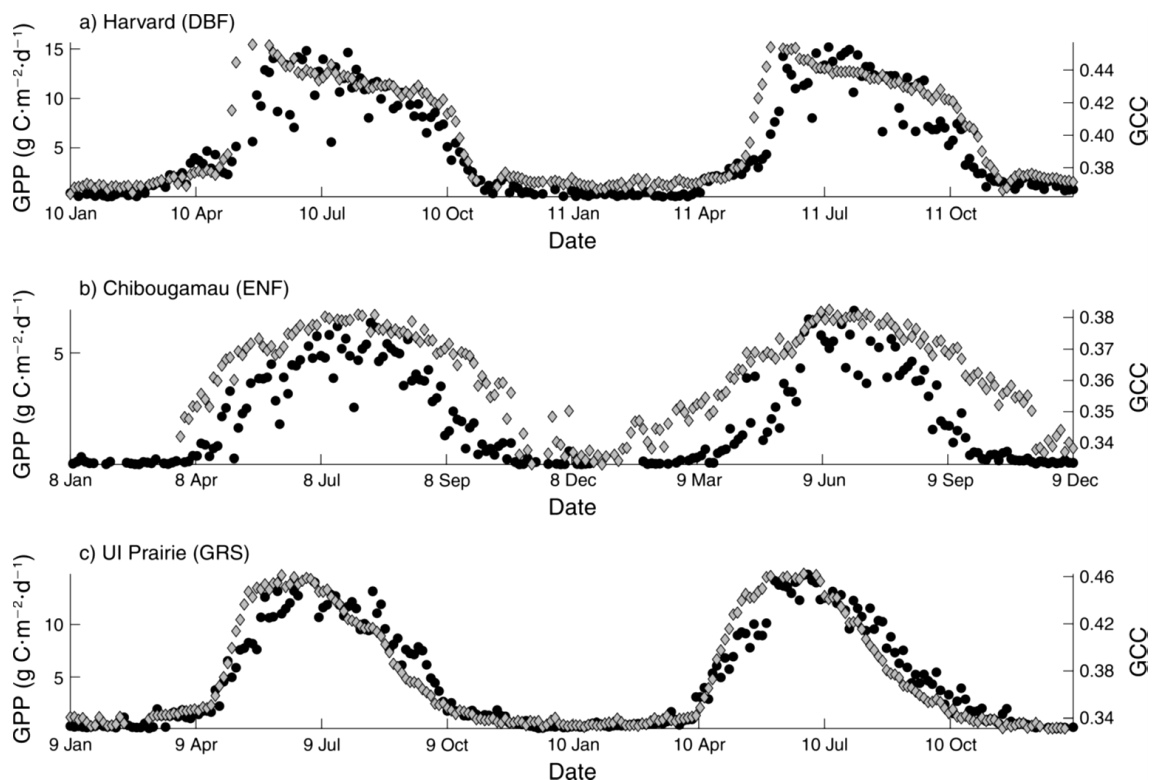
Figure 2-4. Example comparison of time series of GPP (grams of carbon per square meter per day) and the colour index GCC over a deciduous forest (top), evergreen forest (middle) and grassland (bottom), in US. GPP is represented by black circles. Credits[7].

Thereafter, phenophase transition dates from the colour indices time series were compared with transitions dates of GPP (Toomey *et al.*, 2015). Canopy greenness was effective in estimating the beginning and middle of the photosynthetically active period in deciduous forests and crop/grasslands ($0.60 < R^2 > 0.85$), but not in evergreen forests (due to the

---

off phased pattern). However, GCC was not able to accurately detect when GPP increased from zero (i.e., when the ecosystem changed from source to sink of carbon), but rather when GPP reached ~23% of the spring amplitude. For fall events, canopy redness was a better predictor of GPP (R^2~0.6) than greenness indices (R^2~0.4), and the end of growing season, as predicted by the redness index, was better matched to ~15% of the GPP fall amplitude (rather than when GPP became near zero, i.e., when it became a carbon source).

Toomey *et al.* (2015) also found GPP reaching its maximum value 2-4 weeks after the GCC "green peak" in deciduous covers (also noted by Mizunuma *et al.* (2013), Sonnentag *et al.* (2012)), suggesting that deciduous ecosystems keep increasing in photosynthetic capacity until after the maximum greenness value. Nevertheless, the GPP-GCC summer peak occurred at the same time over the evergreen sites. Secondly, only moderate correlations between GPP and canopy greenness were observed in some site-years. The rate of photosynthesis is dependent not only upon canopy biophysical changes (well captured by phenocams) but other abiotic factors (e.g. soil moisture and solar radiation input (Wilkinson *et al.*, 2012)), which can vary from year to year and affect the forest productivity but not canopy colour indices (e.g. GCC) (Mizunuma *et al.*, 2013; Toomey *et al.*, 2015).

Comparing carbon phenology with satellite phenology has proved to be more challenging. Garrity *et al.* (2011) compared LSP phenometrics with carbon flux phenology (CFP), spanning 11 years of eddy covariance measurements over a mixed deciduous forest in Michigan. 13 different data sources were tested to estimate the timing of phenological events, with 10 of them derived from MODIS: NDVI-250 m (1 pixel), NDVI-750 m (3x3 pixels), NDVI-1500 m (5x5 pixels), EVI-250 m (1 pixel), EVI-750 m (3x3 pixels), EVI-1500 m (5x5 pixels), LAI-1 km (1 pixel), LAI-3 km (3x3 pixels), LAI-5 km (5x5 pixels) and LAI-7 km (7x7 pixels). The remaining three data sources were the ground-based fraction of Photosynthetically Active Radiation (fPAR, point), PAI (3600 m^2) and albedo (point). Following function fitting, CFP SOS was identified as the DOY in the spring when a significant increasing sink of carbon is detected and EOS when a significant increasing source of carbon is detected. They found that no single source of data was able to adequately characterize the annual seasonality of canopy photosynthesis, but one or more data set was significantly correlated with a specific carbon transition date. For example, MODIS NDVI- and EVI-derived phenometrics were not significantly correlated with carbon SOS, but MODIS LAI-5 km explained 76% of the variability in carbon SOS (bias = - 5 days). In general, EVI-1500 m had the highest accuracy among the LSP products.

Mizunuma *et al.* (2013) investigated the seasonal relationships between GPP and MODIS NDVI values in a deciduous forest in south England and found only moderate correlations ($0.36 \leq R^2 \geq 0.48$). Wu *et al.* (2017) related phenometrics from GPP and from orbital NDVI (MODIS and SPOT VEGETATION) totalling 376 site-years across the north hemisphere, and found even lower correlations ($R^2 < 0.30$). Besides expected issues of spatial sampling inconsistency (Badeck *et al.*, 2004), Garrity *et al.* (2011)'s outcomes suggest that other indices, rather than NDVI, may be more appropriate to track the annual carbon fluxes. Complementarily, Wu *et al.* (2017) observed that the strengths of LSP and carbon phenology relationships are affected by different fitting algorithms, orbital sensor and plant functional types.

Notably, the end of the photosynthetic active period was more difficult to predict from the MODIS and ground radiometers than the beginning of the photosynthetic active period (Garrity *et al.*, 2011), which echoes other studies (Wu *et al.*, 2017). Furthermore, Garrity *et al.* (2011) noticed that averaged pixels correlated better than single pixels which can be due to single pixels having more low quality observations (which are averaged out after spatial aggregation) and due to the forest phenology and forest structure becoming more similar over larger scales.

In conclusion, phenology plays an important role in regulating the carbon cycles (Richardson *et al.*, 2012). Eddy covariance towers have offered us the opportunity to monitor carbon balances of vegetated ecosystems and understand the influences of key phenological events on ecosystem productivity (Richardson *et al.*, 2007). Nevertheless, it seems that orbital VIs, alone, have difficulty in accurately explaining the seasonal variability of GPP at regional to global scales (Wu *et al.*, 2017).

2.7 UAV for remote sensing and mapping

A new era of fine-scale remote sensing has emerged with the arrival of light-weight UAVs (<10 kg) (Berni *et al.*, 2009; Sharma *et al.*, 2013). Originally employed by the military, such technology has notably expanded into the civil sector in the 2000's, and it has been increasingly applied to numerous purposes (e.g. recreation, cinematography), including remote sensing and mapping of the Earth surface. Coupled with a UAV to create an aerial data acquisition system, a range of sensors have provided very high spatial and temporal resolution data for applications in multiple different disciplines, including vegetation

phenology, as exemplified in Table 2-5. Colomina and Molina (2014) present a comprehensive list of many other UAV applications. Likewise, UAV technology has been increasingly used for commercial purposes (PwC, 2016).

This widespread exploitation of UAVs is due to a series of potential advantages brought by this technology: acquisition of data in (near) real time, lower cost, user-defined temporal and spatial resolution, high-intensity data collection and flexibility regarding the kind of sensor on-board. Additionally, there is the potential of surveying detailed data: over areas with difficult access (e.g. cliffs), where risks are high for manned observations (e.g. landslides (Niethammer *et al.*, 2012)); over specific target areas (e.g. pest outbreak (Lehmann *et al.*, 2015) or wildfire (Yuan *et al.*, 2015)); and at optimal time during the year (e.g. for mapping tree species (Müllerová *et al.*, 2017a)). UAVs can also be particularly helpful for surveying optical time-series data in regions that experience frequent cloud cover, such as Great Britain (Armitage *et al.*, 2013), as the user can optimize the acquisition time to avoid cloud cover (Torres-Sanchez *et al.*, 2013). Finally, the intermediate level of observation provided by UAV data could be helpful for understanding multi-scale processes from ground to airborne to satellite observations (Garzonio *et al.*, 2017).

Table 2-5. Example of different UAV and sensor models applied to different disciplines, showing the range of systems and sensor types applied.

UAV Name	Sensor	Application	Author
QPOD (FW)	COTS (Panasonic)	Forest phenology	Berra *et al.* (2016)
3DR ArduCopter (RW)	COTS (Canon)	Forest phenology	Klosterman *et al.* (2018)
SwingletCAM (FW)	COTS (Canon)	Glacier monitoring	Dall'Asta *et al.* (2017)
Gatewing X100 (FW)	COTS (Ricoh)	Forest classification	Michez *et al.* (2016)
Dragonfly (RW)	COTS (Olympus)	Bottom and water radiance measurements	Montes-Hugo *et al.* (2015)
VulcanUAV (RW)	COTS (Canon)	Potato crop disease monitoring	Gibson-Poole *et al.* (2017)
Iris+ (RW)	COTS (Sony)	Ground cover estimates of crops	Duan *et al.* (2016)
PHawk (FW)	Multispectral camera (Micasense)	Invasive plant species monitoring	Samiappan *et al.* (2017)
Custom-built built (FW)	Multispectral camera (Tetracam)	Vegetation monitoring	Berni *et al.* (2009)
Anteos (RW)	Spectrometer (Ocean optics)	Spectroscopy measurements	Garzonio *et al.* (2017)
AscTecFalcon (RW)	Spectrometer (Ocean optics)	Field spectroscopy measurements	Burkart *et al.* (2014)
Viewer (FW)	Hyperspectral camera (Micro-HyperSpec)	Tree disease detection	Calderon *et al.* (2013)
Aibot X6 (RW)	Hyperspectral camera (Headwall)	Wetland species distribution	Li *et al.* (2017a)
Not provided	Hyperspectral camera (Fabry-Perot)	Biomass and nitrogen content estimations	Pölönen *et al.* (2013)
Aeronavics (RW)	Hyperspectral camera (Headwall)	Mapping of polar vegetation	Malenovský *et al.* (2017)
QPOD (FW)	Thermal camera (Optris)	Forest health monitoring	Smigaj *et al.* (2015)
MikrokopterOktoXL (FW)	Thermal camera (FLIR)	Vineyard water status	Santesteban *et al.* (2017)
Custom-built (RW)	Thermal camera (FLIR)	Coal fire detection	Li *et al.* (2018)
OktoKopter (RW)	LiDAR sensor (Ibeo Lux)	Forest inventory	Wallace *et al.* (2012)
Custom-built (RW)	LiDAR (Hokuyo)	Below-canopy forest survey	Chisholm *et al.* (2013)
Custom-built built (RW)	SAR sensor (In-house built)	Testing UAV SAR capabilities	Aye *et al.* (2017)
DJI S1000 (RW)	SAR sensor (In-house built)	Marine and antarctic monitoring	Li *et al.* (2017b)

FW = Fixed Wing; RW = Rotary Wing;

However, some limitations of UAVs are also recognised. These include relatively small area coverage, that the target area cannot be surveyed (nearly) simultaneously (as it can with spaceborne sensors), that flights cannot be performed in high winds and during precipitation, significant investment in training, time taken for setting up a UAV system (if built in-house built), fixed-wing UAVs requiring flat terrain for landing, the limited payload constraints on sensor types and the mission endurance (Berni *et al.*, 2009; Anderson and Gaston, 2013; Chabot and Bird, 2013; Dandois and Ellis, 2013). The challenge of measuring larger areas is due primarily to battery endurance but also by limits imposed by civil and federal aviation laws, such as requirement to retain line-of-sight during operations (Torresan *et al.*, 2017).

There are also remaining technical challenges in dealing with very high spatial resolution data, such as influence of viewing geometry (Sharma *et al.*, 2013), radiometric calibration and atmospheric correction (Berni *et al.*, 2009) and georeferencing and mosaicking the large amount of images typically acquired (McGwire *et al.*, 2013). These factors can diminish the capability to generate accurate quantitative information (Kelcey and Lucieer, 2012), which is critical in applications such as quantification of land surface parameters or time series analysis (Lebourgeois *et al.*, 2008). Furthermore, a large volume of data can be acquired per study site, the size of which can increase significantly with derivation of photogrammetric and/or remote sensing products, potentially resulting in information management problems (Rychkov *et al.*, 2012). Despite the freedom of choosing which UAV and sensor(s) can be employed, it is necessary to be careful regarding all the technical and operational details needed to acquire a high quality data set; extra efforts might be necessary if using non-scientific sensors (e.g. COTS cameras) as these are not calibrated instruments (Berra *et al.*, 2017).

An important aspect to be observed when choosing a UAV is which category of UAV is optimal for a specific study area: fixed- or rotary-wing. Fixed-wing UAVs have the advantage of covering larger areas, but the target area must be close to relatively flat areas offering an open space zone allowing a safe take-off and landing. On the other hand, rotary-wing are less demanding regarding take-off and landing conditions (as they can fly vertically), and can fly at lower altitudes, but they cover smaller areas (Berni *et al.*, 2009; Anderson and Gaston, 2013; Chabot and Bird, 2013; Dandois and Ellis, 2013). Another advantage of rotary-

wing UAVs is their ability to hover over a selected target for a programmed time, allowing for multiple measurements (e.g. for BRDF investigation (Burkart *et al.*, 2015)).

Many sensors have been miniaturized and/or adapted to be attached on a UAV platform, ranging from low-cost mass-market, amateur and professional, to sensors specifically developed for UAVs (Colomina and Molina, 2014). Van Blyenburgh (2013) identified 406 imaging and ranging instruments specifically designed for UAVs. For simplicity, this study sorted the sensors commonly found on-board UAVs into six broad categories (as exemplified in Table 2-5): 1) COTS (either unmodified, detecting RGB, or modified to sense visible and NIR radiation); 2) multispectral; 3) hyperspectral (either imaging cameras or radiometers); 4) Light Detection And Ranging (LiDAR); 5) Thermal; and 6) Synthetic Aperture Radar (SAR). Among these, COTS cameras have become the most used remote sensing tool to date (Torresan *et al.*, 2017) due to their ease of use, low cost, compact size, low weight and compact data storage (Rabatel *et al.*, 2014). At the other extreme, SAR technology has been one of the most challenging to be miniaturized and fixed on lightweight UAVs (Aye *et al.*, 2017). Nevertheless, due to the rapid technological development and growing interest in this area, the other sensors (categories 2-6, above) are expected to be more commonly used by the research community in lightweight UAVs, although reducing costs of such instruments seems to be critical for some instruments, such as LiDAR (Torresan *et al.*, 2017).

The success of UAVs in remote sensing and mapping applications has been due to not only technological developments in UAVs (including positioning systems) and sensors, but also significant advances in data processing techniques, especially in (digital) photogrammetry and computer vision (Colomina and Molina, 2014). Traditional photogrammetry (Tsingas, 1992) proved not to be ideal for processing blocks of UAV images due to the irregularity of such images, which, in contrast, is no obstacle for approaches based on Structure from Motion (SfM) (Snavely *et al.*, 2008). Interest in UAV-sourced images and SfM has seen a dramatic expansion over the last decade, revolutionizing the fields of aerial remote sensing and mapping (Woodget *et al.*, 2017). Some key aspects of the SfM technique are discussed next.

2.7.1 Structure from Motion
SfM is a technique which aims "*to simultaneously reconstruct the unknown 3D scene structure and camera positions and orientations from a set of feature correspondences*" (Snavely *et al.*, 2008). Originating from the combined efforts and developments of feature

matching algorithms and computer vision in the 1990s (e.g. Förstner (1986), Spetsakis and Aloimonos (1991)), the SfM (and modern computer vision) method has been popularized through its integration into a number of (easy to use) software packages, including Photosynth (Microsoft), PhotoScan Pro (Agisoft LLC, St. Petersburg, Russia) and Pix4Dmapper Pro (Pix4D, Lausanne, Switzerland) (James *et al.*, 2017; Woodget *et al.*, 2017).

SfM is based on principles derived from stereoscopic photogrammetry, i.e., 3D information can be extracted from 2D overlapping, offset images (Koenderink and Vandoorn, 1991)). Nevertheless, unlike traditional photogrammetry, SfM does not require a prior knowledge of the 3D position and orientation of the camera(s), or ground control points (GCP) coordinates, in order to determine the camera pose and reconstruct the scene geometry. Instead, these are solved simultaneously using a highly redundant, iterative bundle adjustment procedure, based on feature correspondences of multiple overlapping, offset images (Westoby *et al.*, 2012). Therefore, the approach is particularly useful for datasets of images acquired by moving sensors capable of viewing and imaging an object from multiple overlapping and offset positions (Westoby *et al.*, 2012), as schematized in Figure 2-5.
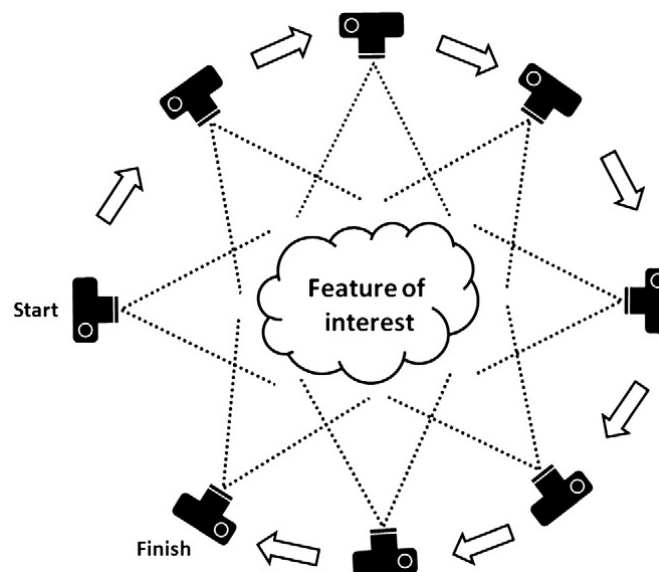
Figure 2-5. The SfM technique uses as input multiple overlapping, offset images to reconstruct the 3D characteristics of a feature of interest and determine the camera pose. Credits[8].

After iteratively feature matching a set of images with SfM (keypoint identification), a sparse 3D point cloud is generated and the camera poses are estimated, but in a relative coordinate system as neither the camera pose nor GCPs are identified a priori (Snavely *et al.*, 2008; Westoby *et al.*, 2012). One key characteristic (and advantage) of SfM is that during

---

[8] Reprinted from Westoby *et al* (2012), with permission from Elsevier.

feature matching, it can overcome common challenges present on UAV images (to a certain degree (James *et al.*, 2017)), such as large variations in illumination conditions and image resolution (or radiometry and scale), tilted images and coverage irregularity. It can also process images acquired with different cameras (Snavely *et al.*, 2008). Another advantage of SfM, compared to traditional photogrammetry, is the full automation of this process: from keypoint extraction to scene geometry reconstruction (Westoby *et al.*, 2012). A comprehensive list of advantages and challenges of SfM is provided in Table 2-6.

Usually, this image-space coordinate system is transformed into a geographical coordinate system through the identification and manual allocation of GCPs (with known geographical coordinates and visible on the images) in the sparse point cloud and selection of an appropriate transformation (Westoby *et al.*, 2012). Alternatively, direct georeferencing could be performed if the UAV has on-board differential GPS (DGPS) to record with high accuracy the camera positions; in this case the point cloud can be georeferenced by simply using the geotags of each image, increasing even further the automation level of the process (Turner *et al.*, 2014). Following georeferencing, an optional step is the densification of the point cloud (using the known camera parameters); the georeferenced point cloud (either sparse or dense) can be exported and/or interpolated to generate a digital surface model (DSM). Ultimately, this model can be used to generate orthophotos or orthomosaics.

The accuracy of these SfM-derived products was investigated in some recent studies. Generally, the positional accuracy of these products was found to be <20 cm, when the point cloud was georeferenced using manually allocated GCPs surveyed with DGPS (Kung *et al.*, 2011; Vallet *et al.*, 2011; Harwin and Lucieer, 2012; Berra *et al.*, 2017). Nevertheless, within a forest context, higher uncertainties are observed when attributes (e.g. height) are extracted from the DSMs. In Chapter 6 of this thesis, UAV-derived tree heights were validated against ground observations yielding a RMSE=1.5 m. Panagiotidis *et al.* (2016) found a RMSE~3 m between measured and UAV-derived tree height. A RMSE of 0.45 m was found by Hernandez *et al.* (2016) when comparing tree heights measured in a forest inventory against the tree heights estimated from UAV canopy height model. Regarding orthomosaics, many studies report that artefacts (e.g. seamlines) are commonly present on orthomosaics, mainly over densely vegetated areas (St-Onge *et al.*, 2015; Haghighattalab *et al.*, 2016; Samiappan *et al.*, 2017)), which can affect the radiometric quality of the mosaics. Overall, the accuracy and quality of the SfM-derived products depends on the quality of the data set, characteristics of the study area and processing tools used (James *et al.*, 2017).

While the SfM approach has a number of advantages, it equally has a number of data collection and data processing challenges (Table 2-6). With the continuous interest in UAV-sourced images and SfM and continuous development and investigation of the quality, precision and accuracy of outputs (particularly intermediate outputs (James *et al.*, 2017)), this method has the potential to evolve, creating new opportunities and insights across all the sectors (science, industry and military) currently benefitting from it (PwC, 2016; James *et al.*, 2017; Torresan *et al.*, 2017; Woodget *et al.*, 2017).

Table 2-6. Advantages and challenges of the SfM approach as identified across a number of studies (Snavely *et al.*, 2008; Coveney and Fotheringham, 2011; Rychkov *et al.*, 2012; Westoby *et al.*, 2012; James *et al.*, 2017; Woodget *et al.*, 2017).

Advantages	Challenges
• Low-cost, effective and user friendly (compared to traditional photogrammetry) • Automatically resolves the (unknown) camera pose and scene geometry from hundreds, thousands of UAV images greatly facilitating DSM and orthomosaic generation • Can overcome common challenges present on UAV images, such as large variations in illumination conditions and image resolution, tilted images and coverage irregularity (it can also process images acquired with different cameras) • Limited hardware needs and portability • Fully automated processing, from keypoint extraction to scene geometry reconstruction • Fully georeferenced, high-resolution, photo-realistic DEM • Appealing products for 3D scene visualization • Point density comparable to TLS- or LiDAR-derived density	▪ A high degree of overlapping is necessary, with offset images from multiple angles. Occlusion can hinder the feature matching process ▪ Lengthy processing time (although this depends upon computational power). As a solution, the original, high resolution images are (or have to be) down resampled to decrease processing time ▪ Large volume of information, potentially bringing information management problems ▪ The effective visualisation and analysis of high resolution point clouds is difficult in many of the current GIS. ▪ Areas with dense (complex) vegetation, or with water bodies (homogeneous texture) or with steep topography are challenging targets for accurate feature matching and consequent topographic reconstruction ▪ Isolating or correcting the exact source of errors (the exact parameter) is challenging within some black-box SfM software, as they seldom provide well explained bundle adjustment reports ▪ Unexpected artefacts

2.8 Conclusion

Because the phenology of vegetated surfaces is linked to many ecosystem processes (e.g. carbon cycles), and because the timing of phenological events can be used as a proxy for climate change, the public and scientific community has showed great interest in this subject (Morisette *et al.*, 2009). While fine detail observations are needed to accurately understand the behaviour of individual organisms and communities, only orbital coarse measurements can provide us with insights at regional and global scales. For this reason, many studies have devoted efforts in linking/understanding ground and satellite observations.

The monitoring of land surface phenology (LSP) has advanced considerably since the start of Landsat era (1970's), as more sensors and more methods were developed and applied to understand how the vegetated land surfaces respond to seasonality (Henebry and de Beurs, 2013; Miao *et al.*, 2013). However, there remains a challenge of how to monitor phenology continuously in an accurate, inexpensive way and over multiple years (Ryu *et al.*, 2012), using observations at multiple scales acquired by different sensors (Hufkens *et al.*, 2012; Henebry and de Beurs, 2013; Nagai *et al.*, 2015; Brown *et al.*, 2016).

Validation of LSP-derived metrics relies upon reference observations being able to take into account the spatio-temporal phenological heterogeneity within the pixel area (Liang *et al.*, 2011). Visual assessments of phenology (the traditional approach) have the advantage of providing adequate temporal resolution to monitor species-specifics phenological changes with clear biophysical meaning, therefore being ideal to validate LSP (Liu *et al.*, 2015), but are difficult to extrapolate over large scales (Beck *et al.*, 2007). In this way, the validation might be compromised due to the classical point vs pixel comparison errors (White *et al.*, 2009). Networks of ground and near-surface sensors have been increasingly used as validation data in substitution to visual assessments, allowing time series of data to be acquired at a high temporal frequency and continuously through multiple years. At this scale, sensors can be set to view a few or several organisms, and the processed data set can allow more objective and direct comparisons with spaceborne measures. Despite these advantages, there are issues related with areal representativeness, as the ground/near-surface sensors' footprint is often not precisely known in relation to the satellite pixel area.

There is therefore a need for an intermediate scale of observation between ground/near-surface and spaceborne level, which could provide data almost as spatially detailed as cameras fixed to a tower to be obtained but over a much larger spatial extent, such

as high resolution imagery acquired at airborne level (Higgins *et al.*, 2011). This level of observation could provide the opportunity for spatial integration across the instrument footprint or to examine individual organisms (Morisette *et al.*, 2002), which could provide a better understanding between ecosystem processes (as observed with LSP) and species-specific phenological events (as observed on the ground and by near-surface sensors).

UAV data could provide such intermediate scale of observation and this assumption is under test in this research project. Data from UAVs have being recognized to play an important role in future vegetation phenology monitoring (Cole *et al.*, 2015; Brown *et al.*, 2016). The user-defined scale and resolution of UAV data can allow monitoring of vegetation phenology from single trees, through plot level, to stand level. It is acknowledged that linking different datasets and developing innovative technologies are key to broadening our understanding of vegetation dynamics (Bater *et al.*, 2011; Brown *et al.*, 2016; Wu *et al.*, 2017).

Chapter 3. Study area and ground data collection methods

3.1 Introduction

While collecting a consistent time series of UAV imagery is essential to fulfil the aim of this research, ground validation data is required in order to provide an opportunity for an assessment of the accuracy of the UAV-derived products, including estimations of phenological events. Summed with Landsat imagery, all these dataset combined can allow for forest phenological events to be monitored at ground, airborne and spaceborne level. This chapter characterizes the chosen study area and describes the sampling design and methods used to acquire ground validation data, whilst the description of UAV (and Landsat) imagery collection is presented in Chapter 4.

3.2 Study area, forest inventory and sampling scheme

The study area consists of c.15 ha of mixed deciduous and conifer woodland surrounded by agricultural fields, at the University of Newcastle, Cockle Park Farm, Northumberland, UK (55.219867°, -1.698661°), and is called Hanging Leaves Woods (Figure 3-1). This site was chosen because it offers diversity in terms of tree species composition, has easy access, it is large enough to be imaged by several Landsat pixels and, most important, it allowed UAV flights to be done with minimal risks over time. Besides this, its proximity to Newcastle upon Tyne maximised data collection time in the field, making it logistically viable to access the area (sometimes 2-3 times per week) for around 5 months over the spring season. Spring phenology was monitored due to its importance within the context of climate change (Menzel, 2002; Polgar and Primack, 2013) and relationship with key transition dates of carbon and energy seasonal cycles (Toomey *et al.*, 2015). While a full year of phenological data would allow a complete phenological cycle to be tracked, collecting data for a longer period of time was not feasible within the timeframe of this study.

Previous studies have characterized the soil within the farm as sandy/clay loams (Wu *et al.*, 2000). The terrain within the woods has relatively flat topography with altitudes of ~75 m. The average temperature around the study area should be in good agreement with measurements taken at a long-term weather station located ~2 km from the woodland (within Cockle Park Farm), data which is available with in Newcastle University (2015). The average

minimum temperature over the period 1897-2011 is 4.8°C (±3.7) and the average maximum temperature is 11.8°C (±4.9). In 2015, the coldest month was January (minimum = 1.2°C, maximum = 6.5°C) and the warmest was August (minimum = 11.0°C, maximum = 19.1°C), based on monthly averaged air temperatures.
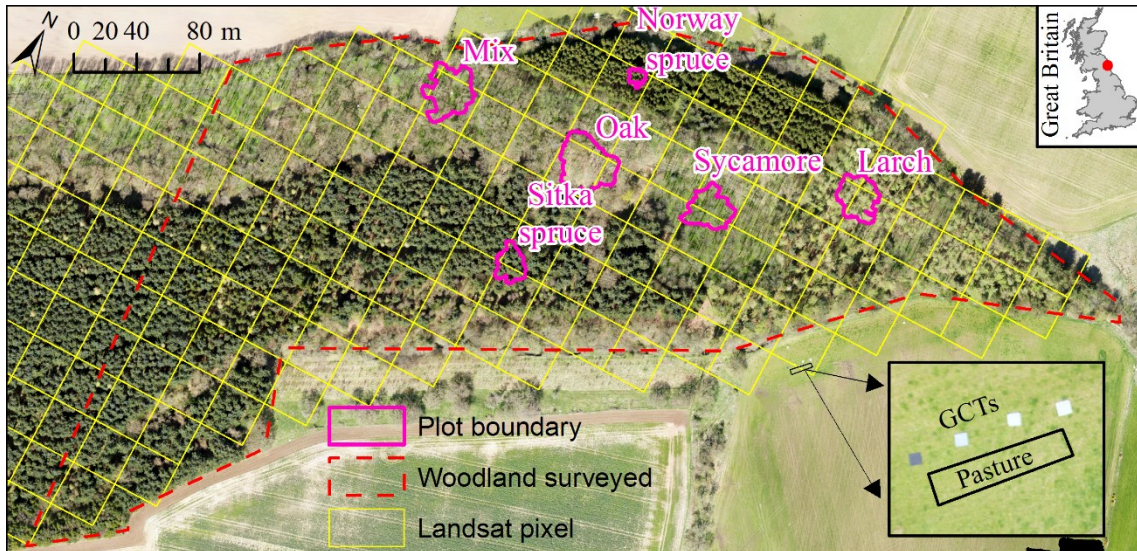
Figure 3-1. Orthomosaic made of UAV images (visible camera) acquired on 21/04/2015 (DOY 111). A Landsat grid is overlaid over the woodland area. Ground validation data were acquired in six different plots (each containing 20 trees), and they consisted of visual assessment of leaf phenology, upward hemispherical photography of canopy closure and frame-style photography of understorey development. Ground Calibration Targets (GCTs) were used to calibrate the images' DN into reflectance (Chapter 4). "Woodland surveyed" shows the extent for which UAV images were successfully acquired across the 18 acquisition dates. The Great Britain national outline is a product of ©Crown copyright and database rights 2016 Ordnance Survey.

Sampling a variety of plots and trees species is important in order to investigate intra- and inter-species differences in leaf phenology (Polgar and Primack, 2011) and to validate UAV-derived phenometrics. While a high intensity sampling scheme would be desirable (Schwartz *et al.*, 2013), this study sampled as many plots and trees as was achievable at that time, based on a reasonable statistical representativeness (section 3.4) and resource availability. Furthermore, a key factor when defining the number of plots was that they could all be surveyed in a single day, assuring a high frequency of data acquisition but keeping the number of sites to a minimum.
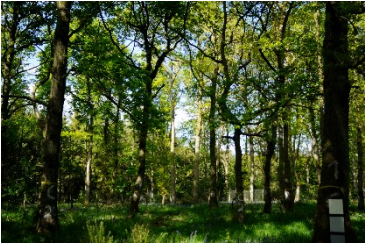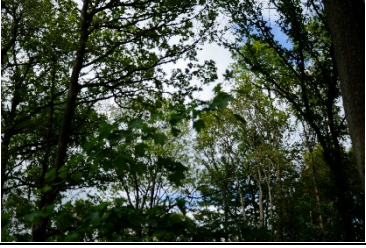
Understorey	Overstorey	Plot name (tree species)
		Larch (Larix decidua)
		Sycamore (Acer pseudoplatanus L.)
		Oak (Quercus petrea)
		Sitka spruce (Picea sitchensis)
		Norway spruce (Picea abies)
		Mixed (Acer pseudoplatanus L. and Quercus robur)

Figure 3-2. General ground overview of the six plots sampled in this study as photographed on 26/05/2015 (DOY=146).

The main tree species within this woodland were identified as being European larch (*Larix decidua*), Sycamore (*Acer pseudoplatanus* L.), Sessile oak (*Quercus petrea*), Sitka spruce (*Picea sitchensis*), Norway spruce (*Picea abies*) and English oak (*Quercus robur*). Even though there are no management records of this woodland, it could be seen that these

species were planted in blocks forming predominantly small stands of single species. However, some areas have a mix of tree species. Therefore, in order to sample individuals from all these main tree species, six plots were installed across the forest (Figure 3-1). Figure 3-2 presents a basic ground overview of the plots along with the tree species occurring at each plot.

The inclusion of evergreen conifer trees (spruces) offers an opportunity to assess seasonal changes in a land cover type where usually only weak seasonal signals are expected (Nagai *et al.*, 2013; Filippa *et al.*, 2016), meaning that the estimation of phenological metrics can be particularly challenging with such dataset (D'Odorico *et al.*, 2015). These six plots also allows investigation and evaluation of broadleaf and needle-leaf species.

The plots were located as far from the forest edges as possible in order to avoid border effects and as far from the other tree species as possible in order to sample a single tree species within a plot (except for the Mixed plot). Firstly, the plot centre was determined and permanently marked with a wood peg (used as reference for hemispherical photos) and the 20 (section 3.4) closest trees to it were identified and tagged to allow visual assessments of leaf phenology to be undertaken in a consistent order. Because the number of trees (20) was the decisive factor limiting a plot boundary, rather than a fixed area (as in White *et al.* (2014)), the plots presented different sizes and shapes. Secondly, geographical coordinates of tagged trees were surveyed with total station, with base coordinates surveyed with stationary Global Navigation Satellite System (GNSS) stations (horizontal and vertical precision <10 mm). These coordinates were afterwards used to analyse and compare UAV-derived phenometrics and visual assessments of leaf phenology (tree level investigation).

Diameter at Breast Height (DBH) and total height were measured for each tree. DBH was measured with a tape measure at a height of 1.3 m. The total tree`s height was measured using a vertex hypsometer (Vertex IV) and transponder (Transponder T3) (Haglof Sweden AB, Langsele, Sweden), for which measurements errors are expected to be around 2%-5% of the tree height (Puliti *et al.*, 2015).

Finally, crown`s diameters were measured with a reel tape aided by a densitometer (GRS Densitometer, Arcata, Canada). A cross-section approach was used, whereas the first section represents the longest crown diameter of the tree being measured.   The two measurements are thereafter averaged to estimate the crown diameter.

Large variations in DBH and height occurred within the Oak and Mixed plots (Table 3-1), and this is due to young (low DBH and height) and mature (high DBH and height) trees growing within the same plot (and due to mixed species in the Mix plot). Even though less variability in height and DBH was found among the trees within the other plots (Table 3-1), it could be inferred (and seen in the field) that Norway spruce was likely the only plot containing even-aged trees (which explains its lowest variability). Norway spruce trees also grow very close each other as indicated by the highest tree density.

Table 3-1. Mean and standard deviation (in brackets) of Diameter at Breast Height (DBH), total height (Ht) and crown diameter measurements at the sample plots. 20 trees were surveyed within each plot.

Plot	DBH (cm)	Ht (m)	Crown diameter (m)	Tree density (N/ha)
Larch	29.6 (±4.6)	21.3 (±2.4)	5.6 (±1.3)	343
Sycamore	27.4 (±5.1)	20.5 (±1.2)	5.1 (±1.7)	341
Oak	35.6 (±12.0)	19.6 (±3.1)	7.9 (±2.9)	199
Sitka spruce	29.2 (±6.1)	19.1 (±0.8)	-	587
Norway spruce	16.5 (±3.5)	15.8 (±0.9)	-	2230
Mixed	29.6 (±10.3)	18.9 (±4.5)	-	257

Following plot installation, extra ground validation data were collected at each plot for purposes of validation of phenological estimates derived from UAV data. They consisted of visual assessment of trees` leaves phenology phases, frame-style photography of understorey and hemispherical photography of overstorey.

3.3 Visual assessment of tree canopy phenology: protocols and procedures

Previous studies have demonstrated that phenological variations between individual trees of the same species in a specific microclimate can be adequately represented with a sample of 30 or more individuals (Vitasse *et al.*, 2009; Schwartz *et al.*, 2013), whilst other studies recommended a minimum sample size of 20 to represent population phenology (West and Wein, 1971; Liang and Schwartz, 2009; Liang *et al.*, 2011). An even smaller minimum number of trees (15) was suggested in tropical forests (Morellato *et al.*, 2010). Concerning temporal resolution, once a week observations have been recommended (Vitasse *et al.*, 2009), but preferentially around twice a week (Schwartz *et al.*, 2013; White *et al.*, 2014), at least

during critical phases (Calders *et al.*, 2015). With these aspects in mind, 20 trees per plot were assessed (a total of 120 trees across the six plots) in a twice per week observation frequency during the critical phases of bud burst and leaf expansion and in a weekly frequency during the other phases (Figure 3-3). The visual assessment of leaf phenology started on 3rd March, 2015, in the leaf-off phase of deciduous trees, and extended up to after the last sampled tree reached full leaf/needle expansion (25th June 2015), totalling 23 observation dates (Figure 3-3).
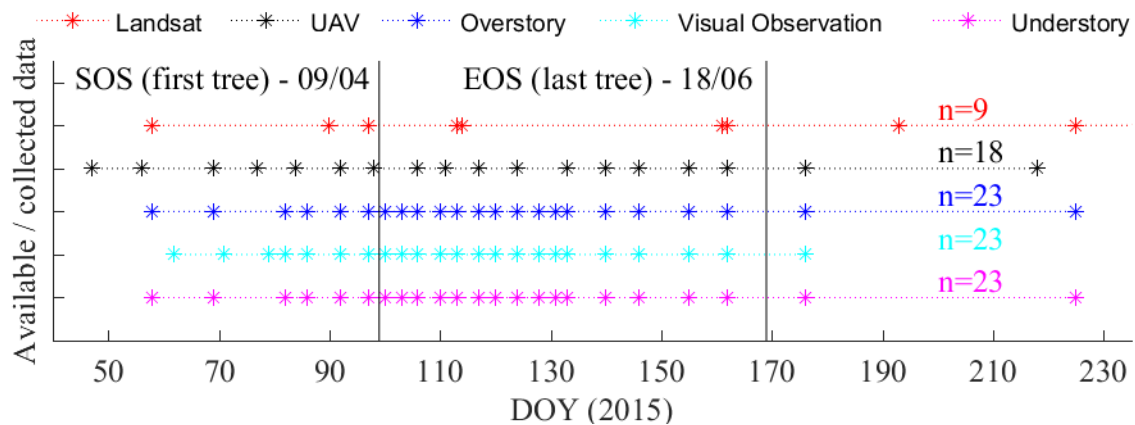
Figure 3-3. Frequency of data collection or data availability (in case of Landsat) over the study area. The total number of observations are given by 'n'. Vertical lines represent the date when the first tree was observed to start the spring season (SOS) and the date when the last tree reached the end of the spring season (EOS). The ground data collection was intensified from ~DOY 90 to ~DOY 130 in order to better monitor SOS.

Clear criteria were used to identify the characteristics of each individual tree`s phenological phases (Table 3-2), and this protocol was based on established protocols used in previous studies (Schwartz *et al.*, 2013; Liu *et al.*, 2015). Each tree within a plot was ranked in accordance with this protocol (Table 3-2) and observations were made from initial bud-burst (code 100) until most trees had reached full leaf expansion (code 675). When necessary, the phenological observations were made with the aid of binoculars.

Table 3-2. Visual phenology protocol as defined by Schwartz *et al.* (2013).

Code	Deciduous phenophase	Percentage	Evergreen conifers	Code
0	No buds visible	0	No buds visible	0
100	Buds visible	<10%	Buds visible	100
110	Buds visible	10-50%	Buds visible	110
150	Buds visible	50-90%	Buds visible	150
190	Buds visible	>90%	Buds visible	190
200	Buds swollen	<10%	Buds swollen	200
210	Buds swollen	10-50%	Buds swollen	210
250	Buds swollen	50-90%	Buds swollen	250
290	Buds swollen	>90%	Buds swollen	290
300	Bud open (leaf visible)	<10%	Bud open (candle visible)	300
310	Bud open (leaf visible)	10-50%	Bud open (candle visible)	310
350	Bud open (leaf visible)	50-90%	Bud open (candle visible)	350
390	Bud open (leaf visible)	>90%	Bud open (candle visible)	390
400	Leaf out (not fully unfolded)	<10%	Candle out (not unfolded)	400
410	Leaf out (not fully unfolded)	10-50%	Candle out (not unfolded)	410
450	Leaf out (not fully unfolded)	50-90%	Candle out (not unfolded)	450
490	Leaf out (not fully unfolded)	>90%	Candle out (not unfolded)	490
500	Full leaf unfolded	<10%	Needles unfolding from candle	500
510	Full leaf unfolded	10-50%	Needles unfolding from candle	510
550	Full leaf unfolded	50-90%	Needles unfolding from candle	550
590	Full leaf unfolded	>90%	Needles unfolding from candle	590
600	Leaf expansion	Size <25% of full		
625	Leaf expansion	Size = 25-50%		
650	Leaf expansion	Size = 50 -75%		
675	Leaf expansion	Size > 75% of full		

3.4 Understorey description and monitoring

The phenology detected by multi-temporal remotely sensed data is usually characterized by not only overstorey vegetation, but also the understorey vegetation (Tuanmu *et al.*, 2010). Forests with similar overstorey but with different understorey vegetation were found to have different seasonal patterns, as derived from MODIS vegetation indices data (Vina *et al.*, 2008; Tuanmu *et al.*, 2010). Furthermore, accurate date estimations of early stages of leaf development from dominant canopies can be hampered by the greening up of understorey vegetation (White *et al.*, 2014), which is expected to occur prior to the forest canopy (Ahl *et al.*, 2006; Richardson and O'Keefe, 2009; Pisek *et al.*, 2015). Nevertheless, distinguishing understorey signals with sensors above the canopy is challenging due to a complex and non-linear interaction of overstorey canopy and understorey plants (Borel and Gerstl, 1994). In order to monitor seasonal trajectories of understorey signals with confidence, some studies have employed sensors on the ground, under the dominant canopy (Rautiainen *et al.*, 2011; Liang *et al.*, 2012). This ground data set can therefore allow the development of the understorey vegetation to be independently monitored, as images are acquired of the understorey vegetation only. Understory photography was the method chosen in this study, as it allows tracking of colour/spectral changes (as opposed to other methods such as repeat vegetation surveys), is easy to deploy and repeat frequently and the dataset can be processed in a manner similar to the other remote sensing products acquired in this study.

The understorey development within the study area`s plots were independently monitored by using a Nikon D300 digital camera with a Nikon AF NIKKOR 28 mm lens. Frame-style photography was taken from a fixed position (wooden peg) slightly outside the plot`s boundary in order to include as much of the plot`s understorey vegetation as possible within the lens` field of view. The digital camera was assembled on a photographic tripod at 1.5 m above this fixed position and pointed towards the plot centre with an angle of ~45° (Figure 3-2, Figure 3-4). Images were then acquired with ISO-400, f/2.8, focus to infinity, auto exposure time and saved in RAW format. Except for the first two and the last date acquisitions, all the other ground image acquisitions (including hemispherical images, section 3.6) were done on the same dates as the visual assessments (Figure 3-2).
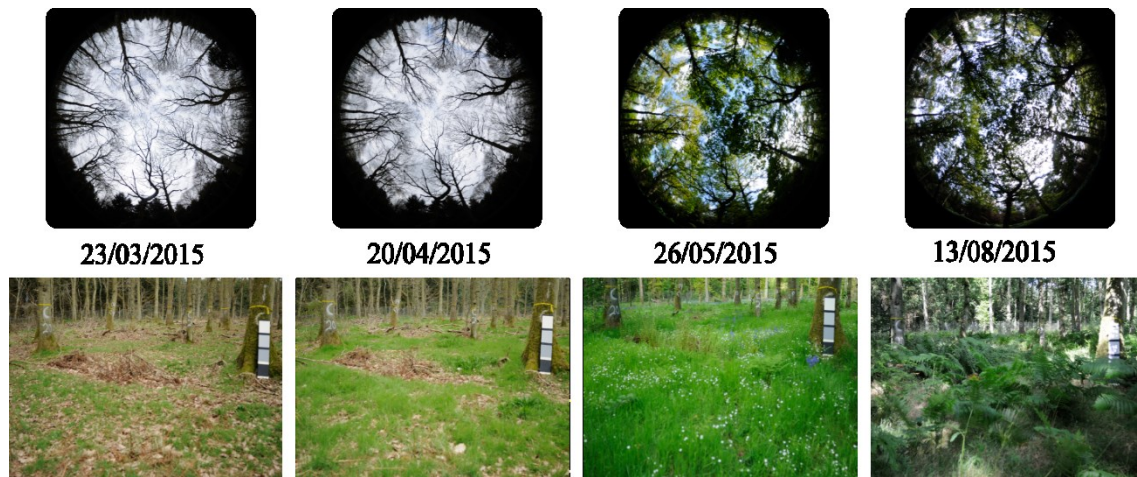
Figure 3-4. Example understorey (bottom) and upward hemispherical (top) photography acquired for the Oak plot on four different dates.

A small lightweight wooden board (0.1 x 0.5 x 0.01 m), which was painted black and three different grey tones with matt paint, was placed vertically within the camera`s field of view on every acquisition date (Figure 3-4). This board was used as a reference calibration target, as it allowed monitoring of the sensitivity of Green Chromatic Coordinate (GCC) values to changes in illumination conditions, as suggested by Sonnentag *et al.* (2012).

3.4.1 Understorey vegetation description

Understorey vegetation species varied across the plots, as identified in Table 3-3 and shown in Figure 3-2. The tallest understorey vegetation was observed within the Larch plot, due mainly to patches of regeneration of sycamore. A mix of grasses and herbs were predominant in the Sycamore, Oak and Mixed plots, with presence of evergreen grasses occurring only in the Sycamore and Mixed plots. On the other hand, the ground within Sitka spruce plot was mostly covered by litterfall (as would be expected in an evergreen forest) with a few ferns occurring in isolated areas. Litterfall also covered the majority of the ground over the Norway spruce plot, but canopy gaps allowed some species of herbs to thrive in this plot.

Table 3-3. Inventory of understorey vegetation occurring within the six plots. The two most dominant understorey species (by cover percentage) are highlighted with bold in each plot; the ground within the Sitka spruce plot was mostly covered by needle litter.

| Understorey species | | Plots | | | | | |
Popular name	Scientific name	Larch	Sycamore	Oak	Sitka s.	Norway s.	Mix
Elder	*Sambucus nigra*	**X**				X	
Stinging nettle	*Urtica dioica*	X	X			X	
Bramble	*Rubus fruticosus*	X	X				X
Wood sorrel	*Oxalis acetosella*	X	X	X		X	
Common male fern	*Dryopteris filix-mas*	X	X	X			**X**
Broad buckler fern	*Dryopteris dilatata*	X		X			X
Yorkshire fog	*Holcus lanatus*	X	X	X			X
Sycamore[*]	*Acer pseudoplatanus L.*	**X**		X			
Creeping bent	*Agrostis stolonifera*		**X**				
Downy oat grass	*Avena pubescens*		X				
Bracken fern	*Pteridium aquilinum*		X	**X**	X		
Bluebell	*Hyacinthoides non-scripta*		**X**	**X**			**X**
Common chickweed	*Stellaria media*			X			X
Hawthorn	*Crataegus monogyna*			X			X
Creeping buttercup	*Ranunculus repens*					X	
Hazel	*Corylus avellana*						X

[*]patches of regeneration.

3.4.2 Understorey image processing

The RAW images were converted into 8 bits TIFF file format using the software ViewNX 2 (Nikon, Surrey, UK). Regions of interest (ROI) were firstly defined within each image (one specific ROI per plot) that maximized the area of understorey at each plot. Average RGB values were extracted from within the images' ROI across all dates. These

colour values were then used to calculate GCC_{DN} (Eq. (3-1)), resulting in GCC_{DN} time series at each plot. Similarly, GCC_{DN} time series were extracted for the calibration board.

$$GCC_{DN} = \frac{G}{G + R + B} \qquad (3-1)$$

where R, G and B are DNs values in the red, green and blue channels.

The time series of GCC_{DN} values from the calibration boards showed, generally, similar mean values (Figure 3-5). However, variations were observed in some dates, which could suggest that this index may not to be totally insensitive to changes in illumination conditions (Toomey *et al.*, 2015). Despite this, the magnitude of the GCC_{DN} variations from the artificial targets were much lower than the amplitude of change in GCC_{DN} detected from the understorey vegetation across the deciduous plots. Furthermore, the understorey GCC_{DN} values followed a stable trend throughout spring and summer at the Sitka spruce plot (Figure 3-5), and this is due to the absence of live understorey (in significant amounts), as this plot was fully covered by litterfall (Figure 3-2). These results indicate that this greenness index can appropriately track seasonal dynamics of understorey vegetation, a subject which will be explored in Chapter 5.
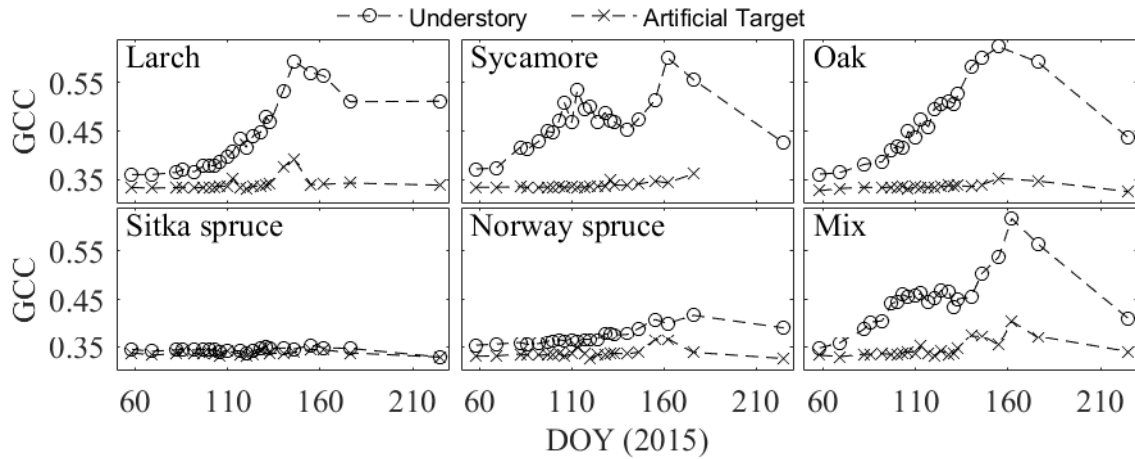
Figure 3-5. Temporal series of GCC_{DN} derived from understorey frame-style photography showing the trajectory of the understorey vegetation and an artificial target.

3.5 Hemispherical photos

An important aspect of characterizing forest stands is acquiring consistent measurements of the forest canopy. LAI, forest light environment and gap fraction are usually the primary metrics of interest due to their influence in ecological and processed-based

canopy photosynthesis models (Chianucci and Cutini, 2013). The canopy openness affects the microclimate, and the assimilation and balance of carbon within a forest (Monte *et al.*, 2007); and it is a key variable in forest management purposes (Toneli *et al.*, 2007). Indirect methods are usually preferred over direct methods to estimate canopy structural metrics due to their lower cost and practicality (Toneli *et al.*, 2007).

Digital Hemispherical Photography (DHP) is an indirect method frequently used to describe structural metrics of vegetation canopies (Ryu *et al.*, 2012; Nagai *et al.*, 2013), as it presents an alternative to other indirect measurement techniques using more sophisticated (and expensive) equipment, such as the LI-COR LAI-2000. Additionally, DHP is a well-established method with well understood errors (unlike Terrestrial Laser Scanner methods (Seidel *et al.*, 2012)) and it measures canopy cover/openness rather than LAI/light penetration (as measured by LAI-2000), providing more direct comparisons to UAV/satellite phenology than light-based methods (e.g. LAI-2000). Similar to the understory photography, DHP is easy to deploy and repeat frequently and the dataset can be processed in a manner similar to the other remote sensing products acquired in this study.

This technique involves the use of a digital camera equipped with a hemispherical ("fish-eye") lens to take photographs of the canopy in either an upward or downward direction and is widely employed to estimate gap fraction or fractional vegetation cover (Demarez *et al.*, 2008; Zhou and Liu, 2015; Schofield, 2016; Xiao *et al.*, 2016). Gap fraction can be defined as the fraction of vegetation (including leaves, stems, and branches) seen from the total area under consideration (Zhou and Liu, 2015; Xiao *et al.*, 2016). The gap fraction is calculated from the hemispherical images through classification, exploiting the contrast between vegetation canopy and either sky or ground in the image, within a specific zenith angle (Demarez *et al.*, 2008; Schofield, 2016).

To monitor gap fraction dynamics of the overstorey, upwards looking images were collected at each plot with the same digital camera used to monitor understorey but with a Sigma 4.5 mm 180 degrees circular fish-eye lens (Figure 3-4). In most cases, images were acquired under optimal conditions, which are when the direct radiation is low, so either when the sky is overcast with clouds or at sunrise or sunset (Welles and Cohen, 1996). Besides this, the following procedure was adopted on every acquisition date in order to minimize methodological errors during image acquisition (Ryu *et al.*, 2012; Sonnentag *et al.*, 2012; Schofield, 2016):

1. Attach fish-eye lens to camera and mount the camera on photography tripod.
2. Align camera lens with ground peg (fixed at the plot centre).
3. Position the camera at 130 cm height.
4. Orientate the camera to the North-South direction. This was done by aligning the camera with extra ground pegs, with the North-South direction determined with aid of a compass.
5. Level the camera by using a bubble level.
6. Take a picture.

The photos were stored in RAW format with autofocus mode, ISO-400, aperture to full priority (f/2.8) and white balance to sunlight, similarly to White *et al.* (2014).

3.5.1 Hemispherical imagery processing

The RAW images were converted into 8 bits TIFF file format using the software ViewNX 2 (Nikon, Surrey, UK). The TIFF images were thereafter processed using the free-software CAN-EYE 6.3 (Weiss and Baret, 2014), in order to extract the canopy gap fraction, similarly to other studies (Demarez *et al.*, 2008; Schofield, 2016). This software was also used to determine the camera + fish-eye lens characteristics (Weiss and Baret, 2014), a calibration step in which the coordinates of the optical centre (Table 3-4) and the projection function were determined. This calibration experiment is described in detail in Weiss and Barret (2014) and summarized below.

Firstly, a small hole has to be made in the fish-eye lens' cap. With the cap on the lens, multiple photographs are taken for several positions of the hole, by simple rotating this cap. The image coordinates of the hole are extracted and a circle is fitted to these positions. The centre of the circle is considered the optical centre.

The projection function characterization consists of taken photographs (at two different distances) of a calibration board containing rulers. The image coordinates are then associated with the distances measured on the rulers, and, by means of trigonometric relationships, the coefficients of the projection function are determined. This function relates the radial distances on the images (pixels) with the angular distances (degrees) within the field of view.

Table 3-4. Processing parameters used for hemispherical photographs in CAN-EYE, adapted from Schofield (2016).

Parameter	Setting	Description
Image size (pixels)	4288, 2848	Determined automatically by software
Optical centre (pixel)	2121, 1453	Centre point of camera + fish-eye lens
Zenith and azimuth angular resolution	5°	Angles for which the Gap Fraction will be computed. Balance between resolution and computational time.
Sub-sampling factor	3	Computational time. One pixel out of three.
Circle of interest	60°	Limit of the image used during the processing. Zenith angles higher >60° are not taken into account due to large occurrence of mixed pixels (canopy and understorey/ground) in these areas.

The first step of image processing is to define the processing parameters (Table 3-4). Afterwards, sets of images are automatically classified into sky (gaps) or vegetation, but the user can manually allocate wrongly classified pixels (visual inspection) to the correct class, in an iterative process. In order to improve the classification performance in each plot, the time series of hemispherical photos were sorted into different groups according to similar illumination conditions (Weiss and Baret, 2014), as observed in the images (cloudy, partially cloudy and clear sky). An individual classification was therefore run for each of these groups. The final output includes a binary image (Figure 3-6) and the canopy structure properties, including gap fraction (for each date and plot).
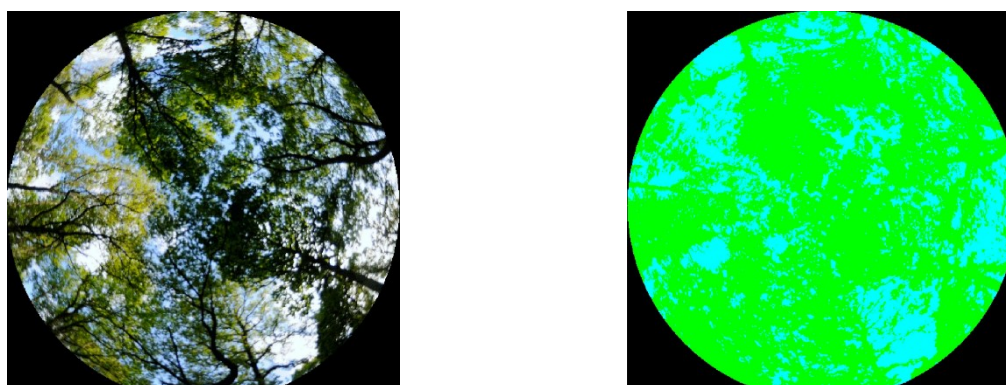
Figure 3-6. Image processing in CAN-EYE. Image on left is input true colour image of 60° circle of interest. Image on right is binary image following classification to sky (blue) or vegetation (green). Image acquired on 26/05/2016 (DOY 146) at the Oak plot.

The quality of the gap fraction estimations derived from the hemispherical images and CAN-EYE are likely affected by a few factors. Firstly, no exposure compensation was applied during the image acquisitions, which may have caused an overestimation of the gap fraction in this research; an underexposure is usually recommended in order to give the best contrast between sky and canopy, consequently increasing the detection of dark objects within the images (plant materials) and reducing the estimated canopy openness (Chen *et al.*, 1991). Secondly, it is up to the user to: 1) sort the time series of hemispherical images into different groups according to similar illumination conditions, and; 2) decide, via visual inspection (as exemplified in Figure 3-6), whether the hemispherical image classification results are consistent within CAN-EYE. These two factors combined add therefore a degree of subjectivity into the processing workflow. Finally, because no validation data was available, it was not possible to quantify the accuracy of the estimates derived with CAN-EYE.

3.6 Spectral data collection

Ground Reflectance Calibration Targets (GCTs) were placed within the UAV survey's coverage (Figure 3-1) on all the image acquisition dates for use in performing radiometric calibration (Section 4.2.5, Chapter 4). These targets comprised of four lightweight wood boards measuring 1.2 x 1.2 x 0.01 m, which were painted black and three different grey tones with matt paint (the final colours were chosen based on a trial-and-error approach, after many on-ground and in-flight tests).

Measurements of relative reflectance were made in the field in order to apply the empirical line method for radiometric and atmospheric correction (Smith and Milton, 1999) and to validate the UAV-derived reflectance estimates (Chapter 4). Spectral measurements were acquired of the four GCTs and diverse natural targets (22) with an ASD field spectrometer (FieldSpec Pro, ASD Inc., CO, U.S.), using an 8 degree fore optic accessory positioned at nadir, 1.5 m above the surface. A 24" white barium sulphate-based panel (LabSphere, Inc. NH, U.S.) was used as a white reference. Five spectral measurements were taken for each target. For the natural targets, the five measurements were made within a 1 m radius area with the central position surveyed with Real Time Kinematic (RTK) Global Navigation Satellite System (GNSS) method. The measurements were made on DOY 111 (straight after the UAV flights), due to the favourable weather conditions.

The natural targets included: two types of crops (6), concrete (1), natural grass (7), pasture (2), grazing-grass (2) and bare soil (4) distributed within 400 m distance of the GCTs and all around the forest area surveyed. Example spectral reflectance of the natural and artificial targets sampled on DOY 111 around Hanging Leaves Woods are presented in Figure 3-7.
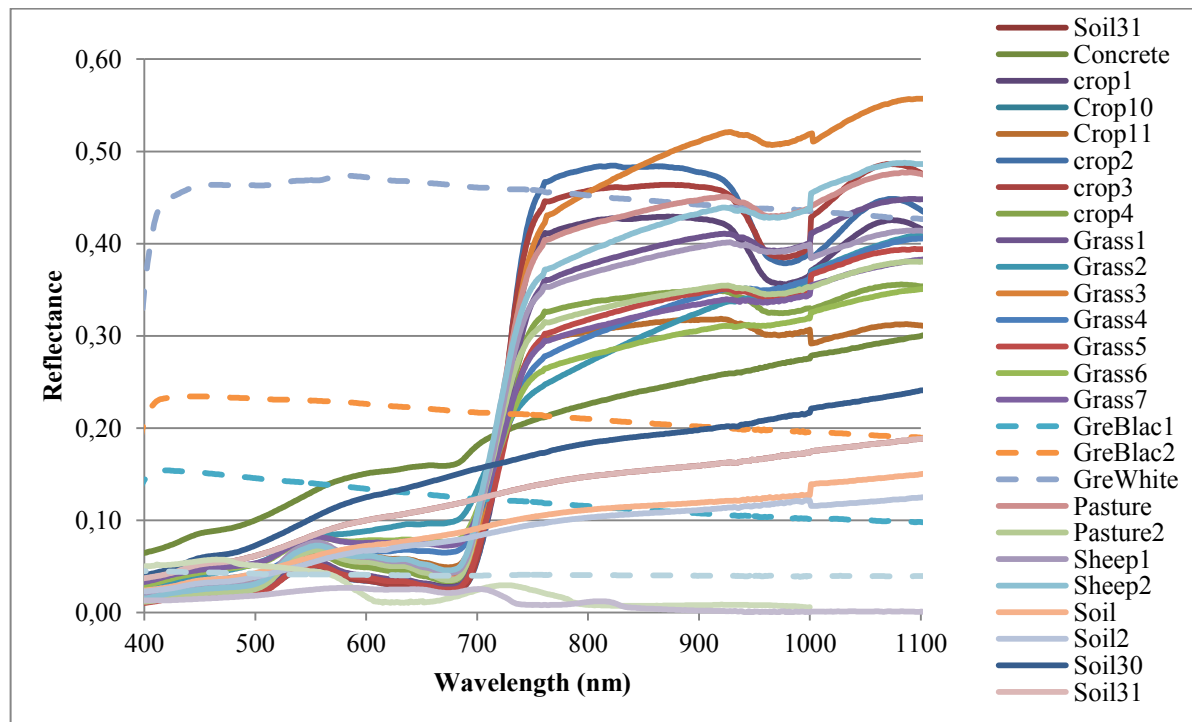
Figure 3-7. Example spectral reflectance of the natural and artificial targets sampled on DOY 111 around Hanging Leaves Woods. The artificial targets are identified with dotted lines.

3.7 Conclusion

One study site (Hanging Leaves Wood) was selected for data collection, as it proved to be of easy access (for both UAV and ground data) and offered diversity in terms of tree species across c. 15 ha. Besides this, a diverse understorey vegetation provides the opportunity and challenge to test UAV-derived products sensitivity over different understorey coverage. Six plots were selected within Hanging Leaves based on tree species, logistical factors and statistical representativeness, for detailed multi-temporal monitoring of individual tree and plot scale phenology. Plot-derived information will be used to validate UAV-derived phenology (Chapter 5). This chapter described the field campaign carried out on these six plots including the sampling designs and data collection protocols. Multi-temporal aerial image acquisition with a UAV, which is in the core of this study, is detailed in Chapter 4.

Chapter 4. Multispectral remote sensing from COTS Cameras on UAVs

4.1 Introduction

This chapter investigates the radiometric quality of the two COTS digital cameras used in this study onboard a UAV, and their potential to retrieve surface reflectance and vegetation indices. First, a short literature review contextualize the benefits and challenges of using COTS + UAV for multispectral remote sensing applications. Collection, processing, calibration and validation of a series of UAV data is described. Finally, the accuracy of the UAV-derived spectral products is presented, alongside with its potential and limitations for vegetation monitoring. This chapter prepares a foundation for using the UAV time series data in forest phenology monitoring, a topic which is explored in Chapter 5 and Chapter 6.

This chapter addresses Objective 2 of this research as presented in Chapter 1: "To retrieve reflectance and vegetation indices from consumer-grade cameras on-board UAVs, for use in vegetation monitoring."

4.2 Background

Recent advances in sensor and imaging technologies have led to COTS digital cameras becoming an attractive option for aerial remote sensing due to their ease of use, low cost, compact size, low weight and compact data storage (Rabatel *et al.*, 2014). Coupled with an UAV to create an aerial imaging system, COTS cameras have provided very high spatial and temporal resolution data for applications in multiple different disciplines (Lebourgeois *et al.*, 2008; Rabatel *et al.*, 2014).

COTS cameras can be used with off-the-shelf configurations (unaltered) or they can be modified to detect near infra-red radiation, once the hot mirror filter is removed (Verhoeven *et al.*, 2009), making it possible to design different camera systems for UAV-based remote sensing dependent on the type of images required. The combination of visible and NIR wavelengths is particularly important in vegetation analysis due to the contrasting way that plant leaves reflect energy in this spectral range, behaviour which is the basis for many VIs, such as the widely used NDVI (Rouse *et al.*, 1973). Because spectral VIs are composed of spectral reflectance from different spectral bands, it is of upmost importance to

retrieve accurate spectral reflectance from COTS cameras. However, COTS cameras are not calibrated instruments and, for multispectral remote sensing applications, an approach needs to be identified to produce radiometrically consistent images from which spectral reflectance can be retrieved (Chavez, 1996; Zaman *et al.*, 2014).

The data recorded by a camera`s sensor can be affected by a combination of effects coming from camera-related factors (vignetting effect, data storage, spectral response functions, exposure settings, post-processing steps) and environment-dependent factors (surface conditions, sun geometry, atmospheric effects, topographic effects) (Jain, 1981; Healey and Kondepudy, 1994; Stow *et al.*, 1996; Lebourgeois *et al.*, 2008; Kelcey and Lucieer, 2012). These effects can diminish the capability to generate accurate quantitative information (Kelcey and Lucieer, 2012), which is critical in applications such as quantification of land surface parameters or time series analysis (Chavez, 1996; Lebourgeois *et al.*, 2008). The retrieval of surface spectral reflectance from COTS cameras needs therefore to take these factors into account.

Several studies have tested the potential of COTS cameras (at ground, UAV and airborne level) to create visible and NIR radiation images (using either a single or dual camera system), but without calibrating the images` digital numbers (DN) to physical units (e.g. reflectance) (Lebourgeois *et al.*, 2008; Verhoeven *et al.*, 2009; Nijland *et al.*, 2014; Yang *et al.*, 2014a; Rasmussen *et al.*, 2016). Comparatively, fewer studies have retrieved surface spectral reflectance from COTS cameras, and this has not always been from fully radiometrically calibrated images due to challenges in identifying all of the camera-related factors, such as the camera spectral sensitivities (Hakala *et al.*, 2010; Mathews, 2015; von Bueren *et al.*, 2015), vignetting effects (Mathews, 2015; von Bueren *et al.*, 2015; Wang and Myint, 2015) and data storage (von Bueren *et al.*, 2015; Rasmussen *et al.*, 2016). In one study, Zaman *et al.* (2014) proposed a workflow to retrieve reflectance from cameras on a UAV which took into account all the camera-related factors; the results looked consistent but were not validated. Therefore, better understanding of the quality of spectral data retrieved from COTS cameras is needed (von Bueren *et al.*, 2015), especially for applications where consistent multi-temporal data sets are required, such as in agricultural and forest monitoring (Rabatel *et al.*, 2014; Yun *et al.*, 2016) and satellite observation validation (Honda *et al.*, 2012).

This chapter tests the ability of two identical COTS cameras on-board a UAV to generate spectral reflectances and calibrated NDVI from hundreds of mosaicked images, for use in vegetation monitoring. To do so, a workflow was designed which brings together well known and standard methods for camera radiometric calibration in order to obtain a well calibrated and characterized reflectance product from COTS UAV sensors for consistent time-series generation. The unique contribution of this paper consists in the analysis of the outcomes of this process: 1) assessing the UAV-retrieved reflectance and NDVI against ground-measured reflectance and NDVI for a number of vegetation types (convolved to the UAV cameras and also to Landsat 8`s Operational Land Imager (L8-OLI) response functions); 2) assessing UAV-derived NDVI against actual Landsat-derived reflectances and NDVI, a step which identified the best RGB channel of the NIR-modified camera to be used as the NIR band in the NDVI calculation; and 3) comparing two approaches for radiometric calibration of the data using empirical line methods and assessing the ability to generate a consistent time series of reflectance and NDVI for forest phenology applications.

4.3 Methodology

4.3.1 Ground and UAV data collection

The study area (Figure 4-1) was flown weekly by one of two fixed-wing UAVs (Quest300 and QPOD - QuestUAV Ltd., Amble, UK) from March to June 2015, with one additional flight in February and one in August, totalling eighteen acquisition dates. The flights were carried out in diverse illumination conditions (due the nature of British weather) but around solar noon when possible. This chapter focuses primarily on a detailed dataset acquired on Day of Year (DOY) 111 (21/04/2015) providing full ground data for calibration, which was acquired under clear, sunny conditions.

The UAVs have a 2 m wingspan and a maximum 5 kg payload, and can fly for approximately 10-15 minutes, depending on their on-board battery life (primarily affected by the air temperature and wind speed); they are equipped with on-board single-frequency GPS receiver (meter accuracy). The UAVs were flown on fully automated routes according to pre-programmed flight plans, which included a flying height of 122 m, 18 m/s average speed, acquisition of one image per 2.2 s and a 80% side-overlap. After covering the entire area once, the UAV flew over it again (same flight) but with the flight plan shifted in order to increase the overlap. The flight paths were adjusted on every flight in order to have flight

lines in an orthogonal angle in relation to the wind direction, ensuring a similar UAV speed across the flight lines and image acquisition at approximate similar distances (to the ground).

Two gimballed COTS Panasonic DMC-LX5 digital cameras (Panasonic UK Ltd., Bracknell, Berkshire, UK) were used concurrently as imaging systems on-board on the UAVs. The cameras have 5.1 mm nominal focal length, 3648 x 2736 pixels (effective pixels 10 megapixels), CCD sensor type with a sensor size of 1/1.63". One Panasonic camera was left un-modified (VIS) and therefore sensitive to visible light; the second Panasonic was modified (MOD) to be sensitive to near NIR wavelengths. The modified camera was purchased pre-modified by the UAV manufacturer (QuestUAV Ltd., Amble, UK), and has had its hot mirror removed and replaced by an external long pass filter (unknown manufacturer, cut-off at 660 nm).
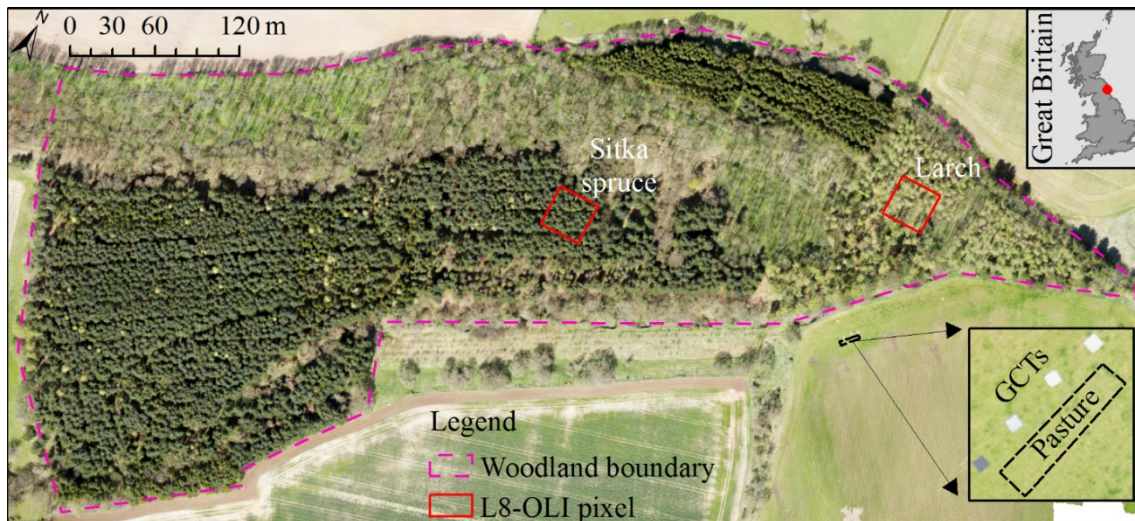
Figure 4-1. Orthomosaic made of UAV images (visible camera) acquired on 21/04/2015 (DOY 111). The location of two Landsat 8-OLI pixels are overlaid in a deciduous (Larch) and evergreen (Sitka spruce) species. Four Ground Calibration Targets (GCTs) are shown in detail. The Great Britain national outline is a product of ©Crown copyright and database rights 2016 Ordnance Survey.

All UAV images were captured on manual settings (ISO-100, shutter speed 1/800 s, aperture f/2 and focus to infinity; these optimal settings were defined after many on-ground and in-flight tests) and saved in RAW format (5 MB each image). Lower ISOs (e.g. 80, 100 or 200) are often used for UAV digital imagery under sunlit conditions because of the increased signal to noise ratio (Ritchie *et al.*, 2008; Mathews, 2014; Yang *et al.*, 2014a). Besides this, a relatively fast shutter speed needs to be employed in order to avoid blurred images from UAV platform movement (Yang *et al.*, 2014a). Since a low ISO and a fast

shutter speed were used, the maximum aperture (f/2) was set in order to avoid excessively dark images.

Eleven to thirteen Ground Control Points (GCPs) were placed over the study area on all the image acquisition dates for use in georeferencing (Section 4.2.6). They consisted of black and white circular tarpaulins (1 m diameter), and have had their position surveyed with RTK- GNSS (outside the forest, horizontal precision ~30 mm and vertical precision ~50 mm) and with static GNSS (inside the forest, horizontal precision ~20 mm and vertical precision ~30 mm). Static GNSS positions were post-processed with Leica Geo Office©.

4.3.2 Spectral sensitivity determination

A digital camera has a few vital components including a lens, a sensor, a colour filter and a hot mirror (Janesick and Blouke, 1987; Mathews, 2015). Two main types of electronic sensors are currently in use, either a charge-coupled device (CCD) or a complementary metal-oxide-semiconductor (CMOS) (Janesick and Blouke, 1987; Aber *et al.*, 2010; Mathews, 2015). These sensors employ a two-dimensional array of semiconductors (photodiodes) to detect light intensity in a monochromatic way (Theuwissen, 1995; Holst, 1998). In order to differentiate between wavelengths and produce true-colour images a Colour Filter Array (CFA) is placed on top of the sensor (Holst, 1998; Yang *et al.*, 2014a). Typically, a three-colour Red-Green-Blue filter is arranged accordingly to a Bayern pattern (Bayer, 1976), which permits only one colour to be measured at each photodiode (pixel). To generate a colour image, the missing colour values are interpolated by using demosaicking algorithms, such as bilinear interpolation (Parulski, 1985). The cameras sensors are usually made of silicon material, which is sensitive not only to visible, but also to NIR wavelengths up to around 1100 nm (Theuwissen, 1995; Hunt, 1996; Aber *et al.*, 2010; Nijland *et al.*, 2014). Since the filter material (CFA) also transmits NIR radiation, the cameras are fitted with a blocking filter (hot mirror) that allows only visible wavelengths to pass through (Holst, 1998; Aber *et al.*, 2010; Nijland *et al.*, 2014). By removing the hot mirror and replacing it by a filter which allows transmittance of near-infrared wavelengths only, a COTS camera can therefore be modified to sense NIR light (Verhoeven *et al.*, 2009; Nijland *et al.*, 2014; Rabatel *et al.*, 2014). Therefore, an imaging system using COTS cameras can potentially be designed to sense visible and NIR wavelengths (Ritchie *et al.*, 2008; Nijland *et al.*, 2014).

However, the use of COTS cameras as multispectral imaging systems is often hampered by a lack of knowledge of their spectral sensitivities, as COTS cameras

manufacturers typically do not publish this information. Also, when cameras are purchased already modified (change of filters), the wavelengths that could be transmitted through that filter are also not always known (as is the case with the modified Panasonic). Therefore, the camera sensitivity needs to be determined by the user (Lelong *et al.*, 2008; Jiang *et al.*, 2013; Darrodi *et al.*, 2015).

An accurate method to measure the sensor sensitivities is to make use of a monochromator (Darrodi *et al.*, 2015). In summary, the monochromatic light produced by this device is photographed by a camera, and a relationship between the image brightness and the monochromator`s spectral radiance is determined in order to calculate the spectral sensitivity of the camera`s sensor (Verhoeven *et al.*, 2009). The Panasonic cameras` spectral sensitivities were measured using a monochromator, the methodology for which is available in detail in Berra *et al.* (2015)[9] and is summarized in the next section.

4.3.3 Spectral sensitivity determination: Retrieving the Relative Spectral Response (RSR) from the cameras

The spectral sensitivities of the Panasonic cameras were measured by recording their response to monochromatic light produced by a double monochromator (OL 750-M-D Double Grating Monochromator (Additive), Optronic Laboratories, Inc., Orlando, Florida, USA) and reflected by an integrating sphere attached at the monochromators exit slit. The light beam is reflected by the spheres interior surface from where images were acquired through a detection port in the integrating sphere.

Optimal camera exposure settings were determined during a preliminary image acquisition (when the monochromatic light with the highest signal intensity came close to saturating the images DNs) and were kept constant throughout the experiment. Both cameras were set to ISO 100 and aperture f/2, but different shutter speeds: VIS (1/5 s) and MOD (1/3.2 s). Each camera was individually exposed to monochromatic light ranging from 370 nm to 750 nm (VIS) and from 630 nm to 1100 nm (MOD) in 10 nm steps, with two images being captured at each step. Therefore, the selected nominal half bandwidth (HBW) was 10 nm (using 1200 g/mm gratings), which is achieved by combining 5 mm slits at the entrance, middle and exit ports (Optronic, 2002). Due to the range of wavelengths being sampled, it was also necessary to vary the lamp voltage and the type of internal filter used (Table 4-1).

---

[9] Berra *et al.* (2015) 'Estimation of the spectral sensitivity functions of un-modified and modified commercial off-the-shelf digital cameras to enable their use as a multispectral imaging system for UAVs', Int. Arch. Photogramm. Remote Sens. Spatial Inf. Sci., XL-1/W4, pp. 207-214.

Table 4-1. Monochromator lamp voltage and internal filter settings used for specific wavelengths being sampled.

Lamp Voltage (V)	19	17	17
Filter (nm)	345	345	599
Wavelengths sampled (nm)	370-500	510-620	630-1100

The RAW images were converted to dark-corrected linear TIFF images accordingly to section 4.3.6. The TIFF image DNs were averaged within a 9 x 9 pixel area in the centre of each image, in order to avoid issues related with the variance of the radiance within the integrating sphere and any differences in the individual pixel response across each camera's image sensor (Darrodi *et al.*, 2015).

The light intensity from the monochromator and its integrating sphere were independently measured using a reference silicon photodiode (OL DH-300C S/N: 12101253, Optronic Laboratories, Inc., Orlando, Florida, USA) in order to identify the relative spectral radiance at each measured wavelength. The settings used mirrored those used at the image acquisition phase (Table 4-1).

The RSR of the RGB channels for a given wavelength λ were calculated as per Eq. (4-1) (Suzuki *et al.*, 2009) and a linear relationship between the input radiance and the output signal is assumed (Darrodi *et al.*, 2015).

$$R(\lambda) = \eta \frac{r(\lambda)}{I(\lambda)}, \quad G(\lambda) = \eta \frac{g(\lambda)}{I(\lambda)}, \quad B(\lambda) = \eta \frac{b(\lambda)}{I(\lambda)}$$

(4-1)

where *r*, *g*, and *b* = the mean spectral response from each camera channel (red, green and blue channels, respectively) given in DN values and calculated from the 9x9 window (output signal); I = the light intensity (monochromator and sphere) given in relative spectral radiance units (input radiance); η = the normalized coefficient.

The η coefficient is applied to generate a relative spectral response (RSR), as it results in lower calibration uncertainties (Darrodi et al. 2015). For each camera, the mean spectral response over all wavelengths were normalized (η) by the maximum signal detected among the RGB channels, which yields dimensionless units with peak equal to 1.

4.3.4 Cameras` RSR

The green channel of the visible camera showed the highest peak in response and a wide band width response (Figure 4-2), likely due to the Panasonic camera using a Bayer

colour filter array (Bayer, 1976). The red channel of the modified camera was the most sensitive to NIR radiation, whereas the green and blue channels have a much lower peak response (both 0.47). The red and green channels have peak response within the red-edge feature of 700~720 nm (Bach and Mauser, 1997; Hunt *et al.*, 2010), while the blue channel peaks within the NIR band, which is in accordance with what would be expected from a Bayer filter (Bayer, 1976; Nijland *et al.*, 2014). For comparison, the L8-OLI bands (Barsi *et al.*, 2014) have narrower response functions and don`t overlap, contrary to the Panasonic's Relative Spectral Response (RSR). The OLI Red band is positioned before and the OLI NIR band is positioned after the red-edge feature, wavelengths which maximize the spectral differences between green vegetation, therefore being ideal for NDVI calculations.
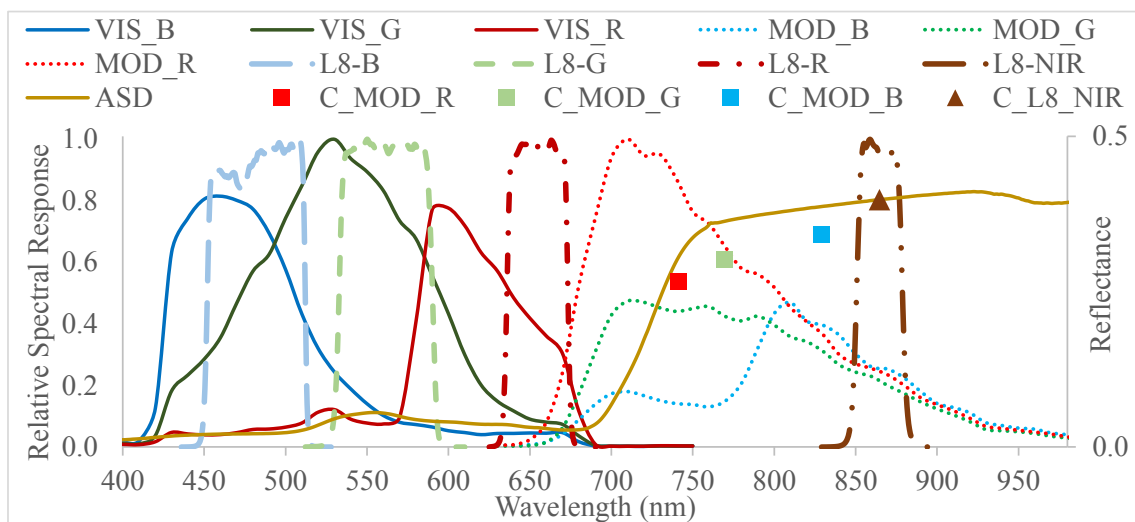
Figure 4-2. Relative spectral response of the unmodified (VIS) and modified (MOD) Panasonic cameras for the red (R), green (G) and blue (B) channels. The Landsat 8`s OLI (L8) band sensitivities are also shown for comparison purposes. The reflectance curve of a grass target (ASD) represents a typical reflectance curve of green vegetation cover, the values of which were convolved (C) using the RGB MOD and L8 NIR bands.

4.3.5 Vignetting correction

Vignetting effect refers to a spatially dependent brightness attenuation (loss of light) occurring away from the image centre, resulting in a radial reduction in digital number (DN) values towards the edge of an image (Bradford and Gross, 1967; Lebourgeois *et al.*, 2008; Kelcey and Lucieer, 2012; Lin, 2014). This effect may be caused by a combination of factors (Sawchuk, 1977; Dinstein *et al.*, 1984; Yu, 2004; Goldman, 2010): 1) geometric optics, which causes an off-axis illumination falloff (modelled as a $\cos^4$ law, modified by focus distance); 2) angular sensitivity of digital optics; 3) blocking of a part of the incident ray bundle by the

effective size of the aperture stop (f-value); and 4) light path blocked by camera elements such as filters on front of lens. The vignetting effect may cause the irradiance measured at the camera sensor to not be equal to the scene radiance that arrives at the camera (Dinstein *et al.*, 1984; Lin, 2014). It is therefore important to remove vignetting effects from the images in applications aiming to measure radiometric quantities (Sawchuk, 1977; Lebourgeois *et al.*, 2008; Goldman, 2010; Lin, 2014).

The most straightforward and accurate approach for calibration of vignetting effects consists of capturing a reference image consisting of a uniform and spectrally homogeneous surface, known as flat field (Muralikrishna *et al.*, 1982; Yu, 2004; Kelcey and Lucieer, 2012; Lin, 2014). Since the flat field surface contains no brightness variations, intensity variations within the flat field imagery can be attributed to radiometric falloff effect of vignetting (Sawchuk, 1977; Kelcey and Lucieer, 2012; Lin, 2014). This effect can be quantitatively assessed and correction factors can be calculated per each pixel within the imagery (Dinstein *et al.*, 1984; Kelcey and Lucieer, 2012). However, these factors can only be applied to images acquired with the same camera, lens, and camera settings (focus and aperture) used to photograph the flat field (Yuanjie *et al.*, 2009; Kelcey and Lucieer, 2012).

The vignetting effect on single images was determined by using the flat field approach (Yu, 2004; Kelcey and Lucieer, 2012). The flat field-based calibration of the Panasonic cameras was performed by taking 100 images of the interior surface a 0.5 m diameter integrating sphere (LabSphere, Inc. NH, U.S.) illuminated by four Quartz-Tungsten-Halogen lamps. The aperture and focus were the same as used during the field campaign, as these parameters modify the vignetting effect (Yu, 2004).

The images were acquired in RAW format and converted to dark-corrected linear TIFF images (Section 4.3.6). For each camera, an averaged flat field image for each RGB colour channel was calculated. A per-pixel correction factor look-up-table (LUT) was calculated (Yu, 2004) and its values were fitted by 8th order polynomial models, resulting in a modelled LUT (Figure 4-3b).

All the RGB channels from both cameras presented a brightness attenuation away from the image centre, but the modified camera was most affected by vignetting (Figure 4-3b). The use of the modelled LUT values (Figure 4-3b) as multiplicative correction factors on individual images can therefore diminish the spatial nonuniformity of pixel intensities substantially (Figure 4-3a). It can be also noted that the centre of the vignetting effect does not

coincide with the image centre, a fact which might be due to the inaccurate sensor position relative to the optics (Lenz and Tsai, 1988; Lebourgeois *et al.*, 2008; Hakala *et al.*, 2010).
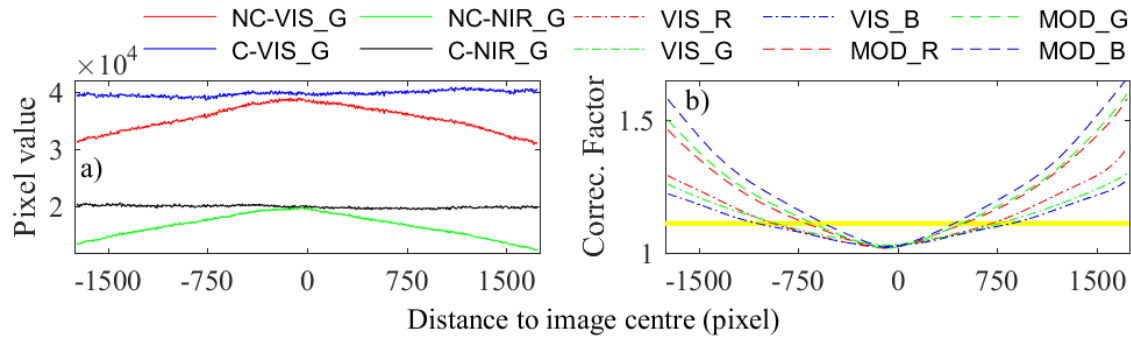
Figure 4-3. (a) Horizontal profiles of a single image taken at the exit aperture of an integrating sphere. The original pixel values (Not Corrected - NC) were corrected (C) with the modelled LUT values. (b) Correction factors (*y-axis*) for the RGB channels of the unmodified (VIS) and modified (MOD) Panasonic cameras. The yellow horizontal line (b) indicates a loss of brightness intensity of 10%.

4.3.6 UAV image corrections and generation of orthomosaics

All the image acquisitions with both Panasonic cameras were made recording the data in RAW format. For airborne remote sensing, it is highly recommended to store the images in a RAW file (Goldberg *et al.*, 1986; Lebourgeois *et al.*, 2008; Verhoeven *et al.*, 2009), as it does not apply any type of image compression and is able to store the original data as generated by the sensor (Nagy, 1985; Said and Pearlman, 1996). The expected result is therefore an image made up of unprocessed, uncompressed pixel data as captured by the sensor, which are of utmost importance for calibration and spectral characterization of a camera (Healey and Kondepudy, 1994). However, since there is not a standard RAW format for COTS cameras, but rather hundreds of them (Verhoeven, 2010), it is necessary to convert to a more common or universal file format (for example TIFF) in order to allow the images to be imported by imaging processing software.

The software DCRaw v9.25 (Coffin, 2015) was used to linearly convert the RAW files into 16 bit TIFF images. During the conversion step, the Panasonic images were also corrected for the effects of the dark current signal by photographing a dark scene 100 times, and subtracting the average dark image values from the RAW images (Chavez, 1996; Stow *et al.*, 1996; Verhoeven *et al.*, 2009; Suomalainen *et al.*, 2014). The code used is available in Berra *et al.* (2015).

The dark-corrected linear TIFF images were corrected for vignetting effects using the modelled LUT values (Section 4.3.5). The corrected images were thereafter mosaicked using the software Agisoft PhotoScan v.2 (Agisoft LLC, St. Petersburg, Russia), which uses computer vision algorithms (Structure from Motion and Multi-View Stereo) to realize image alignment and multi-view stereo-reconstruction (Verhoeven *et al.*, 2012; Mathews, 2015; Puliti *et al.*, 2015). Besides image quality, a key factor to generating good outputs is a high amount of image overlap from multiple views (AgiSoft, 2016). In this study, an overlap of >9 images per point was achieved in all dates.

Orthomosaics were created individually per date and per camera following recommended settings (AgiSoft (2016), Table 4-2), but with two modifications: 1) the dense point cloud was generated using the lowest reconstruction quality, as this produced orthomosaics with less artefacts over the forest area; 2) the orthomosaic was constructed with blending mode deactivated in order to preserve the original DN values. Five ground control points (GCPs) were used to generate georeferenced orthomosaics (5 cm spatial resolution). Six GCPs were used as checkpoints, which revealed a 3D error of <8 cm for the VIS and <11 cm for the MOD orthomosaics. This indicates that VIS and MOD orthomosaics can be combined/registered with a general accuracy of ±11 cm, i.e., ± 2.2 pixels. Besides geolocating the 3D point cloud, allocation of GCPs acts to optimize the camera orientation/position and internal parameters, which allows for more accurate 3D model reconstruction (Puliti *et al.*, 2015), and removal of the effects of lens geometric distortion (Gremban *et al.*, 1988; Sugiura *et al.*, 2005).

Table 4-2. Settings used in Photoscan's pipeline to generate orthomosaics from UAV imagery. This table was adapted from Puliti *et al.* (2015).

Task	Setting
Align Photos	Accuracy: high[b] Pair preselection: generic[b] Key point limit: 40000[b] Tie point limit: 1000[b]
Guided GCPs positioning	-
Optimize camera alignment	Fx, Fy, k1, k2, k3[b]
Build dense cloud	Quality: lowest[a] Depth filtering: aggressive[b]
Build mesh	Surface type: height filed[b] Source data: dense point cloud[b] Face count: High[b] Interpolation: enabled[b]
Build orthomosaic	Blending mode: disabled[a]

[a] Setting chosen using a trial and error approach; [b]Recommended setting in AgiSoft (2016).

4.3.7 Retrieval and validation of reflectance and NDVI

The empirical line method (Smith and Milton, 1999) was applied to retrieve surface reflectance from orthomosaic DNs of DOY 111 (reference date). The ASD measurements of relative spectral reflectance of GCTs and natural targets were corrected to absolute reflectance and convolved to the corresponding Panasonic-specific RSR curves using a MATLAB toolbox (Robinson and MacArthur, 2011). The field spectra were also convolved using the response functions of the L8-OLI sensor in order to compare how the Panasonic bands perform against this state-of-the-art sensor.

The GCTs were identified on the orthomosaics, from which the mean DN values were regressed against the convolved ASD reflectance values, resulting in band-specific calibration coefficients to retrieve surface reflectance from the orthomosaic DNs. NDVI was also calculated, a step in which each MOD RGB band was combined with the VIS R band, in order to test which MOD channel would better perform as NIR band and also which MOD channel would best correlate with the OLI-derived NDVI. The Green Chromatic Coordinate index was also calculated (GCC$_r$, Eq. (4-2)), as it is commonly used to track green leaf phenology (usually composed of uncalibrated DNs rather than spectral reflectances) (Sonnentag *et al.*, 2012; Klosterman *et al.*, 2014; Moore *et al.*, 2016).

$$GCC_r = \frac{\rho_{green}}{\rho_{blue} + \rho_{green} + \rho_{red}}$$ (4-2)

where ρ_{blue}, ρ_{green} and ρ_{red} are the spectral reflectances in the blue, green and red wavelengths.

A time series of L8-OLI and Landsat 7 Enhanced Thematic Mapper Plus (L7-ETM+) atmospherically corrected surface reflectance was downloaded from the United States Geological Survey (USGS) Earth Resources Observation and Science (EROS) centre (https://eros.usgs.gov/) over the study area from January to September 2015 (1 month before and 1 month after the UAV flights). Product guides explain the methods and algorithms used to obtain the surface reflectance (USGS, 2016a; USGS, 2016b), a product which is considered ready to be used, i.e., no further radiometric calibration is required (Liu *et al.*, 2017). 12 out of 68 images (the study site is in an overlap area of paths 203/204 and rows 21/22) were selected, following exclusion of cloud/cloud shadow contaminated images (with aid of quality flags) and ETM+ images with significant data gaps (Scan Line Corrector-off) over the study area. NDVI was calculated using the surface reflectance from the red and NIR bands.

The UAV-retrieved reflectance and NDVI were validated against the ASD ground measurements of reflectance and NDVI of 22 natural targets on DOY 111 and against L8-OLI reflectance and NDVI data (from DOY 113). The mean orthomosaic reflectance value was calculated from within a 1 m radius area, which coincided with the spectroradiometer measurement areas. The comparisons with L8-OLI were made over the area coinciding with the UAV orthomosaic limits (405 Landsat pixels, 36.45 ha). Each L8-OLI pixel value was compared to a mean orthomosaic value extracted from the area corresponding to each L8-OLI pixel. The accuracy of the results was assessed by analysis of scatter plots, R^2 and bias values.

4.3.8 Retrieving time series of reflectance/NDVI: application in forest phenology

Since the GCTs were present on every flight date, the empirical line method was applied through the entire time series to estimate reflectance and NDVI (as in Section 4.2.7). The same GCTs were used on 14 acquisition dates (from DOY 84 to 218) and standard equations were determined using the GCT ground reflectances as measured on DOY 111. However, different GCTs were tested during the first four acquisition dates (DOY 47, 56, 69 and 77), and equations for these days used the GCT reflectances as measured on DOY 77.

Due to variable localised illumination conditions on some dates, it was not always possible to use the four GCTs, as either one (DOY 106 and 133) or two (DOY 124) GCTs exhibited inconsistent illumination relative to the others. The GCTs ground reflectance was assumed to remain constant over time.

Since the GCT ground reflectances were not measured on every acquisition date, the effects of the sun-sensor geometry on the UAV orthomosaics should ideally be accounted for, similarly to Burkart *et al.* (2015). Nevertheless, it proved not to be feasible to quantify the effects of sun-sensor geometry on the UAV images (or on the derived reflectance and NDVI) in this research, as the great majority of the UAV image acquisitions (16/18) were carried out under overcast conditions, due the nature of the British weather. This means that there was no direct sun light (direct radiation) on the objects within the scenes for which the sun-object-sensor geometry could be calculated. The dominance of diffuse light in most acquisitions will likely minimise impacts of sun-sensor geometry (Tagle Casapia, 2017).

In addition to the standard approach to reflectance estimation, a simple new method was tested to produce consistent time series of NDVI. This consists of defining standard equations via the empirical line method on a reference date, forcing the constant to zero (equation C0), and then applying these to the entire time series. This method aims to simplify the calibration procedure, as it reduces the need for GCTs in every field site data acquisition, making it easier to be implemented on an operational basis. This can be a major benefit for time series acquisitions or for surveying of large areas using UAVs, where VIs are required.

The hypothesis is that accurate calibration equations (with intercept zero), determined on a reference date, can be used to generate consistent time series of NDVI. This is expected due to the UAV image DNs being linearly related to measured surface reflectance, as shown here ($R^2 > 0.99$, RMSE<1.2%, Figure 4-4) and elsewhere (Mathews, 2015). Therefore, if it is assumed that only changes in illumination condition affect the image DNs (linearly), and that if the red and NIR bands are consistent with each other, the normalized difference between red and NIR-retrieved surface reflectance (NDVI) will be significantly less affected by changes in illumination conditions, resulting in consistent NDVIs. However, the retrieved spectral reflectances are expected to be biased due to the illumination conditions being different from the reference date (Figure 4-4), meaning that this approach is not suitable if reflectance data is needed.

The C0 approach assumes that the time series of UAV imagery will have the same atmospheric effects as for the reference date. However, it is known that the atmosphere conditions vary in time (Nagol *et al.*, 2009) and residual effects are expected in the NDVI because the red and NIR wavelengths are influenced differently by the atmosphere (Myneni and Asrar, 1994). For satellite sensors, the atmosphere could reduce NDVI dynamics by as much as 10% (Qi *et al.*, 1994; Nagol *et al.*, 2009), but this is dependent of many factors, such as bandwidth and land cover type. These effects, however, can be expected to be smaller for UAV imagery, as low flying heights avoid strong interactions of ground reflected radiation with atmosphere (< 300 m, (Herrero-Huerta *et al.*, 2014)) (122 m in this study).
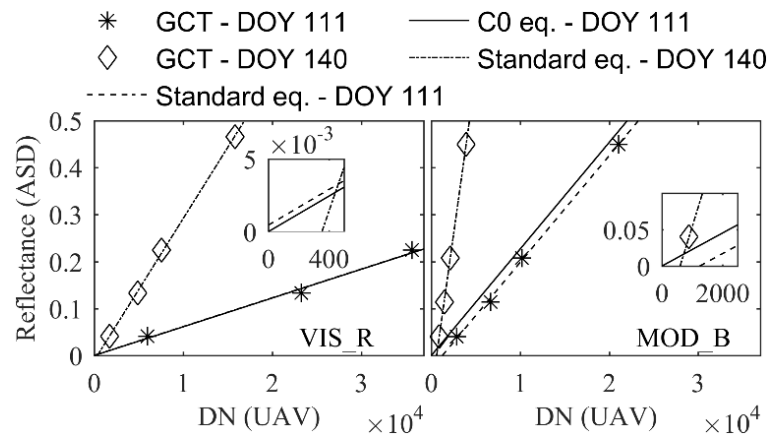
Figure 4-4. Relationship between ground reflectance and UAV orthomosaic DNs over four ground calibration targets (GCTs) for the red channel of the visible camera (VIS_R) and blue channel of the NIR-modified camera (MOD_B). Standard equations on DOY 111 have had their constant set to zero (C0 eq.). Inset enlarged graphs within each graph are included in order to better show the intercepts.

Forcing the intercept from a reference equation to zero is necessary in order to avoid negative reflectances being calculated. For example (Figure 4-4), the standard equation for MOD_B on DOY 111 (sunny) had an intercept of DN=1248; the standard equation for MOD_B on DOY 140 had an intercept of DN=598 and a steeper slope (cloudy conditions), which indicates that very low DNs (<1248) were recorded on DOY 140. If the standard equation from DOY 111 is applied to DOY 140, negative NIR reflectance and unrealistic NDVI values would be retrieved in those areas with DNs<1248. On the other hand, the C0 equation assures that positive (but biased) reflectance will be retrieved, allowing NDVI data to be calculated.

The effect of using the standard (y=ax+b, one different equation per band per date) and the C0 (y=ax, one single equation per band for the entire series) equations were

investigated for three cases. First, the C0 equations were derived from the orthomosaics on DOY 111 and applied to the other orthomosaics (16 dates). The resulting time series of reflectance and NDVI was then compared against estimates obtained with the standard equations over a pasture area located 1 m from the GCTs (Figure 4-1), an area which was verified to have the same illumination conditions as the GCTs. The reflectance and NDVI retrieved by the standard equations can be considered true measurements and can be used as reference.

Second, C0 equations were derived from the orthomosaic on DOY 155 (cloudy day), and were used to retrieve reflectance and NDVI on the reference DOY 111. This allowed the estimates to be compared against the ASD ground measurements of 22 natural targets and against actual L8-OLI data (in a manner similar to Section 4.2.7).

Finally, a time series of UAV-derived reflectance and NDVI was retrieved using standard and C0 (from DOY 111) equations. The series was extracted over one sample area of evergreen (Sitka spruce) and one of deciduous (Larch) stand (L8-OLI pixel size, as shown in Figure 4-1), from which areas the mean values were calculated. The UAV temporal trends were analysed against each other and against a time series of Landsat data (L7-ETM+ and L8-OLI), which in turn allowed assessment of the potential of UAV acquired images to track the expected seasonal patterns (phenology) of this forest.

4.4 Results

4.4.1 Validation of reflectance, NDVI and GCCr on DOY 111
A linear relationship between convolved surface reflectance and orthomosaic DN over the GCTs was observed ($R^2 > 0.99$, RMSE < 1.2%) (Figure 4-4), which allowed the empirical line method to be applied. The results from the standard equations are analysed first.

The derived UAV-reflectances of natural targets were highly correlated with the ASD reflectances convolved to the Panasonic`s RSR ($0.84 \leq R^2 \geq 0.90$), with overestimation in the visible bands (<1%) and underestimation in the NIR bands (<1.5%) (Table 4-3). These small biases are the result of the data points being well distributed around the 1:1 line (Figure 4-5). The comparisons with ASD reflectances convolved to L8-OLI RSR showed slightly lower R^2 for the VIS_R, VIS_G and MOD_R bands, whilst the other bands have the same R^2, with

biases <1% in the visible bands and <11% in the NIR bands (Table 4-3). There were therefore only small differences between the reflectances convolved with the Panasonic cameras and L8-OLI RSRs in the visible bands, but more pronounced differences in the NIR bands, as OLI resulted in higher reflectance values than the MOD Panasonic. The convolution of a green vegetation spectra (Figure 4-2) showed that the NIR-modified Panasonic bands tended to estimate reflectances below the ASD values in the NIR or red-edge wavelengths, whilst the NIR band of OLI was able to simulate more precisely this reflectance.

The comparisons against actual L8-OLI reflectances showed moderate to strong relationships ($0.73 \leq R^2 \geq 0.84$) (Table 4-3). The analysis of the biases in UAV reflectance estimations showed that the direction was the same (except for the green band) and the magnitude was very similar to the comparisons between UAV and ASD convolved to L8-OLI.

Among the MOD-RGB channels, the MOD_B detected NIR reflectance in a way more similar to the L8-OLI NIR band (Figure 4-5), with the highest R^2 and smallest bias (Table 4-3). This behaviour is as expected from the MOD RSRs, as the MOD_B has a higher sensitivity in the NIR and lower sensitivity in the red spectral region (Figure 4-2). The UAV-derived NIR reflectances have a non-linear relationship with ASD measurements convolved to L8-OLI NIR RSR, especially for MOD_R (Figure 4-5). For targets with high NIR reflectance, reflectance is underestimated by the UAV bands, due to the differing RSR functions.

Table 4-3. R^2 and bias (in brackets) values from comparison of reference (ASD, convolved to both Panasonics and L8-OLI RSR) and actual Landsat observations (L8-OLI imagery)) with UAV-derived reflectances and NDVIs. NDVIs were calculated using the MOD_R ($NDVI_R$), MOD_G ($NDVI_G$) and MOD_B ($NDVI_B$) as NIR band. The standard equations ($y = ax + b$) were also tested with their constant forced to zero ($y = ax$), based on the reference DOY 111.

| | UAV vs ASD (n=22)[1] | | | | UAV vs L8-OLI imagery (n=406)[2] | |
| | Panasonic RSR | | L8-OLI RSR | | | |
	$y = ax + b$	$y = ax$	$y = ax + b$	$y = ax$	$y = ax + b$	$y = ax$
VIS_R	$0.86_{(0.009)}$	$0.86_{(0.009)}$	$0.85_{(0.009)}$	$0.85_{(0.008)}$	$0.83_{(0.007)}$	$0.83_{(0.006)}$
VIS_G	$0.84_{(0.009)}$	$0.84_{(0.001)}$	$0.82_{(-0.004)}$	$0.82_{(-0.012)}$	$0.83_{(-0.002)}$	$0.83_{(-0.009)}$
VIS_B	$0.87_{(0.007)}$	$0.87_{(0.006)}$	$0.87_{(0.010)}$	$0.87_{(0.010)}$	$0.84_{(0.008)}$	$0.84_{(0.008)}$
MOD_R	$0.85_{(-0.010)}$	$0.85_{(0.007)}$	$0.83_{(-0.103)}$	$0.83_{(-0.086)}$	$0.73_{(-0.100)}$	$0.73_{(-0.082)}$
MOD_G	$0.88_{(-0.012)}$	$0.88_{(0.009)}$	$0.88_{(-0.080)}$	$0.88_{(-0.059)}$	$0.77_{(-0.081)}$	$0.77_{(-0.060)}$
MOD_B	$0.90_{(-0.013)}$	$0.90_{(0.015)}$	$0.90_{(-0.052)}$	$0.90_{(-0.024)}$	$0.80_{(-0.058)}$	$0.80_{(-0.030)}$
$NDVI_R$	$0.95_{(-0.057)}$	$0.95_{(-0.024)}$	$0.93_{(-0.133)}$	$0.93_{(-0.100)}$	$0.86_{(-0.162)}$	$0.86_{(-0.123)}$
$NDVI_G$	$0.96_{(-0.056)}$	$0.95_{(-0.021)}$	$0.95_{(-0.107)}$	$0.94_{(-0.072)}$	$0.88_{(-0.131)}$	$0.87_{(-0.092)}$
$NDVI_B$	$0.96_{(-0.053)}$	$0.95_{(-0.012)}$	$0.95_{(-0.079)}$	$0.94_{(-0.038)}$	$0.89_{(-0.098)}$	$0.88_{(-0.055)}$
GCCr	$0.80_{(0.001)}$	$0.88_{(-0.023)}$	$0.76_{(-0.068)}$	$0.85_{(-0.099)}$	$0.43_{(-0.050)}$	$0.76_{(-0.095)}$

[1]Comparisons made over natural ground targets; [2]Comparisons made over the whole woodland area and its surroundings.

The UAV-derived NDVIs were highly correlated with the NDVI calculated using ground measurements convolved to Panasonic ($0.95 \leq R^2 \geq 0.96$) and to L8-OLI ($0.93 \leq R^2 \geq 0.95$) RSR, with NDVI using MOD_B as NIR band achieving the highest R^2 and smallest bias (Table 4-3, Figure 4-6). The UAV-derived NDVI was compared against actual Landsat NDVI data and the same benefits of using the MOD_B band were observed (Table 4-3, Figure 4-6). These results indicate that the NDVI calculated using MOD_B as the NIR band produces values closer to the traditional NDVI as calculated with the L8-OLI sensor. Contrary to NDVI, the calculation of GCCr did not improve the relationships observed with the spectral bands alone.

Comparisons were also made with band-specific equations with the constant forced to zero, the results of which for spectral reflectance revealed the same R^2 as the standard equations in all data pairs analysed, i.e. UAV vs ASD and UAV vs L8-OLI imagery data (Table 4-3). The UAV-retrieved reflectances using the C0 equations yielded slightly higher reflectance values than the reflectances retrieved with the standard equations, especially for the NIR bands (Figure 4-5). In terms of NDVI, the C0 equations resulted in either the same or slightly lower (0.01) R^2; the biases were consistently lower than the standard calibration

equation (Table 4-3), resulting in the data points lying closer to the 1:1 line (Figure 4-6). For GCCr, C0 equations improved the relationships, but with higher bias and lower R^2 values than NDVI (using the MOD_B), indicating that GCCr is not advantageous over NDVI, or over the visible bands (Table 4-3). For this reason, the remainder of this chapter focuses on the NDVI analysis.
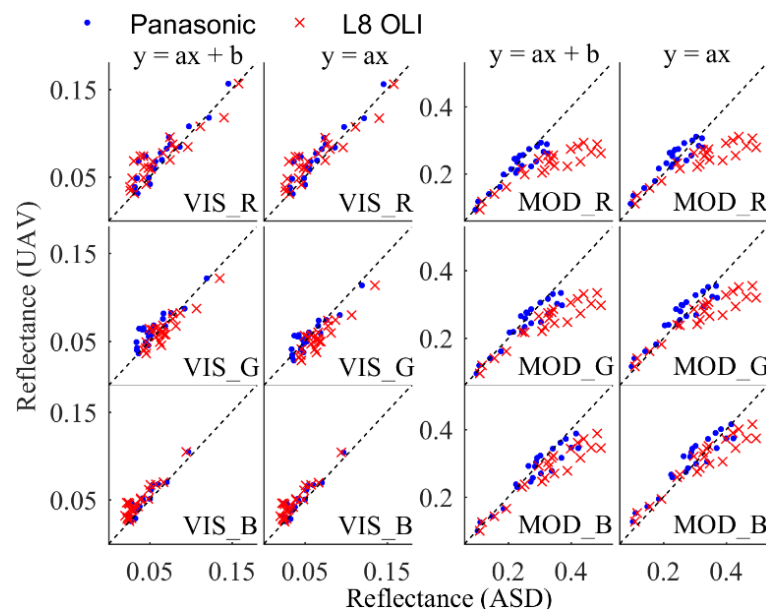
Figure 4-5. Comparison of reference (ASD, convolved to Panasonic cameras and L8-OLI RSR) and retrieved reflectance (UAV) over 22 natural targets. The original equations (y = ax + b) were also tested with their constant forced to zero (y = ax). The dashed line shows the 1:1 relationships.
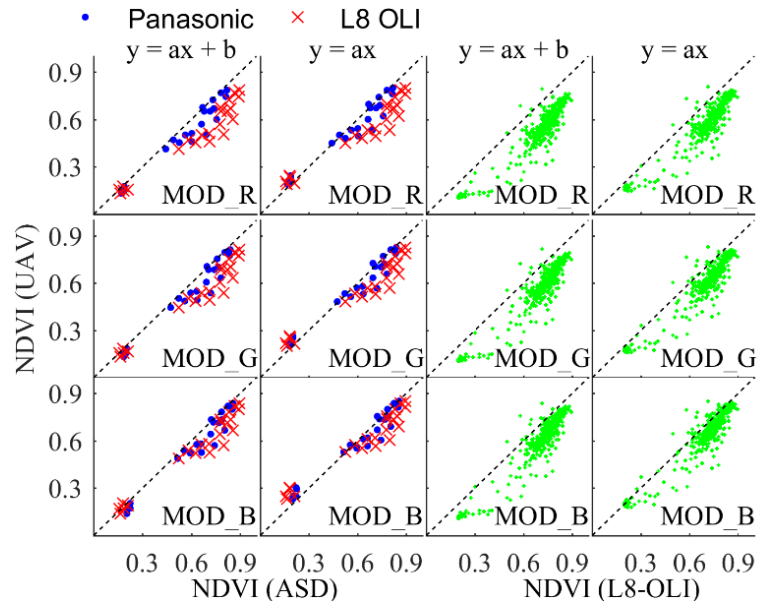
Figure 4-6. UAV-derived NDVI are compared against ASD-derived NDVI, over ground natural targets (convolved to Panasonic and L8-OLI RSR) (1st and 2nd column, n=22) and against actual L8-OLI data, over the whole woodland and its surroundings (3rd and 4th column, n=405). NDVI (UAV) was calculated using the VIS_R channel as red band and the three MOD channels as NIR band. Standard equations are represented by "y = ax + b" and equations with no intercept are "y = ax". The dashed line shows the 1:1 relationships.

4.4.2 Time series applied to forest phenology

The UAV reflectances retrieved using standard equations followed, in general, the pattern as detected by the Landsat sensors, but with some obvious 'spikes' (Figure 4-7 a,b). These spikes were observed to occur on those dates when variable illumination led to a mixture of cloudy and sunny patches in the orthomosaics, with illumination conditions differing between imaging GCTs and vegetation targets. The calculation of NDVI diminished the effects of these abrupt variations in the UAV reflectance time series, resulting in a typical deciduous (Figure 4-7 c) and evergreen (Figure 4-7 d) NDVI temporal trend (Hmimina *et al.*, 2013), similar to those from Landsat, and indicating that COTS cameras can be used to generate consistent vegetation index time-series data. However, the UAV NDVI time series still presented some date-to-date variations (mainly for the evergreen trees, Figure 4-7 d), fluctuations that were not present in the Landsat series. The C0 equations resulted in less date-to-date variation in the NDVI time series (Figure 4-7 g,h), with both the NDVI data and the trend being very similar to the Landsat measurements.
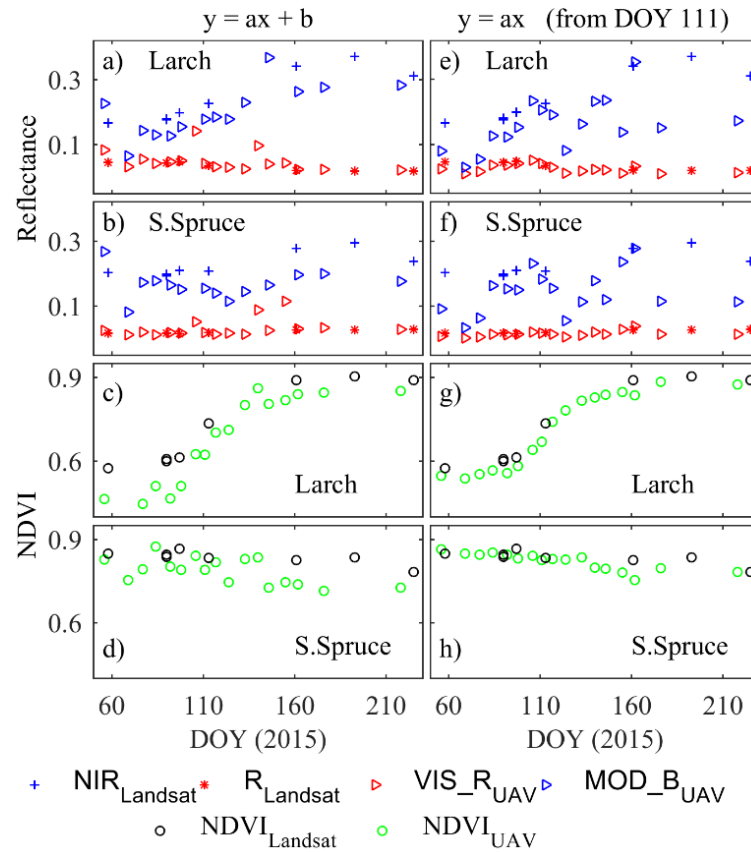
Figure 4-7. Time series of reflectance and NDVI from UAV and Landsat sensors. The UAV reflectances were retrieved via empirical line methods using either one specific equation per day (standard equations) (a-d) or one single equation (C0 equations) from the reference DOY 111 (e-h).

The comparisons between the reflectances retrieved by the standard and C0 equations over the pasture sample revealed poor correlation in the VIS_R (R^2=0.26, RMSE=0.02, *n*=17) and no correlation in the MOD_B (R^2=0.01, RMSE=0.11, *n*=17) bands (Figure 4-8). On the other hand, the NDVIs derived from the two methods presented very similar values through the time series (Figure 4-8) and were strongly correlated with each other (R^2=0.97, RMSE=0.02, *n*=17). This supports the hypothesis that time series of NDVI could be retrieved based on a single calibration equation from a reference date, but date-specific (or illumination conditions-specific) equations are necessary if reflectance is needed. The time series of GCCr derived from the two methods (standard and C0 equations, over the pasture sample) was also investigated but returned only a poor agreement (R^2=0.44, RMSE=0.02, *n*=17).
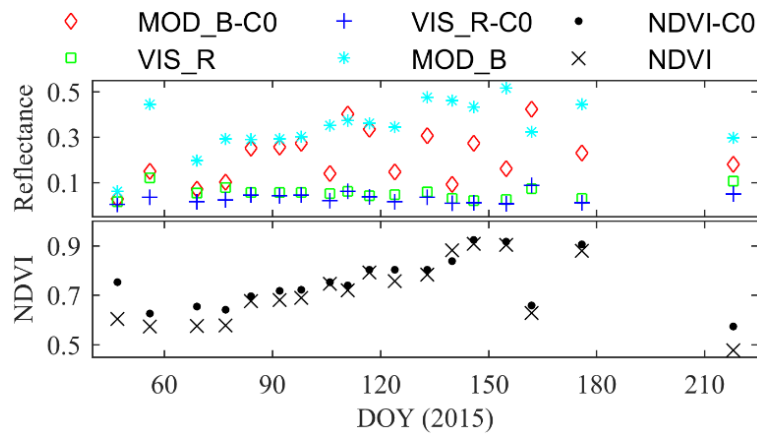
Figure 4-8. Comparison between UAV spectral data retrieved using one different equation per day and one single equation from DOY 111 (indicated as C0) over a pasture sample located 1 m from the GCTs.

Table 4-4. R^2 and bias (in brackets) values between measured (ASD, convolved to both Panasonics and L8-OLI RSR) and estimated (UAV) reflectances and NDVIs on DOY 111. An equation from DOY 155 with constant zero (y = ax) was used to estimate the UAV spectral data on DOY 111.

	UAV vs ASD (n=22)[1]		UAV vs L8-OLI imagery (n=403)[2]
	Panasonic RSR	L8-OLI RSR	
VIS_R	$0.86_{(0.22)}$	$0.85_{(0.22)}$	$0.83_{(0.173)}$
VIS_G	$0.84_{(0.18)}$	$0.82_{(0.16)}$	$0.83_{(0.125)}$
VIS_B	$0.87_{(0.12)}$	$0.87_{(0.12)}$	$0.84_{(0.093)}$
MOD_R	$0.85_{(-0.67)}$	$0.83_{(0.57)}$	$0.73_{(0.435)}$
MOD_G	$0.88_{(-0.72)}$	$0.88_{(0.65)}$	$0.77_{(0.503)}$
MOD_B	$0.90_{(0.78)}$	$0.90_{(0.75)}$	$0.80_{(0.592)}$
NDVI$_R$	$0.94_{(-0.052)}$	$0.93_{(-0.128)}$	$0.86_{(-0.149)}$
NDVI$_G$	$0.95_{(-0.053)}$	$0.94_{(-0.104)}$	$0.87_{(-0.122)}$
NDVI$_B$	$0.95_{(-0.051)}$	$0.94_{(-0.076)}$	$0.88_{(-0.091)}$
GCCr	$0.87_{(-0.074)}$	$0.84_{(-0.077)}$	$0.75_{(-0.073)}$

[1]Comparisons made over natural ground targets; [2]Comparisons made over the whole woodland area and its surroundings.

In the third validation test, the UAV orthomosaic DNs from DOY 111 were converted to reflectance using C0 equations determined on DOY 155, with estimates compared against ASD and Landsat data (Table 4-4). The UAV-derived reflectances had the same R^2 as calculated in Table 4-3, but with significant higher biases (up to 80%). On the other hand, the NDVI presented the same magnitude of biases, with the R^2 being either the same or just 0.01 lower than the values observed in Table 4-3, further confirming that NDVI could be

adequately retrieved from a single C0 equation but single-band reflectance cannot. Similarly, GCCr could also be adequately retrieved (Table 4-4), but the agreements were lower than with NDVI.

4.4.3 UAV VIs vs structure and composition of the woodland

Time series of UAV NDVI and NDVI_C0 were extracted for each of the six plots (average value within the plots boundaries) and fitted by the greendown model (as detailed in Chapter 5) (Figure 4-9, top graph). The RMSE values from this curve fitting were compared against three plot structural metrics (Figure 4-9) in order to investigate if the UAV temporal uncertainty (as mainly observed with NDVI) is related to the canopy structure and composition of the plots (though it was not possible to separate structure and composition in this analysis). Only weak, non-significant, relationships were found between RMSE and the structural metrics ($R^2 < 0.30$). Therefore, there is no strong evidence to confirm that the variability in the UAV VI time series is dependent on the structural variability of this woodland, although this is only assessed for a limited number of plots (n=6), each with different species.
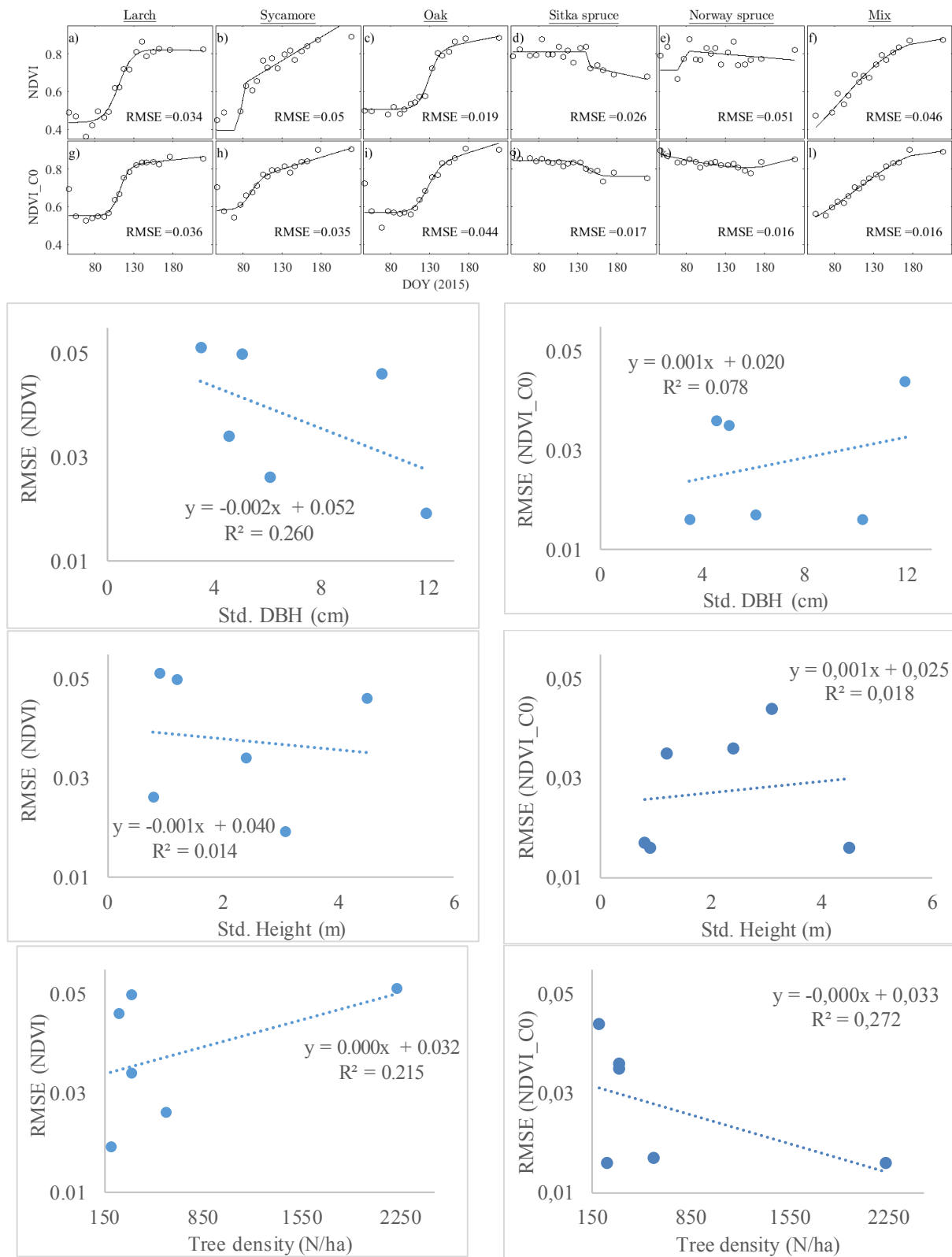
Figure 4-9. Time series of UAV NDVI and NDVI_C0 fitted by the greendown model (as detailed in Chapter 5) across the six plots (top graph). The UAV RMSE values from the fitted UAV VIs were compared against the structural variables of each plot. Std. = Standard deviation. No significant relationships were found ($p<0.05$).

4.5 Discussion

4.5.1 Retrieving reflectance and NDVI from UAV COTS cameras

In this study two COTS cameras were radiometrically calibrated and their potential to be used as multispectral imaging systems was assessed. State-of-the-art equipment was used to accurately determine the vignetting effect and the spectral sensitivity of the COTS cameras. These camera-related characteristics are vital for spectral reflectance measurements, interpretation of the data and comparisons with other sensors.

In general, the correlation of UAV and ground spectral data was high; between 84-90% of the variation in the ground reflectance and 95-96% of the variation in the ground NDVI could be explained by the UAV-retrieved reflectance and NDVI, respectively. These results are similar to studies using scientific cameras (e.g. Tetracam) onboard on UAVs (Berni *et al.*, 2009; Laliberte *et al.*, 2011) and confirm that COTS cameras, following calibration, can yield accurate reflectance and NDVI estimates. It would be valuable, in a future study, to conduct a direct comparison between scientific and COTS multispectral cameras to further assess the quality of COTS-acquired data.

Accurate reflectance estimates can be obtained even when orthomosaics consisted of hundreds of images acquired with COTS cameras, and when a single equation is used to retrieve reflectances based on GCTs appearing only on a single (or a few) images per acquisition. This can be explained, firstly, as a result of a consistent image pre-processing workflow, which generated orthomosaic DNs linearly related to ground reflectances; this indicates that the Panasonic sensors recorded radiance in a linear way and that the methodology used to correct the RAW images was able to preserve this relationship. Secondly, single images acquired with UAVs at low heights can present very strong variation in brightness values due to angular variation of reflectance (bidirectional effect) (Hakala *et al.*, 2010; Rasmussen *et al.*, 2016). This effect can be potentially diminished if an orthomosaic is made of a dataset with high image overlap (>9 per point in this study), acquired within a short period of time (<15 min in this study). In this condition, processing algorithms can select the closest pixels to the nadir angle (among the overlapping images) to form the orthomosaic (AgiSoft, 2016), resulting in orthomosaic pixels which could be assumed to have similar bidirectional effects, at least on flat areas.

Despite this assumption, there should still be some remaining influence of bidirectional effects in the orthomosaic DNs, which will account for some uncertainty in the

retrieved reflectances. The calculation of NDVI is expected to account for some of these effects (Bajwa and Tian, 2002; Matsushita *et al.*, 2007; Samseemoung *et al.*, 2012; Shahtahmassebi *et al.*, 2013), which can explain the better performance of this index over the individual bands alone.

The blue channel from the modified camera was consistently the best candidate to be used as the NIR band either alone or in the NDVI calculation, in agreement with (Verhoeven, 2012) but different from a number of alternative suggestions made in the literature (Dare, 2008; Yang *et al.*, 2014a; Mathews, 2015). Even though the MOD blue channel has lower sensitivity and lower SNR than the MOD red channel, it produces a stronger NIR response and consequently more useful and high quality data for vegetation monitoring. In future studies it may be beneficial to set a modified camera to have a higher exposure than the unmodified one, which would increase the blue channel sensitivity and SNR.

It is known that COTS cameras have the potential to be used as a multispectral sensor (Hakala *et al.*, 2010; Mathews, 2015; von Bueren *et al.*, 2015) but this should be done with care. The RGB response functions of a COTS camera are expected to be wide and overlapping, as shown here and elsewhere (Dare, 2008; Berra *et al.*, 2015), contrary to the narrow, well-defined and non-overlapping RSR present in satellite sensors (Barsi *et al.*, 2014). This RSR overlapping can cause band correlation and a mixed spectral response (Nijland *et al.*, 2014), a fact which could explain why GCCr, a VI based on the VIS camera bands, did not prove to be advantageous over the spectral bands alone. However, by employing two cameras simultaneously (one unmodified and one modified, as in this study) it is possible to acquire two spectrally separated bands, register them together and estimate VIs such as NDVI.

Alternatively, it is possible to use a single modified camera, where customized filters can allow either NIR-R-G (Verhoeven, 2012) or NIR-G-B (Hunt *et al.*, 2010) images to be acquired. The Panasonic cameras (Figure 4-2) could benefit from a NIR-R-G arrangement (for NDVI purposes), as the blue channel has a stronger NIR response. On the other hand, a NIR-G-B approach could be useful if red-edge-based indices are of interest, as the red channel has a strong peak response within the red-edge wavelengths. The great advantage of a single-camera approach is that the three bands are already registered, but this may bring some disadvantages, such as less control of the shape of the NIR band and no standard RGB colour images (Rabatel *et al.*, 2014).

4.5.2 Time series from UAV COTS cameras

UAVs can be particularly helpful to obtain time-series data in regions that experience frequent cloud cover, such as Great Britain (Armitage *et al.*, 2013). In our study area, only 7-9 good quality Landsat images were available, unevenly distributed in time, whilst UAV data were acquired 18 times on a weekly basis. Such temporal resolution can be particularly useful in phenology studies but also for critical situations such as monitoring plant disease or pest attacks (Vega *et al.*, 2015).

The use of calibrated COTS cameras on a UAV allowed a consistent time series of NDVI to be obtained, although this was not always the case for the spectral reflectance. The acquisition of UAV data under cloudy conditions increases considerably the chance of obtaining high temporal resolution optical data, but it can result in difficulties in transforming image DNs to calibrated reflectance using the empirical line method, particularly in orthomosaics acquired during highly variable illumination conditions (patchy cloud), a problem which is also common to other airborne data sets (Hope *et al.*, 2004). Further work on radiometric normalization of images (Lebourgeois *et al.*, 2008) or cloud shadow detection and correction (Bondi *et al.*, 2016) could improve the results.

The calculation of NDVI significantly reduced the impact of varying illumination conditions and shadowing effects, an advantage also noted in other studies (Bajwa and Tian, 2002; Matsushita *et al.*, 2007; Samseemoung *et al.*, 2012; Shahtahmassebi *et al.*, 2013), and this highlights the importance of acquiring visible and NIR images concurrently. This resulted in a consistent time series of NDVI, allowing the expected temporal pattern of a deciduous and evergreen land cover (Hmimina *et al.*, 2013) to be identified (Figure 4-7 c,d).

A similar pattern could be inferred from the Landsat NDVI series (Figure 4-7 c,d), but with a number of significant temporal gaps; a common problem with the Landsat series and other satellite sensors (Fisher *et al.*, 2006). UAV-derived NDVI time series can be used therefore to identify seasonal transitions in vegetation activity with a more appropriate temporal resolution. UAV data can also be used to better understand the fine-scale spatial variability in phenology events occurring at a sub-pixel level for satellite data sets (Hmimina *et al.*, 2013).

The calculation of NDVI using a date-specific empirical line correction was not able to produce a totally noise-free time series (Figure 4-7 c,d), and a simple new approach was observed to improve the results. The use of a single reference equation per band (with

intercept zero), derived from a single date and applied across the whole time series, resulted in a more consistent time series of NDVIs (Figure 4-7 g,h), highly comparable with the Landsat series. These results suggest that it may be sufficient to have GCTs for only one (or a small number of) reference dates and then apply a C0 equation from this date to the whole time series to calculate a series of NDVI values, which could improve the efficiency of data acquisition and processing. However, as our results show, if estimates of spectral reflectance are necessary, rather than NDVI, date-specific (or illumination conditions-specific) calibration equations are clearly vital.

The noise present in the NDVI time series derived with the standard equations can be due to a few factors, which point towards the difficulty in determining well calibrated equations (Smith and Milton, 1999) in every acquisition date. First, it was not always possible to use the four GCTs on some dates as either one or two GCTs had different illumination conditions than the others; a fact which can increase the errors in the estimated reflectances (Smith and Milton, 1999). Secondly, the GCTs were assumed to have a constant reflectance over time. In reality, the GCTs are not lambertian and, ideally, their reflectance should be measured in every date, which was impractical if not impossible on some occasions and would be costly and time consuming in operational contexts. This means that the calibration equations using GCTs` reflectance measured on a different date could be prone to added errors due to BRDF effects (Sandmeier and Itten, 1999). No statistical evidence was found to suggest that the structure and composition of this woodland was related to the variability observed on the UAV VIs (Figure 4-9). It could be expected that a more variable plot could have an uneven canopy surface and be more influenced by sun-sensor geometry and shading (Peddle *et al.*, 1999). Nevertheless, it has to be stressed that only 6 plots were surveyed, meaning that no solid conclusion can be drawn from this analysis and highlighting potential for more research in this aspect.

Finally, the standard equations can suffer uncertainties over very low DNs values, as the intercept value can be higher than the lowest DNs values within in the mosaics. In such a situation, unrealistic reflectance (and NDVI) values will be retrieved, particularly in heavily shadowed areas (due to trees or clouds shadows or a combination of both, intensified by high solar zenith angles). Forcing the constant to zero assumes therefore that all the bands, from both cameras, are perfectly consistent with each other (i.e., when DN = 0, reflectance will be 0), preventing unrealistic reflectance values being retrieved from low DNs values.

4.6 Conclusions

UAVs can acquire consistent fine spatial resolution data at user-controlled revisit periods, without the limitations that result from cloud presence. This represents a great flexibility over spaceborne optical systems, as vegetation changes can be monitored at a higher temporal resolution.

Broad-band surface reflectance and NDVI for vegetated areas can be retrieved with confidence from orthomosaics generated from calibrated COTS cameras onboard a UAV, when UAV data are acquired under clear, sunny conditions. Nevertheless, the wide and overlapping response functions of a COTS camera may limit their potential to be used as a multispectral sensor. However, by employing two cameras simultaneously (one unmodified and one modified, as in this study) it is possible to acquire two spectrally separated bands, register them together and estimate VIs such as NDVI with higher confidence than with the individual spectral bands alone.

It was not entirely possible in this study to generate a consistent time series of reflectance, due to variable illumination conditions during acquisitions on some dates, although further work on normalizing single images could improve the results. On the other hand, the calculation of NDVI, using the blue channel from a modified camera as NIR band, resulted in a stable time series. A more consistent NDVI time series was generated from radiometric calibration equations which have had their constants forced to zero and were based on single date GCTs, as NDVI adequately adjusts for variation in the acquisition conditions.

Chapter 5. Individual tree- and plot-level monitoring of spring phenology

5.1 Introduction

The aim of this chapter is to assess the potential of imagery acquired with a UAV to track spring seasonal changes in a deciduous and evergreen woodland located in a temperate ecosystem. Firstly, potential matches (and lack thereof) in start (SOS), middle (MOS) and end (EOS) of spring season dates as derived from ground visual observations and UAV remote sensing products are investigated, at an individual tree-level. The analysis is then scaled up to a plot level, where UAV-derived and visual observations of spring season dates are compared with dates estimated from ground measurements of canopy cover fraction and understorey greenness and from Landsat (ETM+ and OLI) vegetation indices. Because there are no published methods or workflows for phenology assessment using UAV imagery, this chapter explores methodological options to quantify phenology in order to identify the most accurate approach to detect key spring season dates across a heterogeneous landscape.

This chapter addresses the Objective 3 of this thesis as presented in Chapter 1: "To track tree species-specific spring seasonal changes in a mixed woodland ecosystem, which can provide novel insights into the timing of phenology events between and within tree species". The specific objectives include:

- To identify the most accurate vegetation index and sigmoid-based model for detecting start (SOS), middle (MOS) and end (EOS) of spring season from time series of UAV imagery.
- To examine the relationship between UAV time series and various phenological field metrics (visual assessments of tree leaf phenology, ground-based imagery of canopy closure and understorey development) to better understand what the sensor is characterizing and which phenological stages are most accurately predicted.
- To assess the potential of UAV data to detect the phenology of evergreen trees.
- To characterize potential sources of errors in UAV-derived phenometrics.

5.2 Methodology

The following methodological sections describe how the phenological events were estimated from the time series of UAV imagery, and how the ground validation data were used to assess the quality of these UAV products.

5.2.1 Definition of key phenological events from the visual observations

Leaf phenological stages were visually assessed across six plots (with 20 trees in each plot), from no buds visible (code 0) until full leaf expansion (code 675), resulting in a ground-based phenological time series. Dates of three key phenological observation levels (390, 490, 590) were selected to mark the start (SOS), middle (MOS) and end (EOS) of spring season (Schwartz *et al.*, 2013). SOS is associated with >90% of bud open (leaf/candle visible), MOS with >90% of leaf/candle out (not fully unfolded) and EOS with >90% of full leaf unfolded or >90% of needles unfolded from candle (Figure 5-1). These ground observed physical changes should reflect the spring phenology derived from the UAV and Landsat data set.
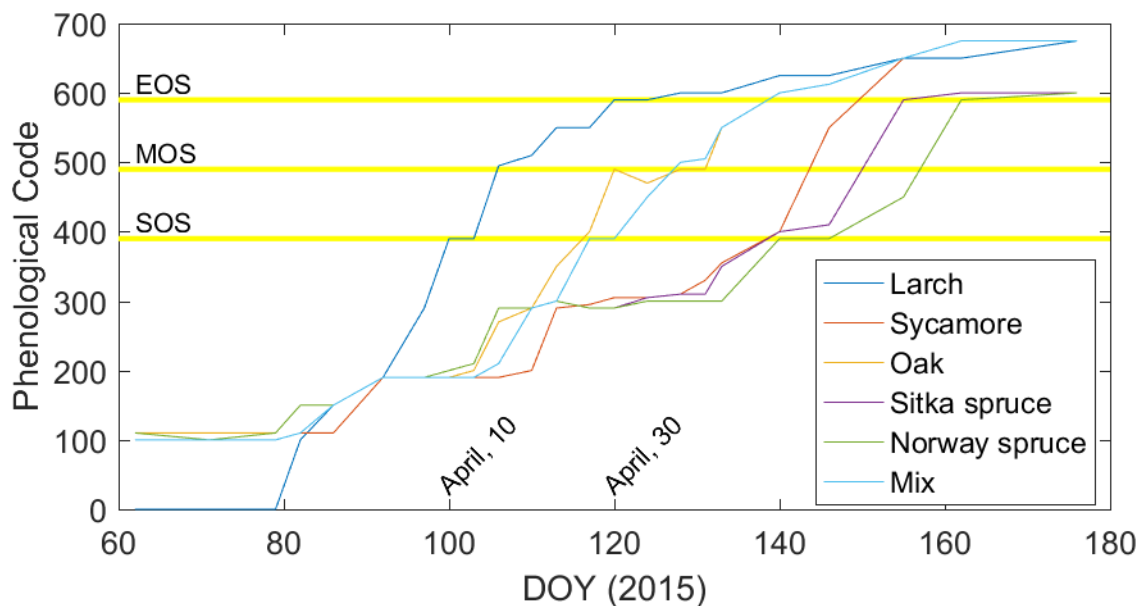
Figure 5-1. Median spring phenological levels (as presented in Chapter 3) observed during the spring season of 2015 for deciduous (Larch, Sycamore, Oak and Mix) and evergreen (Sitka spruce and Norway spruce) tree species. The yellow horizontal lines mark the codes used to represent the observed start (SOS), middle (MOS) and end (EOS) of spring season.

Because the trees were assessed every 3-4 days, these codes were not always observed for all sampled trees. In this case, the dates of key missing codes were estimated by averaging the dates associated with the closest phenological code observed before and after the missing

code. Intra- and inter-specific variability in leaf phenology dates in each plot were then analysed for the codes 390, 490 and 590.

To scale from individual tree phenodates to the plot level, a plot average was calculated based on a tree observation weighted by its plot percent basal area (White *et al.*, 2014). Finally, potential relationships between phenology dates and biophysical parameters (diameter at breast height (DBH) and total height) were investigated with aid of linear regression analysis.

5.2.2 *Identification of tree crowns within the plots*

In order to assess the potential of UAV data to detect tree-level phenology, it is necessary to identify the tree crown boundaries. Since a relatively small number of reference trees were sampled (120), and considering the very high spatial resolution of the UAV orthomosaics (5 cm), tree crowns were extracted by a manual delineation approach in ArcGIS 10.3.1 (ESRI©) (although an automatic tree crown delineation was later employed to analyse phenology at a woodland level (Chapter 6, section 3.3). Firstly, a point data set containing the location and identification of each sampled tree (surveyed in the field, Chapter 3) was overlain on the UAV orthomosaics. Each crown boundary was thereafter drawn based on leaf-on orthomosaics, but the entire time series of visible and NIR orthomosaics was used to aid the image interpretation, allowing individual crowns to be resolved with confidence.

In order to investigate how well the manually delineated tree crowns match with the actual crowns, ground measurements of crown diameter (available at three plots) were compared against crown diameter estimated from the manual delineation. The manual delineation-derived diameter was based on the crown area (assuming a circular shape), whilst the ground-derived diameter represents the average of two cross-section measurements per tree (as detailed in Chapter 3). In general, manual delineation underestimates crown diameter by around 60 cm with a RMSE of 23% (Table 5-1). This difference may be due to the ground method measuring only two crown cross-sections, where one of them includes the longest branch, resulting in an ellipse-shaped crown which can overestimate the crown area if the crown has a very irregular shape. On the other hand, a 5 cm UAV orthomosaic allows a crown`s irregular shape to be visually interpreted and delineated and, in theory, a more precise crown area is estimated. However, further investigations would be necessary to produce more conclusive explanations of these differences.

Table 5-1. Comparison between crown diameters measured on the ground and derived from manual delineation of UAV orthomosaics. Bias refers to manual delineation minus measured on the ground. RMSE is shown as a percentage of the mean measured diameter (Pouliot *et al.*, 2002).

Plot	N	Mean diameter (m)		Bias (m)	Absolute error (m)	RMSE (%)
		Measured on ground	Manual delineation			
Larch	20	5.6	5.1	-0.5	1	22
Sycamore	20	5.1	5.2	0	0.9	21
Oak	20	7.9	6.7	-1.2	1.5	24
Total	60	6.2	5.7	-0.6	1.1	23

The delineated polygons served as region of interest for extraction of DNs from the orthomosaic RGB channels. The 5 cm spatial resolution allowed many pixels to represent a tree crown but, ultimately, an averaged DN value for each RGB channel per tree was calculated in this chapter. A temporal pixel-wise analysis using the original 5 cm spatial resolution may be problematic due to the orthomosaics positional uncertainty ($\pm$ 11 cm, 2.1 pixels, Chapter 4, section 4.3.6), being even more critical when combining visible and NIR orthomosaics for NDVI calculations. Even when time series of imagery are acquired from fixed cameras, the original pixel size is usually down resampled or averaged to increase the confidence of the resulting data set within a region of interest (Julitta *et al.*, 2014).

Alternative approaches were tested to calculate a mean DN in order to diminish the influence of shaded areas and/or understorey vegetation in the final UAV phenology time series. These consisted of calculating the mean DN of all pixels that support a DN value above defined percentiles (10th, 20th, 30th, 40th, 50th, 60th, 70th, 80th and 90th). The mean-lit DNs (sunlit area) could also be an option (Leckie *et al.*, 2005; Lucas *et al.*, 2008), but the values generated by this approach are likely to be very similar to one of the percentiles considered (not necessarily the same percentile through the time series). In theory, the percentile method captures pixels associated with the sunlit area and, compared to the full crown mean, it should diminish the variability associated with the inclusion of shaded areas and/or understorey vegetation.

The mean DNs from each percentile were then used to calculate UAV VIs (section 5.2.3). Thereafter, a sensitivity analysis was carried out in order to indicate the optimal percentile to select pixels values from within tree crowns (section 5.2.5).

5.2.3 Remote sensing products

Time series of data from remote sensing products at ground-, aerial- and spaceborne-level were gathered in this research. Ground data included plot level measurements of understorey GCC_{DN} and canopy gap fraction, as detailed in Chapter 3. Landsat 7 ETM+ and Landsat 8 OLI NDVI and EVI compose the spaceborne data (Chapter 4). Chapter 4 (section 4.3.7 and 4.3.8) also describes the generation of NDVI, $NDVI_{C0}$, GCC_r and $GCC_{r/C0}$ from the UAV imagery (C0 refers to one single equation per band, with no intercept, for the entire series; r refers to reflectance), which are spectral-based VIs, but in this chapter, the colour-based VI GCC_{DN} (i.e., composed of DNs rather than reflectance) is also calculated from the visible orthomosaics, as it is frequently extracted from ground (Julitta *et al.*, 2014) and near-surface (Toomey *et al.*, 2015) remote sensing data. Different combinations of the NIR orthomosaic`s RGB channels were also tested to calculate NIR-based colour indices, but the time series proved to be, in general, noisier than the visible-derived GCC_{DN}, resulting in poorer data quality. For this reason, NIR-based colour indices were not included in the analysis.

The sensitivity of the UAV GCC_{DN} to changes in illumination conditions was analysed by comparing values from selected trees and Ground Calibration Targets (GCTs) (Berra *et al.*, 2016). Mean GCC_{DN} values were extracted from within two individual crowns (manually delineated) of Oak and from within the extent of two GCTs present in the orthomosaics. The GCC_{DN} values of each tree and each GCT were plotted against the DOY when the data were acquired in order to observe the index temporal stability.

5.2.4 Estimating phenodates from time series data

Key spring phenological markers were extracted from the time series of remote sensing products by means of curve fitting. Past studies have not smoothed phenological time series data (e.g. Schwartz *et al.* (2013)), but here the time series of remote sensing data is smoothed in order to diminish the influence of noise in the time series. The original time series data was smoothed using a second-order Savitzky-Golay filter (window size = 5) before the phenological parameters were extracted (Lhermitte *et al.*, 2011; Ryan *et al.*, 2012; Miao *et al.*, 2013).

Three sigmoid-based models were tested to fit the time series of remote sensing data and extract phenological dates related to the growing season, similarly to Klosterman *et al.* (2014). Such models are widely used in phenological studies because phenological profiles

extracted from time series of remotely sensed data follow a relatively well-defined temporal pattern which can be easily represented by a sigmoid logistic growth (Zhang *et al.*, 2003; Fisher *et al.*, 2006; Fisher and Mustard, 2007), at least in deciduous vegetation and many crops (Toomey *et al.*, 2015).

Zhang *et al.* (2003) developed one of the simplest sigmoid-based model (Eq. (5-1)) (termed simple sigmoid by Klosterman *et al.* (2014)), a fact which, associated with its robustness to noise (Fisher *et al.*, 2006), has made it widely used in phenological studies.

$$f(t) = \frac{c}{1 + e^{a+b.t}} + d \qquad (5\text{-}1)$$

where *t* is time in days, *f(t)* is the VI value at time t, *a* and *b* control the timing and rate of increase, *c* + *d* is the maximum VI value, and *d* is the initial background VI value (dormant season).

The second model, termed greendown sigmoid by Klosterman *et al.* (2014), was developed by Elmore *et al.* (2012) and is a modification of the simple sigmoid, as it adds a new parameter (m_7, Eq. (5-2)) to account for summer trends in greenness observed in many forest canopies, mainly when high temporal resolution data are available (e.g. phenocam), thereby fully capturing the phenological dynamic of such canopies (Melaas *et al.*, 2013).

$$f(t) = m_1 + (m_2 - m_7.t).\left(\frac{1}{1 + e^{(m_3 - t)/m_4}} - \frac{1}{1 + e^{(m_5 - t)/m_6}}\right) \qquad (5\text{-}2)$$

where m_3 and m_4 control the phase of green-up; m_5 and m_6 control the phase of senescence; m_7 the summer green-down; $m_1 + m_2$ is the maximum VI value, and; m_1 is the initial background VI value.

The approach of Elmore *et al.* (2012) was further expanded by Klosterman *et al.* (2014) (termed generalized sigmoid) in order to create a highly flexible model (Eq. (5-3). Two additional parameters were introduced (q_i and v_i) to allow different rates of increase near the lower and upper asymptotes of the sigmoid. Besides accounting for the summer trends (a_2 and b_2), the model also tries to account for changes in the dormant season value (a_1).

$$f(t) = (a_1.t + b_1) + (a_2.t + b_2.t + c)$$
$$\left(\frac{1}{\left(1 + q_1.e^{(-h_1.(t-n_1))}\right)^{v_1}} - \frac{1}{\left(1 + q_2.e^{(-h_2.(t-n_2))}\right)^{v_2}} \right) \qquad (5\text{-}3)$$

where a_1, a_2, b_2, q_1, q_2, v_1, v_2, h_1, h_2, n_1 and n_2 are fitting parameters, $b_1 + c$ is the maximum VI value, and b_1 is the initial background VI value.

Contrary to the simple sigmoid, the greendown and generalized models are designed to model a full year of phenological data. However, since this study surveyed only the spring season, the negative part of Eq. (5-2) (containing parameters m_5 and m_6) and Eq. (5-3) (containing parameters q_2, v_2, h_1, h_2 and n_2) were eliminated as they account for autumn trajectories.

To automatically fit and detect phenological transition dates from the remote sensing products, Matlab (R2016a, The Mathworks, Nattick, MA) codes were downloaded and modified from Klosterman *et al.* (2014). The three models were fitted to the spring data using nonlinear regression, starting from an automatically determined first guess of the function parameters (based on relationships/ratios observed in the original data, such as amplitude and mid-point value) and solved through multiple iterations (Fisher and Mustard, 2007; D'Odorico *et al.*, 2015). This was done using the Matlab function lsqnonlin (Nonlinear least-squares solver). The phenological transition dates were identified by using local extremes in the rate of change in the curvature of the fitted models (*k,* Eq. (5-4)) (Zhang *et al.*, 2003; Klosterman *et al.*, 2014):

$$k = \frac{f''(t)}{(1 + f'(t)^2)^{\frac{3}{2}}} \qquad (5\text{-}4)$$

where f' and f'' indicate the first and second derivative of the function f, respectively.

Transitions dates correspond to the times at which the rate of change in curvature (k) exhibits local minima or maximums (Figure 5-2a). These extrema in the rate of change were associated with start (SOS), middle (MOS) and end (EOS) of spring season, as proposed by Zhang *et al.* (2003).

The uncertainty in the estimates of phenological dates were quantified by using the residuals between the model fit and the observed data (Filippa *et al.*, 2016). These residuals were used to generate 100 random samples of new VI time series values (a new VI value is randomly positioned in between the fitted and the original data value), each of which was

used to produce a new set of phenology dates (Figure 5-2b). This procedure resulted in an ensemble of estimated dates from which the inner 95% range was used to quantify an uncertainty estimate of phenophases. This analysis was done with all the remote sensing products used in this research.
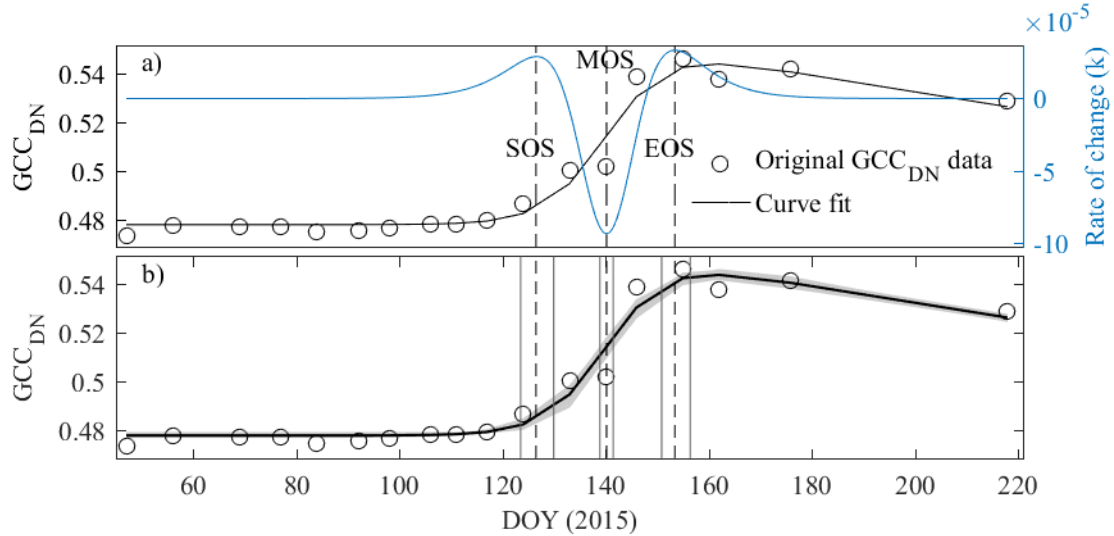
Figure 5-2. a) A sample time series of UAV GCC_{DN} data of an oak tree fitted by the greendown sigmoid model (Eq. (5-1)), from which phenological transition dates (SOS, MOS and EOS) were estimated based on the rate of change of the fitted model. b) The grey lines around the curve fit represent 100 simulated curves on which phenophases were extracted and the two vertical grey lines represent the inner 95% percentile of the 100 replications.

5.2.5 Analysis methods

To evaluate the agreement between UAV-derived phenometric dates versus those obtained from each of the independent data sets (visual assessments, ground photography of understorey and canopy and Landsat), several common measures of statistical agreement were used, including the root-mean-square-error (RMSE), coefficient of determination (R^2) and bias for each case. Because the dependent and independent observations both include significant measurement uncertainty, Reduced Major Axis (RMA) regression (Smith 2009) was used to estimate the slope and intercept (95% confidence interval) on linear regressions (D'Odorico *et al.*, 2015; Melaas *et al.*, 2016) between each independent data set and the UAV-derived phenophases dates.

The analysis was firstly carried out at an individual tree level where UAV derived estimates (from 3 models and 5 vegetation indices) were compared against visual assessments, providing measures of how well the UAV data can predict phenology event dates. These results, along with the model uncertainties (section 5.2.4), allowed identification

of the most robust combination of fitted model and vegetation index to monitor leaf phenology across deciduous and evergreen woodlands. Finally, this best combination was tested regarding the different percentiles methods (section 5.2.3) in order to identify the optimal approach to calculate DNs from within tree crowns (sensitivity analysis). This was based on the examination of R^2, bias, RMSE and number of successfully retrieved phenodates.

The best phenology extraction method for each of the vegetation types (i.e. each plot) was selected to estimate phenodates at a tree and plot level and this was done for each of the remote sensing products separately (UAV, ground photography of understorey and canopy and Landsat). However, because the vegetation types outside the plots were unknown, the best general method across all plots was identified in order to allow phenology monitoring at a woodland scale (Chapter 6).

The phenodates derived from each remote sensing product (using the best model in each plot) were cross compared at a plot level. For the UAV data, the plot boundary was manually delineated on the UAV orthomosaics (following the outer edges of the manually delineated tree crowns, section 5.2.2) and used as region of interest (Figure 5-3) to calculate mean DNs and subsequent phenometrics. The plot area was thereafter used to weight the Landsat NDVI and EVI values, as the plots were intersected by more than one Landsat pixel (Figure 5-3), and the weighted time series used to estimate phenometrics.

For this plot level comparison, it is assumed that the plot area represents the area imaged by the Landsat pixels (900 m^2). In reality, plot and pixel areas differ to different degrees (Larch = 583 m^2, Sycamore = 585 m^2, Oak = 1000 m^2, Sitka spruce = 340 m^2, Norway spruce = 89 m^2, Mix = 780 m^2) because the number of trees (20) was the decisive factor limiting a plot boundary, rather than a fixed area (as in White *et al.* (2014)). This in turn resulted in some plots having a coverage similar to Landsat pixels (e.g. Oak), whilst denser plots (e.g. Norway spruce) may be underrepresenting the Landsat data (Figure 5-3). Additionally, whilst the vegetation types within the plot were identified (including under and overstorey), this information is not available for the Landsat pixel areas, meaning that the phenology detected within the Landsat pixel areas might be influenced by the phenology of plant species which were not monitored in this research.

Figure 5-3. A Landsat grid and the plot boundaries are overlaid over the woodland area. Orthomosaic made of UAV images (visible camera) acquired on 21/04/2015 (DOY 111).

A similar assumption was made for the ground photography data. The understorey-derived GCC_{DN} is expected to represent very precisely the plot area, as specific regions of interest were drawn within the images at each plot (Chapter 3, section 3.5.2). Nevertheless, the exact area and location of the ROIs is not known as the data is not georeferenced; furthermore, because the images were acquired on the ground, on the plot boundaries, some understorey areas are either not captured because they are outside the cameras' field of view or are not visible on the images as they are located behind a tree trunk.

Regarding the hemispherical images, the same circle of interest (zenith angle) was applied to all the hemispherical images across the six plots, meaning that the plot cover fraction can be either under or overrepresented. Cover fraction is also highly sensitive to vegetation density (White et al. 2014), which means that the location of the camera within a plot can have significant impacts on the derived metrics; because this research acquired images from a single position within a plot, the estimated plot cover fraction can therefore be either under or overestimated.

Nevertheless, despite likely areal representativeness discrepancies across the different spatial scales, the ground and orbital data sets are expected to detect the general seasonal pattern of the different land covers, contributing towards a better understanding of the phenology detected by the UAV sensors.

Finally, the sensitivity of the sigmoid fit to the number of UAV data points was tested, in order to verify how different temporal resolutions affect the shape of the curve and phenology estimation. The original, approximately once per week, observations of UAV data were systematically reduced to approximately once every two weeks, to approximately once

every three weeks and to match the Landsat temporal resolution. At an individual tree level, the resulting UAV transition dates were compared against the observed visual assessments, and the effects were quantified by means of analysis of Bias, RMSE and R². Additionally, plot-level phenological curves were plotted for each different temporal resolution.

5.3 Results

5.3.1 Visual observations

Substantial phenological variation was detected between individuals of the same species within some plots. The differences ranged from 7 to 38 days for SOS, 16 to 43 days for MOS and 10 to 29 days for EOS (Table 5-2). Among the deciduous species plots, Larch presented the smallest variation in dates of SOS (7 days), MOS (16 days) and EOS (22 days), whilst Sycamore showed the largest variation in dates of SOS (38 days), MOS (43 days) and EOS (29 days). Considering only the two evergreen species, Sitka spruce presented the largest observed variations in the three phenophases dates, with SOS dates spanning 10 days longer than for Norway spruce, but only a one-day difference was observed for MOS.

The variability within a plot was also examined by counting the trees that reached a key phenophase outside the mean ± one standard deviation date interval (Table 5-2). In general, even when a plot can be considered as having reached a defined phenophase (given by the plot mean), around one quarter of individuals in a plot still lagged considerably.

The plot averages show Larch as being the first species to start the growing season on DOY 101 (April 11, 2015) and, 40 days later, Norway spruce as the last one (May 21, 2015) (Table 5-2). Likewise, Larch was the first species to reach EOS on DOY 118 (April 28, 2015), and, 46 days later Norway spruce reached this same level (June 13, 2015). The very first tree to start the spring season was observed within the Larch plot on DOY 099 (April 09, 2015). At the other extreme, the last tree observed to reach EOS occurred on DOY 169 (June 18, 2015) in the Norway spruce plot. The spring season of this ecosystem lasted, therefore, for 70 days, according to the protocol adopted.

Table 5-2. *In situ* phenology record analysis: First, average (in bold) and last day of year (DOY) when the start (SOS), middle (MOS) and end (EOS) of spring season were observed. SOS is associated with >90% of bud open (leaf/candle visible), MOS with >90% of leaf/candle out (not fully unfolded) and EOS with >90% of full leaf unfolded or >90% of needles unfolded from candle. The 'Variability' shows the difference between the dates that the first and last trees reached each phenophase and the number of trees (in brackets) which reached these phenophases outside a 'normal' interval (mean ± one standard deviation). 20 trees were assessed at each plot.

Plot	Phenophases			Variability		
	SOS	MOS	EOS	SOS	MOS	EOS
[a]Larch	099, **101**, 106	103, **107**, 119	106, **118**, 128	07 (*3*)	16 (*3*)	22 (*5*)
[a]Sycamore	105, **129**, 143	108, **135**, 151	122, **143**, 151	38 (*6*)	43 (*6*)	29 (*4*)
[a]Oak	106, **116**, 124	113, **125**, 137	117, **132**, 140	18 (*4*)	24 (*6*)	23 (*8*)
[b]Sitka s.	122, **135**, 146	140, **149**, 159	151, **159**, 169	24 (*5*)	19 (*6*)	18 (*5*)
[b]Norway s.	132, **141**, 146	151, **158**, 169	159, **164**, 169	14 (*11*)	18 (*3*)	10 (*7*)
[a]Mix	115, **119**, 137	115, **127**, 143	119, **133**, 143	22 (*2*)	28 (*6*)	24 (*4*)
Average	113, **124**, 134	122, **134**, 146	129, **142**, 150	21 (*5*)	25 (*5*)	21 (*6*)

[a]Deciduous; [b]Evergreen;

A comparison of biophysical parameters (DBH and total height) and the 390, 490, and 590 stages for the sampled tree species did not reveal any consistent relationships between biophysical parameters and phenology within each plot (Table 5-3). Significant correlation resulted from the full data set ('All'), but it is difficult to infer any solid relationships due to the weak correlation. In general, the amounts of variation in leaf phenology explained by DBH and total height were low, below 20%, which suggests that the phenology of the investigated species is not dependent on these forest structural parameters, a finding which agrees with Schwartz et al. (2013) and Fisher *et al.* (2006).

Table 5-3. Statistics comparing phenometrics derived from visual assessment (SOS, MOS and EOS) and biophysical variables measured in the field (Ht = total height and DBH = diameter at breast height). Statistics are given (*p<0.05; N is sample size; RMSE is in units of days). 'All' combines the data from the six plots, whilst 'Dec.' combines the Larch, Sycamore, Oak and Mix plots.

Metric	Var.	Stat.	Larch	Sycamore	Oak	Sit.	Nor.	Mix	All	Dec.
SOS	Ht	RMSE	3	15	5	10	5	7	17	16
		R^2	0.13	0.05	0.17	0	0.09	0.02	0.13*	0.01
		r	-0.36	0.21	-0.41	0.04	0.29	0.13	-0.36	-0.09
	DBH	RMSE	2	14	6	10	6	7	16	16
		R^2	0.18	0.07	0.1	0	0	0	0.16*	0.01
		r	-0.42	0.27	-0.31	-0.01	0.01	0.06	-0.39	-0.12
MOS	Ht	RMSE	5	16	9	7	6	8	21	19
		R^2	0.05	0.05	0.08	0	0.03	0.15	0.13*	0
		r	-0.23	0.23	-0.29	0.03	-0.17	0.38	-0.36	-0.01
	DBH	RMSE	4	16	9	6	6	9	20	18
		R2	0.1	0.06	0.05	0.04	0.01	0.11	0.17*	0.01
		r	-0.31	0.25	-0.23	0.2	-0.11	0.33	-0.41	-0.09
EOS	Ht	RMSE	6	14	8	7	4	8	19	16
		R^2	0.12	0.02	0.13	0.1	0.05	0.18	0.15*	0
		r	-0.35	0.15	-0.37	-0.31	-0.22	0.42	-0.38	-0.05
	DBH	RMSE	6	13	9	8	5	8	19	16
		R^2	0.11	0.05	0.05	0	0.02	0.16	0.15*	0
		r	-0.33	0.23	-0.22	-0.03	-0.14	0.39	-0.39	-0.06
		N	20	20	20	20	20	20	120	80

Var. = biophysical variable; Stat. = statistic; Sit. = Sitka spruce; Nor. = Norway spruce; Dec. = deciduous.

5.3.2 Temporal stability of UAV GCC$_{DN}$

The time series of UAV GCC$_{DN}$ values from the GCTs showed, generally, similar mean values (Figure 5-4). However, variations were observed in some dates, which could suggest that this index may not to be totally insensitive to changes in illumination conditions (Toomey *et al.*, 2015). It was noticed that with sunny UAV images, the DNs from each of the RGB channels within the GCT area varied consistently, which in turn resulted in very similar UAV GCC$_{DN}$ values among sunny images. However, cloudy UAV images result in the blue channel`s DNs varying differently from the green and red channel, which in turn introduced some variation in the UAV GCC$_{DN}$ values. The blue channel of consumer-grade cameras is known to be more sensitive to changes of incident radiation (Richardson *et al.*, 2007; Sonnentag *et al.*, 2012). However, despite this, the magnitude of the UAV GCC$_{DN}$ variations

from the GCTs were much lower than the amplitude of change in GCC$_{DN}$s detected within the trees crown of deciduous trees.
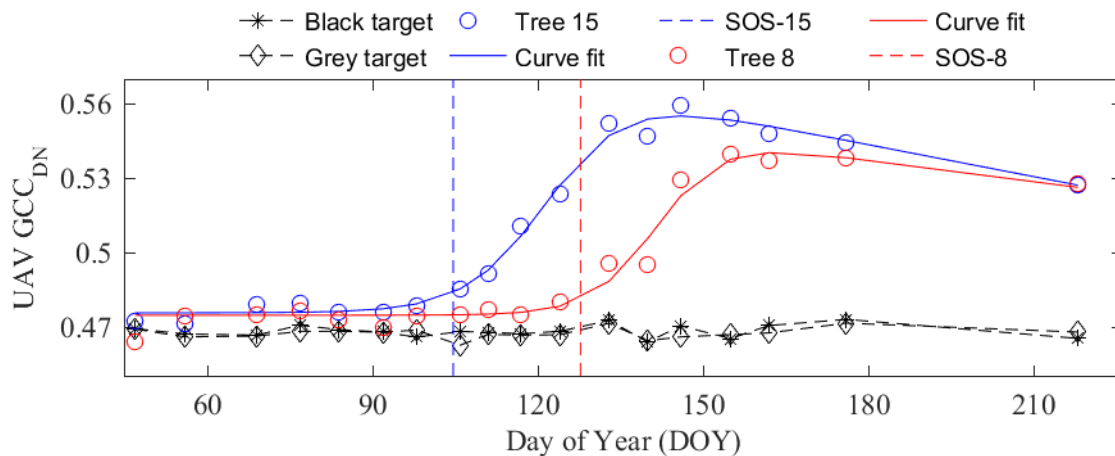
Figure 5-4. Temporal series of GCC$_{DN}$ derived from imagery acquired with a fixed-wing UAV flown over sessile oaks from 25/02/2015 (DOY 56) to 06/08/2015 (DOY 218). GCC$_{DN}$ values were calculated from within individual crowns of four trees (C8, C13, C15 and C18). The vertical lines mark the Start of Season (SOS) of each tree, which correspond to the observed phenological code ">90% buds open (leaf visible)". The graph also shows GCC$_{DN}$ values of two artificial ground calibration targets (Black and Grey1 target). Available in Berra *et al.* (2016).

Next three sections examine optimal percentile, fitting model and vegetation index to estimate canopy phenometrics from UAV data. Because the UAV-GCC$_{DN}$ data fitted by the greendown model provided estimates of tree-level phenology dates with less uncertainties (section 5.3.4 and section 5.3.5), section 5.3.3 focuses on GCC$_{DN}$ data fitted by greendown model.

5.3.3 Sensitivity of UAV data mean values calculated from different percentiles

UAV-derived phenometrics were firstly calculated using time series of vegetation indices based on the mean DN of all pixels from within a tree crown, but this approach showed to be particularly problematic over plots with strong influence of understorey vegetation signal, as exemplified in Figure 5-5a. It resulted in the absence of a winter baseline, preventing a rapid increase in vegetation indices values, which in turn caused the sigmoid models (section 5.2.4) to have a high failure rate in estimating spring phenometrics. The lack of a winter base line makes accurate estimations of phenodates difficult (Toomey *et al.*, 2015). For this reason, the percentiles were tested.
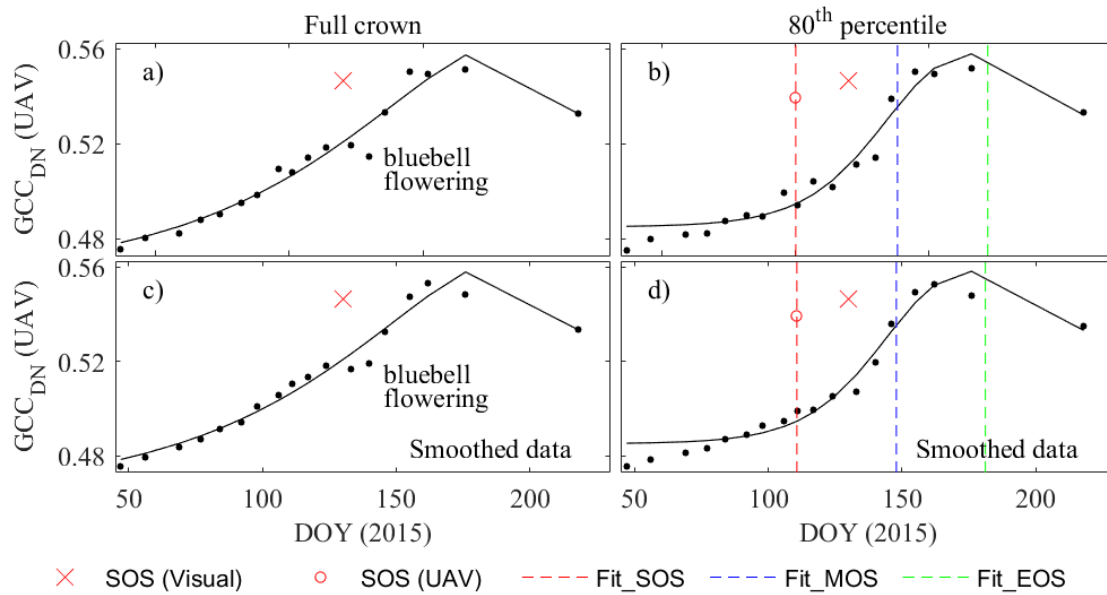
Figure 5-5. Effect of the 80th percentile on the UAV GCC$_{DN}$ time series data (black dots) and consequent phenometric estimations in the Sycamore plot. The data (smoothed with a Savitzky–Golay filter in c) and d)) are fitted by the greendown model (solid line), with phenometrics marked by the vertical dashed lines (preceded by 'Fit_' in the legend). The model failed to estimate phenometrics in a) and c). The averaged SOS from visual assessments is also shown for comparison purposes.

The sensitivity analysis did not detect a single approach (single index with a single fitting method) as being optimal in all plots and for all the three phenometrics (Figure 5-6). For example, the highest R^2 for the SOS metric is returned by the 90th percentile approach for Larch, Sycamore, Sitka spruce and Mix the 20th percentile for Oak and the 70th percentile for Norway spruce. In terms of RMSE for SOS, Larch and Oak have very similar magnitudes regarding different approaches to extracting crown pixels (percentiles), whilst Sycamore has the lowest value with the 80th percentile, Sitka spruce with the 90th percentile, Norway spruce with the 70th percentile and Mixed with the 90th percentile.

Sycamore was very sensitive to the percentile used regarding the number of successfully retrieved metrics (Figure 5-6z). The full crown mean, along with the lower percentiles approaches, failed to extract metrics in more than half of the cases, whilst higher percentiles were increasingly successful to detect phenometrics from the fitted data. It is likely that higher percentiles prioritize sunlit pixels, diminishing the influence of understorey/shading and resulting in a stronger seasonal signal, as exemplified in Figure 5-5b. Sitka spruce presented very variable magnitudes of R^2, RMSE and Bias depending on the percentile and seasonal transition. Middle and end of season statistics for Norway spruce plot

were also highly variable to the different approaches, contrary to SOS, which presented rather stable magnitudes of R^2, RMSE and Bias.

In general, the 80th percentile was the threshold for which lower uncertainties were found and this was particularly evident with the SOS of the deciduous trees (Figure 5-6), the phenometric which is usually of greatest interest in phenology studies. For this reason, the 80th percentile was the threshold chosen to calculate the mean DN from within a UAV orthomosaic polygon (tree crown), a value which was then used to calculate GCC_{DN}, GCC_{r}, $GCC_{r/C0}$, NDVI and $NDVI_{C0}$.
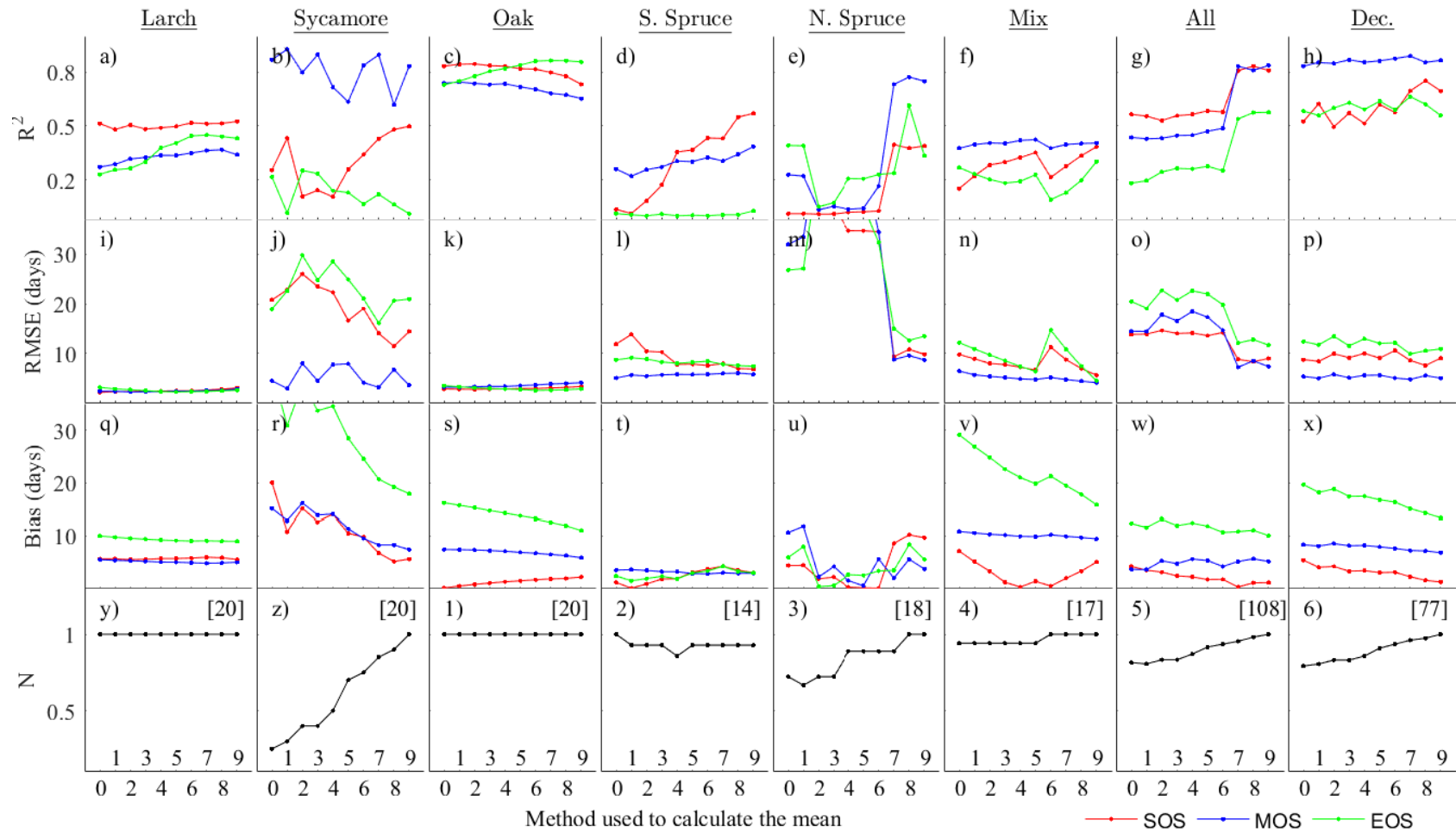
Figure 5-6. Sensitivity analysis of different methods tested to calculate the mean UAV imagery`s DN from within a polygon (tree crown in this case): '0' uses all the values (full crown), '1' uses the values above the 10th percentile, '2' above the 20th percentile and so on up to '9' (90th percentile). The statistics refer to comparisons made between visual assessments of leaf phenology and UAV GCC$_{DN}$-derived phenometrics using the greendown model. 'All' combines the data from the six plots, whilst 'Dec.' combines Larch, Sycamore, Oak and Mix plots. Sample size (N) is normalized by the maximum sample size (shown in between brackets) in order to facilitate visual comparisons. Bias is presented in absolute units.

5.3.4 Performance of the three logistic fit models

Among the five vegetation indices derived from the UAV orthomosaics, GCC_{DN} and $GCC_{r/C0}$ presented time series with the least noise (at a tree individual level), which in turn allowed clearer seasonal trends to be depicted (Figure 5-7), ultimately resulting in more precise phenodate estimates (Figure 5-8, Figure 5-9). Because GCC_{DN} performed, generally, better than $GCC_{r/C0}$, emphasis will be given therefore to the GCC_{DN}-related results in the analysis and discussion.

The greendown and generalized model were found to fit the time series of UAV data better than the simple model in most cases (Figure 5-7), which in turn resulted in lower RMSE values (Table 5-4). The generalized model was formulated to have high flexibility, a characteristic which can provide the best representation of the vegetation dynamics (Figure 5-7b), but can also cause it to be highly sensitive to noise (or outliers), as mainly observed with the NDVI (Figure 5-7o), and $NDVI_{C0}$ (Figure 5-7q) times series. On the other hand, the simple model is the least flexible and it was not able to adequately fit the green peak of the vegetation (point of maximum GCC_{DN}), an important feature detected by the UAV-GCC_{DN} data (Figure 5-7b,c), which yielded the simple model the highest RMSE (Table 5-4). The greendown model has an intermediate flexibility, which proved to be the most suitable for the UAV time series of data, as it can adequately fit the green peak of the vegetation and is less sensitive to outliers than the generalized model. Nevertheless, for specific cases where the time series of data has either low variability (Figure 5-7d) or follows a simple sigmoid behaviour (Figure 5-7a,i), any of the models could be equally appropriate to fit these data.

Residuals from curve fitting were used to calculate measures of the statistical uncertainty in UAV-derived phenometric dates (Table 5-5), providing the best phenology extraction method for each of the vegetation types and the best general method across the plots. The greendown model resulted in the least uncertain date estimates in half of the plots (Sycamore, Sitka spruce and Mix), whilst the simple model achieved the best performance in the remaining plots. Overall, the greendown model resulted in the least uncertain date estimates, as observed when either all or deciduous only plots are considered (Table 5-5). For the UAV data set, phenometric dates estimated by the three models were also compared against visual assessments of leaf phenology in order to evaluate the accuracy of these models.
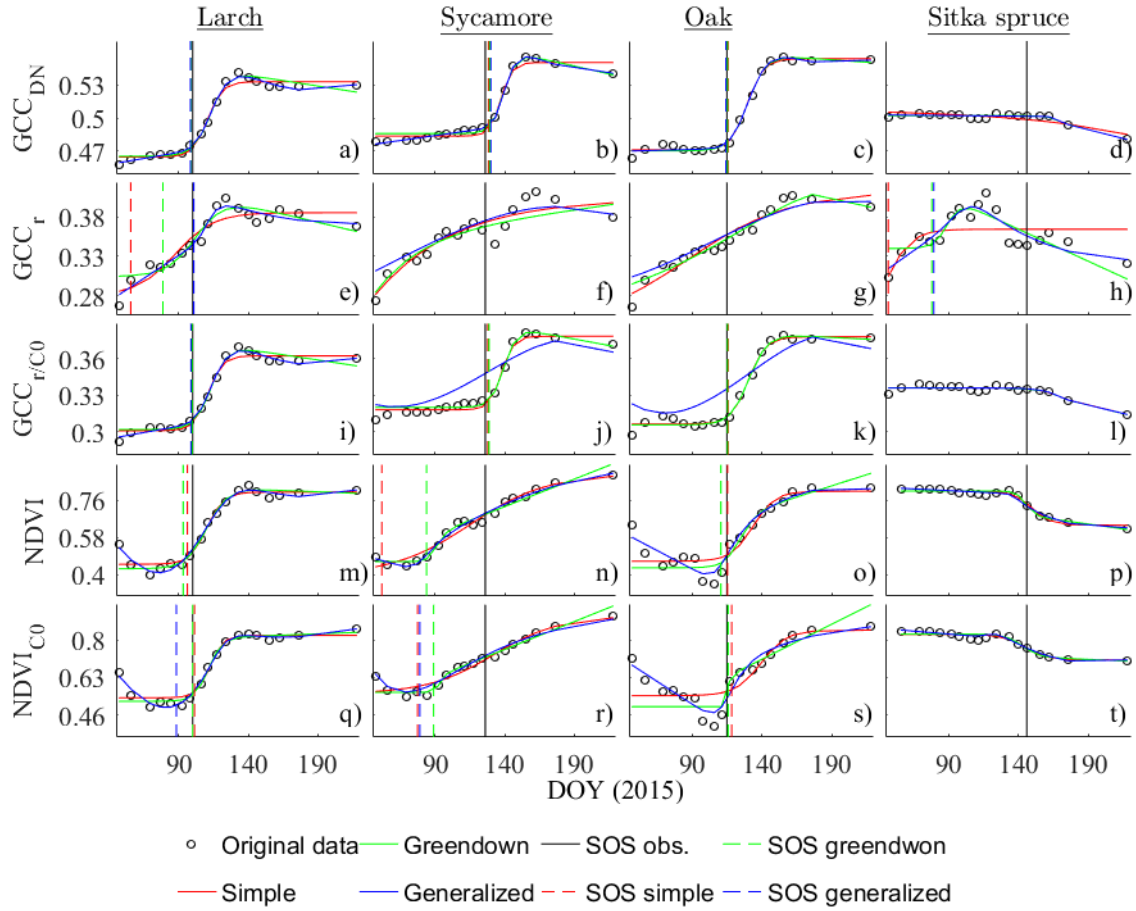
Figure 5-7. Example of four trees (one per plot) for which five UAV remote sensing products (GCC$_{DN}$, GCC$_r$, GCC$_{r/C0}$, NDVI and NDVI$_{C0}$) were derived and fitted by the three different sigmoid models (simple, greendown and generalized) in order to estimate the start of spring season (SOS). The visually assessed SOS (SOS obs.) is also shown for reference. The original data is derived from the 80th percentile approach.

Table 5-4. Average RMSE (dimensionless) for the fitted UAV-GCC$_{DN}$ (80th percentile). 'All' combines the data from the six plots, whilst 'Dec.' combines Larch, Sycamore (Syca.), Oak and Mix plots.

Index	Model	Larch	Syca.	Oak	Sitka s.	Norway s.	Mix	All	Dec.
	simple	0.004	0.007	0.004	0.004	0.003	0.005	0.005	0.005
GCC$_{DN}$	greendown	0.004	0.006	0.003	0.002	0.003	0.003	0.004	0.004
	generalized	0.002	0.006	0.006	0.002	0.003	0.004	0.004	0.005

The visually observed phenological dates showed varying degrees of correspondence to UAV-derived dates, depending on the sigmoid model and seasonal transition (Table 5-6), in a manner similar to the uncertainty analysis (Table 5-5). This means that there was not a

unique model performing best in all the different land cover types and for all the three phenometrics. The highest R^2 for SOS, for example, was achieved using the simple sigmoid in the Oak plot (0.78), the greendown sigmoid in the Larch (0.51), Sycamore (0.48), Norway spruce (0.38) and Mix plot (0.33), and the generalized model in Sitka spruce (0.64) plot (Table 5-6). Similarly to results from Table 5-5, the greendown model resulted in the least uncertain date estimates in half of the plots (Sycamore, Sitka spruce and Norway spruce), whilst the simple model achieved the best performance in the remaining plots.

Start of season statistics from all ('All') and only deciduous ('Dec.') trees grouped together (Table 5-6) were used therefore as a decisive factor (similarly to the percentile sensitivity analysis) to identify the optimal model across the different vegetation types. Even though the generalized model presented uncertainty values very close to the greendown model for deciduous trees, it has had considerable failures to mark phenometrics (as given by N in Table 5-6) (these missing retrievals can be explained by the failure of the fitting function to converge because of poor data quality (e.g. noise and data gaps) or weak seasonal signal (D'Odorico *et al.*, 2015). Therefore, the greendown model presented the best overall performance with RMSE values of 8 days for 'All' and 8 days for 'Dec.'.

Table 5-5. Statistical uncertainty (days) in estimated phenology dates from each tree using UAV-GCC$_{DN}$ data (80th percentile). This is calculated as the average width of inner 95% confidence intervals for each phenology date. SOS, MOS and EOS are start, middle and end of spring season, respectively. 'All' combines the data from the six plots, whilst 'Dec.' combines Larch, Sycamore, Oak and Mix plots. The last row shows the least uncertain model at each plot considering the combined results as observed with SOS, MOS and EOS; when two models have the same performance, the model with the least number of parameters (i.e. the simpler) is chosen. S = simple; GD = greendown.

Metric/Index	Model	Larch	Sycamore	Oak	Sitka s.	Norway s.	Mix	All	Dec.
SOS/GCCDN	simple	3	8	2	5	4	3	4	4
	greendown	2	4	2	2	5	2	3	3
	generalized	3	4	13	1	12	4	6	6
MOS/GCCDN	simple	1	4	1	5	1	2	2	2
	greendown	1	3	1	1	7	1	2	1
	generalized	1	4	12	3	25	3	8	5
EOS/GCCDN	simple	2	8	2	6	3	3	4	4
	greendown	2	5	2	2	7	3	3	3
	generalized	2	4	13	3	39	3	11	6
best model		*S*	*GD*	*S*	*GD*	*S*	*GD*	*GD*	*GD*

Table 5-6. Statistics comparing phenometrics derived from visual assessment and from UAV-GCC$_{DN}$ data (80th percentile), at individual tree level. RMSE is derived from RMA regression models. Bias refers to the average of the differences between UAV and visual observations. *N* is the number of observations for which the models were successful in extracting the phenometrics (20 is the maximum at each plot). Bias and RMSE are in units of days. 'All' combines the data from the six plots, whilst 'Dec.' combines the Larch, Sycamore (Sycam.), Oak and Mix plots. Nor. = Norway spruce. Best model selected as in Table 5-5.

Metric	Model	Statistic	Larch	Sycam.	Oak	Sitka	Nor.	Mix	All	Dec.
SOS	simple	RMSE	3	29	3	45	13	8	19	17
		R2	0.45	0.13	0.78	0	0.12	0.28	0.37	0.25
		Bias	-7	-20	2	-9	5	3	-4	-6
		N	20	20	20	9	14	17	100	77
	greendown	RMSE	3	11	3	7	11	7	8	8
		R2	0.51	0.48	0.78	0.55	0.38	0.33	0.83	0.75
		Bias	-6	-5	2	3	10	3	1	-2
		N	20	18	20	13	18	17	106	75
	generalized	RMSE	3	12	3	16	15	7	9	7
		R2	0.51	0.32	0.82	0.64	0.12	0.12	0.85	0.8
		Bias	-4	1	0	9	13	4	4	0
		N	20	8	14	4	20	12	78	54
MOS	simple	RMSE	3	6	4	47	8	5	13	6
		R2	0.35	0.63	0.64	0	0.23	0.35	0.55	0.8
		Bias	2	-2	5	-21	2	6	1	3
		N	20	20	20	9	14	17	100	77
	greendown	RMSE	3	7	4	6	10	4	8	6
		R2	0.37	0.62	0.67	0.34	0.77	0.4	0.81	0.85
		Bias	5	8	6	-3	6	10	6	7
		N	20	18	20	13	18	17	106	75
	generalized	RMSE	3	10	4		21	5	11	6
		R2	0.28	0.33	0.67		0.16	0.24	0.76	0.8
		Bias	4	4	6	-2	4	9	5	6
		N	20	8	14	4	20	12	78	54
EOS	simple	RMSE	2	14	3	10	17	5	13	8
		R2	0.41	0.24	0.87	0.55	0.03	0.29	0.55	0.71
		Bias	6	15	8	-16	8	12	8	10
		N	20	20	20	9	14	17	100	77
	greendown	RMSE	2	21	3	8	13	7	13	11
		R2	0.44	0.06	0.86	0.01	0.61	0.2	0.58	0.62
		Bias	9	19	12	-3	8	18	11	14
		N	20	18	20	13	18	17	106	75
	generalized	RMSE	3	12	3	22	23	4	15	7
		R2	0.41	0.07	0.88	0.39	0.35	0.47	0.53	0.68
		Bias	10	7	15	-8	5	18	10	13
		N	20	8	14	4	20	12	78	54
	best model		*S*	*GD*	*S*	*GD*	*GD*	*S*	*GD*	*GD*

Residuals from curve fitting were also used to calculate measures of the statistical uncertainty in ground photography- and Landsat-derived phenometric dates, providing the best phenology extraction method for each of the vegetation types and the best general method across the woodland. For Landsat time series data, the simple model presents the best fitting option in five out of six plots, and is the best model across the plots (Table 5-7, Table 5-8). A similar outcome was observed with the canopy gap fraction time series (Table 5-9). Despite the simple model performing best in four out of six plots with the understorey ground photography data, the greendown was the best model to extract phenometrics across all of the plots combined (Table 5-10).

Table 5-7. Statistical uncertainty (days) in estimated phenology dates from the Landsat NDVI pixels intersecting the plots. See Table 5-5 for a full explanation.

Metric/Index	Model	Larch	Sycamore	Oak	Sitka s.	Norway s.	Mix	All	Dec.
SOS/NDVI	simple	3	14	6	-	0	3	5	6
	greendown	4	15	5	54	0	2	13	6
	generalized	15	48	-	16	-	6	21	23
MOS/NDVI	simple	3	4	0	-	0	1	2	2
	greendown	3	8	2	25	0	4	7	4
	generalized	6	38	-	16	-	2	15	15
EOS/NDVI	simple	8	18	6	-	0	3	7	9
	greendown	10	32	5	30	0	7	14	13
	generalized	20	33	-	17	-	6	19	20
best model		*S*	*S*	*GD*	*S*	*S*	*S*	*S*	*S*

Table 5-8. Statistical uncertainty (days) in estimated phenology dates from the Landsat EVI pixels intersecting the plots. See Table 5-5 for a full explanation.

Metric/Index	Model	Larch	Sycamore	Oak	Sitka s.	Norway s.	Mix	All	Dec.
SOS/EVI	simple	4	8	4	3	11	4	6	5
	greendown	5	-	17	1	11	13	9	12
	generalized	36	54	53	-	26	62	46	51
MOS/EVI	simple	3	5	1	1	11	2	4	3
	greendown	5	-	24	0	12	6	9	12
	generalized	21	54	53	-	26	62	43	48
EOS/EVI	simple	7	11	6	5	33	5	11	8
	greendown	12	-	48	2	23	19	21	26
	generalized	61	54	60	-	26	68	54	61
best model		*S*	*S*	*S*	*GD*	*S*	*S*	*S*	*S*

Table 5-9. Statistical uncertainty (days) in estimated phenology dates from the canopy gap fraction (Fc) in each plot. See Table 5-5 for a full explanation.

Metric/Index	Model	Larch	Sycamore	Oak	Sitka s.	Norway s.	Mix	All	Dec.
SOS/Fc	simple	2	1	0	-	1	0	1	1
	greendown	3	3	0	-	1	3	2	2
	generalized	4	70	3	27	4	2	18	20
MOS/Fc	simple	1	1	1	-	0	1	1	1
	greendown	1	0	0	-	0	2	1	1
	generalized	2	70	5	30	2	2	19	20
EOS/Fc	simple	3	2	1	-	1	1	2	2
	greendown	3	4	1	-	1	5	3	3
	generalized	7	70	5	34	2	5	21	22
best model		*S*	*S*	*S*	*GN*	*S*	*S*	*S*	*S*

Table 5-10. Statistical uncertainty (days) in estimated phenology dates from the understorey ground photography in each plot. See Table 5-5 for a full explanation.

Metric/Index	Model	Larch	Sycamore	Oak	Sitka s.	Norway s.	Mix	All	Dec.
SOS/GCCDN	simple	3	14	4	67	5	0	16	5
	greendown	3	-	4	6	4		5	4
	generalized	3	28	-	-	-	46	24	26
MOS/GCCDN	simple	2	3	5	59	3	17	15	6
	greendown	2	-	3	4	6		3	3
	generalized	2	44	-	-	-	47	31	31
EOS/GCCDN	simple	3	12	10	94	8	32	27	15
	greendown	4	-	7	6	10		7	5
	generalized	4	63	-	-	-	48	40	38
best model		*S*	*S*	*GD*	*GD*	*S*	*S*	*GD*	*GD*

The method that provides the best estimation of phenology for each of the vegetation types, for each remote sensing product, was chosen to estimate the seasonal transition dates in this chapter. Nevertheless, the best overall model is selected in Chapter 6, where the analysis is expanded to the whole woodland.

5.3.5 Comparisons of visual assessments to estimates from UAV time-series data

Among the five UAV-derived indices (GCC_{DN}, GCC_r, $GCC_{r/C0}$, NDVI and $NDVI_{C0}$), the GCC_{DN}-estimated phenodates were consistently most closely associated with the visual assessment of SOS and MOS, whilst $GCC_{r/C0}$ returned the best association with EOS (Figure 5-8, Figure 5-9). Among these three metrics, the best match occurred with SOS dates (Figure 5-8a), whilst the weakest relationship occurred with EOS dates (Figure 5-8c). GCC_{DN} had the highest number of successfully retrieved phenodates (Figure 5-8). Therefore, in general, GCC_{DN} performed slightly better than $GCC_{r/C0}$ in detecting phenology.

The SOS and MOS derived from GCC_{DN} matched visual assessments with similar values of R^2 (0.83 and 0.82, respectively) and RMSE (8 and 9 days, respectively) (Figure 5-8a,b). The visually assessed EOS dates were less consistent with GCC_{DN} time-series estimates ($R^2 = 0.60$), presenting a RMSE of 13 days (Figure 5-8c). UAV-GCC_{DN} estimates were biased at 1 (SOS), 5 (MOS) and 10 (EOS) days later with respect to visual assessment for the dates when >90% of buds were open, dates when >90% of leaf/candle were out and dates when >90% of leaf/needles were fully unfolded, respectively. This indicates that as spring progressed, the UAV-GCC_{DN} estimates were increasingly later in comparison to the leaf phenology observations, as better seen in the Figure 5-9.

The major difference observed with EOS comparisons may be due to the phenological code used to mark EOS, which assessed levels of leaf/needle unfolding, but not their expansion to an adult full size. Even though this later stage could be assessed with confidence across the broadleaf plots, it proved to be impractical across needleleaf plots (3 out of 6) as needle expansion levels (e.g. 25% of full size) are hard to evaluate due to their small size. Therefore, the selected EOS code represents the maximum leaf/needle development that could be observed with confidence across all the tree species. Consequently, the greenness UAV index peaked consistently later than the observed EOS, resulting in a large lag between field and UAV metrics for end of spring season (Figure 5-9).
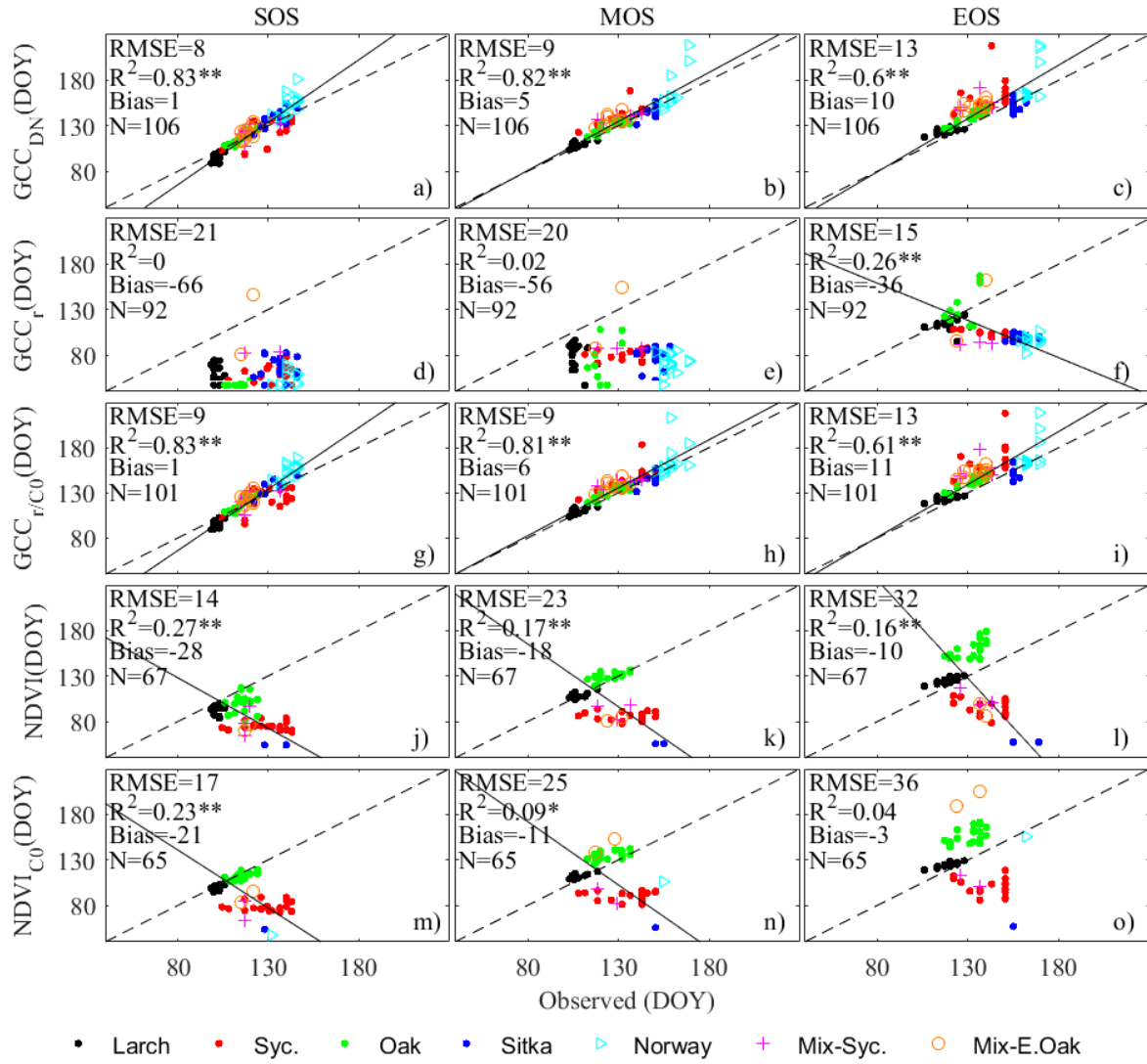
Figure 5-8. Scatter plots of start of start (SOS), middle (MOS) and end (EOS) of season, where each data set represents all trees from all plots. The visually assessed dates are compared against dates estimated from the five UAV remote sensing derived products. UAV phenometrics are calculated based on the least uncertain sigmoid model per plot (Table 5-5, Table 5-6) (Sycamore, Sitka spruce, Norway spruce and Mix = Greendown model; Larch and Oak = Simple model). Statistics are given (**$p<0.001$, *$p<0.05$; N is sample size). Bias refers to the average difference between UAV and visual observations. Dashed lines represent the 1:1 line and solid lines are reduced major axis (RMA) regression models.

Phenometric dates derived from NDVI and $NDVI_{C0}$ time-series showed poor or no significant agreement ($0.09 \leq R^2 \leq 0.27$) with the visually assessed dates (Figure 5-8j-o). The phenodates derived from these two UAV spectral indices presented large mismatches with the visually assessed dates (Figure 5-9), with RMSEs of around 1 month and negative bias of up to 28 days (earlier with respect to visual assessment) (Figure 5-8j-o). This in turn resulted in NDVI and $NDVI_{C0}$ UAV estimated dates consistently exceeding the spring phenology season length as visually assessed in the field (Figure 5-9). These two indices were also less

successful (in terms of function convergence) in extracting phenodates (NDVI, *N*=67; NDVI $_{C0}$, *N*=65) from the time series of data than GCC$_{DN}$ (*N*=106) (Figure 5-8). Similarly, GCC$_r$ also returned poor or no significant relationships with visual observations, but with significantly higher biases. These results can be associated with the presence of noise in some of the individual tree time series, as exemplified in Figure 5-7 and observed with other trees (not shown), which contributes towards a weak seasonal signal and poor data quality (at least at an individual tree level).
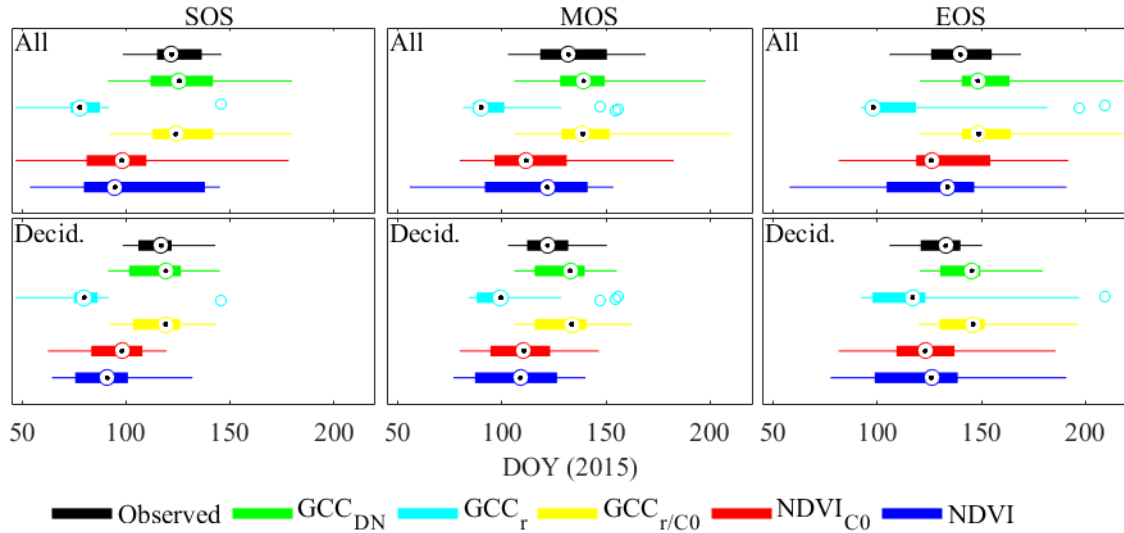
Figure 5-9. Box plots of start (SOS), middle (MOS) and end (EOS) of spring season, at tree level, as visually observed in the field and estimated (greendown model) from the three UAV remote sensing derived products (GCC$_{DN}$, NDVI and NDVI $_{C0}$) (80th percentile) for all plots together and the deciduous ('Decid.') plots only. For each graph, the central mark represents the median, the edges of the box are the 25th and 75th percentiles, the whiskers extend to the most extreme data points not considered outliers (<3 times the standard deviation).

The comparison between UAV and visual observations across all trees grouped together suggest that higher uncertainties occur within the evergreen species, as the data points related to these species are the ones more distant from the 1:1 line (Figure 5-8a-c and shown in detail in Figure 5-10). The box plots analysis also shows that the range of the dates from all trees is considerable larger than when only the deciduous trees are investigated (Figure 5-9).

UAV-derived SOS dates were predicted more accurately across the deciduous plots. Among the four deciduous plots (Figure 5-10a-c,f), Larch and Oak presented the best agreement with the visual assessment (Figure 5-10a,c) and this is due to a stronger and well-characterized seasonal signal in these two plots (Figure 5-11m,o). This result can be related to different types of understorey vegetation present in these four plots. While Larch and Oak

plots had non-vegetative understorey over winter, evergreen understorey (grasses, Chapter 3, section 3.5.1) was present in the Sycamore and Mix plots. Sitka spruce had a relative good agreement with visual observations (RMSE = 7 days), but the model converged in only 13 trees.

The RMSE of 'All' and the deciduous group has the same magnitude as the approximate temporal resolution of the UAV data acquisitions (8 days). Within this RMSE magnitude is also included the uncertainty of the visual observations, which it was not possible to quantify, but it could be reasonable to assume errors of around 3.5 days (revisit frequency of the visual assessments). Previous studies have calculated the statistical uncertainty in SOS phenology dates derived from visual assessments as 7 days (Klosterman *et al.*, 2014) and ± 3 days (Schaber, 2002). UAV GCC_{DN} can therefore be assumed to estimate SOS dates at tree individual level with an accuracy better than 1 week (at least from deciduous trees).
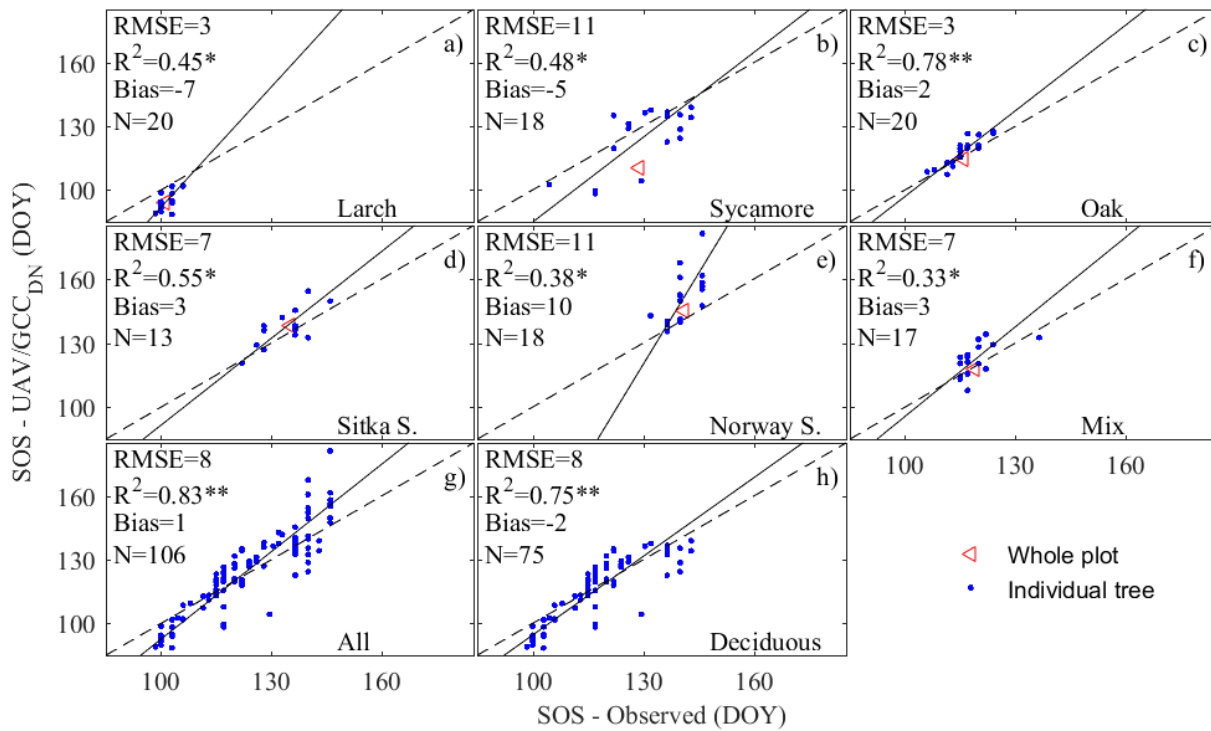
Figure 5-10. Scatter plots of start of season (SOS) for individual trees. The UAV-GCC_{DN} data series (80th percentile) were fit with the least uncertain sigmoid model in each plot (Table 5-5, Table 5-6) (Sycamore, Sitka spruce, Norway spruce and Mix = Greendown model; Larch and Oak = Simple model). 'All' combines the data from the six plots, whilst 'Deciduous' combines Larch, Sycamore, Oak and Mix plots. Statistics are given (**$p<0.001$; *$p<0.05$; N is sample size). Bias refers to the average difference between UAV and visual observations. 'Whole plot' represents the mean of the observed SOSs against the UAV SOS derived from the whole plot (this data point is not included in the statistics). Dashed lines represent the 1:1 line and solid lines are Reduced Major Axis (RMA) regression models.

5.3.6 Plot level comparison of ground photography, UAV and Landsat phenology

Similar to the tree level analysis (section 5.3.5), all the remote sensing products were fitted by the best model in each plot (section 5.3.4). In areas of deciduous woodland, where the understorey vegetation greened up earlier than the overstorey (Sycamore, Oak and Mix; Figure 5-11), Landsat predicted SOS consistently earlier than visual assessments (bias (NDVI) = - 35 days, bias (EVI) = - 27 days, n = 3). This suggests that increases in Landsat NDVI and EVI values from the winter baseline is triggered predominantly by the understorey development. As a consequence, Landsat MOS was the metric most closely related with the onset of leaf development (SOS) as visually observed on the ground. Because orbital sensors integrate ecosystem dynamics rather than only leaf phenology, differences between start of season detected by satellites and measured on the ground may be substantial (White *et al.*, 2009).

On the other hand, the use of the 20% brightest pixels from UAV orthomosaics to generate a GCC_{DN} time series of data reduced the influence of understorey vegetation (Sycamore, Oak and Mix; Figure 5-11), resulting in a closer agreement between UAV and visually observed SOSs (bias = -7 days, n = 3). Because of this higher degree of similarity between UAV and visual observations of leaf phenology, UAV-derived SOS dates are, generally closer to Landsat MOS than Landsat SOS dates.

Nevertheless, Landsat and UAV estimates of SOS, MOS and EOS were very similar over the plot in which the understorey greened up after the dominant trees (Larch; Figure 5-11), i.e., where the understorey did not contribute to the signal resulting from the early stages of bud/leaf development. This later understorey development resulted in a well-defined winter baseline in both data sets, a characteristic which can benefit accurate phenometric estimation (Toomey *et al.*, 2015).

Across the four deciduous plots, the canopy photo metric (Figure 5-11 s,t,u,x) detected the start of season consistently later in relation to visual assessments (bias = 11 days, n = 4), UAV (bias = 18 days, n = 4) and Landsat (bias (NDVI) = 40 days, bias (EVI) = 33 days, n = 4) derived estimates. The cover fraction was not sensitive to early biophysical changes such as bud open (leaf visible). This digital field metric appears to be sensitive only after bud burst has finished (leaves expanding). A much steeper and narrower region of rapid change results from the photo metric logistic fit (except at the Mix plot, where a very low cover fraction occurred likely due to a large forest gap right above the camera location).

An unexpected, but interesting, seasonal profile was observed in one of the evergreen plots. Cover fraction values of evergreen canopies detected by upward hemispherical images are expected to follow a relatively flat profile throughout the year, as observed with the Norway spruce (Figure 5-11w) and noted elsewhere (Nagai *et al.*, 2012; Nagai *et al.*, 2013). However, a substantial increase in canopy openness was observed in the Sitka spruce plot with the development of spring/summer (Figure 5-11v), which was due to a severe defoliation, likely caused by an outbreak of *Elatobium abietinum* (green spruce aphid). The effect of such defoliation was also detected by the UAV and Landsat remote sensing products as the VIs experienced lower values towards summer. However, Landsat NDVI and EVI values were sensitive to the lower amount of green material only a few weeks later than UAV GCC_{DN}, highlighting the potential of UAV imagery for forest disease or pest monitoring.

Since the aphid outbreak occurred after the bud break and needle unfolding from candles (at least at the Sitka spruce plot), these phenological stages were enough to increase the UAV GCC_{DN} and Landsat EVI values, allowing SOS estimates (Figure 5-11j,p), but did not change the Landsat NDVI trend (Figure 5-11d). Significant changes in the Landsat NDVI trend, and consequent SOS estimate, only occurred in the summer, likely due to the defoliation. This observation could suggest that Landsat EVI is more sensitive than NDVI to detect subtle variations in evergreen phenology. However, a few deciduous trees were scattered over the four Landsat pixels intersecting the Sitka spruce plot, which could also suggest that EVI was more sensitive to the dynamics of such deciduous trees.

In the healthy Norway spruce plot, UAV and Landsat NDVI retrieved similar SOS dates, but Landsat EVI detected SOS a few weeks earlier. It can be noticed that understorey vegetation grew in this plot (Figure 5-11z3) and it is likely contributing to the Landsat data signal. Besides that, Norway spruce composes the smallest plot (89 m^2, Figure 5-3), which can increase the uncertainties in the cross comparison with a 900 m^2 Landsat pixel.

A more representative cross-comparison between UAV and Landsat phenometrics is presented in Chapter 6, by means of expanding the analysis to the entire woodland.
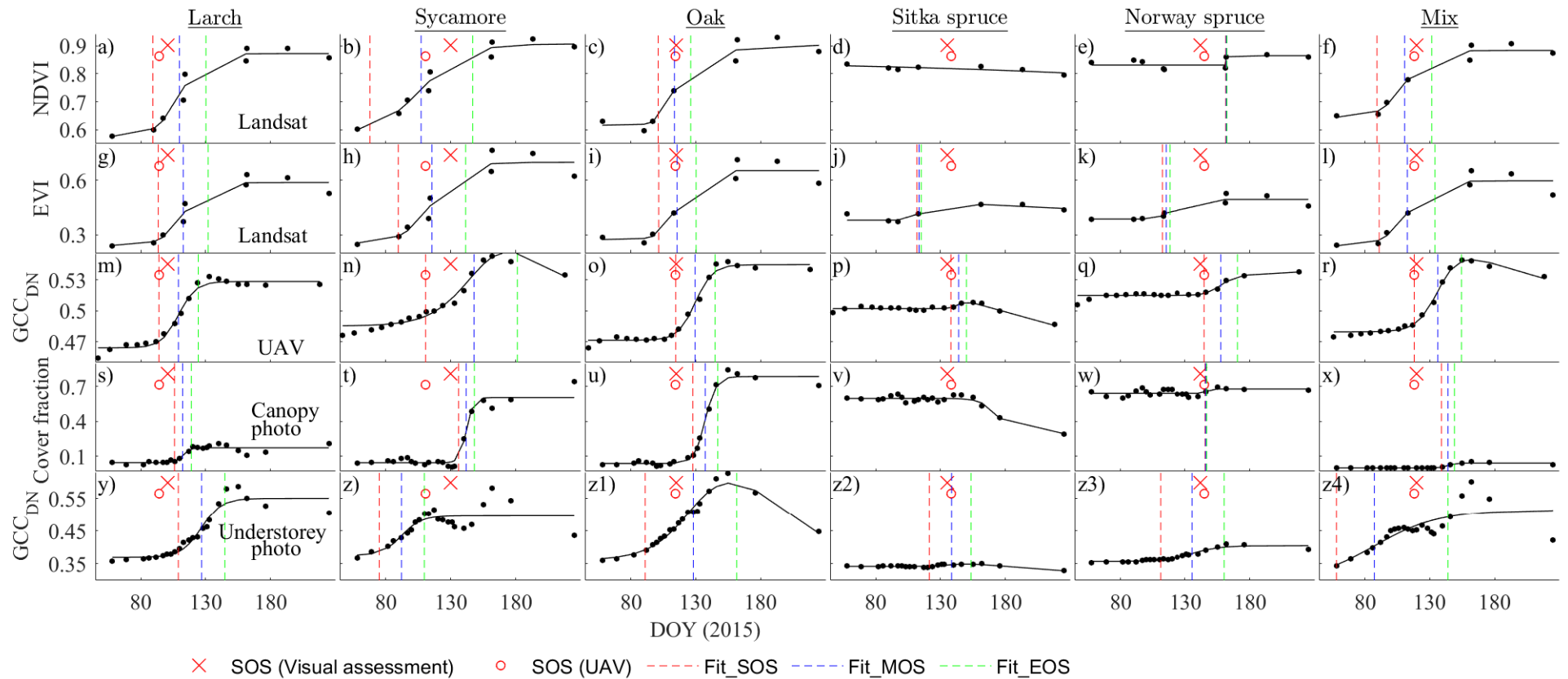
Figure 5-11. Plot level comparison between Landsat (a-l), UAV (m-r), hemispherical (looking up) (s-x) and frame-style (looking at understorey) (y-z4) ground photography. The time series of data (black dots) are fitted by the "best model" (solid line) (as presented in Table 5-6, Table 5-7, Table 5-8, Table 5-9 and Table 5-10), with phenometrics marked by the vertical dashed lines (preceded by 'Fit_' in the legend). Landsat data are weighted by the plot area. The UAV GCC_DN data represent the 80th percentile from within each plot. The averaged SOS from visual assessments and the UAV SOS are also shown for comparison purposes.

Finally, another interesting feature occurred in the Sycamore and Mix plot due to bluebell (*Hyacinthoides non-scripta*) flowering, as detected by the understorey photography (Figure 5-11 z,z4). Instead of an expected sustained increase of GCC_{DN} values up to a summer peak, a temporary change of direction (decrease) occurred before the maximum GCC_{DN} value (Figure 5-11z,z4). Analysis of original understorey photography revealed that the dates of GCC_{DN} decrease match with the bluebell flowering period (~08/05/2015 to ~26/05/2015). The abundant presence of blue flowers in these plots will have increased the blue channel's DN values on the ground photos, consequently decreasing the greenness detected by the GCC_{DN} index. Such an effect was also detected on the UAV GCC_{DN} time series when the average of the full crown was tested (Figure 5-5a), a trend which largely disappeared when the average of the brightest pixels was used (Figure 5-5b). Therefore, these results suggest that different understorey species can have significant influence on the integrated ecosystem signal (agreeing with Tuanmu *et al.* (2010)), especially with very high spatial resolution optical sensors.

5.3.7 Sensitivity of sigmoid fit to the temporal resolution of UAV data

Reducing the UAV data temporal resolution can have a significant effect on the shape of the sigmoid curve (Figure 5-13) and accuracy of the derived phenometrics (Table 5-11, Figure 5-12). Systematically reducing the UAV observations to ~once every 2 weeks had little effect on the shape of the seasonal curve (Figure 5-13) and slightly reduced the accuracy of the derived phenometrics (for example, for SOS of the deciduous group, RMSE remained 8 days, whilst R^2 reduced from 0.75 to 0.74 and bias increased from -2 to -7 days, Table 5-11). On the other hand, reducing UAV observations to ~once every 3 weeks has profound effect on the shape of the fitted data and increased significantly the phenometric prediction uncertainties (for example, for SOS of the deciduous group, RMSE increased from 8 to 15 days, bias from -2 to 27 days and R^2 reduced from 0.75 to 0.31, Table 5-11), as better seen in the Figure 5-12.

When the UAV series was reduced to replicate the Landsat temporal resolution, the shape of the curve was remarkably different from the original curve and the accuracy of the UAV transition dates varied accordingly to the distribution of the points. Among the three phenometrics, SOS returned generally higher accuracies (Figure 5-12), as there were more data points to characterize the lower asymptote, than the middle season greening-up (MOS)

and upper asymptote (EOS) (Figure 5-13). The temporal gap of around 1 and half moths in the series increased considerably the uncertainty in the MOS and EOS predictions. For example, for MOS of deciduous covers, R² decreased from 0.85 to 0.03, for EOS, R² decreased from 0.62 to 0 (Table 5-11). Also, EOS was detected remarkably earlier as a consequence of the absence of data points to characterize the peak of vegetation greening-up (Figure 5-13y-z4).
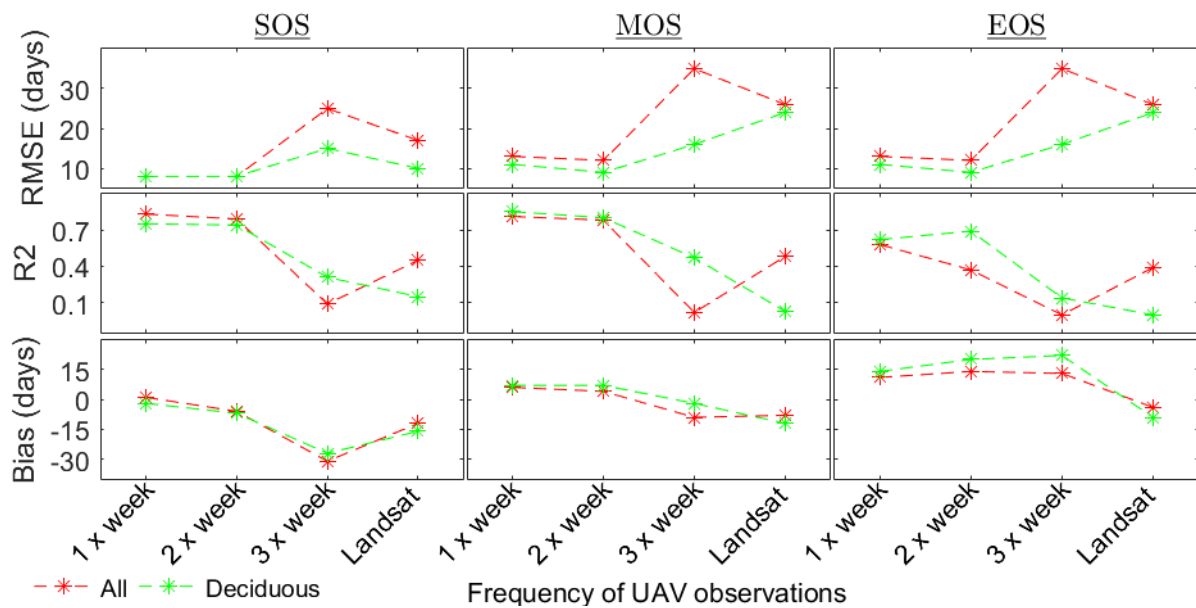
Figure 5-12. Sensitivity of the greendown model fit to the number of UAV GCC data points (80th percentile), at an individual tree level. UAV phenometric dates derived from each different temporal resoltuion are compared against visual assessment dates. 'All' combines the data from the six plots, whilst 'Dec.' combines the Larch, Sycamore, Oak and Mix plots.

Table 5-11. Sensitivity of the greendown model fit to the number of UAV GCC data points (80th percentile), at an individual tree level. UAV phenometric dates are compared against visual assessment dates. RMSE (days) is derived from RMA regression models. Bias (days) refers to the average of the differences between UAV and visual observations. N is the number of observations for which the model was successful in extracting the phenometrics (20 is the maximum at each plot). 'All' combines the data from the six plots, whilst 'Dec.' combines the Larch, Sycamore, Oak and Mix plots.

Plot	Number of UAV Observations	N	SOS			MOS			EOS		
			RMSE	R^2	Bias	RMSE	R^2	Bias	RMSE	R^2	Bias
Larch	18[*]	20	3	0.51	-6	2	0.37	5	2	0.44	9
	10[&]	20	4	0.44	-14	4	0.23	2	4	0.1	12
	7[∞]	20	8	0.39	-32	4	0.52	2	4	0	28
	7[#]	20	3	0.54	-12	2	0.33	0	2	0	6
Sycamore	18	18	11	0.48	-5	21	0.62	8	21	0.06	19
	10	18	7	0.46	-11	8	0.74	7	8	0.05	22
	7	15	13	0.16	-43	36	0.12	-10	36	0.03	21
	7	20	8	0.08	-31	6	0.18	-24	6	0	-18
Oak	18	20	3	0.78	2	3	0.67	6	3	0.86	12
	10	20	3	0.72	-3	3	0.68	9	3	0.84	21
	7	20	6	0.4	-17	7	0.57	0	7	0.31	19
	7	18	6	0.01	-5	47	0	-6	47	0.01	-8
Sitka s.	18	13	7	0.55	3	8	0.34	-3	8	0.01	-3
	10	13	8	0.07	0	7	0.23	-6	7	0.03	-6
	7	11	38	0.13	-49	12	0.06	-35	12	0.01	-11
	7	11	30	0	-1	29	0.19	-12	29	0.07	-16
Norway s.	18	18	11	0.38	10	13	0.77	6	13	0.61	8
	10	12	14	0	-1	10	0.32	-6	10	0.05	-1
	7	9	44	0.1	-40	67	0.44	-33	67	0.38	-25
	7	20	17	0.03	-1	23	0.28	6	23	0.05	22
Mix	18	17	7	0.33	3	7	0.4	10	7	0.2	18
	10	17	5	0.39	-2	5	0.38	11	5	0.16	26
	7	17	11	0.18	-20	5	0.13	-1	5	0.14	21
	7	17	5	0.12	-14	6	0.26	-16	6	0.17	-17
All	18	106	8	0.83	1	13	0.81	6	13	0.58	11
	10	100	8	0.79	-6	12	0.78	4	12	0.37	14
	7	92	25	0.09	-31	35	0.02	-9	35	0	13
	7	106	17	0.45	-12	26	0.48	-8	26	0.39	-4
Dec.	18	75	8	0.75	-2	11	0.85	7	11	0.62	14
	10	75	8	0.74	-7	9	0.8	7	9	0.69	20
	7	72	15	0.31	-27	16	0.47	-2	16	0.14	22
	7	75	10	0.15	-16	24	0.03	-12	24	0	-9

[*]Full data set (~once per week); [&]~once every 2 weeks; [∞]~ once every 3 weeks; [#]~ similar to Landsat;
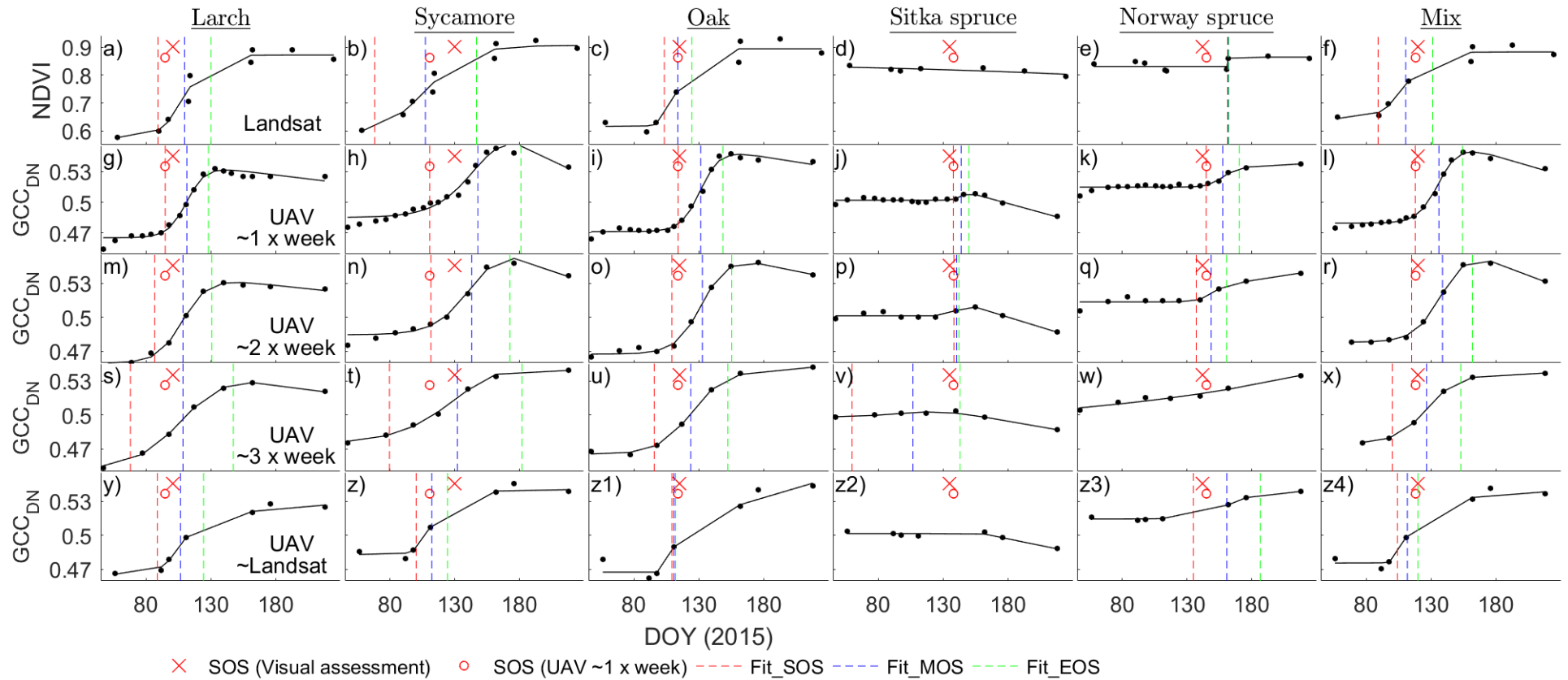
Figure 5-13. Plot level analysis of the sensitivity of the sigmoid fit (greendown model) to the number of UAV data points (80th percentile from within each plot): the original ~once per week observations (g-l) was systematically reduced to ~once every two weeks (m-r), to ~once every three weeks (s-x) and to match the Landsat temporal resolution (y-z4). The weighted Landsat NDVI series is shown for reference (a-f), data which is fitted by the simple model. The phenometrics are marked by the vertical dashed lines (preceded by 'Fit_' in the legend). The averaged SOS from visual assessments and the UAV SOS derived from the full data set are also shown for comparison purposes.

5.4 Discussion

5.4.1 Spring phenology at an individual tree-level

Visual assessments of species-specific individual tree phenology revealed a spatially heterogeneous ecosystem, where differences between the first and last trees reaching key spring phenological events were up to ~40 days within some plots. Substantial intraspecific phenological variations were also observed by Schwartz *et al.* (2013) (up to 2-3 weeks) and by White *et al.* (2014) (up to 30 days), across temperate forests. A noticeable phenological variation among species (interspecific) also occurred in this study (up to ~40 days), with more distinct differences between needleleaf and broadleaf species. This unequal budburst and leaf development can be due to several factors acting together, such as hereditary influences (Kadomatsu, 1997; Morin *et al.*, 2010), influence of site-specific factors (e.g. precipitation, soil conditions and microclimate) (Fisher *et al.*, 2006; Ibáñez *et al.*, 2010), mechanical damage (e.g. extreme weather conditions (Ryu *et al.*, 2012) or pest attacks (Mizunuma *et al.*, 2013)), micro-habitat characteristics (Oliveira *et al.*, 1994) and different requirements of warming in the spring, winter chilling and photoperiod (Hunter and Lechowicz, 1992; Polgar and Primack, 2013). Furthermore, the exact physiological control mechanisms of temperate tree's leaf out is not totally understood (Polgar and Primack, 2013).

Such large variation in timing of leafing-out, despite the trees growing in close proximity (10-30 m), may have implications for studies using ground and near-surface sensors, viewing a small number of trees, to validate satellite-based phenometrics or to characterize the phenology of a population. There are also implications for coarse spatial resolution satellite data, as there is an intrinsic averaging and missing of potential to distinguish these differences in phenology within the pixel area. UAVs represent a potential opportunity to adequately sample this heterogeneity in leaf phenology as they allow data at a fine spatial scale, over relatively larger areas, to be obtained (Dandois and Ellis, 2013; Berra *et al.*, 2016). The data generated by UAV COTS cameras is similar to near-surface digital repeat photography in the sense that time series data are generated, but also visual interpretation of organisms can be made from the images (Sonnentag *et al.*, 2012; Klosterman *et al.*, 2014).

The within-plot variability in phenology, as assessed by ground observations, was consistently detected by the UAV dataset, providing a new methodological approach to track phenological dynamics within plant communities. An individual tree level detection of spring phenological transition dates was possible due to the user-defined temporal (~7 days) and

spatial (5 cm) resolution with which the UAV data was acquired in this research. Overall, UAV SOS could be predicted with an accuracy of 8 days across the six plots (six tree species) and also 8 days when only deciduous trees were considered. Because the validation was based on visual assessments, which itself is not free of uncertainties (Schaber, 2002; Klosterman *et al.*, 2014), it would be reasonable to expect higher accuracies from these UAV estimates.

Among the three metrics (SOS, MOS and EOS), SOS returned the most accurate estimates, indicating that this metric represents the transition phase between bud open/leaf out. Accurate estimations of SOS dates is of upmost importance as the onset of spring is related with many ecosystem processes, such as total seasonal evapotranspiration and carbon accumulation (Ricciuto *et al.*, 2008; Toomey *et al.*, 2015), and can be an indicator of climate change (Menzel, 2002; Polgar *et al.*, 2013; Polgar and Primack, 2013). Within a climate change context, monitoring techniques which are able to capture the individual phenology of the plants are needed, as not all species are responding similarly (Thompson and Clark, 2008; Vitasse *et al.*, 2009; Ibáñez *et al.*, 2010). UAV data, as presented in this chapter, could meet this need by providing measurements at a detailed biological scale. Therefore, UAV data could potentially contribute to phenology studies by providing local-scale measurements meeting two research needs: 1) plant- and plot-based scale (Lechowicz, 1984; Hunter and Lechowicz, 1992; Schaber and Badeck, 2003) and 2) continuously in space, similar to remote sensing satellites (Fisher *et al.*, 2006; White *et al.*, 2014). Like all other methods, the methodology adopted in this research also has some limitations and caveats, which are discussed next.

5.4.2 Sensitivity of fitting models, VIs and understorey vegetation

Since it has been suggested that different combinations of VIs, fitting models and plant functional types can affect the certainty of phenometric estimates (Klosterman *et al.*, 2014; Wu *et al.*, 2017), this research undertook a comprehensive comparison of these combinations, which is particularly critical when new sensors are tested (White *et al.*, 2009; Wu *et al.*, 2017). Not surprisingly, the accuracy and statistical uncertainties of UAV-derived phenometrics were dependent upon such combinations, but also upon the metric analyzed (SOS, MOS and EOS). Different combinations can affect the RMSE, magnitude and direction of bias when comparing phenometrics derived from visual assessments and from UAV data.

Uncertainties in the model fitting, which could propagate into the phenological date estimations (Klosterman *et al.*, 2014; Baumann *et al.*, 2017), were quantified by simulating phenology curves based on fitting residuals. There was not a single logistic model fitting

consistently the UAV remote sensing data better across all plots and for all three metrics (SOS, MOS and EOS), even though the greendown model was the one with the best general performance. This is in accordance with other studies (White *et al.*, 2014; Filippa *et al.*, 2016), and suggests that the best model will depend upon which remote sensing data is being used, which land cover type is being monitored and which metric is of interest.

An ensemble of five UAV-derived VIs (GCC_{DN}, GCC_r, $GCC_{r/C0}$, NDVI and $NDVI_{C0}$) were used to track the phenology of evergreen and deciduous plots (section 5.2.3), but the color index GCC_{DN} better represented the tree level dynamic of this ecosystem (section 5.3.5). While consistent NDVI and $NDVI_{C0}$ time series could be retrieved using the average from within a 30 x 30 m area (Landsat pixel size, Chapter 4), a poor quality time series was generally observed at a tree crown scale. GCC_{DN}, on the other hand, resulted in a clearer and stronger seasonal signal.

It is inferred that, at small spatial scales, GCC_{DN} is better able to take into account the different illumination conditions experienced in some acquisition dates than NDVI and $NDVI_{C0}$. Because GCC_{DN} uses only VIS orthomosaic data (i.e., data from a single camera), the three RGB channels should be affected similarly by the varying illumination conditions, independent of the spatial scale in which the data are aggregated. On the other hand, DNs from the VIS and NIR orthomosaics (i.e., data from two cameras) are used in the NDVI and $NDVI_{C0}$ calculations and, at small spatial scales (tree crown), any difference in the VIS and NIR orthomosaics might be enhanced.

Firstly, even though the COTS cameras were flown concomitantly, they were located at ~10 cm apart in the UAV frame, resulting therefore in slightly different view angles. Secondly, VIS and NIR orthomosaics can be co-registered with an accuracy of ±11 cm (~2.1 pixels, Chapter 4), which may influence analysis over smaller crowns. Thirdly, VIS and NIR orthomosaics might be experiencing very different illumination conditions over small areas due to substantial time lags between the original visible and NIR single images chosen to compose the respective orthomosaics. This lag could be due to one of the cameras failing to record an image at a programmed time, while the other does. In such a case, the VIS and NIR orthomosaics` DNs are affected differently by varying illumination conditions (as exemplified in Figure 5-14), hampering the ability of NDVI to normalize for this effect. Finally, since the VIS and NIR orthomosaics were processed as two independent datasets within Photoscan, the location and amount of artifacts (commonly present in UAV-derived orthomosaics (St-Onge *et al.*, 2015; Haghighattalab *et al.*, 2016; Samiappan *et al.*, 2017)) might be different for the

two orthomosaics (Figure 5-15). Therefore, the combination of all these factors resulted in a noisier UAV NDVI and $NDVI_{C0}$ time series, contributing towards a weak seasonal signal and less accurate phenological date estimates at an individual tree-level scale.

Visible camera | NIR camera
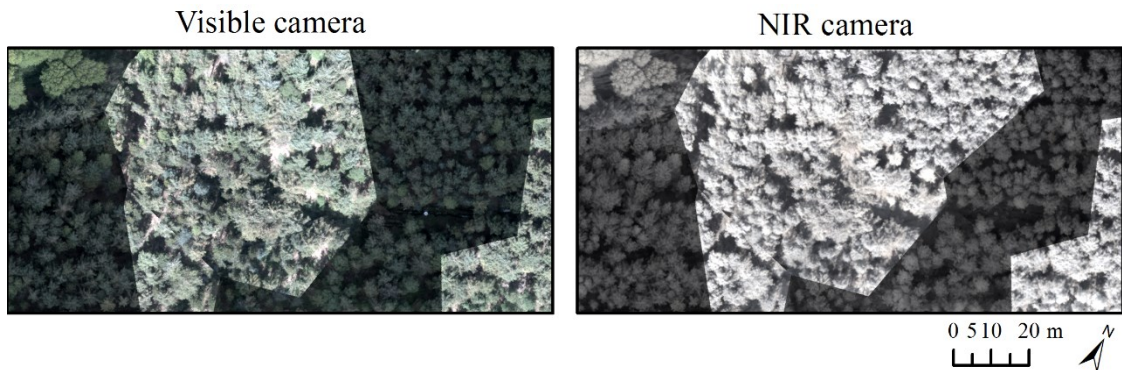
Figure 5-14. Example of orthomosaics made of UAV images acquired under variable illumination conditions at Hanging Leaves Wood (DOY 155, 04/06/2015). Some areas of the visible and NIR orthomosaic are affected differently by varying illumination conditions.

Visible camera | NIR camera
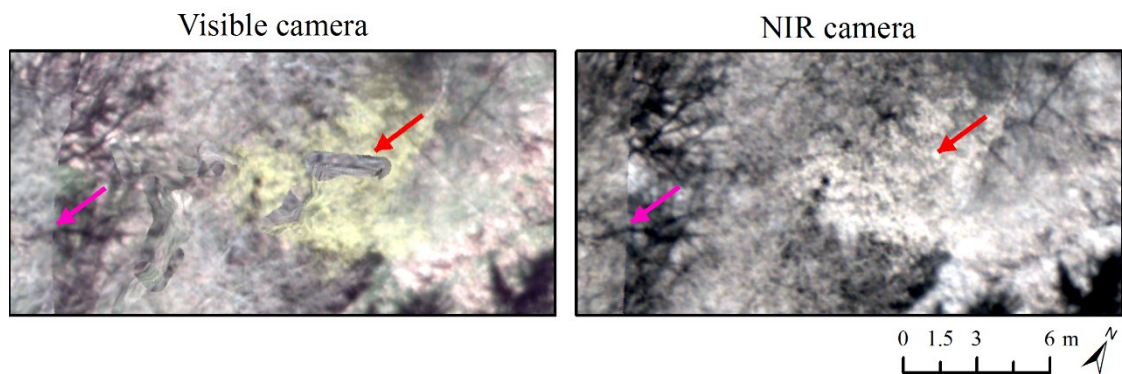
Figure 5-15. An example of artifacts present on the UAV orthomosaics (DOY 111, 21/04/2015). The pink arrows point to similar artifacts (seam line) occurring at the same location on both visible and NIR orthomosaics, whereas the red arrows point to a location where an artifact was present only on the visible orthomosaic.

Nevertheless, a better quality time series of UAV spectral VIs could potentially be achieved at small spatial scales. A noisy series could be smoothed out by using filters such as Savitzky–Golay (SG) before the phenological parameters being extracted (Lhermitte *et al.*, 2011; Ryan *et al.*, 2012; Miao *et al.*, 2013). In this study, SG filter was tested with the UAV time series of data, but, the observations proved to be not dense enough in order to avoid important phenological characteristics being eliminated with smoothing within some plots. This is because the frequency of UAV data acquisition was decreased after the last tree to reach EOS was observed, and flights were only done on two extra dates, which proved to be not ideal for the evergreen species as they greened-up later. It is recommended, in future studies, to maintain the same frequency of UAV observations up to ~1-2 months after EOS,

which could therefore allow smoothing techniques to be applied with higher confidence, if needed.

Alternatively, it is possible to use a single modified camera recording visible and near infrared wavelengths (Hunt *et al.*, 2010; Verhoeven, 2012; Berra *et al.*, 2015). Because the three bands are already registered, NDVI could potentially be calculated more consistently at small spatial scales, similarly to GCC_{DN} from an unmodified camera. It would be valuable, in a future study, to test a dual-camera system composed of an unmodified COTS camera (for GCC_{DN}) and a modified camera, as proposed above, specifically for NDVI. Furthermore, non-COTS multispectral sensors, such as Tetracam® (Berni *et al.*, 2009; Laliberte *et al.*, 2011; Del Pozo *et al.*, 2014) and MicaSense® (Samiappan *et al.*, 2017), are an option and could be advantageous in this sense.

This study also tested the potential of an unmodified COTS camera to produce time series of spectral VIs, which eliminate difficulties related to band registration. Results achieved with the GCC_r show that a single camera approach might not be enough to produce consistent time series of spectral VIs at a tree crown scale (Figure 5-7). This can be due to difficulties in deriving well calibrated standard equations in every acquisition date (as discussed in section 4.5.2, Chapter 4), complicated by the low spectral reflectance difference among the visible bands (~0.02). However, by using C0 equations, $GCC_{r/C0}$ performed nearly as efficient as GCC_{DN} in the detection of phenological events, indicating that the C0-derived visible band reflectances were consistent with each other.

Besides heterogeneity in dominant tree species composition, different understorey covers may have significant impacts on land phenology detection, if their phenological events are off-phased (Tuanmu *et al.*, 2010; Liu *et al.*, 2017). In this study, the phenology signal detected by the UAV was influenced by the understorey and a sunlit-pixel-based method was used to diminish such influence at a tree-level scale. The use of the 20% brightest pixels within a tree crown (80% percentile approach), acted mainly to flatten the winter baseline, resulting in a stronger seasonal signal. This can be explained as this approach tends to select pixels associated with tree`s branches, targets from which the greenness values are expected to be significantly modified only after budburst. For this reason, the UAV phenometrics extracted using the 80% percentile approach can be considered to represent canopy phenology rather than land surface phenology. Nevertheless, residual effects are expected due to the complex way in which energy interacts within a forest environment (Jacquemoud *et al.*, 2000). Future studies could further explore the high spatial and temporal resolution of UAV

data to better differentiate understorey community phenology and decouple this effect from canopy phenology.

Finally, more accurate and precise spring phenological transition dates were detected from UAV time series having well-characterized winter base lines and summer plateaus, as observed at the Larch and Oak plots (section 5.3.6). Plots with only a few data points to characterize either the winter baseline (e.g. Sycamore) or the summer plateau (e.g. Norway spruce) returned less certain estimates. This suggests that in order to characterize spring events of different species, it would be beneficial to start the data collection from start of winter up to the end of summer, a time span which could allow detection of the winter baseline and the summer plateau of a wide range of species (at least in this ecosystem), besides being beneficial for smoothing techniques.

5.4.3 Phenology of evergreen trees

Contrary to optical satellite sensors, near-surface cameras (phenocams) have been more successful in detecting the less pronounced seasonality of canopy greenness in evergreen stands (Richardson *et al.*, 2009; Sonnentag *et al.*, 2012). Similarly to phenocams, the UAV dataset used in this research also detected the weaker seasonal signal of evergreen trees (in relation to deciduous ones), but without the issue of camera-target distance commonly reported in phenocam studies (i.e., further trees have weaker response) (Richardson *et al.*, 2009; Ide and Oguma, 2010; Mizunuma *et al.*, 2013), as the UAV flew at a programmed constant height. Evergreen phenological dates were therefore estimated from the UAV time series of data, but comparisons with visual observations revealed less accurate results (in relation to deciduous trees), which can be due to a combination of factors.

Firstly, less accurate visual assessments were likely achieved from evergreen trees as their phenological events are less contrasting than observed on deciduous trees. Secondly, UAV SOS dates were biased consistently later (up to two weeks) in relation to visual assessments of SOS, suggesting that the remote sensing SOS might be related to later needle development phases, rather than >90% of bud open (candle visible). Because the same phenological code was used to represent SOS across the two plant functional types, these findings suggest that a different observed phenological event might be more appropriate to represent the start of spring season of evergreen trees. Thirdly, the evergreen trees` seasonal signal had a smaller amplitude than that detected from deciduous trees, meaning that the time series of UAV data can be more sensitive to noise, consequently increasing the statistical

uncertainty in estimated phenology dates. Therefore, it would be beneficial in future studies to increase the camera sensitivity in order to have a stronger temporal profile.

One of the stands (Norway spruce) leafed out very late in spring (~21st May, 2015) and only a couple of UAV data points were available to characterize the summer peak and summer plateau, making the model fitting especially challenging towards the end of spring and resulting in highly uncertain EOS predictions (Table 5-5). The other evergreen stand (Sitka spruce) leafed out 6 days earlier (on average), but a pest attack changed its expected temporal dynamic over summer, resulting in an even smaller signal amplitude, which caused the least certain estimates among the six plots (Table 5-5). Therefore, it was not possible to fully understand the spring temporal dynamic of this plant functional type from the UAV dataset, highlighting the need for further investigations within this field. Nevertheless, these results also show a potential opportunity in tree pest/disease detection, biotic stresses which could be detected in a way similar using ground and near-surface time series images (Ide and Oguma, 2010; Mizunuma *et al.*, 2013).

5.4.4 Cross-scalar phenology from ground, UAV and satellite at plot level

The plot-averaged visual assessments of leaf development (SOS) had a close match with UAV SOS, but pronounced differences occurred with Landsat SOS. This confirms the ability of UAV data in detecting leaf canopy dynamics (by using the 20% brightest values), while Landsat tracks the overall ecosystem dynamic. While this cross-comparison has uncertainties related to areal and statistical representativeness, the overall dynamic of this ecosystem should be captured by the multi-sensor, multi-scalar observations.

The spring onset of deciduous plots (3 out of 4) detected by both Landsat EVI and NDVI was biased earlier in relation to the UAV GCC$_{DN}$, similarly to studies comparing satellite to near-surface phenology (Soudani *et al.*, 2008; Hufkens *et al.*, 2012), with Landsat NDVI detecting SOS earlier than Landsat EVI, confirming findings of White *et al.* (2014). At the sampled plots, evidence from the understorey ground photography suggests that early understorey development should be driving this pattern, as UAV and Landsat SOS dates were very similar over the plot (Larch) where understorey greened up later than the upper canopy. This outcome could be anticipated as, generally, understorey is expected to green-up earlier than overstorey in temperate forests (Augspurger and Bartlett, 2003; Augspurger *et al.*, 2005), increasing the signal detected by satellite VIs (Garrity *et al.*, 2011; Henebry and de Beurs, 2013; White *et al.*, 2014). Such an effect would also be detectable in the UAV VI time series, if not selecting the 20% brightest values within a plot (Figure 5-5). Other factors, such as

snow melt (Delbart *et al.*, 2006) and significant topography variation (Fisher and Mustard, 2007), could also bias phenometric estimates, but these were not present in the study area.

Because Landsat VIs underestimated the onset of leaf canopy phenology where understorey and overstorey phenologies were off-phased, Landsat MOS was the metric most closely associated with the UAV-derived and visual assessments of SOS. Despite a relatively small number of plots being analyzed, these findings confirm the challenge of relating LSP with leaf/canopy phenology and defining comparable phenological metrics (Fisher *et al.*, 2006; White *et al.*, 2014).

Phenological metrics as derived from ground measurements of canopy cover fractions had large mismatches with Landsat, UAV and visual assessments. Cover fraction measurements were not sensitive to subtle changes in leaf development, resulting in a sudden beginning and end of spring season. Cover fraction is also highly sensitive to vegetation density (White et al. 2014), which means that in a forest/woodland with unevenly spaced trees (as in this study), the location of the camera within a plot can have significant impacts on the derived metrics. Therefore, canopy structure, as estimated from upward hemispherical photo, may not be representative of the changes observed in remote sensing vegetation indices and ocular observations, which is in accordance with other studies (White *et al.*, 2014). Similar conclusions were drawn from comparisons of under-canopy light sensor measurements against visually recorded phenology, as these instruments did not detect substantial changes until the leaves had emerged fully from the buds (Schwartz *et al.*, 2013).

5.5 Conclusion

This study investigated the potential of a UAV remote sensing platform to monitor spring phenological events of a temperate forest at an individual tree- and plot-level, providing a new methodological approach to track local scale dynamics of vegetated surfaces. The start of season metric could be predicted with an accuracy better than 1 week for deciduous covers and within 2 weeks for evergreen covers. The potential of UAV data for tracking the subtle temporal signal from evergreen trees is promising, but further studies are needed to better understand the phenology of this plant functional type from a UAV perspective.

The airborne characteristic of UAV time series can allow fine details to be resolved, similarly to near-surface optical sensors, but with the advantage of producing synoptic and georeferenced information. Because of this ability to provide measurements at a detailed biological scale, differences in phenological behaviours of individual plants within plots were consistently tracked by the UAV data set, matching ground visual assessments.

Accuracy of UAV-derived phenological metrics estimates depends upon a combination of factors such as datasets available, methodological choice, metric of interest and characteristics of the study area. Asynchrony in timing of winter dormancy breaking between understorey and overstorey vegetation can be responsible for large mismatches between upper canopy leaf phenology and land surface phenology. Furthermore, the simple colour index GCC_{DN} proved to be more robust than spectral indices to track greenness dynamics of individual trees, which could simplify data acquisition and processing, but may be less suitable for linking directly with satellite data.

Chapter 6. Individual tree-level phenology across a woodland

6.1 Introduction

The potential and accuracy of UAV orthomosaic time series for tracking individual-tree level phenology was investigated across 6 selected plots in Chapter 5. This chapter expands the analysis over the whole woodland, exploiting therefore the full areal coverage of the UAV dataset acquired in this research. This is done by automating the tree crown detection and delineation, making it easier to implement on an operational basis.

Besides providing the opportunity to examine leaf phenology of individual trees over a relatively larger area, this information will also allow validation of Landsat LSP products in a novel way: because of the airborne characteristic of UAV time series data, the canopy phenology of all individual trees within a Landsat pixel can be detected in a manner similar to satellite sensors, i.e., synoptically. This chapter seeks to achieve the final aim of this research: to quantify and understand the spatiotemporal variability in leaf phenology within Landsat pixels. Therefore, this chapter addresses the Objective 4 and Objective 5 of this research as presented in Chapter 1: "To examine the spatial and temporal characteristics of canopy phenology across an entire woodland at a fine-scale perspective. This could allow investigation of the variability in phenology within tree species and with tree species composition." and "To assess and better understand the fine-scale spatial variability in phenology events occurring at a sub-pixel level for widely-used satellite data sets."

The specific objectives are:

- To automatically detect tree crowns from UAV orthomosaics in order to allow individual tree-level phenology to be monitored and mapped across the whole mosaic extent.
- To analyse spatial patterns of key phenological dates among the different tree species.
- To cross-compare UAV- and Landsat-derived phenometrics in order to understand the variability in phenology within Landsat pixels.

6.2 Methodology

The description, implementation and accuracy assessment of a tree crown delineation approach composes the main body of this methodological section. Additionally, the techniques used to cross-compare UAV- and Landsat-derived phenometrics are presented. The methods used to extract phenometrics from the UAV and Landsat data are described in Chapter 5.

6.2.1 Automatic tree crown delineation based on canopy height model

Aerial mapping of 3D forest structure has been largely undertaken with the aid of Airborne Laser Scanning (ALS) technology (Duncanson *et al.*, 2014; Silva *et al.*, 2016), and, more recently, UAV imagery has emerged as a feasible and cost-effective local scale option for this purpose (Lim *et al.*, 2015; Puliti *et al.*, 2015; St-Onge *et al.*, 2015; Hernandez *et al.*, 2016; Panagiotidis *et al.*, 2016; Nevalainen *et al.*, 2017). This is possible due to advances in structure-from-motion techniques, which have allowed Digital Terrain Models (DTMs) and Digital Surface Models (DSMs) to be generated out of a 3D photogrammetric point clouds (St-Onge *et al.*, 2015). In a forest environment, the underlying ground topography (DTM) can be reconstructed based on points classified/selected as ground (Panagiotidis *et al.*, 2016). A Canopy Height Model (CHM) can therefore be obtained by subtracting these two elevation models and forest attributes (e.g. total tree height, tree crown area) can be retrieved at an individual tree level, similarly to ALS data (Hernandez *et al.*, 2016).

There are many approaches available to detect and delineate tree crowns from a CHM, including region growing (Culvenor, 2002), valley-following (Gougeon, 1995) and watershed (Meyer and Beucher, 1990). The accuracy of single-tree-level attributes estimation can be affected by the delineation method chosen but also, it can be highly dependent on the forest structure under investigation (Ke and Quackenbush, 2011; Silva *et al.*, 2016). Individual tree level prediction accuracies of complex canopy structures (e.g. old broadleaf forest and uneven aged trees) are usually lower than those found in simpler and more homogeneous structures (e.g. conifer-dominated forests and same age plots) (Duncanson *et al.*, 2014; Li *et al.*, 2016).

In this research, the automatic tree crown delineation across the entire study area was achieved by using a watershed-based approach, as proposed by Panagiotidis *et al.* (2016), who used very high resolution UAV imagery, similar to the imagery available in this study, as input data to delineate tree crowns. Because watershed algorithm is easy to be implemented and improved, well developed (Zhen *et al.*, 2016) and is commonly available in GIS software,

watershed is frequently used to perform crown delineation from a CHM (Mei and Durrieu, 2004; Edson and Wing, 2011; Ke and Quackenbush, 2011; Zaki *et al.*, 2015; Panagiotidis *et al.*, 2016). Panagiotidis *et al.* (2016)`s original workflow, which used only 3D data, was modified in this study to also include spectral information in the processing chain (Figure 6-1) in order to increase the delineation accuracy.
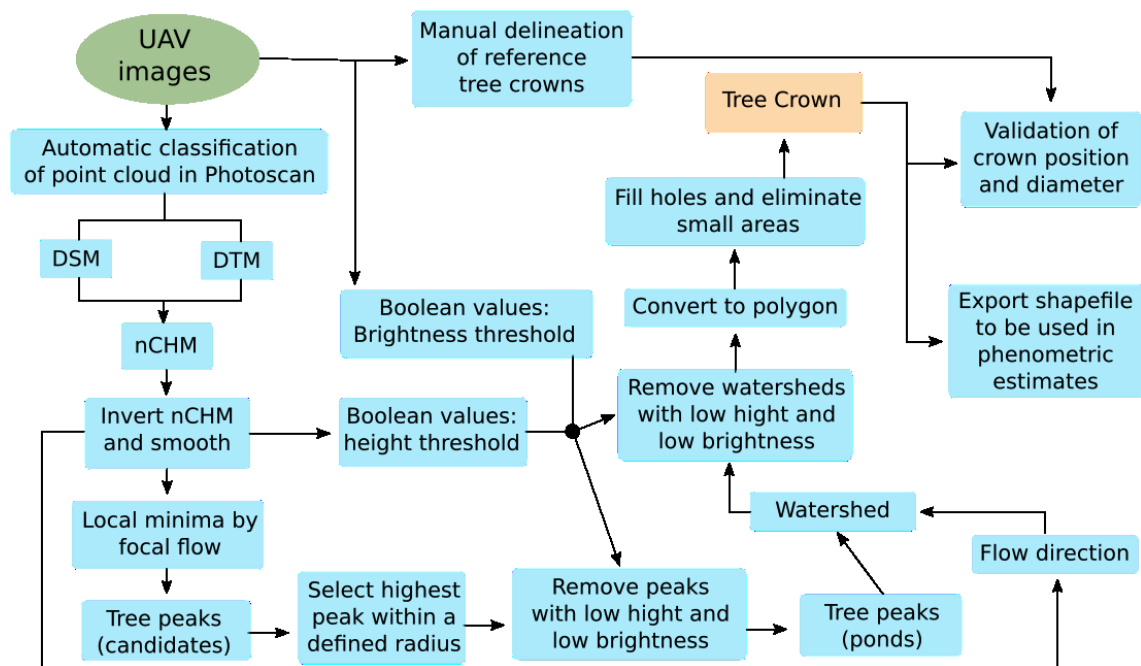
Figure 6-1. Flowchart of the UAV data processing for automatic delineation of tree crowns. Modified from Panagiotidis *et al.* (2016).

UAV images from two dates were used as input to generate a Canopy Height Model (CHM). Unlike the orthomosaic time series generation (Chapter 4), all the visible-camera images available on these two dates (two flights per date) were used as input in Photoscan in order to produce a denser point cloud, resulting in a more detailed 3D model and potentially minimizing occlusion problems (St-Onge *et al.*, 2015; Nevalainen *et al.*, 2017). The DTM was derived from a UAV acquisition date corresponding to deciduous leaf-off phase (DOY 77, 18/03/2015) in order to have a higher density of points representing the ground, at least over deciduous covers. UAV images acquired during a deciduous leaf-on phase were used to derive a DSM (DOY 218, 06/08/2015).

After image alignment within Photoscan (498 out of 499 aligned on DOY 77 and 429 out of 429 on DOY 218), the resulting sparse point cloud was georefenced by using all GCPs available (13). Thereafter, the camera parameters were optimized and a denser point cloud was generated, similar to that described in Chapter 4, but using a high quality reconstruction

setting within Photoscan (AgiSoft, 2016). From the dense point cloud of DOY 77 (122 points/m^2), an automatic classification (within Photoscan) detected points associated with the ground. This classification is based on three user-defined parameters (maximum angle = 15°; maximum distance = 1 m, and; cell size = 150 m), values which were determined based on a trial and error approach. The point cloud is firstly divided into the chosen cell size (150 m represents the approximate size of the largest evergreen stand (closed canopy), where fewer ground points are likely to be present), and the lowest point within each cell is detected. An initial terrain model is triangulated from these points. Afterwards, the remaining points are iteratively checked and added to the ground class if they satisfy the specified angle and distance (in relation to the terrain model) (Axelsson, 2000; AgiSoft, 2016). A DTM is then build based on the selected ground points employing the "Enabled (default)" interpolation option within PhotoScan. The DSM was constructed using the entire dense point cloud from DOY 218 (110 points/m^2), using the same interpolation option. The DSM and DTM were exported as raster files (10 cm spatial resolution) to be used as input in ArcGIS 10.3.1 (ESRI©).

ArcGIS`s model builder was used to automate the tree crown delineation (Figure 6-1). Firstly, a normalized CHM (nCHM) was calculated by subtracting the DTM from the DSM. The nCHM was then inverted to allow the Inverse Watershed Segmentation (IWS) method (Edson and Wing, 2011) to be applied, whereby each segment is considered as an individual hydrologic drainage basin. Besides the inverted surface, a watershed approach also needs markers or 'ponds' (tree peaks in this case), which was achieved using the following three steps:

1) Determination of local minima by focal flow statistics. This step returned many tree peaks, not only over crown areas but also on the ground, so a cleaning and selection was applied.

2) Selection of the highest peak from within a defined circular radius (focal statistics). The optimal radius was determined per woodland type, based in a trial and error approach (Larch = 2 m; Sycamore = 2.2 m; Oak = 2.7 m; Sitka spruce = 1.5 m; Norway spruce = 0.9 m, and; Mix = 2.4 m).

3) Removal of peaks with low height (below the average CHM value of a 5x5 m window) and low brightness. This later step was added into the Panagiotidis *et al.* (2016)`s workflow by defining a brightness threshold (either 20% or 30% percentiles, dependent on woodland type) from the visible and NIR orthomosaics of DOY 218. This was undertaken in order to eliminate peaks located either on the

edge of crowns or very close to the crown (peaks which were not eliminated by the height threshold alone).

Watershed segmentation was then applied by using both the selected tree peaks (imitating ponds) and the nCHM-derived flow direction as inputs (Figure 6-1). The later raster was created using the `Flow direction` tool within ArcMap, where each output cell represents the direction of flow from the elevation surface (nCHM). Since the segmentation results in a continuous raster, segments falling into areas of low height or low brightness were removed using the same thresholds mentioned above.

Finally, the resulting watersheds were converted to polygons. Any hole inside a polygon was filled and polygons with small areas (1-3 m^2, dependent on woodland type) were either merged with adjacent ones or eliminated. The remaining polygons represent the tree crowns and they were exported as a shapefile in order to allow for accuracy checks and phenology events to be estimated across the whole study area.

6.2.2 Automatic tree crown delineation: Accuracy assessment

The validation/reference data consisted of manually delineated crowns, a common approach when high or very high resolution imagery is available (Pouliot *et al.*, 2002; Ke and Quackenbush, 2011). Besides the 20 trees per plot sampled for phenology studies (already delineated, Chapter 5), 20 more tree crowns (surrounding these plots) were manually delineated on the UAV orthomosaics (as described in Chapter 5), resulting in 40 crowns per woodland type (Larch, Sycamore, Oak, Sitka spruce, Norway spruce and Mixed).

The watershed-derived tree crowns were quantitatively evaluated at both plot and individual tree level, following the method proposed by Ke and Quackenbush (2011). Plot level assessment consisted of quantifying the tree count errors, i.e., comparing the crown count estimation against the number of reference crowns. However, this analysis, does not quantify wrongly/correctly delineated crowns and Ke and Quackenbush (2011) proposed a confusion table in order to evaluate individual tree level accuracy from both a reference crown and delineated crown perspective. The method is illustrated in Figure 6-2 with an interpretation provided in Table 6-1. In summary, the approach quantifies correctly detected tree crows, and errors due to omission, commission and under- and over-segmentation.

	(i)	(ii)	(iii)	(iv)	(v)
(a) Reference crown perspective	0:1		1:1	2:1	1:1
(b) Delineated crown perspective		1:0	1:1	1:1	1:3
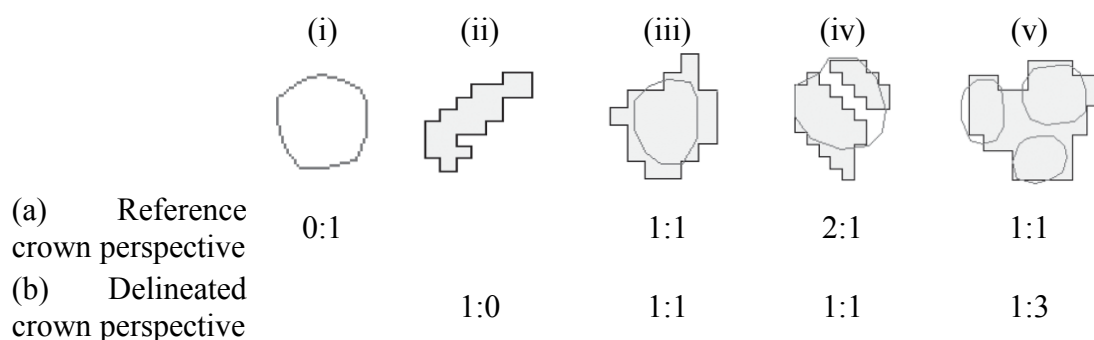
Figure 6-2. Detection scenarios from (a) reference and (b) crown perspectives with reference crowns shown as circular polygons and delineated crowns as filled polygons (Ke and Quackenbush, 2011). An interpretation of these five cases (i-v) is given in Table 6-1.

Table 6-1. Interpretation of the detection scenarios showed in Figure 6-2.

Case	Interpretation
(i)	Simple omission (0 delineated: 1 reference).
(ii)	Simple commission (1 delineated: 0 reference).
(iii)	Perfect match, i.e., correctly delineated tree (1 delineated: 1 reference) in both perspectives.
(iv)	Commission from over-segmentation. One reference crown is delineated as two crowns, so a '2 delineated: 1 reference' ratio from a reference perspective. However, from the delineated crown perspective, each delineated crown sees only one reference crown (1 delineated: 1 reference).
(v)	Omission due to under-segmentation. A group of reference trees is delineated as a single one, resulting in a '1 delineated: 3 reference' ratio under the delineated perspective. From a reference crown perspective, however, each reference tree sees only one delineated polygon, so the '1 delineated: 1 reference' ratio.

The results from this confusion matrix are thereafter translated in terms of producer`s (PA) and user`s (UA) accuracy. PA calculates the probability of a reference tree being correctly delineated (Eq. (6-1)) and UA represents the probability that a delineated tree will correctly represent a reference tree (Eq. (6-2)) (Ke and Quackenbush, 2011):

$$PA = \frac{N_p}{N_r} \qquad\qquad (6\text{-}1)$$

$$UA = \frac{N_p}{N_d} \qquad\qquad (6\text{-}2)$$

where N_p is the number of correctly delineated trees; N_r is the number of reference trees and N_d is the number of delineated trees.

A final accuracy assessment (for the crown delineation) was undertaken by comparing the delineated crown diameter against the reference diameters, but considering only the correctly delineated tree crowns (case (iii), Figure 6-2). This involved calculation of mean error, absolute error and RMSE values.

Tree heights derived from the CHM ('tree peaks', Figure 6-1) were linearly regressed against observed tree heights (section 3.3, Chapter 3) in order to quantify the accuracy of the UAV-derived CHM. An intersection test selected the observed vs estimated pairs of data; if the geolocation of an observed height (point) intersects an automatic delineated crown (polygon), then the observed tree height value is associated with the polygon`s tree peak value.

6.2.3 Mapping tree-level phenology and comparing with Landsat phenology

UAV-derived individual-tree level phenodates were estimated across the entire study area using the automatically detected tree crowns as regions of interest. These phenodates were extracted from UAV GCC_{DN} time series (80th percentile approach) fitted by the greendown model, based on the findings presented in Chapter 5. Besides allowing a detailed phenology map to be produced, UAV estimates were compared against Landsat land surface phenology (fitted by the simple model, following findings from Chapter 5) in order to understand leaf phenology variability within Landsat pixels. In a first analysis, in order to explicitly illustrate individual tree variability, each UAV tree phenodate was regressed against the intersecting Landsat pixel`s phenodate, i.e., a data point was formed by an individual tree phenodate and a Landsat pixel phenodate.

Afterwards, two approaches were used to scale from UAV to the Landsat pixel level: 1) a mean UAV phenodate was calculated based on individual-tree phenodates weighted by the percent crown area within each Landsat pixel area, an approach which is similar to the percent basal area (White *et al.*, 2014); and 2) mean UAV DNs were extracted from within each Landsat grid cell, the values of which were converted to vegetation indices in order to estimate UAV phenodates in a manner more similar to Landsat data, i.e., considering a continuous landscape (30 x 30 m) instead of isolated tree crowns.

For these comparisons, three Landsat VIs were used: NDVI, EVI and GCC$_L$ ($_L$ is for Landsat) (Eq. (6-3)), whereas GCC$_L$ is intended to provide the most direct comparison with UAV GCC$_{DN}$.

$$GCC_L = \frac{\rho_{green}}{\rho_{blue} + \rho_{green} + \rho_{red}}$$ (6-3)

where ρ_{blue}, ρ_{green} and ρ_{red} are spectral reflectances in the blue, green and red wavelengths, respectively.

Whilst only UAV GCC$_{DN}$ was used during the tree-level analysis, UAV NDVI and UAV NDVI$_{C0}$ were also included for the mean UAV DNs analysis (approach "2" above), as consistent time series could be calculated from these VIs at a 30 m spatial scale (Chapter 4). This also allowed the dynamics of different UAV- and Landsat-based VIs time series to be compared, rather than phenodates. In order to do this, the temporal resolution of the UAV data was reduced to match Landsat. For each available Landsat date (pixel-wise), the closest UAV acquisition date was selected to compose a pair of observations, resulting in between 7 and 9 pairs of data (due to L7-ETM+ data gaps (scan line corrector-off)). The congruence of the UAV and Landsat products (phenodates and VI time series) was analysed with aid of linear regression, as in Chapter 5.

6.3 Results

6.3.1 Accuracy of the automatic tree crown delineation

No difference was detected between the number of observed and detected trees in the Larch and Mix plots, whilst underestimation of the number of trees was observed for Sycamore, Sitka spruce and Norway spruce, contrary to overestimation for the Oak plot (Table 6-2). However, this tree counting does not provide the proportion of correctly delineated trees, information that is given by the reference/crown perspective confusion matrix (Table 6-3). An overall accuracy of 63% was detected across all woodland types, as given by the producer`s (PA) and user`s (UA) accuracy. Conifer species were more accurately delineated with PA ranging from 73% to 80% (UA from 78% to 82%), whilst broadleaf species achieved lower PAs (43% to 57%, with UA from 43% to 63%). Only 1 tree (out of 240) was omitted and no simple commission errors were observed. Over-segmentation affected mainly the Oak and Mix plots, predominantly with 2 segments (2:1 in the reference

crown perspective) and not more than 3 segments per tree. These two plots were also the most affected by under-segmentation (1:2 and 1:3 in the delineated crown perspective). Examples of the results are showed in Figure 6-3, where manual and automatic delineated polygons are overlaid on the UAV orthomosaic (all the automatic delineated crowns can be seen in Figure 6-11a).

Table 6-2. Tree count estimation error at plot level. Every automatically delineated crown (Estimated) represents one tree.

Plot	Reference	Estimated	Difference (%)
Larch	40	40	0
Sycamore	40	35	-13
Oak	41	51	24
Sitka spruce	40	39	-3
Norway spruce	40	36	-10
Mix	40	40	0
Total	241	241	0

Table 6-3. Accuracy assessment of automatically delineated tree crowns. "1:1" shows the correctly delineated trees, or perfect matches. 40 reference trees were sampled in each plot, totalling 240 reference trees.

Plot	Reference crown perspective				Delineated crown perspective				1:1	PA[1] (%)	UA[2] (%)
	0:1	1:1	2:1	3:1	1:0	1:1	1:2	1:3			
A	0	34	6	0	0	39	1	0	31	78	78
B	0	32	8	0	0	29	6	0	23	57	66
C	1	29	10	1	0	44	5	2	21	51	41
D	0	36	4	0	0	35	3	1	32	80	82
E	0	35	5	0	0	33	3	0	29	73	81
F	0	26	12	2	0	33	5	2	17	43	43
All	1	192	45	3	0	213	23	5	153	63	63

[1]Producer`s accuracy; [2]User`s accuracy; A=Larch; B=Sycamore; C=Oak; D=Sitka spruce; E=Norway spruce; F=Mix. A, D and E are conifers; the others are broadleaf species.
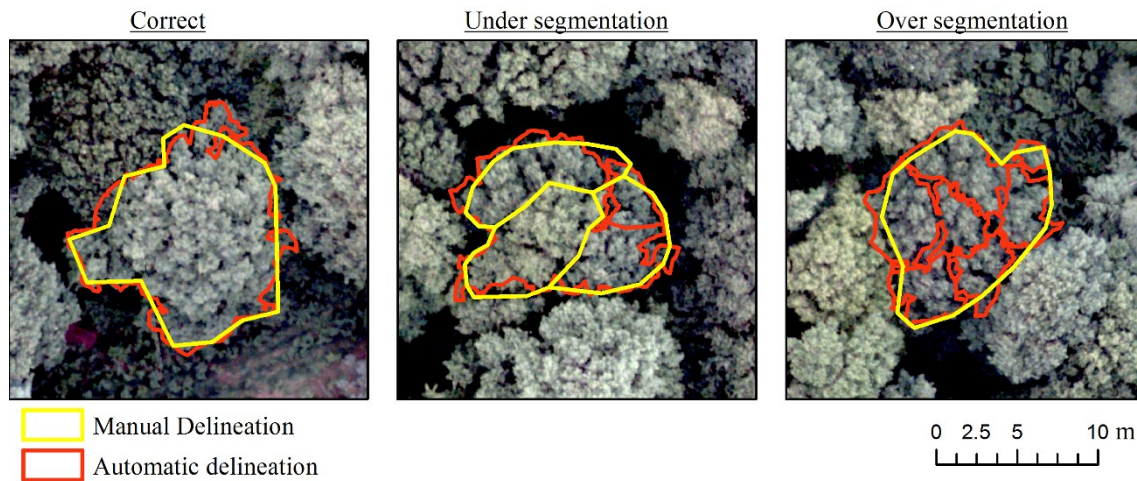
Figure 6-3. Examples comparing manual vs automatic delineation of oak tree crowns for three cases: correct detection, under segmentation and over segmentation. The background orthomosaic is made of visible camera UAV images, acquired on 25/06/2015.

For correctly delineated crowns, crown diameters were underestimated by around 21 cm (absolute error of 42 cm and RMSE of 11%) across the six plots, with the best match occurring for the Oak plot (RMSE = 6%) and the largest mismatch for Sitka spruce (RMSE = 19%) (Table 6-4). This underestimation tendency means that the automatically delineated crown area is smaller than the reference crown, and this can be due to: 1) generalization of the crown shape during manual delineation, i.e., not cutting into the crown between branches when drawing crown boundaries; and 2) to the exclusion of areas with low brightness and low height during the automatic delineation (Figure 6-1), which can favor the upper canopy.

Table 6-4. Summary statistics of crown diameter from correctly delineated tree crowns (Perfect 1:1, Table 6-3). Each plot has 40 reference tree crowns. Bias is calculated as reference less delineated crowns, so a negative bias indicates underestimation of tree crown diameter. RMSE is shown as a percentage of the mean measured diameter (Pouliot *et al.*, 2002).

Plot	Tree crowns (Perfect matches)	Mean reference diameter (m)	Bias (m)	Absolute error (m)	RMSE (%)
Larch	31	5.3	-0.08	0.41	10
Sycamore	23	6.2	-0.34	0.45	9
Oak	21	7.9	-0.08	0.34	6
Sitka spruce	32	4.0	-0.47	0.57	19
Norway spruce	29	2.3	-0.18	0.26	13
Mix	17	6.3	-0.13	0.49	10
Total	153	5.3	-0.21	0.42	11
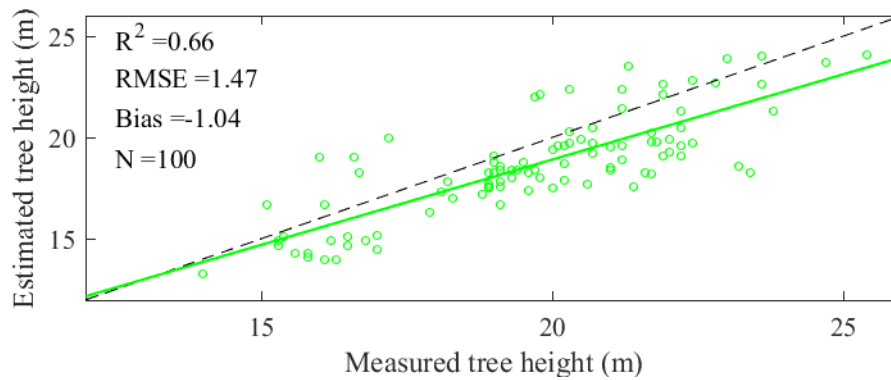
Figure 6-4. Tree heights estimated from a UAV-derived Canopy Height Model (CHM) are validated against ground measured tree heights (hypsometer + transponder), across six woodland plots. The dashed line represents the 1:1 line and the solid line a linear regression model.

Tree heights derived from the UAV CHM were underestimated by ~1 m (Figure 6-4), with taller trees contributing the most for this tendency, as indicated by the negative slope of the linear equation. This underestimation could be due to the spatial smoothing applied on the original CHM, as it tends to flatten the CHM surface. Generally, tree heights could be estimated from the UAV CHM with an uncertainty of ~1.5 m, as given by the RMSE value (Figure 6-4).

Decreasing image resolution, in general, increased delineation error (Figure 6-5), agreeing with Pouliot *et al.* (2002). An exception was detected with Oak trees, which could be due to their larger crowns (diameter of ~8 m). In this case, the spatial degradation can smooth out large gaps within a tree crown, reducing over-segmentation. The highest spatial resolution data (10 cm) was therefore used for the automatic tree crown delineation.

A last check evaluated to what extent automatic and manual tree crown delineation influence phenological metrics estimation. The average SOS date estimated from the automatic delineated crowns (126±10 days) was remarkably similar to the reference one (127±10 days) (Figure 6-6). A similar tendency was found for MOS (142±9 days for reference and 141±9 days for automatic) and EOS (155 ±13 days for reference and 155 ±13 days for automatic). This indicates that, despite an overall automatic delineation accuracy of 63% (Table 6-3), the automatic delineation method is as accurate as the manual delineation to detect the overall canopy phenology of this woodland.
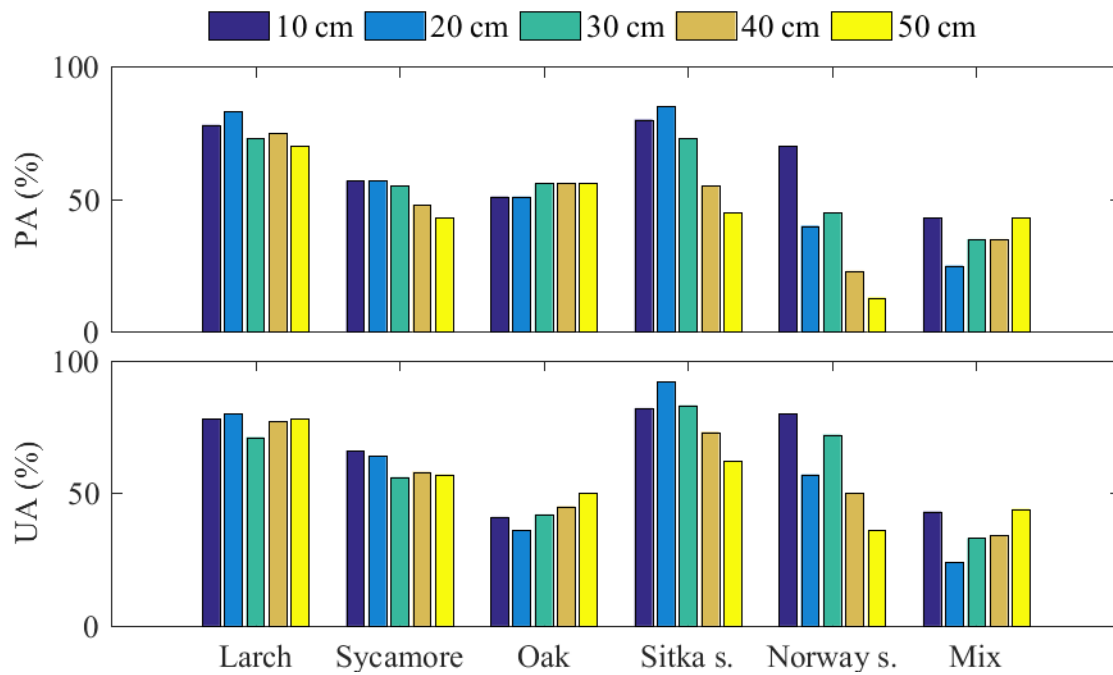
Figure 6-5. Effects of spatial resolution degradation (UAV-derived CHM and orthomosaics) in the Producer`s (PA) and User`s (UA) accuracy assessment of tree crown delineation across six different test sites. 40 reference tree crowns were considered in each test site.
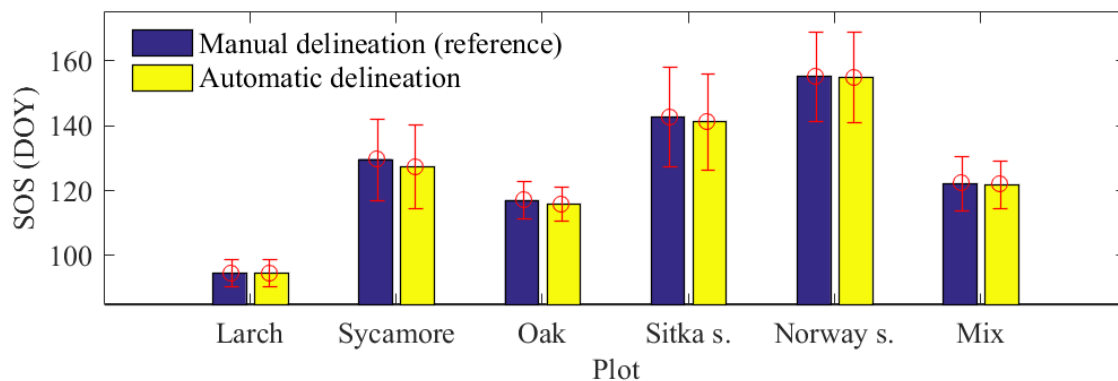
Figure 6-6. Individual tree-level prediction of SOS using as region of interest either manually or automatically delineated tree crowns. Each bar represents the average SOS date (± 1 standard deviation) as calculated from the reference and estimated crowns (Table 6-2). Predictions are based on UAV GCC$_{DN}$ (80th percentile) fitted by the greendown model.

6.3.2 Comparing UAV- and Landsat-based VIs time series

The general comparison between UAV and Landsat VIs time series (Landsat pixel scale, i.e., 30 x 30 m) considered the whole (Figure 6-7) and only deciduous (Figure 6-8) areas. UAV and Landsat VIs relationships are significant in all cases, but with various degrees of correspondence dependent on the pair of VIs ($0.45 \leq R^2 \leq 0.92$), indicating that the different VIs are detecting different land surface dynamics. This is somewhat expected as different VIs have different sensitivities in discriminating vegetation dynamics (Huete *et al.*, 2002).

Among the pairs compared (Figure 6-7, Figure 6-8), UAV $NDVI_{C0}$ has the best overall agreement with Landsat NDVI. While UAV NDVI vs Landsat NDVI and UAV GCC_{DN} vs Landsat GCC_L have slightly better R^2 values than with UAV $NDVI_{C0}$ vs Landsat NDVI, UAV $NDVI_{C0}$ is better distributed around the one-to-one line, resulting in lower bias values (Figure 6-7, Figure 6-8). This suggests that Landsat NDVI values can be better predicted by UAV $NDVI_{C0}$, confirming the quality of the adjusted NDVI ($NDVI_{C0}$), as showed in Chapter 4.

There are substantial improvements in the relationships when evergreen trees are excluded from the analysis, especially between Landsat NDVI and UAV VIs ($R^2 \geq 0.9$; Figure 6-8 d,e,f). The deciduous-restricted comparison also reveals data gaps within the range of VI values (Figure 6-8). This reflects the effect of temporal gaps in the Landsat VI time series, as only poor quality Landsat scenes were available from DOY 114 to DOY 161 (24th April to 10th June, 2015), a critical period of deciduous vegetation green-up.
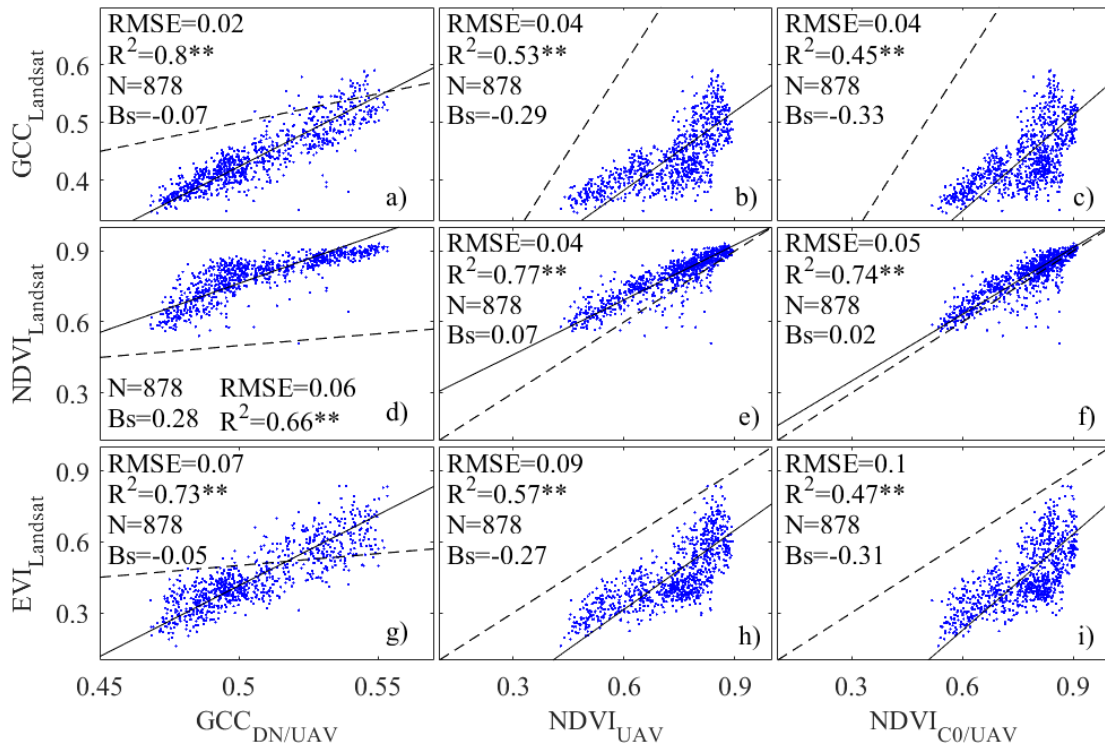
Figure 6-7. Comparison between UAV- and Landsat-based VI time series, at a Landsat pixel scale, considering the whole woodland. UAV VIs are based on the mean of the whole polygon (Landsat grid). Dashed lines represent the 1:1 line and solid lines are reduced major axis (RMA) regression models (**$p<0.001$; *$p<0.05$; *N* is sample size).
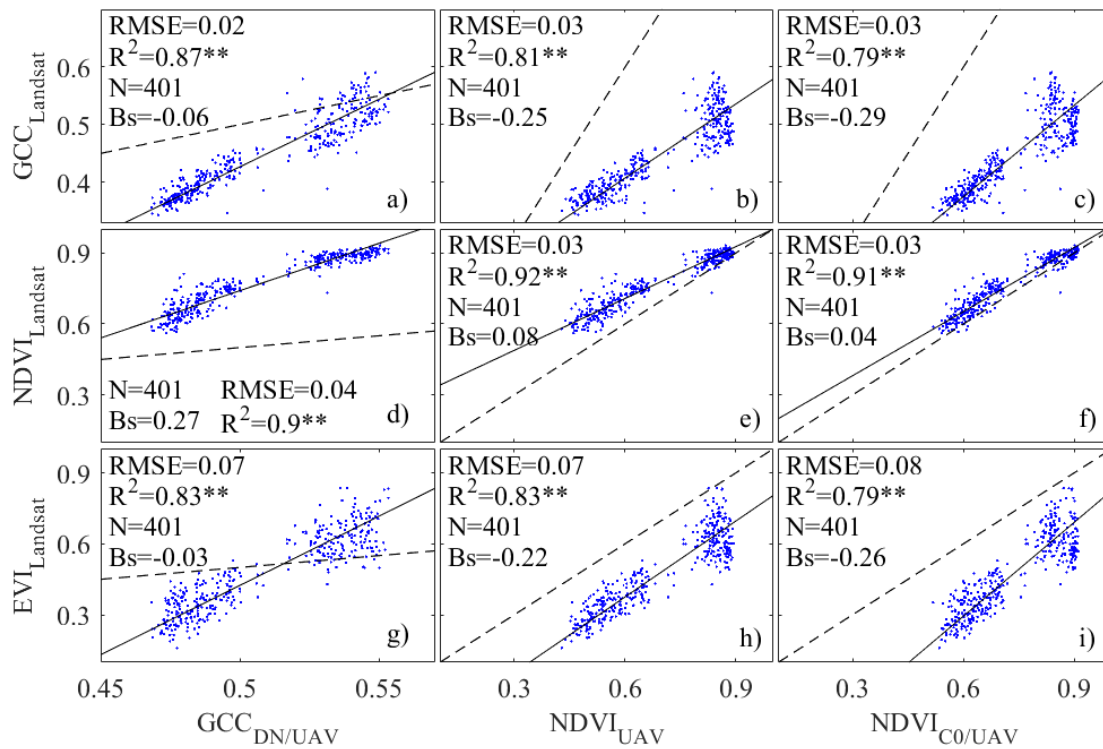
Figure 6-8. Comparison between UAV- and Landsat-based VI time series, at a Landsat pixel scale, considering deciduous areas only. UAV VIs are based on the mean of the whole polygon (Landsat grid). Dashed lines represent the 1:1 line and solid lines are reduced major axis (RMA) regression models (**$p<0.001$; *$p<0.05$; N is sample size).

6.3.3 Individual tree-level phenology of a small woodland

Analysis of boxplots (Figure 6-10) and visual inspection of the date of onset from the UAV-derived map (Figure 6-11a) show substantial intra- and inter-specific variability in individual-tree level leaf phenology across a 15 ha woodland (middle and end of spring season maps can be seen in Appendix A; the limits of the land covers used as region of interest to calculate boxplot statistics can be seen in Appendix B). Larch trees leafed out consistently earlier than the others species (Figure 6-10), as also shown by the blue tones in the eastern part of the woodland (Figure 6-11a), and present the least intra-specific variation in SOS dates. The Larch cover has a significant number of outliers (Figure 6-10) which is likely due to the presence of Sitka spruce trees within the defined limit of this land cover (as Sitka spruce leafed out later than Larch). The temporal profiles of selected adjacent individual trees where there is large variation in SOS confirms this inference (Figure 6-9); a significant increase in the GCC values of the evergreen Sitka spruce trees, and consequent detection of SOS, occurred ~80 days later than with Larch individuals (Figure 6-9), explaining therefore the contrasting blue and red tones of adjacent trees in the southern area near the Sycamore plot (Figure 6-11a).
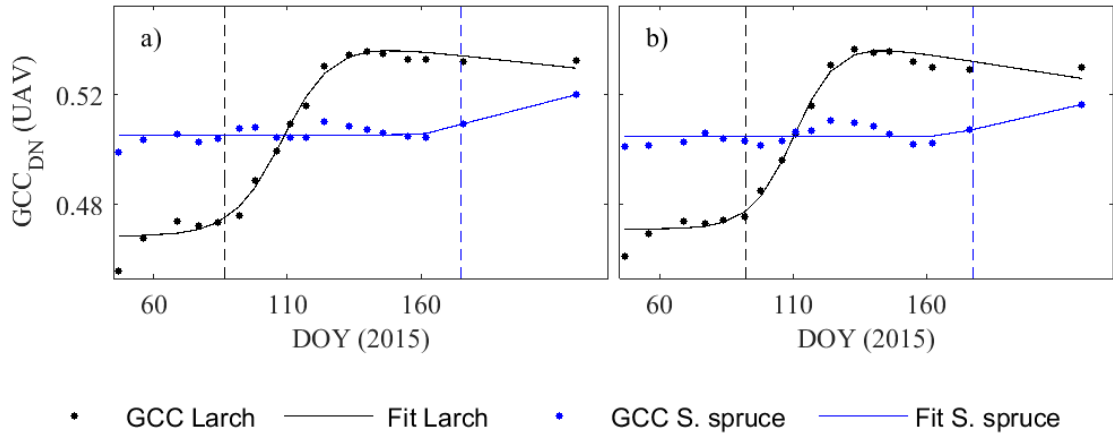
Figure 6-9. Example phenology curves of adjacent individual trees with very different SOS dates (marked by the vertical lines).

At the other extreme, later onset dates consistently occurred in the Norway spruce compartment, as quantified in Figure 6-10 and showed by the yellow-red tones in Figure 6-11a. Intermediate dates of SOS occurred with the deciduous broadleaf species (as sampled in the Sycamore, Oak and Mix plots). Sitka spruce started the growing season, in general, after the broadleaf deciduous but before Norway spruce. These spatio-temporal patterns of onset dates show a correlation with tree species communities, matching the chronological order of visually assessed leaf phenology events within the six plots (Chapter 5). This shows the potential of such products for mapping tree species distribution.
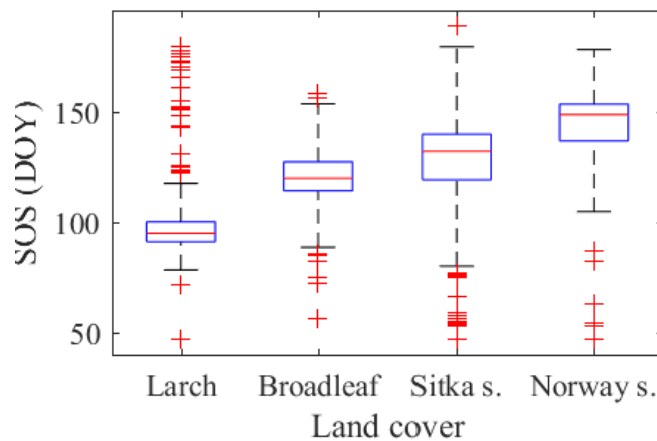
Figure 6-10. Boxplots of SOS dates of individual trees ($n = 4354$), as mapped in Figure 6-11. For each boxplot, the central mark represents the median, the edges of the box are the 25th and 75th percentiles, the whiskers extend to the most extreme data points not considered outliers (<2 times the standard deviation). Broadleaf encompasses the Sycamore, Oak and Mix plots.

Across the Sitka spruce area, a considerable number of trees have no SOS estimates (as shown by the red coloured tones in Figure 6-11a). This could be due to the defoliation caused by the aphid outbreak (as mentioned in the plot level analysis, Chapter 5), which may have attacked some trees more severely, impeding needle unfolding and consequently limiting greening up and significant increases of UAV GCC_{DN} values. In such a case, the resulting GCC_{DN} time series was observed to have either no seasonal pattern and the sigmoid model failed to converge or a significant rate of change occurring only when the GCC_{DN} trend decreased due to the defoliation in summer (as the decrease rather than an expected increase was detected as the SOS date). The estimated SOS was therefore considered a failure because the resulting SOS date does not represent the natural phenomenon of SOS. Also, the majority of individual trees with the highest uncertainties in SOS dates were detected within the Sitka spruce land cover, which is likely due to this weak seasonal response (Figure 6-12). Infestations or diseases can change the forest structure and photosynthetic capacity over time (Fisher *et al.*, 2006; Wilkinson *et al.*, 2012; Mizunuma *et al.*, 2013; Moore *et al.*, 2016), resulting in unexpected derived phenometrics. This fact and the presence of other tree species within the defined Sitka spruce land cover area (e.g. Larch, which has earlier leaf out) resulted in the highest variability in SOS dates across this area (Figure 6-10).
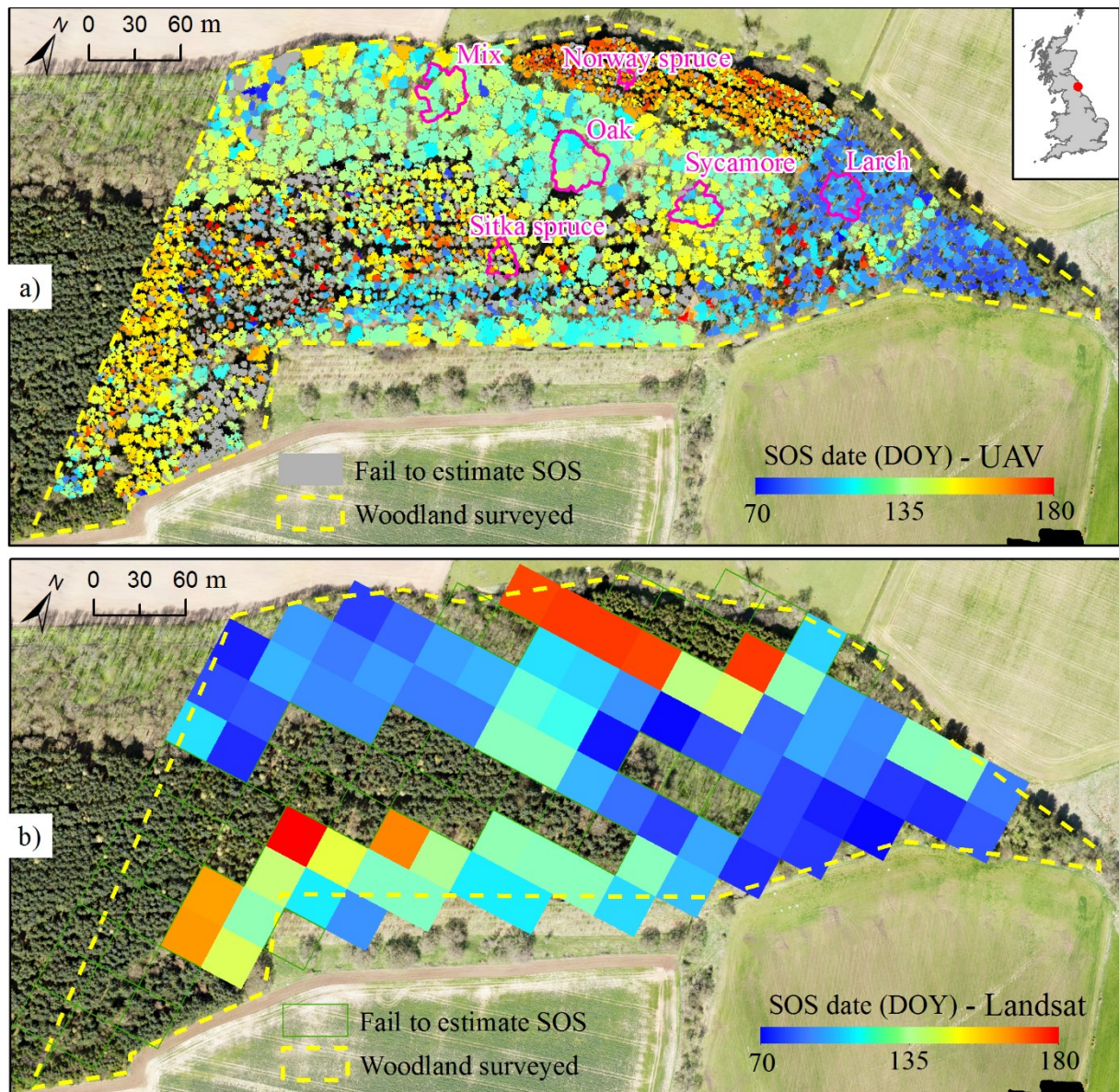
Figure 6-11. a) Individual tree-level prediction of SOS using UAV GCC_{DN} (80th percentile; fitted by the greendown model), and b) pixel-level prediction of SOS using Landsat NDVI (fitted by the simple model). Cooler colours indicate earlier onset and leaf-out, warmer colours are later onset and canopy development. The six ground validation plots contain 20 trees each and give an idea of the tree species spatial distribution. Background orthomosaic made of UAV images (visible camera) acquired on 21/04/2015 (DOY 111).
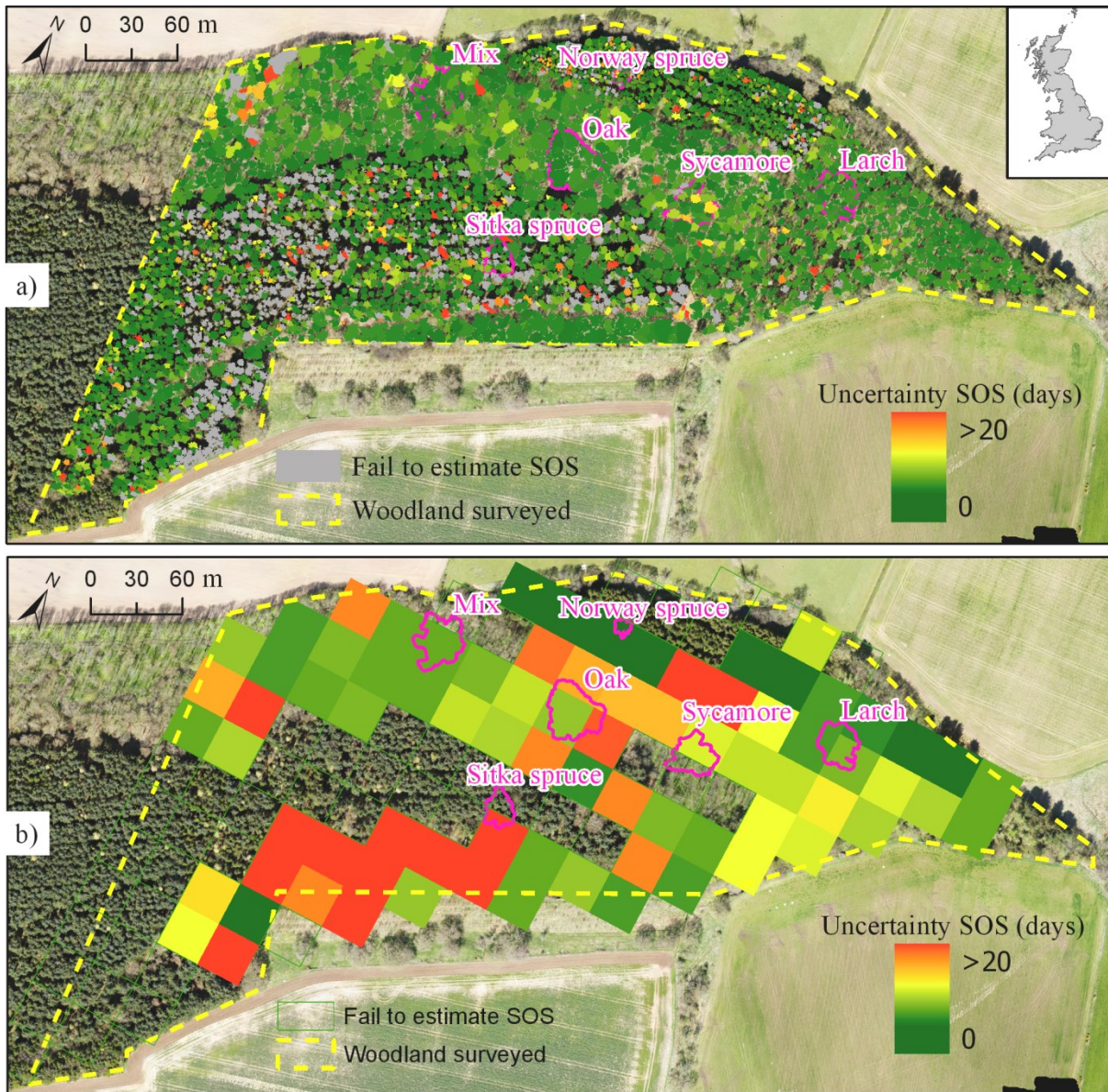
Figure 6-12. a) Uncertainty in the individual tree-level prediction of SOS using UAV GCC$_{DN}$ (80th percentile; fitted by the greendown model), and b) uncertainty in the pixel-level prediction of SOS using Landsat NDVI (fitted by the simple model). Uncertainty is calculated as the average width of inner 95% confidence intervals for each phenology date based on 100 replications. The six ground validation plots contain 20 trees each and give an idea of the tree species spatial distribution. Background orthomosaic made of UAV images (visible camera) acquired on 21/04/2015 (DOY 111).

A SOS map was also generated based on Landsat NDVI time series (Figure 6-11b) (MOS and EOS maps can be seen in Appendix A). Despite species-related patterns being less clearly depicted (in comparison to the UAV individual tree-level map), some broader inferences can be drawn. Visual assessments (Chapter 5) and the UAV SOS map (Figure 6-11a) showed Larch as the first tree species to start the spring season, a dynamic which was not observed on the Landsat SOS map (Figure 6-11b). Instead, areas in and around the

Sycamore and Mix plots had the earliest SOS dates, which could be due to the early understorey development, as noticed in the plot-level analysis (Chapter 5). Either very late or no SOS estimate were, generally, observed over the Sitka spruce area, which can be due to the combined effects of weak seasonal signal and the aphid outbreak (Chapter 5), which in turn resulted in highly uncertain SOS estimates (Figure 6-12b). Landsat pixels intersecting Oak and Larch plots seem to reproduce more closely the phenology patterns observed at a leaf/canopy level. Unrealistic SOS dates were predicted to have occurred after DOY 250 (7th September, 2015) for some pixels in the northeast and southwest part of the woodland; these pixels were assigned to the class "Failure to estimate SOS" as they do not represent the biological event of SOS (Figure 6-11b). This is probably due to spectral influence coming from the crop fields bordering the woodland, as investigation of the spectral profiles revealed that border and crop pixels had similar temporal dynamics (Figure 6-13). Crop fields can have sharp phenological changes, in relation to natural vegetation, due to its relatively short life span (Zhang *et al.*, 2017).
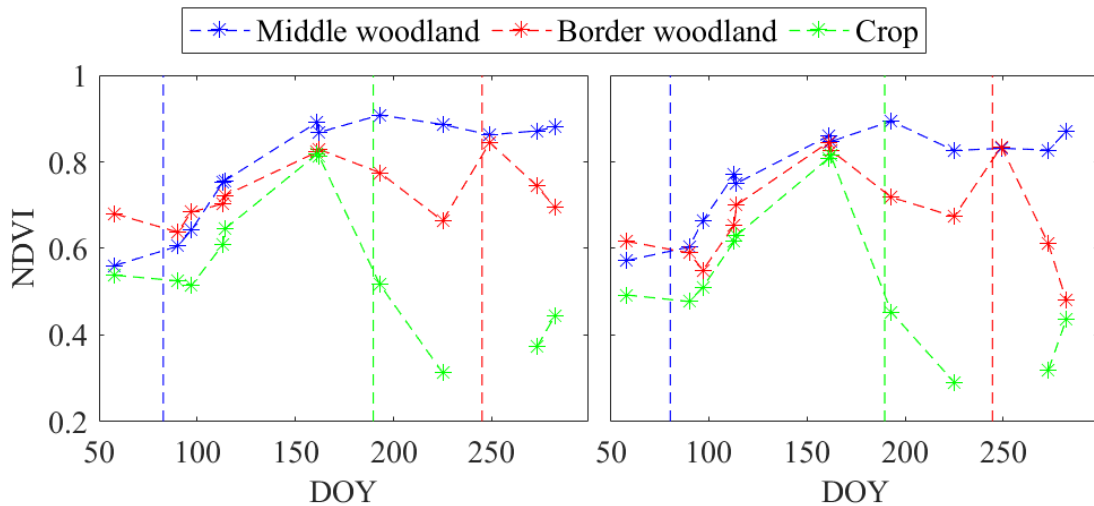
Figure 6-13. Time series of Landsat NDVI. Each graph is composed of three adjacent Landsat pixels located in the middle of the woodland (Larch land cover), border of the woodland and crop field. SOS dates for each spectral curve are marked by vertical lines.

Linking/comparing such integrated landscape processes (Figure 6-11b) with fine detail information (Figure 6-11a) can therefore be challenging. The high degree of variability in canopy phenology at small spatial scales mapped in the study area (Figure 6-11a) resulted in distinct differences in estimates of spring transition dates between UAV and Landsat data (Figure 6-14) (comparisons with Landsat EVI and Landsat GCC produced similar results, which can be seen in Appendix D). Large temporal gradients of individual tree-level leaf phenology occurred within Landsat pixel areas across the woodland (RMSE≤36 days; Figure

6-14g,i,k), resulting in poor or no correlation between UAV and Landsat phenometrics ($R^2 \leq 0.1$), even after mixed (evergreen + deciduous) and evergreen land covers were masked out ($R^2 \leq 0.04$; Figure 6-14a,c,e). While this analysis illustrates very well the variability in tree leaf phenology occurring within Landsat pixels (left column, Figure 6-14), the comparison can be misleading due the different scales the two data sets are compared, i.e., one tree canopy against one Landsat pixel.

UAV tree-level phenometrics were therefore averaged (crown weighted) to match the Landsat scale (right column, Figure 6-14), but this resulted in only slight improvements in the relationships ($0.01 \leq R^2 \leq 0.11$). This suggests that the average phenology of the dominant canopies (as mapped by UAV data) may lag considerably from the Landsat land surface phenology (LSP), as also detected at the plot-level analysis (Chapter 5). Furthermore, it was particularly challenging to relate UAV and Landsat phenology over areas with evergreen forests, where uncertainties (RMSE) reached over one month (Figure 6-14h,j,l).
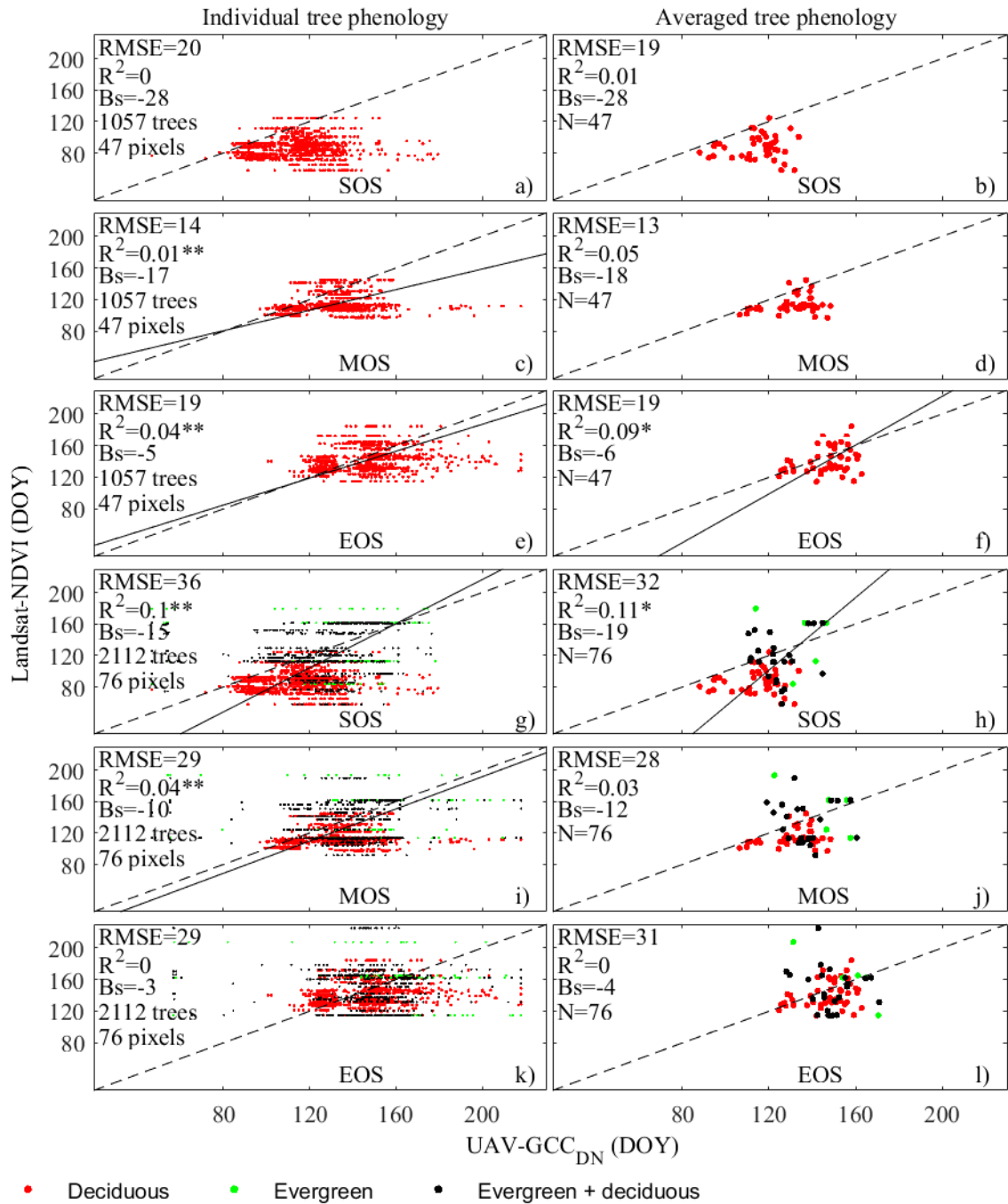
Figure 6-14. Landsat land surface phenology (simple model) compared with UAV-derived tree-level phenology (greendown model), considering every tree as a data point (left column) and averaged tree leaf phenology (right column). Pure deciduous covers are shown separately (a-f). The greendown model was fitted to the remote sensing data. Bias (Bs) is calculated relative to UAV, so a negative bias indicates that the corresponding Landsat estimate is earlier. Dashed lines represent the 1:1 line and solid lines are reduced major axis (RMA) regression models. Statistics are given (**$p<0.001$; *$p<0.05$).

In a final analysis, UAV orthomosaic DNs were aggregated up to the Landsat scale (i.e., the region of interest was the entire Landsat pixel area rather than just tree crowns), where phenometric cross-comparisons could be expected to produce better agreements since

the UAV data set is now related (explicitly) to land surface phenology (Figure 6-15, Figure 6-16, Figure 6-17). UAV NDVI and UAV $NDVI_{C0}$ are included in this analysis, as consistent time series could be calculated from these VIs at a 30 m spatial scale (Figure 6-7, Figure 6-8, Chapter 4), but not at a tree level (Chapter 5). Therefore, UAV phenodates from three VIs (GCC_{DN}, NDVI and $NDVI_{C0}$) are compared with Landsat dates from GCC, EVI and NDVI time series.

Distinct differences in the phenological events predicted by the different UAV and Landsat VIs are clearly evident (Figure 6-15, Figure 6-16, Figure 6-17), with UAV data explaining less than 50% of the variability in Landsat-based estimates of spring transition dates in any of the comparison cases. Compared to the deciduous averaged tree-level phenology (R^2 of 0.01, 0.05 and 0.09 for SOS, MOS and EOS, respectively; Figure 6-14b,d,f), statistical measures were, generally, stronger for SOS ($0 \leq R^2 \leq 0.50$) and MOS ($0 \leq R^2 \leq 0.34$), but weaker for EOS ($0 \leq R^2 \leq 0.23$) (considering deciduous covers only; Figure 6-15, Figure 6-16 and Figure 6-17).

Spatial patterns of phenology dates estimated from the spectral index UAV $NDVI_{C0}$ matched more closely the Landsat NDVI metrics ($0.03 \leq R^2 \leq 0.25$; Figure 6-15c,f,i), mirroring the VI time series comparisons (Figure 6-7, Figure 6-8). Among the three phenometrics derived from UAV $NDVI_{C0}$ and Landsat NDVI, the mid-spring mark (MOS) returned the best match (RMSE=10 days; Figure 6-15f) and EOS the highest uncertainty (RMSE=20 days; Figure 6-15i). Therefore, these findings suggest that less uncertainty in the validation of satellite phenology products can be achieved if reference and satellite data are similar. Regarding Landsat NDVI and EVI, UAV GCC_{DN} best matched both Landsat EVI ($0.0 \leq R^2 \leq 0.2$; Figure 6-16a,d,g) and Landsat NDVI ($0.02 \leq R^2 \leq 0.50$; Figure 6-17a,d,g), also agreeing with the VI time series comparisons, but the uncertainties were higher ($4 \leq RMSE \leq 16$ days) than Landsat NDVI vs UAV $NDVI_{C0}$ comparisons.
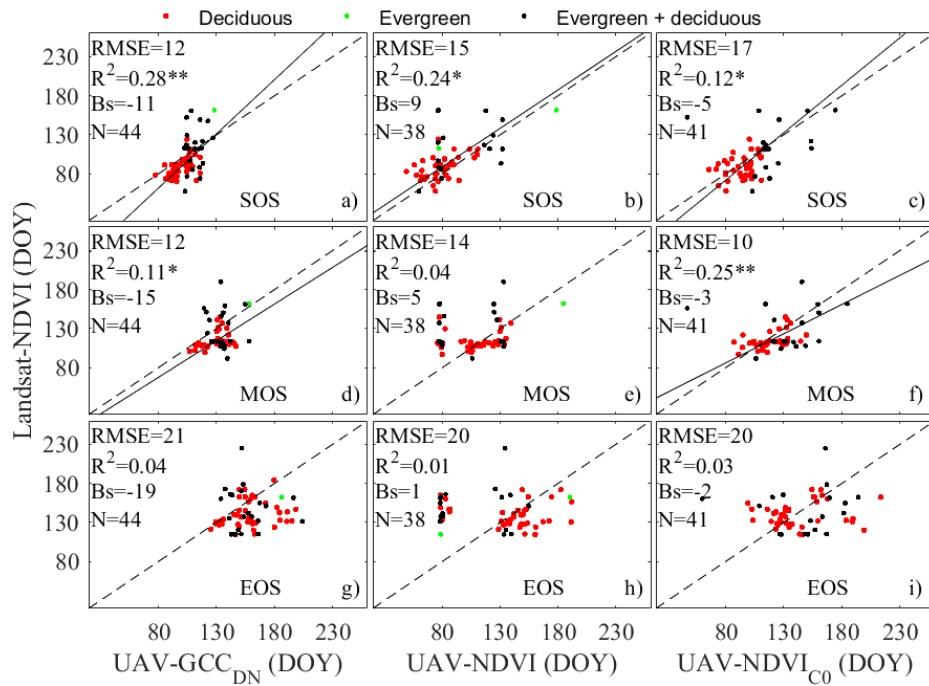
Figure 6-15. Scatterplots of the comparison between UAV and Landsat estimated phenodates. 'Evergreen' and 'Evergreen + deciduous' are shown but not taken into account for the statistics calculation. The UAV indices were based on the mean of the whole polygon (Landsat grid) for this comparison. Bias (Bs) is calculated relative to UAV. Dashed lines represent the 1:1 line and solid lines are reduced major axis (RMA) regression models. **$p<0.001$. *$p<0.05$.
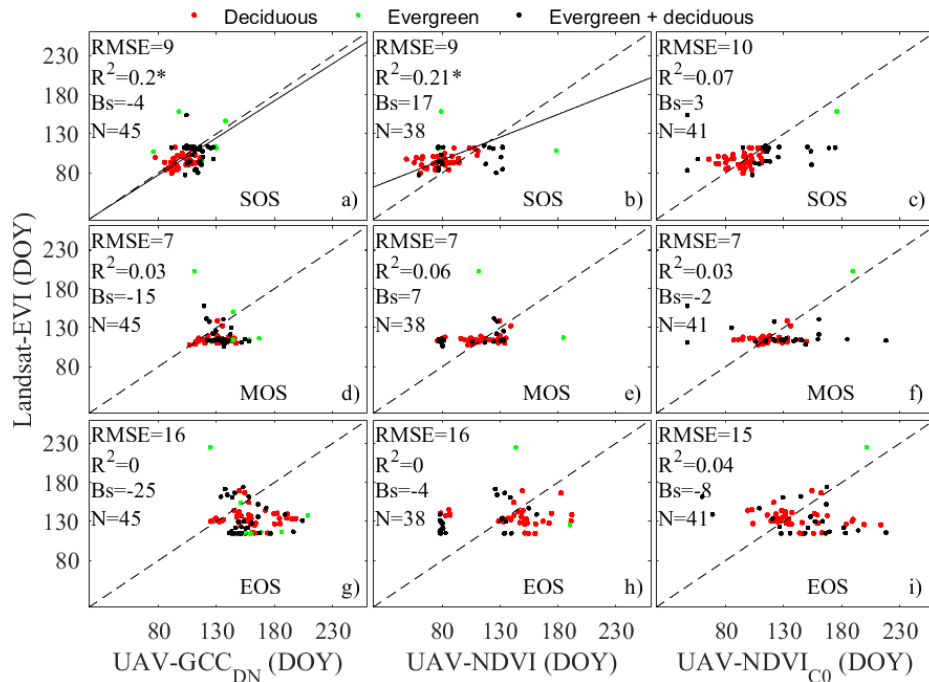

Figure 6-16. Scatterplots of the comparison between UAV and Landsat estimated phenodates. 'Evergreen' and 'Evergreen + deciduous' are shown but not taken into account for the statistics calculation. The UAV indices were based on the mean of the whole polygon (Landsat grid) for this comparison. Bias (Bs) is calculated relative to UAV. Dashed lines represent the 1:1 line and solid lines are reduced major axis (RMA) regression models. **$p<0.001$. *$p<0.05$.
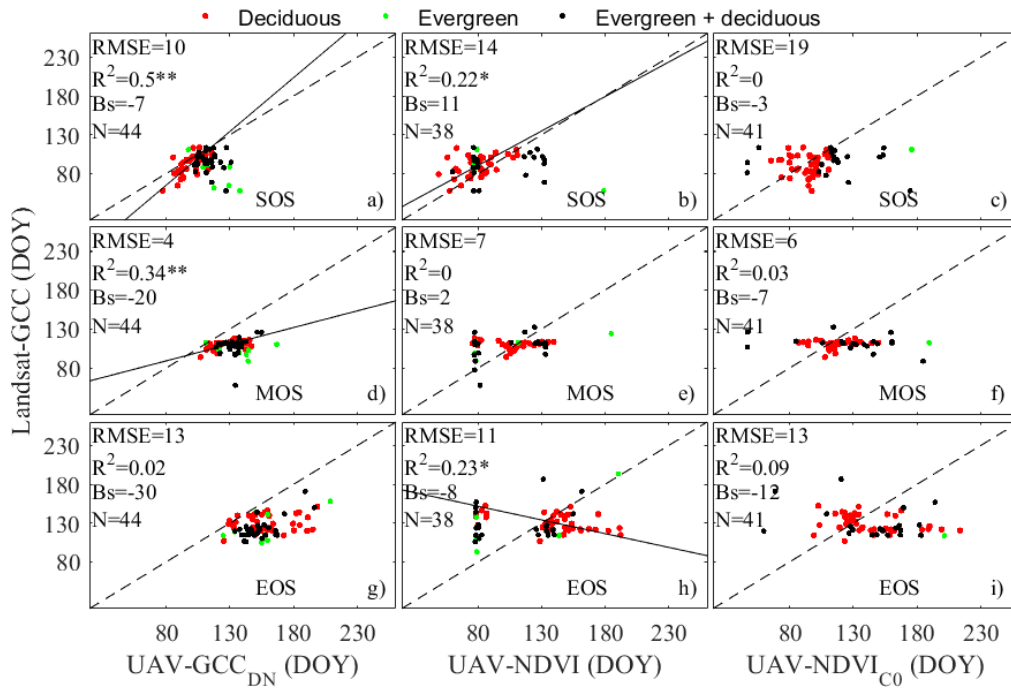
Figure 6-17. Scatterplots of the comparison between UAV and Landsat estimated phenodates. 'Evergreen' and 'Evergreen + deciduous' are shown but not taken into account for the statistics calculation. The UAV indices were based on the mean of the whole polygon (Landsat grid) for this comparison. Bias (Bs) is calculated relative to UAV. Dashed lines represent the 1:1 line and solid lines are reduced major axis (RMA) regression models. **$p<0.001$. *$p<0.05$.

Despite the poor or moderate correlations found between UAV and Landsat phenometrics, a few general inferences can be drawn from the cross-comparisons:

- Among the three phenometrics, EOS returned, generally, the poorest matches (average $R^2=0.07$), with no significant relationships in eight out of nine comparison cases (Figure 6-15, Figure 6-16, Figure 6-17).

- There is a better agreement when MOS dates (average RMSE = 12 days) are considered rather than SOS (average RMSE = 18 days) or EOS (average RMSE = 21 days) (Figure 6-15, Figure 6-16, Figure 6-17).

- Evergreen areas add significant uncertainty in phenological date predictions. Following exclusion of evergreen covers, the average RMSE improved from 30 to 16 days in the UAV canopy vs Landsat comparison (Figure 6-14, right column); at a Landsat scale comparison (Figure 6-15, Figure 6-16, Figure 6-17), the average RMSE of MOS estimates, for example, improved from 42 days to 12 days.

- Spatial averaging (or aggregation) of UAV data tends to improve the agreements with Landsat derived phenology, but significant discrepancies remain.

162

6.4 Discussion

6.4.1 Automatic tree crown delineation

Tree crowns were automatically delineated from high resolution photogrammetric point clouds, alongside orthomosaic spectral information from UAV data, allowing tree-level phenometrics estimation across the entire extent of the aerial survey. Because the upper canopy is usually brighter than the background cover, the spectral information showed to be particularly useful to eliminate those watershed areas do not belonging to tree crowns (i.e., darkest areas), therefore improving the crown`s limits detection. The delineation accuracy found in this research (40-80%) is within the range reported in the literature (Lim *et al.*, 2015; Li *et al.*, 2016; Panagiotidis *et al.*, 2016; Thiel and Schmullius, 2016) and once more indicates that complex forest structures (as in the Oak and Mix plots in this study) are challenging environments for automatic extraction of tree attributes (Duncanson *et al.*, 2014). Future studies in this research field, could take advantage of the high temporal and spatial resolution of UAV imageries to iteratively improve the delineation accuracy by exploiting the phenological variability of individual plants growing adjacent to each other.

The uncertainties of this watershed-based method proved to be not significant for monitoring the overall canopy phenology of the sampled plots, as SOS dates estimated from manually and automatically delineated crowns differed by only one day (Figure 6-6). Nevertheless, consideration is needed regarding the possible effects for individual tree-level phenology estimates more generally. Trees with multiple segments (over-segmentation) will be considered multiple trees, but the multiple segments should return very similar estimates of phenological events dates (assuming budburst occurs evenly within a same crown). On the other hand, trees clustered under one segment (under-segmentation) will be treated as a single tree and the estimated phenological events should: 1) reproduce the average behavior of the cluster, if the individuals start the growing season on similar dates, or 2) if the clustered trees leaf out on very different dates, the estimated start of spring date may be more closely associated with the first tree to leaf out within the cluster (especially if selecting the brightest pixels from within a region of interest, as the 80th percentile approach).

The latter case may have implications on estimating phenological behavior at large scales. For example, if phenological event dates of such clusters are aggregated up to a moderate/coarse spatial resolution satellite pixel area, the UAV-derived canopy phenology may be biased earlier, i.e. the aggregated leaf out date will be estimated earlier in the year.

6.4.2 Mapping individual tree level phenology across continuous areas

Studies using remote sensing to monitor phenology have used, until now, medium to coarse resolution imagery from sensors such as Landsat, MODIS, AVHRR and SPOT-Vegetation, which allow regional to global patterns to be observed but cannot resolve spcecies-scale seasonal dynamics (Fisher and Mustard, 2007; White *et al.*, 2009; Miao *et al.*, 2013; Melaas *et al.*, 2016). In this study, an effective approach for mapping phenology of overstorey vegetation at a detailed biological scale and across local spatial extents was proposed by using time series of UAV remotely sensed data.

Phenological maps of individual trees, such as the ones generated across the 15 ha woodland in this study, represent a powerful tool to visually represent spatio-temporal patterns in canopy phenology. Such georeferenced information potentially brings the opportunity to track the phenological behaviour of all individual trees in the upper canopy (dependent upon a robust automatic tree crown delineation approach), and can aid in understanding processes occurring at very fine scales.

An individual-tree SOS map clearly showed the spatio-temporal patterns in leaf phenology of this woodland, demonstrating how contrasting canopy phenological events can be within Landsat pixels. Therefore, heterogeneity in canopy phenology can still be an issue even at the spatial resolution scale of Landsat, agreeing with other studies (Fisher *et al.*, 2006; Liu *et al.*, 2017). This demonstrates that caution should be taken when using Landsat to understand coarser spatial resolution LSP, based on the assumption that the vegetation phenology within the 30 m scale would be relatively homogeneous (Fisher and Mustard, 2007; Liu *et al.*, 2017).

It is somewhat surprising that the UAV data was able to only explain <50% of the variation in phenodates estimated by the Landsat sensors, as the phenology of (theoretically) every tree within a Landsat pixel was detected by the UAV data. Previous studies have indicated that if the validation dataset is able to account for the spatial heterogeneity in timing of phenological events and heterogeneity in species composition within a pixel area, then low uncertainties in the estimated phenodates could be expected (Liang *et al.*, 2011; Liu *et al.*, 2015). However, a close analysis to the two datasets indicates that several causes may have contributed for the pronounced differences between UAV and Landsat phenology.

6.4.3 Sources of uncertainties on UAV vs Landsat phenometric comparisons

The plant functional types present (e.g., deciduous forest, evergreen forest, grassland) notably influence the ability of VIs to be used in monitoring spring phenology (Wu *et al.*, 2017). Evergreen areas, or areas with a low fraction of deciduous coverage, can add significant uncertainty in phenological predictions from orbital sensors (Hmimina *et al.*, 2013; Klosterman *et al.*, 2014). In this study area, the inclusion of evergreen areas in the UAV vs Landsat comparisons of phenodates increased RMSE values to over 1 month, dependent upon the metric analysed (Figure 6-14). This could be explained by the subtle seasonal signal produced by evergreen covers, which may not be detected by the Landsat sensors, therefore hampering time series fitting and predictions. In addition, as discussed in Chapter 5, a severe pest attack caused defoliation over the largest evergreen stand (Sitka spruce), decreasing even more the signal amplitude of this land cover and making it challenging to detect even with UAV sensors. Finally, it is inferred that seasonal changes in leaf pigmentation (chlorophyll content) of existing needles may be driving the temporal pattern depicted by VIs of conifer forests rather than the appearance of new needles and shed of old ones (Richardson *et al.*, 2009; Sonnentag *et al.*, 2012; Toomey *et al.*, 2015).

Spatial misalignment of the different remote sensing data sets and the measurements derived from them may also be a contributing factor (Xin *et al.*, 2013). While UAV orthomosaics are georeferenced with a decimeter accuracy, Landsat products (Level 1T) are expected to have a planimetric accuracy of ~12 m (Storey *et al.*, 2014). Therefore, comparing a Landsat pixel with the same area of an UAV orthomosaic, one can expect misregistration inconsistencies. Moreover, a cubic convolution resampling is applied when generating Level 1 products (USGS, 2016b), meaning that the spectral information of a Landsat pixel is influenced by its neighbours pixels.

Different temporal resolutions between UAV and Landsat datasets could also add uncertainty. The frequency of high-quality satellite observations can have substantial impact on phenological detections during periods of phenological changes (Fisher *et al.*, 2006; Zhang *et al.*, 2009; Zhang, 2015; Baumann *et al.*, 2017; Zhang *et al.*, 2017), which could bias estimated spring onset by over one week dependent upon configurations of image availability (Melaas *et al.*, 2013; White *et al.*, 2014). In this research, because the study site is located in a Landsat path overlap zone, it is theoretically possible to have one cloud-free image every 7-9 days. However, only 7-9 good quality images remained after a quality check, unevenly distributed in time and with a temporal gap of 47 days from 24th April to 10th June, 2015, a

key period of vegetation green-up. On the other hand, a consistent temporal resolution of around one observation per week was achieved with the UAV.

Temporal asynchronies between canopy leaf phenology and land surface phenology (LSP) can result in very different VI dynamics, affecting mainly SOS estimates (Liu *et al.*, 2017). Landsat LSP detected the start of season consistently earlier (29 days) than the weighted average canopy SOS of deciduous trees detected by the UAV (Figure 6-14), mirroring comparisons between orbital and ground phenology (Fisher *et al.*, 2006; Soudani *et al.*, 2008; Hmimina *et al.*, 2013). Earlier understorey development could be the major driver of such LSP dynamic in the study area, as the majority of deciduous Landsat pixels fall over areas with evergreen grasses. These understorey species should be similar to the ones occurring in Sycamore and Mix plots, where ground photography detected earlier green-up (Chapter 5). Besides the influence of understorey development, a lack of VI observations during short periods straight after budburst may shift the modelled VI series to the left causing an earlier departure from the winter plateau (Hmimina *et al.*, 2013).

SOS dates detected by UAV and Landsat exhibited greater similarity when the UAV phenometrics referred explicitly to LSP, with various degrees of correspondence dependent upon the VIs used (Figure 6-15, Figure 6-16 and Figure 6-17). This will reflect the understorey contribution to the UAV observations, causing the UAV phenology curve to depart earlier from its winter plateau, as UAV data is now explicitly integrating land surface dynamics, similar to the Landsat sensors. Despite some improvements in the SOS comparisons at this scale (RMSE = 14 days, best scenario; Figure 6-15c), MOS seems to be the most comparable phenological transition date between UAV and Landsat (RMSE = 10 days, best scenario; Figure 6-15f).

Some studies have observed that the middle of spring season metric could be predicted with less uncertainties from orbital sensor data than start and end of season (Hufkens *et al.*, 2012; Hmimina *et al.*, 2013). It has been suggested that start and end of spring season are less robust to data gaps, as different temporal resolutions can alter substantially the steepness of the fitted curve, impacting especially the metrics close to the lower (e.g. SOS) and upper (e.g. EOS) asymptote and resulting in larger bias (Hufkens *et al.*, 2012; Hmimina *et al.*, 2013). Furthermore, the better agreement of MOS when comparing canopy phenology with LSP (RMSE = 13 days; Figure 6-14d) suggests that orbital sensors are more sensitive to overall canopy change rather than early stages of bud opening/leaf development, which is in agreement with other studies (Fisher and Mustard, 2007; Melaas *et al.*, 2013). Similar

conclusions were drawn from comparisons of carbon fluxes vs phenocam phenology (Toomey *et al.*, 2015) and *in situ* NDVI vs MODIS NDVI (Hmimina *et al.*, 2013). However, the ecological meaning of this metric (MOS), which represents around 50% of the spring amplitude, is unclear and so its utility may be limited (Hufkens *et al.*, 2012).

Comparison of transitions dates detected by the different VIs show that each VI retrieves different information associated with LSP dynamics, agreeing with Hufkens *et al.* (2012). In this study, the adjusted $NDVI_{C0}$ time series had a very close match with the Landsat NDVI time series ($R^2 = 0.91$; Figure 6-8f), which could explain the slightly better relationships between phenometrics derived from Landsat NDVI and UAV $NDVI_{C0}$. In terms of UAV GCC_{DN}, an index which is commonly available from phenocam networks (Brown *et al.*, 2016), none of the Landsat indices (GCC_L, NDVI and EVI) performed consistently better in all the three phenometrics comparisons (i.e., SOS, MOS and EOS). Despite previous studies have found EVI to be, generally, more appropriate than NDVI to track forest phenology (Liang *et al.*, 2011; Klosterman *et al.*, 2014; White *et al.*, 2014; D'Odorico *et al.*, 2015; Baumann *et al.*, 2017), it is difficult to be conclusive about the advantage of EVI in this study because of the poor/moderate relationships.

6.4.4 Potential of UAV data as a tool for ground validation

Measurements of individual tree or species-specific phenology that is so aptly captured in field surveys, but is lost in satellite pixel-based studies (White *et al.*, 2014), can potentially be achieved by sensors onboard a UAV. Contrary to field surveys which have to sample an ecosystem due to costs constrains or natural limitations, the approach proposed in this study offers the chance to measure all the trees within a small area, i.e., it is possible to census the plants phenological behaviour within this area. This could be useful for many ecological applications, such as tree species or plant communities mapping (Lisein *et al.*, 2015; Michez *et al.*, 2016) and predicting bird phenology (Cole *et al.*, 2015).

The UAV fine-scale information could be integrated spatially to investigate landscape phenology at systematically larger scales (up the UAV coverage extent), allowing broad patterns to emerge (Klosterman *et al.*, 2018). The different aggregated levels of phenology can facilitate a multi-scale investigation of seasonal patterns of vegetation and its relation with local processes. Besides supporting ecology-related studies, this has also applications in calibrating ecosystem measures as detected from ground/near-surface and orbital sensors.

Phenocams and eddy covariance measurements play a crucial role in helping to improve our understanding of local-scale phenology and can also be used to validate satellite observations. Nevertheless, there are some aspects of these ground/near-surface measurements that could be better understood by comparison with UAV time series data.

Despite the broad use of phenocams (Brown *et al.*, 2016), there are still uncertainties related to the effect of their oblique viewing angles on the temporal trajectory of canopy greenness (Keenan *et al.*, 2014). Furthermore, inclined phenocams can only monitor one side of a tree crown, each of which has a different sensor-target distance; this can impact on data quality as further targets will have weaker signals and stronger atmospheric influence (Richardson *et al.*, 2009). A UAV data set, preferably acquired using the same camera as the phenocam, could provide an insight into whether these issues have significant impacts on the phenocam-derived phenological signal. In addition, even though phenocams provide a means for direct comparisons with satellites phenometrics, the precise areal representativeness of the phenocam images is usually not known as they are not georeferenced; a defined ROI within a phenocam image is therefore assumed to represent the satellite pixel(s) area. The UAV georeferenced information could be used to investigate issues related to areal representativeness. The findings of such comparisons could have great impact for the many studies using phenocams, as efforts are being made towards a global phenocam network (Brown *et al.*, 2016).

When comparing near-surface remote sensing phenology to satellite phenology, there is an expected uncertainty due to the different view geometries from these sensors (Mizunuma *et al.*, 2013; Liu *et al.*, 2017). While satellite sensors have synoptic views (Landsat has nadir/near-nadir view (Liu *et al.*, 2017)), near-surface sensors are often close to the horizontal (e.g., more than 70° (Liu *et al.*, 2017)), which may result in near-surface sensors receiving a smaller contribution from the understorey vegetation (Hufkens *et al.*, 2012; Mizunuma *et al.*, 2013; Liu *et al.*, 2017). This different contribution may bring difficulties in linking LSP observations (Mizunuma *et al.*, 2013). This problem is minimized when using ground truth data from a UAV remote sensing platform, as the UAV orthomosaics are expected to be composed of nadir/near-nadir pixels (Chapter 4). In fact, very good relationships between UAV $NDVI_{C0}$ and Landsat NDVI were observed ($R^2 > 0.7$), especially over deciduous areas ($R^2 > 0.9$), mirroring *in situ* (radiometer) and MODIS NDVI comparisons ($R^2 = 0.92$) carried out by Hmimina *et al.* (2013). This should also reflect the fact that the UAV data used in this study offered the opportunity to match very precisely the area of the Landsat pixel.

One of the ultimate applications of UAV-derived phenology would be the validation of satellite LSP products at an appropriate spatiotemporal scale. Because the UAV-derived information is synoptic and georeferenced, comparisons with satellite can be done very precisely (unlike for other near-surface vs. orbital remote sensing comparisons), across areas (local scale) comparable with medium and moderate spatial resolution satellite pixels (e.g. Landsat, MODIS), removing the spatial scale representativeness issue (Zhang *et al.*, 2017). Furthermore, the ability to monitor species-specific phenology with UAVs could help in understanding the effects of the underlying spatial complexity and heterogeneity of the objects which might be present within the resolved satellite scene (White *et al.*, 2009). For example, the effects of the background cover, such as snow and understorey vegetation, which can bias and even hamper LSP transition date estimates (Delbart *et al.*, 2005; White *et al.*, 2009), could be better understood with UAV data, as this can allow tracking of canopy phenology, as opposed to ecosystem dynamics detected by satellites. This would provide new insights into the ecological and biophysical meaning of the spectral information within the satellite pixels.

The findings of this research support the use of UAV data for this application, as canopy spring phenology of individual trees were consistently detected across a 15 ha woodland (Figure 6-11). In addition, the 5 cm spatial resolution of the UAV imagery has allowed the effects of understorey cover into canopy phenological metric estimations to be investigated; ultimately, the brightest pixels within a tree crown diminishes uncertainties caused by understorey contribution (Figure 5-5, Chapter 5). Nevertheless, poor relationships were found between UAV- and Landsat-derived phenometrics in this study ($R^2 < 0.50$, section 6.3.3), indicating that there are remaining challenges to be addressed in order to better understand the potential of UAV data sets for satellite phenology validation purposes. One of the most important remaining questions is: How much of this unexplained variability is due to the different temporal resolutions of the two data sets (Landsat data had a 47 days temporal gap, section 6.3.2, Chapter 6)? Further studies are necessary to investigate whether the relationship between UAV- and Landsat-derived phenometrics would actually improve if the two data sets would have the same (or very similar) temporal resolution. Furthermore, the positional uncertainty of Landsat pixels (~12 m) was not taken into account when comparing with UAV products, which may have implications over areas with pronounced heterogeneity in timing of phenological events.

6.5 Conclusions

An effective approach for mapping phenology of overstorey vegetation at a detailed biological scale and across local spatial extents was proposed in this study by using time series of UAV remotely sensed data. An opportunity is now available to track very fine scale phenological changes over contiguous vegetation communities, information which could aid in further understanding of phenological triggers and biophysical processes of different plant functional types during the critical time of growing season onset.

This research has showed that UAV data has the potential to capture species-specific phenology, as opposed to the overall phenological dynamics recorded by orbital sensors. Nevertheless, satellites remain the only feasible tool for large and global scale monitoring of Earth dynamics (Liu *et al.*, 2017), so is important to continuously improve and refine our understating of LSP with aid of different multi-scale ground truth data.

Chapter 7. General discussion and conclusion

7.1 Introduction

The current absence of an intermediate scale of observation, between ground/near-surface and spaceborne level, in forest phenology studies was identified from the literature review (addressing **Objective 1**), setting the research gap to be pursued in this study. The aim of this research is to assess the potential of UAV data to track the temporal dynamics of spring phenology, from the individual tree to woodland scale, and to cross-compare UAV results against ground and satellite observations, in order to better understand characteristics of UAV data and assess potential for use in validation of satellite-derived phenology. To achieve this, UAV flights were carried out during the spring season of 2015, over Hanging Leaves Wood, Northumberland, UK, in tandem with an intensive ground campaign (photography of the understorey, photography of the overstorey and visual observations of canopy development) for validation purposes.

This chapter will discuss how the main findings of this research : 1) address the research aim and objectives; 2) contribute to the field of vegetation phenology research; and 3) can add value to other fields of knowledge related to phenology of vegetated surfaces. Potential applications of the methodology developed in this research in a broader context are presented, finishing with a discussion of the potential future of quantifying forest phenology.

7.2 Key Findings

Overall, the thesis has shown that:

1) Calibrated COTS cameras on-board a UAV can allow consistent time series of fine spatial resolution reflectance (under stable illumination conditions) and vegetation indices to be acquired, at user-controlled revisit periods (section 4.4, Chapter 4).

2) Although times series of NDVI could be retrieved with confidence at a 30 m Landsat scale (section 4.4.2, Chapter 4), GCC_{DN}, an index based on DNs from a single unmodified camera, proved to be advantageous at a tree crown scale (section 5.3, Chapter 5), as higher quality time series were retrieved and GCC_{DN}-estimated phenodates were consistently most closely associated with the visual assessments of spring canopy phenology.

3) Local-scale georeferenced measurements of individual tree spring phenology were consistently detected from UAV data over contiguous vegetation communities. The SOS metric could be predicted with an accuracy better than 1 week for deciduous canopies and within 2 weeks for evergreen canopies, compared to ground observations (section 5.3.5, Chapter 5).

4) Spatio-temporal variations in canopy phenology occurring below the pixel scale of the Landsat sensors could be consistently resolved, revealing how contrasting canopy phenology and land surface phenology can be, even over small spatial scales (sections 6.3.3 and 6.3.4, Chapter 6).

7.3 Summary of results

COTS cameras were used on-board the UAV and the radiometric quality of the UAV imagery was investigated to assess its ability to be used to retrieve reflectance and NDVI. To do so, the cameras spectral sensitivity and vignetting effect were determined, RAW images were linearly converted into TIFF format and image DNs were calibrated into reflectance using the empirical line method. The UAV products were successfully validated against ground ($0.84 \leq R^2 \geq 0.96$) and Landsat ($0.73 \leq R^2 \geq 0.89$) measurements (addressing **Objective 2**). In the case of reflectance, it was not possible to generate a fully consistent time series, due to variable illumination conditions during a number of acquisition dates. However, the calculation of $NDVI_{C0}$ (derived from calibration equations with intercept zero) resulted in a more stable UAV time series, which was consistent with a Landsat series of NDVI, extracted over a deciduous and evergreen woodland (**Key finding 1**). This consistency was confirmed when UAV $NDVI_{C0}$ and Landsat NDVI time series were compared across the entire woodland ($R^2 = 0.74$), with substantial improvements in the relationships when evergreen trees were excluded from the analysis ($R^2 = 0.91$) (section 6.3.2, Chapter 6).

The time series of UAV data were further used to detect SOS, MOS and EOS dates at an individual tree-level (addressing **Objective 3**). In general, UAV-derived SOS could be predicted more accurately than MOS and EOS, with an accuracy of less than 1 week for deciduous woodland and within 2 weeks for evergreen (**Key finding 3**). At an individual tree-level, the colour index GCC_{DN} resulted in a higher quality time series than $NDVI/NDVI_{C0}$, as

NDVI/NDVI$_{C0}$ combines spectral bands from two different cameras and any differences (for example, in illumination conditions) were found to be enhanced at the fine spatial scale of acquisition (**Key finding 2**). Analysis at the plot level compared the phenology derived from ground, UAV and Landsat data. The plot-averaged visual assessments of leaf development (SOS) had a close match with UAV SOS, but pronounced differences occurred with Landsat SOS dates. Evidence from understorey photography showed that asynchrony in timing of winter dormancy breaking between understorey and overstorey vegetation could be the main driver of such differences.

The UAV data were used to predict phenological events of individual trees across the whole woodland, following the implementation of an automatic tree crown delineation approach. An individual-tree SOS map clearly showed the spatio-temporal patterns in leaf phenology of the woodland (addressing **Objective 4**), demonstrating how contrasting canopy phenological events can occur within the extent of a single Landsat pixel (**Key finding 4**). This accounted for the poor relationships found between UAV- and Landsat-derived phenometrics (R^2<0.50) in this study (addressing **Objective 5**).

7.4 Implications of the key findings

Plant phenology is considered an interdisciplinary environmental science, as it brings together more than one branch of knowledge (e.g. ecology, climatology and remote sensing) in order to better understand the mechanisms behind the seasonality of vegetated land surfaces (Schwartz, 2013; Tang *et al.*, 2016). In this sense, the new perspective on phenology offered by the UAV-based approach presented in this research could find implications across these different disciplines. The fine-scale information offered by the UAV means that analysis and/or comparisons with other data sources can be done from the individual tree, to the plot and ecosystem level (up the UAV coverage extent).

7.4.1 Use of UAV data for vegetation phenology monitoring
The use of UAVs represents a novel way to monitor plant phenology, at an intermediate level of observation between ground/near-surface and orbital scales, in a synoptic and georeferenced fashion. Contrary to field surveys which have to sample a population due to time and costs constraints, the approach proposed in this study offers the chance to individually measure all the dominant trees within a small area (15 ha in this study),

i.e., it is possible to census the plants phenological behaviour within this area. This can provide a comprehensive insight into how the ecosystem is functioning, being useful for many ecological/phenological applications.

Intra- and inter-specific phenological differences across the contiguous landscape can be resolved, quantified and mapped (as long as species can also be identified and mapped, as discussed in section 7.5). Phenological maps of individual trees (as shown in Figure 6-10, Chapter 6) represent a powerful tool to visually represent spatio-temporal patterns in canopy phenology, in complement to quantitative analysis.

Combining the potential of UAV time series data to predict phenology at an individual tree-level, with the potential for mapping tree species distribution, can be useful to monitor possible changes on phenological patterns and species distribution across a forest due to climate change. The abundance and distribution of tree species may change with climate change (Walther *et al.*, 2002; Ray *et al.*, 2010; Polgar and Primack, 2013); some species may become better adapted to a different climate scenario, expanding their dominance at a community level, affecting the tree species sociological positions and ultimately shifting the phenology of the whole forest (Willis *et al.*, 2010; Fridley, 2012). This can have influence on water, carbon and energy cycles, as these ecosystem processes are tightly coupled with the vegetation seasonal activities. Furthermore, shifts in plant phenology and/or tree species abundance may affect ecosystem trophic interactions (Polgar and Primack, 2013; Cole *et al.*, 2015) and biodiversity (Rogers *et al.*, 2017). For example, some bird species synchronize their reproductive period with the appearance of specific larvae in order to assure abundance of food for the new offspring; such larvae hatch when new leaves of specific tree species appear in spring (Cole *et al.*, 2015). Therefore, if a mismatch between food abundance and breeding times occurs, the population of such bird species can be disrupted. This might be particularly problematic for those migrant bird species with fixed migration times (Miller-Rushing *et al.*, 2008). Therefore, changes in timing of leafing out or tree species abundance can result in phenological mismatches between trophic levels, causing cascade effects through these levels.

Future climate change could result in earlier budburst and later leaf abscission in temperate species, lengthening the growing season (Norby *et al.*, 2003). However, this could also increase risks of frost damage, increasing uncertainties of ecological interpretations in growing season length (Norby *et al.*, 2003). Phenological observations at a high temporal and spatial resolution should therefore be able to detect this damage as a separate event in order to

avoid biasing the estimates of phenological metrics. UAV time series data could potentially detect such abiotic stress in a way similar using ground and near-surface time series images (Ide and Oguma, 2010; Mizunuma *et al.*, 2013). Severe frosts can kill leaves and diminish the amount of green vegetation, an event which is expected to cause abrupt changes in the seasonal trajectories of vegetation indices detected at a high spatio-temporal resolution, as previously detected by phenocams (Hufkens *et al.*, 2012).

Predictions from plant phenological models could be validated and refined with the aid of UAV fine-scale observations. This would benefit a wide range of disciplines due to the multiple applications of such models in (Chuine *et al.*, 2013): forecasting the effects of climate change on plant phenology (Hanninen and Tanino, 2011; Mulder *et al.*, 2017); improvement of tree growth/forest productivity models (Kramer and Hänninen, 2009; Lempereur *et al.*, 2017); predicting the timing of pollen production, particularly of allergenic pollens (Garcia-Mozo *et al.*, 2009; Khwarahm *et al.*, 2017); predictions of tree species distribution changes (Morin *et al.*, 2008; Case and Lawler, 2017), macro-scale phenological analysis (macroecology) (Phillimore *et al.*, 2013).

7.4.2 Use of UAV data for validation and up-scaling

The UAV fine-scale information could be integrated spatially to investigate landscape phenology at systematically larger scales (up the UAV coverage extent), allowing broad patterns to emerge. The different aggregated levels of phenology can facilitate a multi-scale investigation of seasonal patterns of vegetation and its relation with local processes. Besides supporting ecology-related studies, this has also applications in calibrating ecosystem measures as detected from ground/near-surface and orbital sensors.

Phenocams and eddy covariance measurements play a crucial role in helping to improve our understanding of local-scale phenology and can also be used to validate satellite observations. Nevertheless, there are some aspects of these ground/near-surface measurements that could be better understood by comparison with UAV time series data.

Despite the broad use of phenocams (Brown *et al.*, 2016), there are still uncertainties related to the effect of their oblique viewing angles on the temporal trajectory of canopy greenness (Keenan *et al.*, 2014). Furthermore, inclined phenocams can only monitor one side of a tree crown, each of which has a different sensor-target distance; this can impact on data quality as further targets will have weaker signals and stronger atmospheric influence (Richardson *et al.*, 2009). A UAV data set, preferably acquired using the same camera as the

phenocam, could provide an insight into whether these issues have significant impacts on the phenocam-derived phenological signal. In addition, even though phenocams provide a means for direct comparisons with satellites phenometrics, the precise areal representativeness of the phenocam images is usually not known as they are not georeferenced; a defined region of interest within a phenocam image is therefore assumed to represent the satellite pixel(s) area. The UAV georeferenced information could be used to investigate issues related to areal representativeness. The findings of such comparisons could have great impact for the many studies using phenocams, as efforts are being made towards a global phenocam network (Brown *et al.*, 2016).

One of the ultimate applications of UAV-derived phenology would be the validation of satellite LSP products at an appropriate spatiotemporal scale. Because the UAV-derived information is synoptic and georeferenced, comparisons with satellite can be done very precisely, across areas (local scale) comparable with medium and moderate spatial resolution satellite pixels (e.g. Landsat, MODIS). Furthermore, the ability to monitor species-specific phenology with UAVs could help in understanding the effects of the underlying spatial complexity and heterogeneity of the objects which might be present within the resolved satellite scene (White *et al.*, 2009). For example, the effects of the background cover, such as snow and understorey vegetation, which can bias and even hamper LSP transition date estimates (Delbart *et al.*, 2005; White *et al.*, 2009), could be better understood with UAV data, as this can allow tracking of canopy phenology, as opposed to ecosystem dynamics detected by satellites. This would provide new insights into the ecological and biophysical meaning of the spectral information within the satellite pixels.

The findings of this research support the use of UAV data for this application, as canopy spring phenology of individual trees were consistently detected across a 15 ha woodland (Figure 6-10, Chapter 6). In addition, the 5 cm spatial resolution of the UAV imagery has allowed the effects of understorey cover into canopy phenological metric estimations to be investigated; ultimately, the brightest pixels within a tree crown diminishes uncertainties caused by understorey contribution (Figure 5-5, Chapter 5). Nevertheless, poor relationships were found between UAV- and Landsat-derived phenometrics in this study (R^2<0.45, section 6.3.4, Chapter 6), indicating that there are remaining challenges to be addressed in order to better understand the potential of UAV data sets for satellite phenology validation purposes. One of the most important remaining questions is: How much of this unexplained variability is due to the different temporal resolutions of the two data sets (Landsat data had a 47 days temporal gap, section 6.3.2, Chapter 6)? Further studies are

necessary to investigate whether the relationship between UAV- and Landsat-derived phenometrics would actually improve if the two data sets would have the same (or very similar) temporal resolution. Furthermore, the positional uncertainty of Landsat pixels (~12 m) was not taken into account when comparing with UAV products, which may have implications over areas with pronounced heterogeneity in timing of phenological events.

As the UAV fine spatial scale can be degraded to match a satellite coarser spatial resolution data, which can allow assessment of common approaches used to gap-fill (temporal compositing) and smooth satellite time series data (Atkinson *et al.*, 2012). Contrary to spaceborne optical systems, UAVs are not limited by cloud presence and can potentially acquire data at user-controlled revisit periods, offering, therefore, an appropriate temporal resolution to investigate the effects of gap-fill and smoothing techniques.

7.4.3 Use of UAV data for understanding of vegetation dynamics and fluxes

Phenology plays an important role in regulating the carbon cycles (Richardson *et al.*, 2012). Eddy covariance towers offer the opportunity to monitor carbon balances of vegetated ecosystems and understand the influences of key phenological events on ecosystem productivity (Richardson *et al.*, 2007) and the underlying physiological processes related to plant phenology (Wu *et al.*, 2017).

Flux tower estimations can characterize whether a vegetated ecosystem is acting as a sink or source of carbon over time, events which are closely associated with vegetation phenology (Wilkinson *et al.*, 2012; Mizunuma *et al.*, 2013). Plant species heterogeneity, due to expected phenological and functional differences, can make the interpretation of the seasonality of flux data more difficult (Gamon, 2015; Wang *et al.*, 2016a), as different spatial patterns of canopy phenology can influence the temporal dynamic of carbon exchange estimates (Schwartz *et al.*, 2013). In this sense, the fine-scale observation offered by the methodology in this study could contribute towards a better understanding of the influences of key phenological events within the flux tower footprint; for example, in investigating which tree species, or which integrated area around the tower, is driving the overall seasonal change in flux dynamics.

Time series of spectral reflectance (under stable illumination conditions) and NDVI (at 30 m spatial scale) were consistently retrieved from the UAV data set (Chapter 4). UAV NDVI could be calibrated against flux tower measurements in order to estimate landscape productivity, similarly to Wang *et al.* (2016b), who used airborne NDVI data for this purpose.

Furthermore, the UAV NDVI series could improve understanding of the eddy covariance measurements: For instance, Wang *et al.* (2016a) investigated the areal representativeness around flux towers by using time series of Landsat NDVI, which proved to be not ideal due to temporal gaps in the series caused by cloud-contamination (a limitation not experienced by UAVs).

Spectral radiometers are often mounted in flux towers in order to record the seasonality of the reflected radiance around the tower. The resulting measurements can be used to better understand the links between spectral reflectance/VIs and vegetation productivity (Eklundh *et al.*, 2011). In addition, such measurements are analogous to quantities measured by satellites (Richardson *et al.*, 2013b), allowing tracking of the seasonal dynamics of the ecosystem in a manner similar to satellite sensors (Hmimina *et al.*, 2013). As in the case of phenocam networks, the UAV measurements could be cross-compared with tower-mounted spectral radiometer measurements, in order to investigate issues related to areal representativeness, spatial heterogeneity and influence of viewing angle. However, such potential spectral-related applications from a COTS camera can be only feasible if following a well-defined radiometric calibration, as proposed in Chapter 4. Additionally, the deployment of UAVs over flux towers located in the middle of forests/woodlands can be challenging due to operational constraints.

However, such potential spectral-related applications from a COTS camera (as discussed in this section – 7.4.3) can be only feasible if following a well-defined radiometric calibration, as proposed in Chapter 4. Additionally, the deployment of UAVs (mainly fixed-wing) over flux towers located in the middle of forests/woodlands can be challenging due to operational constraints.

7.5 Implications of UAV time series more broadly

Besides vegetation canopy phenology monitoring (Zhang *et al.*, 2003; Ahl *et al.*, 2006), land surface phenology derived from time series of remotely sensed data has applications in: 1) land cover classification (DeFries *et al.*, 1995); 2) vegetation change detection (de Beurs and Henebry, 2005); 3) invasive plant mapping and monitoring (Morisette *et al.*, 2006; Müllerová *et al.*, 2017b); and 4) mapping of understorey vegetation (Tuanmu *et al.*, 2010). The success of these applications depends upon the remote sensing data's ability to discriminate the different cover types or/and plant species. Because different plant species or

different cover types are expected to have different phenological behaviours, a time series of UAV data can be used to identify/map the different plant species (Müllerová *et al.*, 2017a) and/or cover types based on this phenological asynchrony. For example, images acquired at the most distinct phenological phase in the year are likely to improve the land cover classification accuracy and better discriminate between invasive and natural vegetation (Müllerová *et al.*, 2017a). Another application includes reproductive phenology monitoring, where UAV time series data could be applied, for instance, to detect the date of peak flowering, similarly to Crimmins and Crimmins (2008).

While this research did not attempt using UAV time series for such applications, the results suggest that the reliability of a species-specific classification depends on different tree species leafing-out on distinct periods of time (asynchrony in phenology). For example, Larch trees leafed out consistently earlier within the woodland and are easily distinguishable on the phenological map (Figure 6-10, Chapter 6). On the other hand, a wide inter-specific variability in phenology across the broadleaved species (three tree species) was found (Figure 6-9, Figure 6-10, Chapter 6), meaning that it would be challenging to discriminate these species based on their discrete phenometrics. Other methods, such as temporal trajectory techniques (Lhermitte *et al.*, 2011), where objects are grouped accordingly to their temporal trends similarity, could aid in plant species mapping.

Climate change may also alter the habitat/environmental suitability (suitability indicates "*how well a tree species is matched to site conditions*" (Ray *et al.*, 2010)) of some species (Rogers *et al.*, 2017), where potential impacts may be more severe across managed forests, due to the inherently low species diversity (Ray *et al.*, 2010). Monitoring continued suitability of individual tree species (current and new) can indicate which species are more resilient to a changing climate, data which can aid in defining forest planning and forest management practices (Ray *et al.*, 2010). Time series of UAV data could be a valuable remote sensing tool for assessments of species suitability by means of providing detailed data about plant health and growth at specific (trial) sites. Tree growth rates could be calculated based on tree height and tree crown diameter, which can be estimated from UAV-derived canopy height model, as presented in Chapter 6 (section 6.3.1) and elsewhere (Silva *et al.*, 2016). Pest outbreaks and tree diseases can also change the structural and spectral characteristics of tree canopies, which, dependent upon the severity, can be identified from UAV imagery products, such as VIs (Calderon *et al.*, 2013). Detailed and continuous information from test sites is essential for plant vulnerability assessment in face of a changing environment (Ray *et al.*, 2010).

Temporal series of imagery of the canopy also have the potential to track biotic and abiotic stresses events (Ide and Oguma, 2010; Mizunuma *et al.*, 2013), the potential, for which, as discussed previously, has implications for species suitability monitoring. In this study, the defoliation of an evergreen stand (due to a pest attack) was detected from the UAV images around two to three weeks earlier than from Landsat images (section 5.3.6, Chapter 5). In this way, besides detecting early symptoms of diseases or pests, continued monitoring with a UAV could aid in tracking the response or resilience of individuals to such stress and their potential recovery. Nevertheless, covering large areas with UAVs will remain a challenge (Matese *et al.*, 2015).

Precision farming and crop management are applications which can also benefit from a consistent time series of UAV data. By using high spatio-temporal observations, the current state of a crop can be assessed or inspected and (near-real time) management decisions made accordingly (Burkart *et al.*, 2017; Ni *et al.*, 2017). Pasture quality (von Bueren *et al.*, 2015), crop yield estimation (Liu *et al.*, 2016), crop growth monitoring (Ni *et al.*, 2017), water stress, crop disease and disease development monitoring (Calderon *et al.*, 2013; Gibson-Poole *et al.*, 2017) are some of the possible applications. In general, spectral (e.g. NDVI) and colour (e.g. GCC) indices can successfully track the quality of the target crop (Berni *et al.*, 2009; Burkart *et al.*, 2017; Ni *et al.*, 2017). UAVs have been extensively applied in agriculture-related research due the possibility to employ them at a specific time of interest, as some crops can have a relatively quick growing cycle, and due to the very high spatial resolution data, which can offer detailed information of crops status (Liu *et al.*, 2016; Burkart *et al.*, 2017).

Affordability and operability of a UAV platform are important aspects to be considered in the field of applied agriculture. The findings in this research inform that low cost COTS camera can be calibrated to generate consistent reflectance (under stable irradiance) and VIs. The option of using such relatively cheap sensors, but yet resulting in good quality data, is key if one wants to make UAV platforms accessible to farmers. This research also demonstrates the feasibility of calculating NDVI from single calibration equations (section 4.4.2, Chapter 4). This method simplifies the calibration procedure, as it reduces the need for GCTs in every field site data acquisition, making it easier to be implemented on an operational basis. This can be a major benefit for time series acquisitions or for surveying of large farms using UAVs.

7.6 Future phenological-related research and challenges of using UAVs

Acquisition of a full year time series of UAV data would bring the opportunity for further research, expanding the framework proposed in this study. This would allow a complete phenological cycle to be tracked, meaning that temporal dynamics of autumn (alongside with spring) phenology could also be monitored. Generally, autumn phenology is predicted less consistently than spring phenology (Bater *et al.*, 2011; Zhao *et al.*, 2012; Klosterman *et al.*, 2014). Furthermore, a complete annual time series of VI can allow derivation of several additional phenometrics (Table 2-3), including length of the growing season. Ultimately, the methodology could be expanded to a larger number of sites or over multiple years, fully testing the capacity of UAV data sets across a wider ranges of phenological behaviours. Furthermore, the potential for obtaining individual-based phenology observations from UAV data means that UAV data could be used as a complement, and ultimately, as a substitute to ground-based phenological observations.

Nevertheless, all these potential applications depend strongly on more automated data collection, making a UAV remote sensing platform easy and fast to deploy on an operational basis. On-board RTK-GPS for high accuracy positioning (Turner *et al.*, 2016; Dall'Asta *et al.*, 2017) seems to be a critical point, as such technology can eliminate the need for GCPs on every acquisition date, allowing for direct georeferencing (Dall'Asta *et al.*, 2017). In addition, on-board sensors recording levels of irradiance concurrent with image acquisition could improve the characterization of derived spectral products (e.g. reflectance and NDVI) (Honkavaara *et al.*, 2009; Hakala *et al.*, 2013). Due to the rapid technological development and growing interest in this area, such sensors are already available and could be easily deployed on UAV platforms; although reducing costs of such instruments seems to be critical to make them more commonly used by the research community.

While UAVs have allowed democratization of data acquisition (Woodget *et al.*, 2017), it can take a considerable amount of time to learn how to safely operate a UAV and understand all the requisites necessary to acquire high quality images. If using a COTS camera for quantitative remote sensing applications, it is critical to perform a comprehensive radiometric calibration, which demands expert knowledge and advanced calibration equipment. Scientific multispectral cameras (e.g. MicaSense (Samiappan *et al.*, 2017) or Tetracam (Matese *et al.*, 2015)) are an option to retrieve high quality spectral measurements without the need (for the user) to determine some of the sensor`s radiometric characteristics (e.g. the spectral response function) (Matese *et al.*, 2015); but, appropriate post-processing

steps are still needed in order to retrieve consistent physical units. Another advantage of non-COTS cameras is that by using a single camera to acquire visible and near-infrared imagery, issues related to varying illumination conditions are minimized when calculating VIs and multispectral analysis can be realized with confidence, as the spectral bands do not overlap (Berni *et al.*, 2009). However, such cameras can be expensive for some users.

Although UAVs can allow a detailed analysis of spatial and temporal patterns across the landscape, this is only feasible at a local scale. There is therefore a remaining challenge in measuring larger areas, which could be useful, for example, to investigate the seasonal signal of low spatial resolution imagery (>250 m) or to have a representative sample of a large forest ecosystem. Nevertheless, with the continuous technological advances, civil UAVs are expected to provide longer flying times, which could allow larger areas to be surveyed. However, this benefit can be limited by aviation regulations within each country, such as requirement to retain line-of-sight during operations (Torresan *et al.*, 2017).

7.7 Future of quantifying forest phenology

Multi-scale, multi-discipline, multi-sensor and multi-site seems to be the likely future approach for quantifying and better understanding the phenology of the land surface. UAVs are expected to play an increasing role within this context, alongside well-established near-surface remote sensing techniques. Multichannel, hyperspectral and lidar sensors are likely to be popularized, as long as technological advances permit miniaturization and lower costs of these sensors.

Multispectral and hyperspectral sensors with a broader range of wavelengths (visible to middle-infrared) (Yamamoto *et al.*, 2016) would allow analysis to move beyond solely visible and NIR wavelengths, incorporating a wider range of vegetation indices (optimal wavelengths could be selected). For example, mid-infrared based VIs (e.g. NDWI) have shown to be effective in detecting seasonal patterns of vegetation in regions of high snowfall (Delbart *et al.*, 2005; Delbart *et al.*, 2015). Hyperspectral data-derived sun-induced chlorophyll fluorescence can track seasonal variations of photosynthesis (Garzonio *et al.*, 2017), which can be a proxy for carbon cycles. Hyperspectral sensors could provide insights into seasonal dynamics of specific biochemical attributes of vegetation (e.g., leaf water and pigment content) (Gholizadeh *et al.*, 2016). Time series of lidar data (Sankey *et al.*, 2017) could better characterize the seasonal development of canopy structure (e.g. LAI or plant area

index (PAI)). Therefore, such leaf proprieties-related data (biochemistry and structure) can track the seasonality of plant physiology and offer an opportunity to better understand (Keenan *et al.*, 2014; Yang *et al.*, 2014b): 1) the physiological meaning of VI-derived phenological metrics; and, 2) the relationships between seasonal patterns of canopy colour/spectral proprieties and changes in biophysical/biochemical proprieties.

Gigapixel imaging, where a pan-tilt-zoom camera system records overlapped images (Brown *et al.*, 2016), can allow individual trees located kilometres away from the camera to be resolved within an image. Such a system has the potential to provide near-surface remote sensing measurements over larger spatial areas (dependent upon the camera position), while allowing hundreds (perhaps thousands) of trees to be individually monitored. However, deploying such a technology on a UAV would be a challenge. Because multiple images have to be acquired from the same position, only a highly stable rotary wing UAV would be suitable.

Low-cost COTS cameras onboard UAVs are expected to play an important role in tracking vegetation phenology. The affordability and good quality of data from such sensors, summed with the UAV deployment flexibility (Burkart *et al.*, 2017), are characteristics which make UAV COTS an attractive remote sensing system for local scale vegetation phenology monitoring. The derivation of NDVI proved to be problematic at small spatial scales in this study, but it is inferred that a single modified COTS camera would improve the NDVI temporal consistency. Continued research within this field is expected (Berra *et al.*, 2017; Burkart *et al.*, 2017; Gibson-Poole *et al.*, 2017), which can provide a better understanding of the quality and potential of UAV COTS cameras for vegetation phenology applications.

Finally, the fusion of Landsat 8 with Sentinel-2 imagery (Wang *et al.*, 2017) is expected to improve LSP characterization at medium spatial resolution scales (10-30 m), as the likelihood of obtaining a dense time series at these scales will increase. This would facilitate cross-scalar comparisons with ground, near-surface and airborne measurements and calibration of coarse resolution land surface phenology (e.g. MODIS). Nevertheless, even at a 10 m spatial scale, species-specific phenology cannot be resolved and so the importance of a UAV remote sensing approach for fine-scale validation purposes remains. Moreover, UAV time series data could be used as an independent observation to assess the performance of the combined Sentinel-2 and Landsat 8 data.

7.8 Recommendations for UAV data acquisition and processing for phenology studies

A fixed-wing UAV (either Quest300 or QPod) was used to acquire time series of imagery to monitor phenology of a 15 ha woodland in this study. Using a fixed-wing UAV was only possible as the woodland was surrounded by relatively flat crop fields, providing very good ground conditions for taking-off and landing. Other study areas where open spaces are not available close by, rotary-wing UAVs might be a better (if not the only) choice, but smaller areas are likely to be surveyed.

Regarding sensors on-board UAVs, this study has used time series data acquired with two COTS cameras, but scientific cameras are recommended in future studies if spectral reflectance and derived spectral VIs are needed. If using a COTS camera for retrieval of time series of reflectance and VIs, it is critical to perform a comprehensive radiometric calibration, which demands expert knowledge and advanced calibration equipment, which can end up adding substantial costs to the whole process. Scientific multispectral cameras (e.g. MicaSense (Samiappan *et al.*, 2017) or Tetracam (Matese *et al.*, 2015)) are an option to retrieve high quality spectral measurements without the need (for the user) to determine some of the sensor`s radiometric characteristics (e.g. the spectral response function) (Matese *et al.*, 2015); but, appropriate post-processing steps are still needed in order to retrieve consistent physical units. Another advantage of non-COTS cameras is that by using a single camera to acquire visible and near-infrared imagery, issues related to varying illumination conditions are minimized when calculating VIs and multispectral analysis can be realized with confidence, as the spectral bands do not overlap (Berni *et al.*, 2009). Nevertheless, such cameras are expensive for some users and if the aim is only to estimate the date of a phenological event, uncalibrated COTS cameras can still be a valuable option. It was shown that GCC_{DN}, an index based on DNs from a single unmodified camera, generated high quality time series and GCC_{DN}-estimated phenodates were consistently most closely associated with the visual assessments of spring canopy phenology than other VIs.

Independent of the camera and UAV model, a key aspect is acquiring a UAV data set which can allow high quality time series of orthomosaics to be generated. This can be achieved by acquiring high quality UAV images, with a high overlap and at varying viewing angles, as these characteristics are beneficial if processing the block of UAV images with a SfM-based software (e.g. PhotoScan and Pix4D), as discussed in section 2.7. Additionally, because time series data at an individual tree level is needed, an accurate georeferencing approach should be utilised by using either GCPs surveyed with DGCPs (as in this study,

generating a position accuracy of ±11 cm) or geotags from the original images (direct georeferencing) if a high accuracy GPS is available on-board the UAV.

Regarding the frequency of image acquisition, this study worked with a temporal resolution of ~1 week, but acquisition flights once ~every 2 weeks are an alternative option. Systematically reducing the UAV observations to ~once every 2 weeks had little effect in the shape of the seasonal curve and slightly reduced the accuracy of the derived phenometrics (for example, for SOS of the deciduous group, RMSE remained 8 days, whilst R^2 reduced from 0.75 to 0.74 and bias increased from -2 to -7 days, Table 5-11); temporal resolutions coarser than this can increase significantly the phenometric prediction uncertainties and are not advised (section 5.3.7). The key aspect is to maintain an evenly distributed in time data acquisition without large temporal gaps, otherwise the certainty of the different phenometrics can vary greatly according to the distribution of the data points (as observed when the UAV series was reduced to replicate the Landsat temporal resolution ((section 5.3.7))).

The methodological choice used in this research for estimating tree level phenology from UAV data can be considered successful and can be recommended in future studies. After producing a time series of UAV orthomosaics, the first step is to define the ROIs representing the individual trees. If a plot level analysis is required (relatively small number of trees), a manual delineation of ROIs is preferred. Otherwise, if the whole extent of the UAV orthomosaic is intended, an automatic tree crown detection and delineation should be used in order to make it easier to implement on an operational basis. Following the definition of ROIs, an approach should be used to extract time series data from within the ROIs. This study identified the mean DN of all pixels that support a DN value above the 80% percentile as being optimal, as it diminished the influence of shaded areas and/or understorey vegetation in the final UAV phenology time series; it is recommended therefore to test the optimal percentile within a ROI instead of using the general mean in future studies. The mean DNs from each ROI is then used to calculate time series of UAV VIs, from which phenometrics are extracted. This study used the rate of change from curve fitting (sigmoid models) to automatically identify SOS, MOS and EOS and, overall, the greendown model (section 5.2.4) performed best and is therefore the recommended model for fitting UAV time series data.

7.9 Conclusion

This research has investigated the potential and quality of UAV imagery to track the temporal dynamics of spring phenology. Firstly, the radiometric quality of two COTS cameras onboard a UAV was tested by means of calibrating DNs to reflectance and VIs and cross-validating results with ground and Landsat observations. Secondly, time series of UAV data were applied to monitor vegetation phenology at an individual tree and plot level, the results of which were validated against ground and Landsat observations. Finally, the spring phenology of the entire woodland was investigated, at an individual tree and Landsat pixel scale.

Although a dual COTS camera system, following calibration, could produce consistent time series of UAV NDVI at a Landsat 30 m scale (which indicates the UAV data's potential to validate medium resolution satellite data), GCC based on uncalibrated digital numbers (GCC$_{DN}$), derived from a single unmodified COTS camera, proved to be more appropriate to track the canopy phenology of individual trees in this study. Calculation of GCC$_{DN}$ simplifies data acquisition and processing and is a measure commonly available from phenocams, but may be less suitable for linking directly with reflectance-based satellite data. Therefore, there is future opportunity to investigate whether NDVI derived from a single modified COTS camera or multispectral sensor would produce robust time series measures at small spatial scales.

The use of UAVs as an airborne remote sensing platform makes it feasible to observe fine-scale phenology, similarly to near-surface optical sensors, but with the advantage of producing synoptic and georeferenced information, characteristics which can increase similarities with satellite observations. While phenological events in deciduous canopies can be tracked with confidence, the phenology of evergreen covers is more challenging to detect due to the weaker seasonal signal. Nevertheless, it is inferred that increasing the camera`s sensitivity could allow a better tracking of the subtle temporal signal from evergreen trees, but further studies are needed to better understand the phenology of this plant functional type from a UAV perspective.

Overstorey phenology within a Landsat 30 m pixel can be highly heterogeneous and off-phased in comparison with understorey phenology, making interpretation of satellite LSP products in such conditions a challenging task. The fine-scale information derived from UAV data can be useful in helping to improve our understanding of the effects of vegetation

heterogeneity, and asynchrony between understorey and overstorey phenology, on LSP products.

An opportunity is now available to track very fine scale phenological changes, over contiguous vegetation communities, across local spatial extents. This information could aid in further understanding of phenological triggers and biophysical processes of different plant functional types during the critical time of growing season onset. Continued research with similar techniques would further advance the synergism of multi-scale remote sensing observations of vegetation phenology.

Appendices

Appendix A. MOS and EOS maps
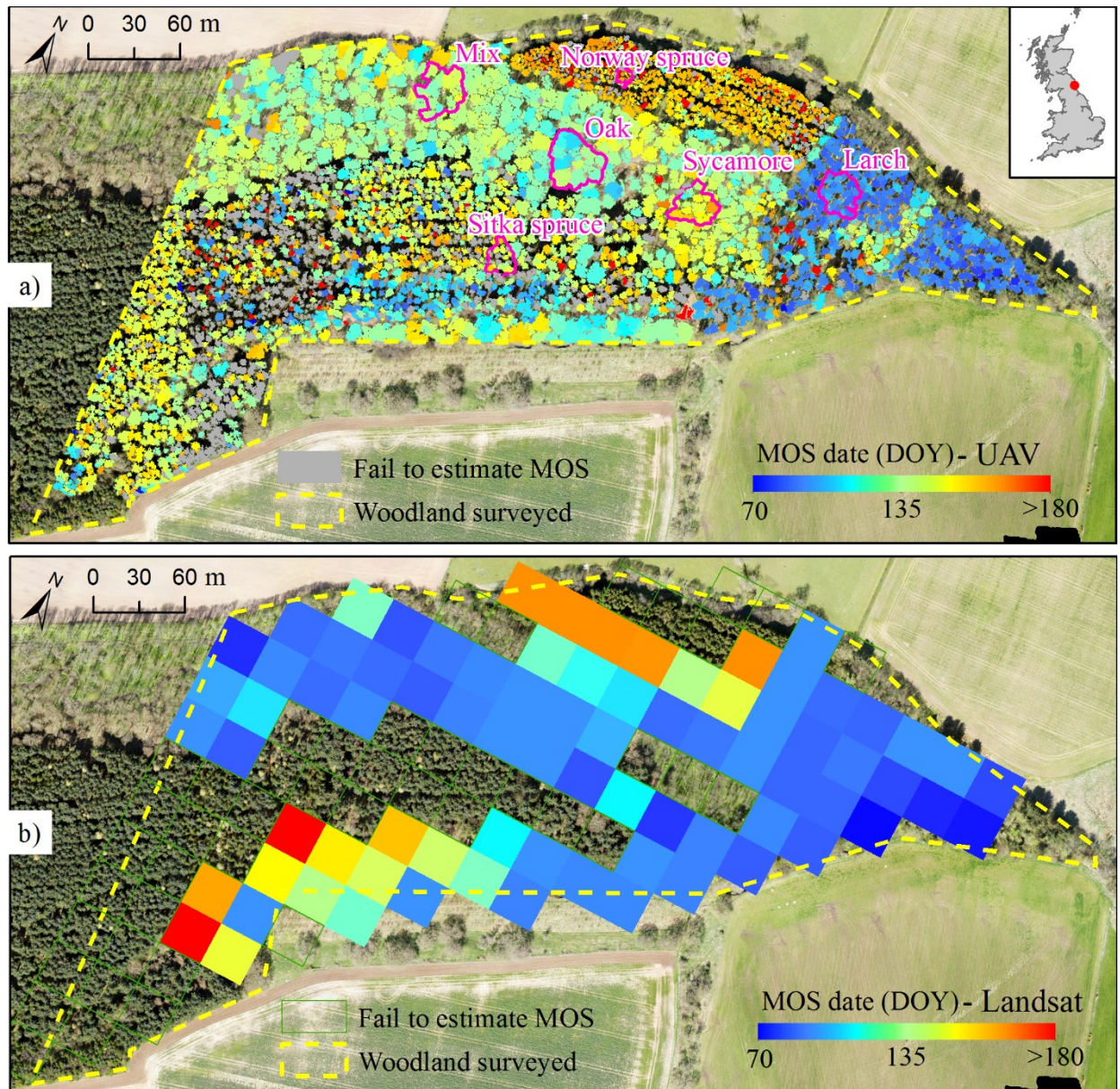
Figure A1. Individual tree-level prediction of MOS using UAV GCC_{DN} (80th percentile; fitted by the greendown model) (a) and pixel-level prediction of MOS using Landsat NDVI (fitted by the simple model) (b). Cooler colours indicate earlier onset and leaf-out, warmer colours are later onset and canopy development. The six ground validation plots contain 20 trees each and give an idea of the tree species spatial distribution. Background orthomosaic made of UAV images (visible camera) acquired on 21/04/2015 (DOY 111).
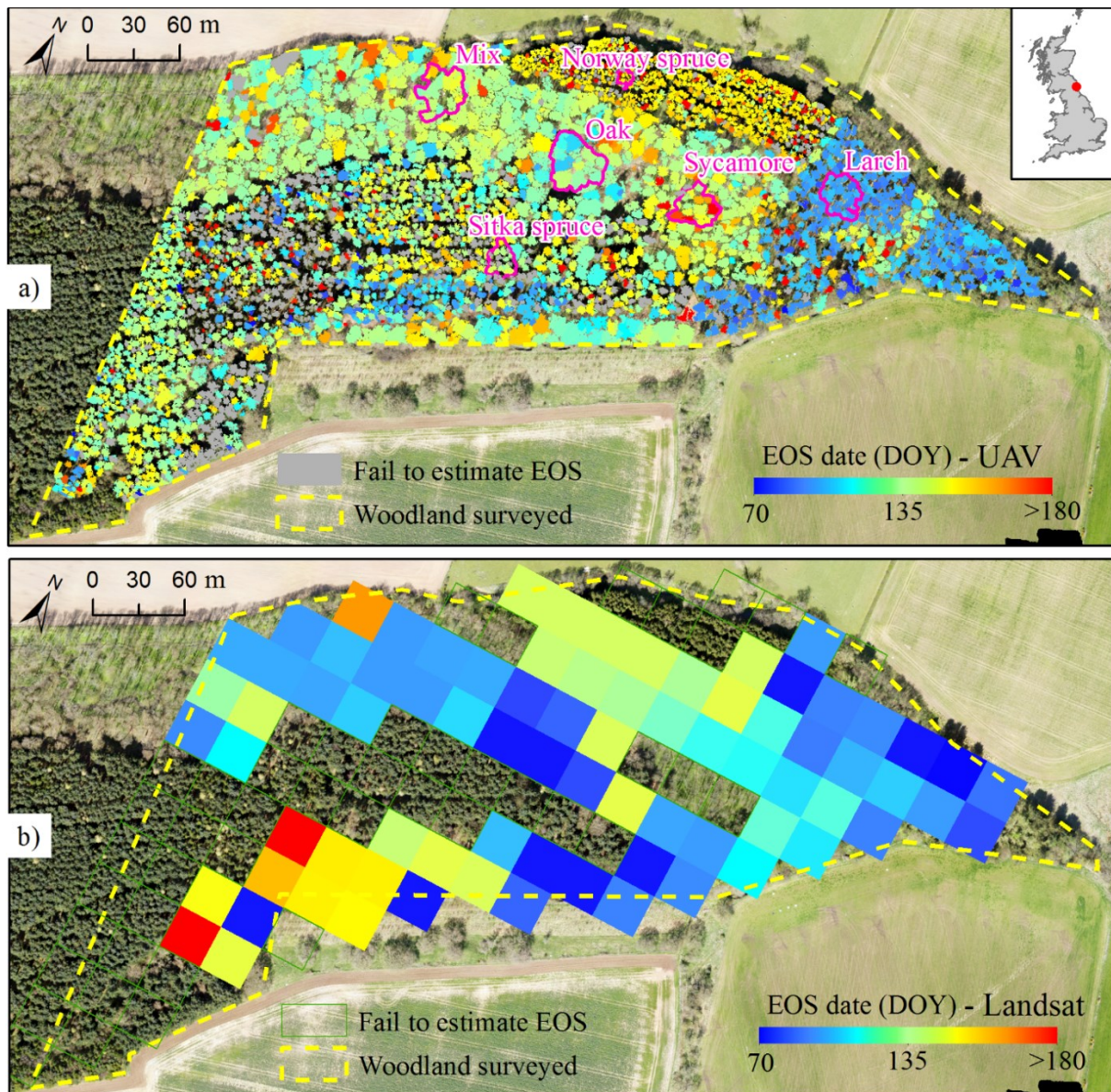
Figure A2. Individual tree-level prediction of EOS using UAV GCC$_{DN}$ (80th percentile; fitted by the greendown model) (a) and pixel-level prediction of EOS using Landsat NDVI (fitted by the simple model) (b). Cooler colours indicate earlier onset and leaf-out, warmer colours are later onset and canopy development. The six ground validation plots contain 20 trees each and give an idea of the tree species spatial distribution. Background orthomosaic made of UAV images (visible camera) acquired on 21/04/2015 (DOY 111).

Appendix B. Land cover types

Figure B1. The study area was divided into four main land covers in order to group the main tree species. The six ground validation plots contain 20 trees each. Background orthomosaic made of UAV images (visible camera) acquired on 21/04/2015 (DOY 111).

Appendix C. Canopy phenology (UAV) vs land surface phenology (Landsat)
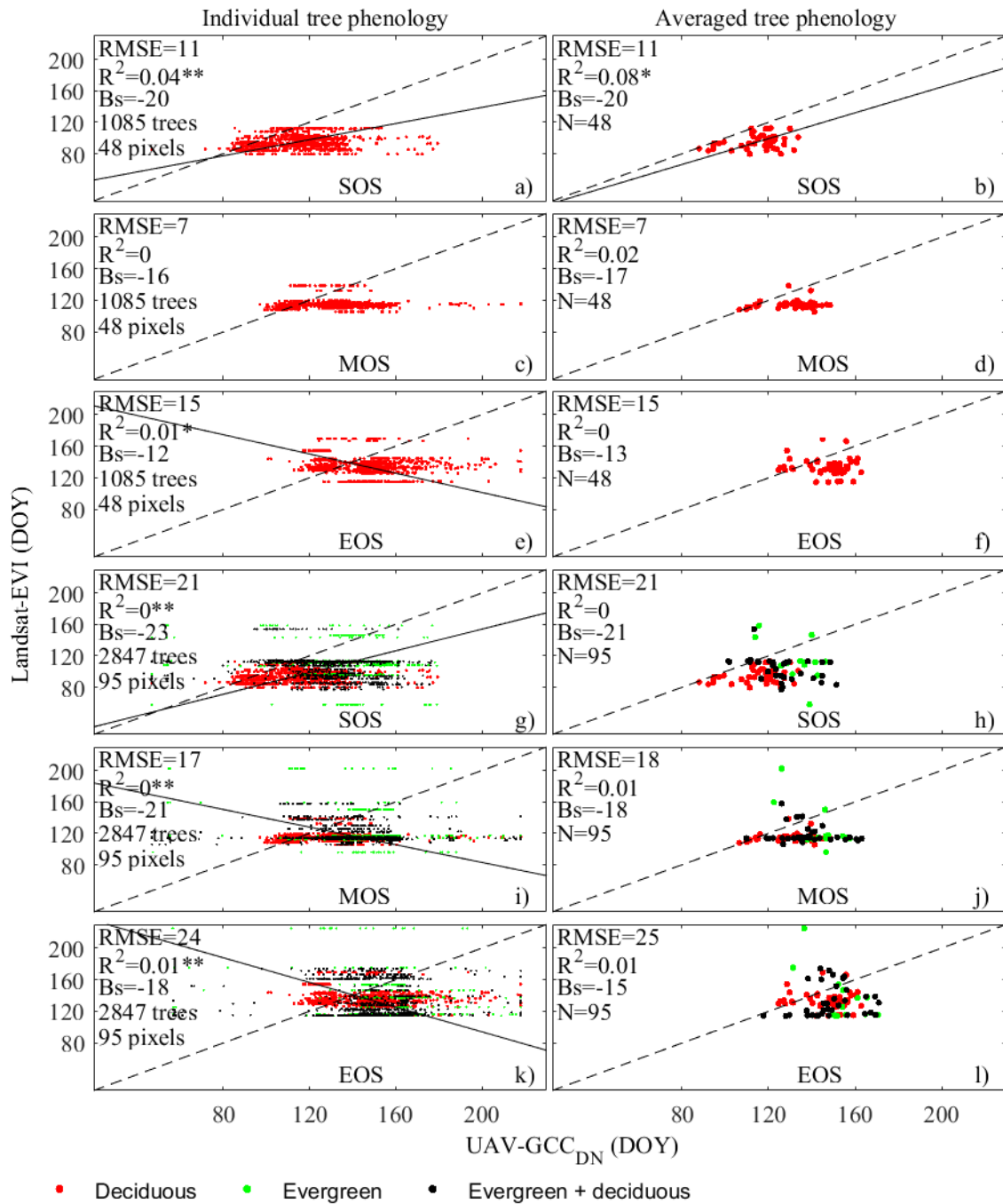
Figure C1. Landsat land surface phenology (simple model) compared with UAV-derived tree-level phenology (greendown model), considering every tree as a data point (left column) and averaged tree leaf phenology (right column). Pure deciduous covers are shown separately (a-f). The greendown model fitted the remote sensing data. Bias (Bs) is calculated relative to UAV, so a negative bias indicates that the corresponding Landsat estimate is earlier. Dashed lines represent the 1:1 line and solid lines are reduced major axis (RMA) regression models. Statistics are given (**$p<0.001$; *$p<0.05$).
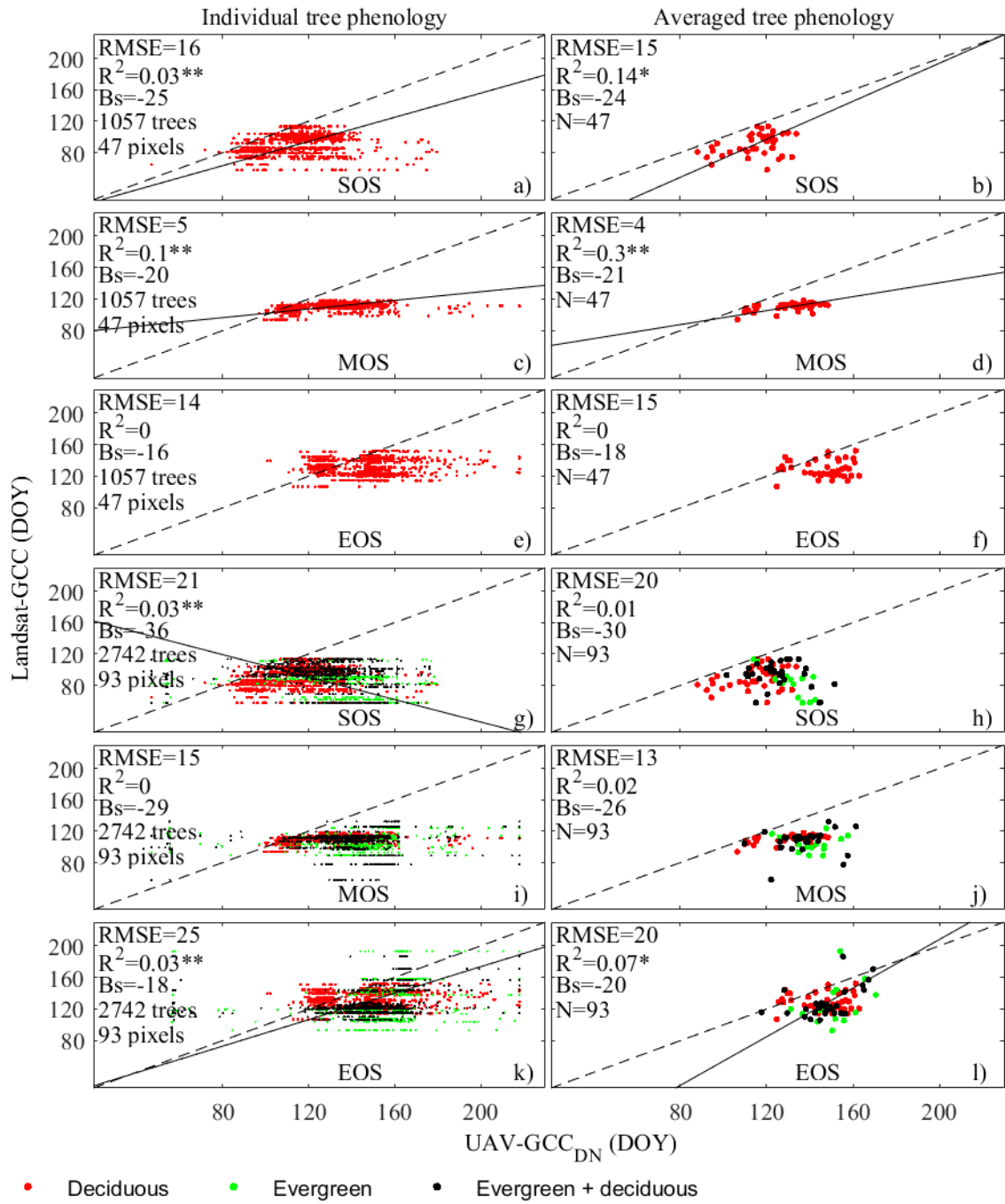
Figure C2. Landsat land surface phenology (simple model) compared with UAV-derived tree-level phenology (greendwon model), considering every tree as a data point (left column) and averaged tree leaf phenology (right column). Pure deciduous covers are shown separately (a-f). The greendown model fitted the remote sensing data. Bias (Bs) is calculated relative to UAV, so a negative bias indicates that the corresponding Landsat estimate is earlier. Dashed lines represent the 1:1 line and solid lines are reduced major axis (RMA) regression models. Statistics are given (**$p<0.001$; *$p<0.05$).

Appendix D. LSP (UAV) vs LSP (Landsat)
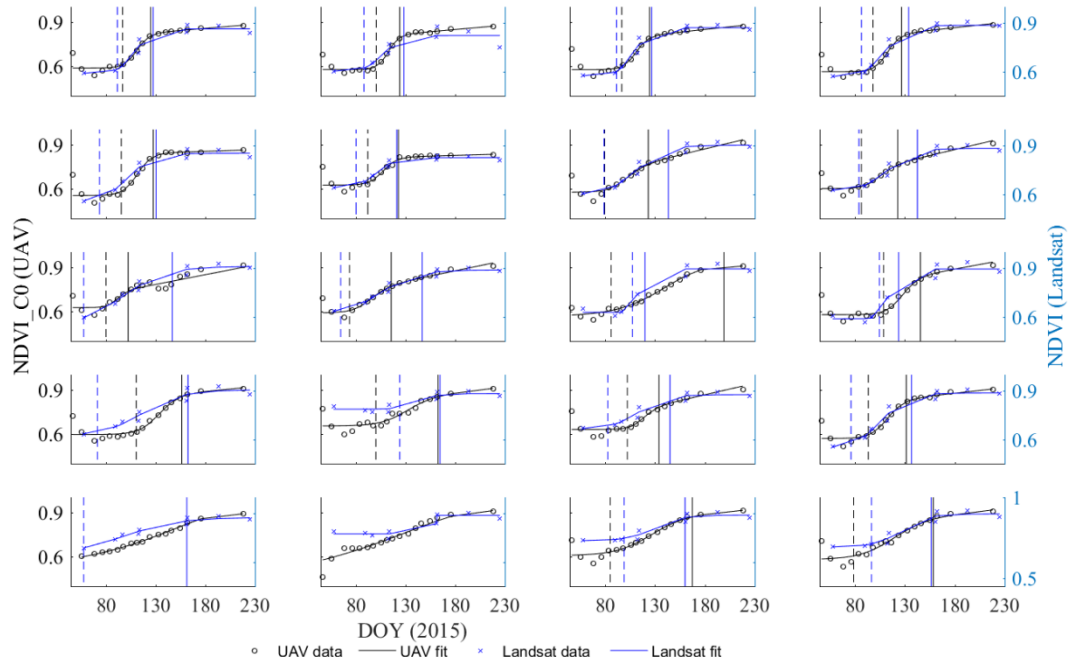
Figure D1. Example comparison of 20 samples of UAV and Landsat data (and derived phenometrics), where both data set represent land surface phenology. UAV orthomosaic DNs were aggregated up to the Landsat scale (i.e., the region of interest was the entire Landsat pixel area rather than just tree crowns). Landsat data are fitted by the simple model and UAV data by the greendown model. Start and end of spring season dates for each spectral curve are marked by vertical lines.

References

Aber, J.S., Marzolff, I. and Ries, J. (2010) *Small-Format Aerial Photography: Principles, Techniques and Geosciences Applications*. Oxford, UK: Elsevier.

AgiSoft (2016) 'Agisoft PhotoScan User Manual: Professional Edition, Version 1.2'. St. Petersburg, Russia, p. 103. Available at: http://www.agisoft.com/pdf/photoscan-pro_1_2_en.pdf.

Ahl, D.E., Gower, S.T., Burrows, S.N., Shabanov, N.V., Myneni, R.B. and Knyazikhin, Y. (2006) 'Monitoring spring canopy phenology of a deciduous broadleaf forest using MODIS', *Remote Sensing of Environment*, 104(1), pp. 88-95.

Anderson, K. and Gaston, K.J. (2013) 'Lightweight unmanned aerial vehicles will revolutionize spatial ecology', *Frontiers in Ecology and the Environment*, 11(3), pp. 138-146.

Armitage, R.P., Alberto Ramirez, F., Mark Danson, F. and Ogunbadewa, E.Y. (2013) 'Probability of cloud-free observation conditions across Great Britain estimated using MODIS cloud mask', *Remote Sensing Letters*, 4(5), pp. 427-435.

Atkinson, P.M., Jeganathan, C., Dash, J. and Atzberger, C. (2012) 'Inter-comparison of four models for smoothing satellite sensor time-series data to estimate vegetation phenology', *Remote Sensing of Environment*, 123, pp. 400-417.

Augspurger, C.K. and Bartlett, E.A. (2003) 'Differences in leaf phenology between juvenile and adult trees in a temperate deciduous forest', *Tree Physiology*, 23(8), pp. 517-525.

Augspurger, C.K., Cheeseman, J.M. and Salk, C.F. (2005) 'Light gains and physiological capacity of understorey woody plants during phenological avoidance of canopy shade', *Functional Ecology*, 19(4), pp. 537-546.

Axelsson, P. (2000) 'DEM generation from laser scanner data using adaptive TIN models', *International Archives of Photogrammetry and Remote Sensing*, 33(B4/1; PART 4), pp. 111-118.

Aye, S.Y., Liu, W., Feng, H. and Ng, B.P. (2017) 'Study of multi-rotor UAV SAR processing', *2017 IEEE Radar Conference (RadarConf)*. 8-12 May 2017.

Bach, H. and Mauser, W. (1997) *Improvements of plant parameter estimations with hyperspectral data compared to multispectral data*.

Badeck, F.W., Bondeau, A., Bottcher, K., Doktor, D., Lucht, W., Schaber, J. and Sitch, S. (2004) 'Responses of spring phenology to climate change', *New Phytologist*, 162(2), pp. 295-309.

Badhwar, G.D. (1984) 'Automatic corn-soybean classification using Landsat MSS data. I. Near-harvest crop proportion estimation', *Remote Sensing of Environment*, 14(1), pp. 15-29.

Bajwa, S.G. and Tian, L. (2002) 'Multispectral CIR image calibration for cloud shadow and soil background influence using intensity normalization', *Applied engineering in agriculture*, 18(5), p. 627.

Baret, F. and Guyot, G. (1991) 'Potential and limits of vegetation índices for LAI and APAR assessment', *Remote Sensing of Environment. S*, 3.

Barsi, J., Lee, K., Kvaran, G., Markham, B. and Pedelty, J. (2014) 'The Spectral Response of the Landsat-8 Operational Land Imager', *Remote Sensing*, 6(10), p. 10232.

Bartholomé, E. and Belward, A.S. (2005) 'GLC2000: a new approach to global land cover mapping from Earth observation data', *International Journal of Remote Sensing*, 26(9), pp. 1959-1977.

Bater, C.W., Coops, N.C., Wulder, M.A., Hilker, T., Nielsen, S.E., McDermid, G. and Stenhouse, G.B. (2011) 'Using digital time-lapse cameras to monitor species-specific understorey and overstorey phenology in support of wildlife habitat assessment', *Environmental monitoring and assessment*, 180(1-4), pp. 1-13.

Baumann, M., Ozdogan, M., Richardson, A.D. and Radeloff, V.C. (2017) 'Phenology from Landsat when data is scarce: Using MODIS and Dynamic Time-Warping to combine multi-year Landsat imagery to derive annual phenology curves', *International Journal of Applied Earth Observation and Geoinformation*, 54, pp. 72-83.

Bayer, B.E. (1976) 'Color imaging array'. Google Patents.

Beck, P.S.A., Jönsson, P., Høgda, K.A., Karlsen, S.R., Eklundh, L. and Skidmore, A.K. (2007) 'A ground-validated NDVI dataset for monitoring vegetation dynamics and mapping phenology in Fennoscandia and the Kola peninsula', *International Journal of Remote Sensing*, 28(19), pp. 4311-4330.

Berni, J.A.J., Zarco-Tejada, P.J., Suarez, L. and Fereres, E. (2009) 'Thermal and Narrowband Multispectral Remote Sensing for Vegetation Monitoring From an Unmanned Aerial Vehicle', *IEEE Transactions on Geoscience and Remote Sensing*, 47(3), pp. 722-738.

Berra, E., Gibson-Poole, S., MacArthur, A., Gaulton, R. and Hamilton, A. (2015) 'Estimation of the spectral sensitivity functions of un-modified and modified commercial off-the-shelf digital cameras to enable their use as a multispectral imaging system for UAVs', *Int. Arch. Photogramm. Remote Sens. Spatial Inf. Sci.*, XL-1/W4, pp. 207-214.

Berra, E.F., Gaulton, R. and Barr, S. (2016) 'Use of a digital camera onboard a UAV to monitor spring phenology at individual tree level', *2016 IEEE International Geoscience and Remote Sensing Symposium (IGARSS)*. 10-15 July 2016. Available at: http://ieeexplore.ieee.org/ielx7/7592514/7728980/07729904.pdf?tp=&arnumber=7729904&isnumber=7728980.

Berra, E.F., Gaulton, R. and Barr, S. (2017) 'Commercial Off-the-Shelf Digital Cameras on Unmanned Aerial Vehicles for Multitemporal Monitoring of Vegetation Reflectance and NDVI', *Ieee Transactions on Geoscience and Remote Sensing*, 55(9), pp. 4878-4886.

Bondi, E., Salvaggio, C., Montanaro, M. and Gerace, A.D. (2016) 'Calibration of UAS imagery inside and outside of shadows for improved vegetation index computation', *SPIE Commercial and Scientific Sensing and Imaging*. Maryland, US, April 19, 2016. pp. 98660J: 1-7. Available at: http://dx.doi.org/10.1117/12.2227214.

Borel, C.C. and Gerstl, S.A.W. (1994) 'Nonlinear spectral mixing models for vegetative and soil surfaces', *Remote Sensing of Environment*, 47(3), pp. 403-416.

Boschetti, M., Boschetti, L., Oliveri, S., Casati, L. and Canova, I. (2007) 'Tree species mapping with Airborne hyper-spectral MIVIS data: the Ticino Park study case', *International Journal of Remote Sensing*, 28(6), pp. 1251-1261.

Bothmann, L., Menzel, A., Menze, B.H., Schunk, C. and Kauermann, G. (2017) 'Automated processing of webcam images for phenological classification', *Plos One*, 12(2).

Bradford, R.E. and Gross, J.F. (1967) 'Conditioning of digitized TIROS and ESSA satellite vidicon data', *Computerized Imaging Techniques*. International Society for Optics and Photonics.

Bradley, B.A. and Mustard, J.F. (2008) 'Comparison of phenology trends by land cover class: a case study in the Great Basin, USA', *Global Change Biology*, 14(2), pp. 334-346.

Brown, L.A., Dash, J., Ogutu, B.O. and Richardson, A.D. (2017) 'On the relationship between continuous measures of canopy greenness derived using near-surface remote sensing and satellite-derived vegetation products', *Agricultural and Forest Meteorology*, 247(Supplement C), pp. 280-292.

Brown, T.B., Hultine, K.R., Steltzer, H., Denny, E.G., Denslow, M.W., Granados, J., Henderson, S., Moore, D., Nagai, S., SanClements, M., Sanchez-Azofeifa, A., Sonnentag, O., Tazik, D. and Richardson, A.D. (2016) 'Using phenocams to monitor our changing Earth: toward a global phenocam network', *Frontiers in Ecology and the Environment*, 14(2), pp. 84-93.

Burkart, A., Aasen, H., Alonso, L., Menz, G., Bareth, G. and Rascher, U. (2015) 'Angular Dependency of Hyperspectral Measurements over Wheat Characterized by a Novel UAV Based Goniometer', *Remote Sensing*, 7(1), pp. 725-746.

Burkart, A., Cogliati, S., Schickling, A. and Rascher, U. (2014) 'A Novel UAV-Based Ultra-Light Weight Spectrometer for Field Spectroscopy', *Ieee Sensors Journal*, 14(1), pp. 62-67.

Burkart, A., Hecht, V.L., Kraska, T. and Rascher, U. (2017) 'Phenological analysis of unmanned aerial vehicle based time series of barley imagery with high temporal resolution', *Precision Agriculture*.

Calderon, R., Navas-Cortes, J.A., Lucena, C. and Zarco-Tejada, P.J. (2013) 'High-resolution airborne hyperspectral and thermal imagery for early, detection of Verticillium wilt of olive using fluorescence, temperature and narrow-band spectral indices', *Remote Sensing of Environment*, 139, pp. 231-245.

Calders, K., Schenkels, T., Bartholomeus, H., Armston, J., Verbesselt, J. and Herold, M. (2015) 'Monitoring spring phenology with high temporal resolution terrestrial LiDAR measurements', *Agricultural and Forest Meteorology*, 203(0), pp. 158-168.

Campoy, J.A., Ruiz, D. and Egea, J. (2011) 'Dormancy in temperate fruit trees in a global warming context: A review', *Scientia Horticulturae*, 130(2), pp. 357-372.

Canisius, F., Shang, J., Liu, J., Huang, X., Ma, B., Jiao, X., Geng, X., Kovacs, J.M. and Walters, D. (2017) 'Tracking crop phenological development using multi-temporal polarimetric Radarsat-2 data', *Remote Sensing of Environment*.

Case, M.J. and Lawler, J.J. (2017) 'Integrating mechanistic and empirical model projections to assess climate impacts on tree species distributions in northwestern North America', *Global Change Biology*, 23(5), pp. 2005-2015.

Chabot, D. and Bird, D.M. (2013) 'Small unmanned aircraft: precise and convenient new tools for surveying wetlands', *Journal of Unmanned Vehicle Systems*, 1(1), pp. 15-24.

Chavez, P.S. (1996) 'Image-based atmospheric corrections revisited and improved', *Photogrammetric Engineering and Remote Sensing*, 62(9), pp. 1025-1036.

Chen, J., Jönsson, P., Tamura, M., Gu, Z., Matsushita, B. and Eklundh, L. (2004) 'A simple method for reconstructing a high-quality NDVI time-series data set based on the Savitzky–Golay filter', *Remote sensing of Environment*, 91(3), pp. 332-344.

Chen, J.M., Black, T.A. and Adams, R.S. (1991) 'Evaluation of hemispherical photography for determining plant area index and geometry of a forest stand', *Agricultural and Forest Meteorology*, 56(1), pp. 129-143.

Chianucci, F. and Cutini, A. (2013) 'Estimation of canopy properties in deciduous forests with digital hemispherical and cover photography', *Agricultural and Forest Meteorology*, 168(Supplement C), pp. 130-139.

Chisholm, R.A., Cui, J., Lum, S.K.Y. and Chen, B.M. (2013) 'UAV LiDAR for below-canopy forest surveys', *Journal of Unmanned Vehicle Systems*, 1(01), pp. 61-68.

Christensen, J.H., Hewitson, B., Busuioc, A., Chen, A., Gao, X., Held, R., Jones, R., Kolli, R.K., Kwon, W.K. and Laprise, R. (2007) 'Regional climate projections', in *Climate Change, 2007: The Physical Science Basis. Contribution of Working group 1 to the Fourth Assessment Report of the Intergovernmental Panel on Climate Change*. Cambridge University Press, Cambridge, United Kingdom and New York, NY, USA: University Press, Cambridge, pp. 847-940.

Chuine, I., Kramer, K. and Hänninen, H. (2013) 'Plant Development Models', in Schwartz, M.D. (ed.) *Phenology: An Integrative Environmental Science*. Dordrecht: Springer Netherlands, pp. 275-288.

Coffin, D. (2015) *DCRAW: User Commands*. Available at: https://www.cybercom.net/~dcoffin/dcraw/dcraw.1.html (Accessed: 01/06/2015).

Cole, E.F., Long, P.R., Zelazowski, P., Szulkin, M. and Sheldon, B.C. (2015) 'Predicting bird phenology from space: satellite-derived vegetation green-up signal uncovers spatial

variation in phenological synchrony between birds and their environment', *Ecology and Evolution*, 5(21), pp. 5057-5074.

Colomina, I. and Molina, P. (2014) 'Unmanned aerial systems for photogrammetry and remote sensing: A review', *ISPRS Journal of Photogrammetry and Remote Sensing*, 92, pp. 79-97.

Cong, N., Piao, S., Chen, A., Wang, X., Lin, X., Chen, S., Han, S., Zhou, G. and Zhang, X. (2012) 'Spring vegetation green-up date in China inferred from SPOT NDVI data: A multiple model analysis', *Agricultural and Forest Meteorology*, 165(0), pp. 104-113.

Coveney, S. and Fotheringham, A.S. (2011) 'TERRESTRIAL LASER SCAN ERROR IN THE PRESENCE OF DENSE GROUND VEGETATION', *Photogrammetric Record*, 26(135), pp. 307-324.

Crimmins, M.A. and Crimmins, T.M. (2008) 'Monitoring plant phenology using digital repeat photography', *Environmental Management*, 41(6), pp. 949-958.

Culvenor, D.S. (2002) 'TIDA: an algorithm for the delineation of tree crowns in high spatial resolution remotely sensed imagery', *Computers & Geosciences*, 28(1), pp. 33-44.

D'Odorico, P., Gonsamo, A., Gough, C.M., Bohrer, G., Morison, J., Wilkinson, M., Hanson, P.J., Gianelle, D., Fuentes, J.D. and Buchmann, N. (2015) 'The match and mismatch between photosynthesis and land surface phenology of deciduous forests', *Agricultural and Forest Meteorology*, 214–215, pp. 25-38.

Dall'Asta, E., Forlani, G., Roncella, R., Santise, M., Diotri, F. and Morra di Cella, U. (2017) 'Unmanned Aerial Systems and DSM matching for rock glacier monitoring', *ISPRS Journal of Photogrammetry and Remote Sensing*, 127, pp. 102-114.

Dandois, J.P. and Ellis, E.C. (2013) 'High spatial resolution three-dimensional mapping of vegetation spectral dynamics using computer vision', *Remote Sensing of Environment*, 136, pp. 259-276.

Dare, P.M. (2008) 'Small format digital sensors for aerial imaging applications', *XXI ISPRS Congress*. Beijing. ISPRS, pp. 533 - 538. Available at: http://citeseerx.ist.psu.edu/viewdoc/download?doi=10.1.1.697.126&rep=rep1&type=pdf.

Darrodi, M.M., Finlayson, G., Goodman, T. and Mackiewicz, M. (2015) 'Reference data set for camera spectral sensitivity estimation', *Journal of the Optical Society of America A*, 32(3), pp. 381-391.

de Beurs, K.M. and Henebry, G.M. (2005) 'Land surface phenology and temperature variation in the International Geosphere-Biosphere Program high-latitude transects', *Global Change Biology*, 11(5), pp. 779-790.

DeFries, R., Hansen, M. and Townshend, J. (1995) 'Global discrimination of land cover types from metrics derived from AVHRR pathfinder data', *Remote Sensing of Environment*, 54(3), pp. 209-222.

Del Pozo, S., Rodríguez-Gonzálvez, P., Hernández-López, D. and Felipe-García, B. (2014) 'Vicarious radiometric calibration of a multispectral camera on board an unmanned aerial system', *Remote Sensing*, 6(3), pp. 1918-1937.

Delbart, N., Beaubien, E., Kergoat, L. and Le Toan, T. (2015) 'Comparing land surface phenology with leafing and flowering observations from the PlantWatch citizen network', *Remote Sensing of Environment*, 160(0), pp. 273-280.

Delbart, N., Kergoat, L., Le Toan, T., Lhermitte, J. and Picard, G. (2005) 'Determination of phenological dates in boreal regions using normalized difference water index', *Remote Sensing of Environment*, 97(1), pp. 26-38.

Delbart, N., Le Toan, T., Kergoat, L. and Fedotova, V. (2006) 'Remote sensing of spring phenology in boreal regions: A free of snow-effect method using NOAA-AVHRR and SPOT-VGT data (1982-2004)', *Remote Sensing of Environment*, 101(1), pp. 52-62.

Delbart, N. and Picard, G. (2007) 'Modeling the date of leaf appearance in low-arctic tundra', *Global Change Biology*, 13(12), pp. 2551-2562.

Delbart, N., Picard, G., Le Toan, T., Kergoat, L., Quegan, S., Woodward, I.A.N., Dye, D. and Fedotova, V. (2008) 'Spring phenology in boreal Eurasia over a nearly century time scale', *Global Change Biology*, 14(3), pp. 603-614.

Demarez, V., Duthoit, S., Baret, F., Weiss, M. and Dedieu, G. (2008) 'Estimation of leaf area and clumping indexes of crops with hemispherical photographs', *Agricultural and Forest Meteorology*, 148(4), pp. 644-655.

Dinstein, I., Merkle, F., Lam, T.D. and Wong, K.Y. (1984) 'IMAGING-SYSTEM RESPONSE LINEARIZATION AND SHADING CORRECTION', *Optical Engineering*, 23(6), pp. 788-793.

Dostalova, A., Milenkovic, M., Hollaus, M. and Wagner, W. (2016) 'Influence of Forest Structure on the Sentinel-1 Backscatter Variation-Analysis with Full-Waveform LiDAR Data', *Living Planet Symposium*.

Duan, T., Zheng, B., Guo, W., Ninomiya, S., Guo, Y. and Chapman, S.C. (2016) 'Comparison of ground cover estimates from experiment plots in cotton, sorghum and sugarcane based on images and ortho-mosaics captured by UAV', *Functional Plant Biology*, 44(1), pp. 169-183.

Duncanson, L.I., Cook, B.D., Hurtt, G.C. and Dubayah, R.O. (2014) 'An efficient, multi-layered crown delineation algorithm for mapping individual tree structure across multiple ecosystems', *Remote Sensing of Environment*, 154, pp. 378-386.

Eastman, J.R., Sangermano, F., Machado, E.A., Rogan, J. and Anyamba, A. (2013) 'Global Trends in Seasonality of Normalized Difference Vegetation Index (NDVI), 1982–2011', *Remote Sensing*, 5(10), pp. 4799-4818.

Edson, C. and Wing, M.G. (2011) 'Airborne Light Detection and Ranging (LiDAR) for Individual Tree Stem Location, Height, and Biomass Measurements', *Remote Sensing*, 3(11), p. 2494.

Eklundh, L., Jin, H., Schubert, P., Guzinski, R. and Heliasz, M. (2011) 'An optical sensor network for vegetation phenology monitoring and satellite data calibration', *Sensors*, 11(8), pp. 7678-7709.

Elmore, A.J., Guinn, S.M., Minsley, B.J. and Richardson, A.D. (2012) 'Landscape controls on the timing of spring, autumn, and growing season length in mid-Atlantic forests', *Global Change Biology*, 18(2), pp. 656-674.

Filippa, G., Cremonese, E., Migliavacca, M., Galvagno, M., Forkel, M., Wingate, L., Tomelleri, E., Morra di Cella, U. and Richardson, A.D. (2016) 'Phenopix: A R package for image-based vegetation phenology', *Agricultural and Forest Meteorology*, 220, pp. 141-150.

Fisher, J.I. and Mustard, J.F. (2007) 'Cross-scalar satellite phenology from ground, Landsat, and MODIS data', *Remote Sensing of Environment*, 109(3), pp. 261-273.

Fisher, J.I., Mustard, J.F. and Vadeboncoeur, M.A. (2006) 'Green leaf phenology at Landsat resolution: Scaling from the field to the satellite', *Remote sensing of environment*, 100(2), pp. 265-279.

Förstner, W. (1986) 'A feature based correspondence algorithm for image matching', *International Archives of Photogrammetry and Remote Sensing*, 26(3), pp. 150-166.

Franklin, J. (1986) 'Thematic mapper analysis of coniferous forest structure and composition', *International Journal of Remote Sensing*, 7(10), pp. 1287-1301.

Fridley, J.D. (2012) 'Extended leaf phenology and the autumn niche in deciduous forest invasions', *Nature*, 485(7398), pp. 359-U105.

Friedl, M.A., Henebry, G., Reed, B. and Huete, A. (2006) 'Land surface phenology: a community white paper requested by NASA'.

Frolking, S., Milliman, T., McDonald, K., Kimball, J., Zhao, M.S. and Fahnestock, M. (2006) 'Evaluation of the SeaWinds scatterometer for regional monitoring of vegetation phenology', *Journal of Geophysical Research-Atmospheres*, 111(D17).

Gamon, J.A. (2015) 'Reviews and Syntheses: optical sampling of the flux tower footprint', *Biogeosciences*, 12(14), pp. 4509-4523.

Garcia-Mozo, H., Galan, C., Belmonte, J., Bermejo, D., Candau, P., de la Guardia, C.D., Elvira, B., Gutierrez, M., Jato, V., Silva, I., Trigo, M.M., Valencia, R. and Chuine, I. (2009) 'Predicting the start and peak dates of the Poaceae pollen season in Spain using process-based models', *Agricultural and Forest Meteorology*, 149(2), pp. 256-262.

Garrity, S.R., Bohrer, G., Maurer, K.D., Mueller, K.L., Vogel, C.S. and Curtis, P.S. (2011) 'A comparison of multiple phenology data sources for estimating seasonal transitions in deciduous forest carbon exchange', *Agricultural and Forest Meteorology*, 151(12), pp. 1741-1752.

Garzonio, R., Di Mauro, B., Colombo, R. and Cogliati, S. (2017) 'Surface Reflectance and Sun-Induced Fluorescence Spectroscopy Measurements Using a Small Hyperspectral UAS', *Remote Sensing*, 9(5), p. 472.

Gates, D.M. (1970) 'Physical and physiological properties of plants', in *Remote Sensing with Special Reference to Agriculture and Forestry: With Special Reference to Agriculture and Forestry*. Washington, DC: National Academy of Sciences, pp. 164-223.

Gholizadeh, A., Misurec, J., Kopackova, V., Mielke, C. and Rogass, C. (2016) 'Assessment of Red-Edge Position Extraction Techniques: A Case Study for Norway Spruce Forests Using HyMap and Simulated Sentinel-2 Data', *Forests*, 7(10).

Gibson-Poole, S., Humphris, S., Toth, I. and Hamilton, A. (2017) 'Identification of the onset of disease within a potato crop using a UAV equipped with un-modified and modified commercial off-the-shelf digital cameras', *Advances in Animal Biosciences*, 8(2), pp. 812-816.

Gitelson, A.A., Kaufman, Y.J. and Merzlyak, M.N. (1996) 'Use of a green channel in remote sensing of global vegetation from EOS-MODIS', *Remote Sensing of Environment*, 58(3), pp. 289-298.

Givnish, T. (2002) *Adaptive significance of evergreen vs. deciduous leaves: solving the triple paradox*.

Glenn, E.P., Huete, A.R., Nagler, P.L. and Nelson, S.G. (2008) 'Relationship between remotely-sensed vegetation indices, canopy attributes and plant physiological processes: what vegetation indices can and cannot tell us about the landscape', *Sensors*, 8(4), pp. 2136-2160.

Goldberg, M., Boucher, P. and Shlien, S. (1986) 'Image compression using adaptive vector quantization', *IEEE Transactions on Communications*, 34(2), pp. 180-187.

Goldman, D.B. (2010) 'Vignette and Exposure Calibration and Compensation', *Pattern Analysis and Machine Intelligence, IEEE Transactions on*, 32(12), pp. 2276-2288.

Gougeon, F.A. (1995) 'A Crown-Following Approach to the Automatic Delineation of Individual Tree Crowns in High Spatial Resolution Aerial Images', *Canadian Journal of Remote Sensing*, 21(3), pp. 274-284.

Gremban, K.D., Thorpe, C.E. and Kanade, T. (1988) 'Geometric camera calibration using systems of linear equations', *Robotics and Automation, 1988. Proceedings., 1988 IEEE International Conference on*. IEEE.

Haghighattalab, A., González Pérez, L., Mondal, S., Singh, D., Schinstock, D., Rutkoski, J., Ortiz-Monasterio, I., Singh, R.P., Goodin, D. and Poland, J. (2016) 'Application of unmanned aerial systems for high throughput phenotyping of large wheat breeding nurseries', *Plant Methods*, 12(1), p. 35.

Hakala, T., Honkavaara, E., Saari, H., Makynen, J., Kaivosoja, J., Pesonen, L. and Polonen, I. (2013) 'SPECTRAL IMAGING FROM UAVS UNDER VARYING ILLUMINATION CONDITIONS', in Grenzdorffer, G. and Bill, R. (eds.) *Uav-G2013*. pp. 189-194.

Hakala, T., Suomalainen, J. and Peltoniemi, J.I. (2010) 'Acquisition of Bidirectional Reflectance Factor Dataset Using a Micro Unmanned Aerial Vehicle and a Consumer Camera', *Remote Sensing*, 2(3), pp. 819-832.

Hanninen, H. and Tanino, K. (2011) 'Tree seasonality in a warming climate', *Trends in Plant Science*, 16(8), pp. 412-416.

Harwin, S. and Lucieer, A. (2012) 'Assessing the Accuracy of Georeferenced Point Clouds Produced via Multi-View Stereopsis from Unmanned Aerial Vehicle (UAV) Imagery', *Remote Sensing*, 4(6), pp. 1573-1599.

Healey, G.E. and Kondepudy, R. (1994) 'RADIOMETRIC CCD CAMERA CALIBRATION AND NOISE ESTIMATION', *Ieee Transactions on Pattern Analysis and Machine Intelligence*, 16(3), pp. 267-276.

Heilman, J.L., Kanemasu, E.T., Bagley, J.O. and Rasmussen, V.P. (1977) 'Evaluating soil moisture and yield of winter wheat in the Great Plains using Landsat data', *Remote sensing of Environment*, 6(4), pp. 315-326.

Henebry, G.M. and de Beurs, K.M. (2013) 'Remote sensing of land surface phenology: A prospectus', in *Phenology: An Integrative Environmental Science*. Springer, pp. 385-411.

Hernandez, J.G., Gonzalez-Ferreiro, E., Sarmento, A., Silva, J., Nunes, A., Correia, A.C., Fontes, L., Tomé, M. and Diaz-Varela, R. (2016) 'Using high resolution UAV imagery to estimate tree variables in Pinus pinea plantation in Portugal', *2016*, 25(2).

Herrero-Huerta, M., Hernández-López, D., Rodriguez-Gonzalvez, P., González-Aguilera, D. and González-Piqueras, J. (2014) 'Vicarious radiometric calibration of a multispectral sensor from an aerial trike applied to precision agriculture', *Computers and Electronics in Agriculture*, 108, pp. 28-38.

Higgins, S.I., Delgado-Cartay, M.D., February, E.C. and Combrink, H.J. (2011) 'Is there a temporal niche separation in the leaf phenology of savanna trees and grasses?', *Journal of Biogeography*, 38(11), pp. 2165-2175.

Hilker, T., Gitelson, A., Coops, N., Hall, F. and Black, T.A. (2011) 'Tracking plant physiological properties from multi-angular tower-based remote sensing', *Oecologia*, 165(4), pp. 865-876.

Hill, R.A., Wilson, A.K., George, M. and Hinsley, S.A. (2010) 'Mapping tree species in temperate deciduous woodland using time-series multi-spectral data', *Applied Vegetation Science*, 13(1), pp. 86-99.

Hmimina, G., Dufrêne, E., Pontailler, J.Y., Delpierre, N., Aubinet, M., Caquet, B., de Grandcourt, A., Burban, B., Flechard, C. and Granier, A. (2013) 'Evaluation of the potential of MODIS satellite data to predict vegetation phenology in different biomes: An investigation using ground-based NDVI measurements', *Remote Sensing of Environment*, 132, pp. 145-158.

Holst, G.C. (1998) 'CCD arrays, cameras, and displays'.

Honda, Y., Kajiwara, K., Sharma, R., Ono, A., Imaoka, K., Murakami, H., Hori, M., Ono, Y. and Rostand, D. (2012) 'Land validation for GCOM-C1/SGLI using UAV', in Meynart, R., Neeck, S.P. and Shimoda, H. (eds.) *Sensors, Systems, and Next-Generation Satellites Xvi*. Bellingham: SPIE.

Honkavaara, E., Arbiol, R., Markelin, L., Martinez, L., Cramer, M., Bovet, S., Chandelier, L., Ilves, R., Klonus, S., Marshal, P., Schlapfer, D., Tabor, M., Thom, C. and Veje, N. (2009) 'Digital Airborne Photogrammetry-A New Tool for Quantitative Remote Sensing?-A State-of-the-Art Review On Radiometric Aspects of Digital Photogrammetric Images', *Remote Sensing*, 1(3), pp. 577-605.

Hope, A.S., Pence, K.R. and Stow, D.A. (2004) 'NDVI from low altitude aircraft and composited NOAA AVHRR data for scaling Arctic ecosystem fluxes', *International Journal of Remote Sensing*, 25(20), pp. 4237-4250.

Huete, A., Didan, K., Miura, T., Rodriguez, E.P., Gao, X. and Ferreira, L.G. (2002) 'Overview of the radiometric and biophysical performance of the MODIS vegetation indices', *Remote sensing of environment*, 83(1), pp. 195-213.

Huete, A.R. (1988) 'A soil-adjusted vegetation index (SAVI)', *Remote Sensing of Environment*, 25(3), pp. 295-309.

Hufkens, K., Friedl, M., Sonnentag, O., Braswell, B.H., Milliman, T. and Richardson, A.D. (2012) 'Linking near-surface and satellite remote sensing measurements of deciduous broadleaf forest phenology', *Remote Sensing of Environment*, 117, pp. 307-321.

Hunt, E.R., Jr., Hively, W.D., Fujikawa, S.J., Linden, D.S., Daughtry, C.S.T. and McCarty, G.W. (2010) 'Acquisition of NIR-Green-Blue Digital Photographs from Unmanned Aircraft for Crop Monitoring', *Remote Sensing*, 2(1), pp. 290-305.

Hunt, R. (1996) 'Why is black-and-white so important in color?', *Color and Imaging Conference*. Society for Imaging Science and Technology.

Hunter, A.F. and Lechowicz, M.J. (1992) 'Predicting the timing of budburst in temperate trees', *Journal of Applied Ecology*, pp. 597-604.

Ibáñez, I., Primack, R.B., Miller-Rushing, A.J., Ellwood, E., Higuchi, H., Lee, S.D., Kobori, H. and Silander, J.A. (2010) 'Forecasting phenology under global warming', *Philosophical Transactions of the Royal Society of London B: Biological Sciences*, 365(1555), pp. 3247-3260.

Ide, R. and Oguma, H. (2010) 'Use of digital cameras for phenological observations', *Ecological Informatics*, 5(5), pp. 339-347.

IPCC (2014) 'Climate change 2014: synthesis report. Contribution of Working Groups I, II and III to the fifth assessment report of the Intergovernmental Panel on Climate Change' Pachauri, R.K., Allen, M.R., Barros, V.R., Broome, J., Cramer, W., Christ, R., Church, J.A., Clarke, L., Dahe, Q. and Dasgupta, P. Geneva, Switzerland: IPCC, p. 151. Available at: https://www.ipcc.ch/report/ar5/syr/.

Isaacson, B., Serbin, S. and Townsend, P. (2012) 'Detection of relative differences in phenology of forest species using Landsat and MODIS', *Landscape Ecology*, 27(4), pp. 529-543.

Jackson, R.D. and Huete, A.R. (1991) 'Interpreting vegetation indices', *Preventive Veterinary Medicine*, 11(3), pp. 185-200.

Jacquemoud, S., Bacour, C., Poilve, H. and Frangi, J.P. (2000) 'Comparison of four radiative transfer models to simulate plant canopies reflectance: Direct and inverse mode', *Remote Sensing of Environment*, 74(3), pp. 471-481.

Jain, A.K. (1981) 'IMAGE DATA-COMPRESSION - A REVIEW', *Proceedings of the Ieee*, 69(3), pp. 349-389.

James, M.R., Robson, S., d'Oleire-Oltmanns, S. and Niethammer, U. (2017) 'Optimising UAV topographic surveys processed with structure-from-motion: Ground control quality, quantity and bundle adjustment', *Geomorphology*, 280, pp. 51-66.

Janesick, J. and Blouke, M. (1987) 'Sky on a chip: the fabulous CCD', *Sky and Telescope*, 74.

Jenkins, J.P., Richardson, A.D., Braswell, B.H., Ollinger, S.V., Hollinger, D.Y. and Smith, M.L. (2007) 'Refining light-use efficiency calculations for a deciduous forest canopy using simultaneous tower-based carbon flux and radiometric measurements', *Agricultural and Forest Meteorology*, 143(1), pp. 64-79.

Jensen, J.R. (2007) *Remote Sensing of the Environment: An Earth Resource Perspective*. Pearson Prentice Hall.

Jiang, J., Liu, D., Gu, J. and Susstrunk, S. (2013) 'What is the space of spectral sensitivity functions for digital color cameras?', *Applications of Computer Vision (WACV), 2013 IEEE Workshop on*. IEEE.

Jones, M.O., Jones, L.A., Kimball, J.S. and McDonald, K.C. (2011) 'Satellite passive microwave remote sensing for monitoring global land surface phenology', *Remote Sensing of Environment*, 115(4), pp. 1102-1114.

Jonsson, P. and Eklundh, L. (2002) 'Seasonality extraction by function fitting to time-series of satellite sensor data', *Geoscience and Remote Sensing, IEEE Transactions on*, 40(8), pp. 1824-1832.

Jorde, D. (2016) *Phenology of the North Calotte*. Available at: https://www.miljolare.no/en/ (Accessed: 18/08/2016).

Julitta, T., Cremonese, E., Migliavacca, M., Colombo, R., Galvagno, M., Siniscalco, C., Rossini, M., Fava, F., Cogliati, S., Morra di Cella, U. and Menzel, A. (2014) 'Using digital camera images to analyse snowmelt and phenology of a subalpine grassland', *Agricultural and Forest Meteorology*, 198–199, pp. 116-125.

Kadomatsu, M. (1997) 'Differences in phenology of Quercus collected from northeastern China, eastern Hokkaido and western Honshu', *Research Bulletin of the Hokkaido University Forests*, 54(2), pp. 188-201.

Kanemasu, E.T. (1974) 'Seasonal canopy reflectance patterns of wheat, sorghum, and soybean', *Remote Sensing of Environment*, 3(1), pp. 43-47.

Ke, Y. and Quackenbush, L.J. (2011) 'A comparison of three methods for automatic tree crown detection and delineation from high spatial resolution imagery', *International Journal of Remote Sensing*, 32(13), pp. 3625-3647.

Keenan, T.F., Darby, B., Felts, E., Sonnentag, O., Friedl, M.A., Hufkens, K., O'Keefe, J., Klosterman, S., Munger, J.W., Toomey, M. and Richardson, A.D. (2014) 'Tracking forest phenology and seasonal physiology using digital repeat photography: a critical assessment', *Ecological Applications*, 24(6), pp. 1478-1489.

Kelcey, J. and Lucieer, A. (2012) 'Sensor correction of a 6-band multispectral imaging sensor for UAV remote sensing', *Remote Sensing*, 4(5), pp. 1462-1493.

Khwarahm, N.R., Dash, J., Skjoth, C.A., Newnham, R.M., Adams-Groom, B., Head, K., Caulton, E. and Atkinson, P.M. (2017) 'Mapping the birch and grass pollen seasons in the UK using satellite sensor time-series', *Science of the Total Environment*, 578, pp. 586-600.

Kimball, J.S., McDonald, K.C., Running, S.W. and Frolking, S.E. (2004) 'Satellite radar remote sensing of seasonal growing seasons for boreal and subalpine evergreen forests', *Remote Sensing of Environment*, 90(2), pp. 243-258.

Klosterman, S., Melaas, E., Wang, J., Martinez, A., Frederick, S., O'Keefe, J., Orwig, D.A., Wang, Z., Sun, Q., Schaaf, C., Friedl, M. and Richardson, A.D. (2018) 'Fine-scale perspectives on landscape phenology from unmanned aerial vehicle (UAV) photography', *Agricultural and Forest Meteorology*, 248(Supplement C), pp. 397-407.

Klosterman, S.T., Hufkens, K., Gray, J.M., Melaas, E., Sonnentag, O., Lavine, I., Mitchell, L., Norman, R., Friedl, M.A. and Richardson, A.D. (2014) 'Evaluating remote sensing of deciduous forest phenology at multiple spatial scales using PhenoCam imagery', *Biogeosciences*, 11(16), pp. 4305-4320.

Koenderink, J.J. and Vandoorn, A.J. (1991) 'AFFINE STRUCTURE FROM MOTION', *Journal of the Optical Society of America a-Optics Image Science and Vision*, 8(2), pp. 377-385.

Kramer, K. and Hänninen, H. (2009) 'The Annual Cycle of Development of Trees and Process-Based Modelling of Growth to Scale Up From the Tree To the Stand', in Noormets, A. (ed.) *Phenology of Ecosystem Processes: Applications in Global Change Research*. New York, NY: Springer New York, pp. 201-227.

Kung, O., Strecha, C., Beyeler, A., Zufferey, J.C., Floreano, D., Fua, P. and Gervaix, F. (2011) 'THE ACCURACY OF AUTOMATIC PHOTOGRAMMETRIC TECHNIQUES ON ULTRA-LIGHT UAV IMAGERY', in Eisenbeiss, H., Kunz, M. and Ingensand, H. (eds.) *International Conference on Unmanned Aerial Vehicle in Geomatics*. pp. 125-130.

Laliberte, A.S., Goforth, M.A., Steele, C.M. and Rango, A. (2011) 'Multispectral remote sensing from unmanned aircraft: image processing workflows and applications for rangeland environments', *Remote Sensing*, 3(11), pp. 2529-2551.

Lebourgeois, F., Pierrat, J.-C., Perez, V., Piedallu, C., Cecchini, S. and Ulrich, E. (2010) 'Simulating phenological shifts in French temperate forests under two climatic change scenarios and four driving global circulation models', *International Journal of Biometeorology*, 54(5), pp. 563-581.

Lebourgeois, V., Bégué, A., Labbé, S., Mallavan, B., Prévot, L. and Roux, B. (2008) 'Can commercial digital cameras be used as multispectral sensors? A crop monitoring test', *Sensors*, 8(11), pp. 7300-7322.

Lechowicz, M.J. (1984) 'Why Do Temperate Deciduous Trees Leaf Out at Different Times? Adaptation and Ecology of Forest Communities', *The American Naturalist*, 124(6), pp. 821-842.

Leckie, D.G., Gougeon, F.A., Tims, S., Nelson, T., Burnett, C.N. and Paradine, D. (2005) 'Automated tree recognition in old growth conifer stands with high resolution digital imagery', *Remote Sensing of Environment*, 94(3), pp. 311-326.

Lehmann, J.R.K., Nieberding, F., Prinz, T. and Knoth, C. (2015) 'Analysis of Unmanned Aerial System-Based CIR Images in Forestry-A New Perspective to Monitor Pest Infestation Levels', *Forests*, 6(3), pp. 594-612.

Lelong, C.C.D., Burger, P., Jubelin, G., Roux, B., Labbé, S. and Baret, F. (2008) 'Assessment of unmanned aerial vehicles imagery for quantitative monitoring of wheat crop in small plots', *Sensors*, 8(5), pp. 3557-3585.

Lempereur, M., Limousin, J.M., Guibal, F., Ourcival, J.M., Rambal, S., Ruffault, J. and Mouillot, F. (2017) 'Recent climate hiatus revealed dual control by temperature and drought on the stem growth of Mediterranean Quercus ilex', *Global Change Biology*, 23(1), pp. 42-55.

Lenz, R.K. and Tsai, R.Y. (1988) 'Techniques for calibration of the scale factor and image center for high accuracy 3-D machine vision metrology', *IEEE Transactions on pattern analysis and machine intelligence*, 10(5), pp. 713-720.

Lhermitte, S., Verbesselt, J., Verstraeten, W.W. and Coppin, P. (2011) 'A comparison of time series similarity measures for classification and change detection of ecosystem dynamics', *Remote Sensing of Environment*, 115(12), pp. 3129-3152.

Li, D., Guo, H.D., Wang, C., Li, W., Chen, H.Y. and Zuo, Z.L. (2016) 'Individual Tree Delineation in Windbreaks Using Airborne-Laser-Scanning Data and Unmanned Aerial Vehicle Stereo Images', *Ieee Geoscience and Remote Sensing Letters*, 13(9), pp. 1330-1334.

Li, F., Yang, W., Liu, X., Sun, G. and Liu, J. (2018) 'Using high-resolution UAV-borne thermal infrared imagery to detect coal fires in Majiliang mine, Datong coalfield, Northern China', *Remote Sensing Letters*, 9(1), pp. 71-80.

Li, Q., Wong, F. and Fung, T. (2017a) 'Assessing the utility of UAV-borne hyperspectral image and photogrammetry derived 3D data for wetland species distribution quick mapping', *The International Archives of Photogrammetry, Remote Sensing and Spatial Information Sciences*, 42, p. 209.

Li, W., Zhang, H. and Osen, O.L. (2017b) 'A UAV SAR Prototype for Marine and Arctic Application', (57748), p. V07BT06A002.

Liang, L., Schwartz, M. and Fei, S. (2012) 'Photographic assessment of temperate forest understory phenology in relation to springtime meteorological drivers', *International Journal of Biometeorology*, 56(2), pp. 343-355.

Liang, L. and Schwartz, M.D. (2009) 'Landscape phenology: an integrative approach to seasonal vegetation dynamics', *Landscape Ecology*, 24(4), pp. 465-472.

Liang, L., Schwartz, M.D. and Fei, S. (2011) 'Validating satellite phenology through intensive ground observation and landscape scaling in a mixed seasonal forest', *Remote Sensing of Environment*, 115(1), pp. 143-157.

Lim, Y.S., La, P.H., Park, J.S., Lee, M.H., Pyeon, M.W. and Kim, J.-I. (2015) 'Calculation of Tree Height and Canopy Crown from Drone Images Using Segmentation', *Journal of the Korean Society of Surveying, Geodesy, Photogrammetry and Cartography*, 33(6), pp. 605-614.

Lin, S. (2014) 'Calibration of Radiometric Falloff (Vignetting)', in Ikeuchi, K. (ed.) *Computer Vision*. Springer US, pp. 74-76.

Lisein, J., Linchant, J., Lejeune, P., Bouché, P. and Vermeulen, C. (2013) 'Aerial surveys using an Unmanned Aerial System (UAS): comparison of different methods for estimating the surface area of sampling strips', *Tropical Conservation Science*, 6(4).

Lisein, J., Michez, A., Claessens, H. and Lejeune, P. (2015) 'Discrimination of Deciduous Tree Species from Time Series of Unmanned Aerial System Imagery', *Plos One*, 10(11).

Liu, H.J., Kang, R., Ustin, S., Zhang, X.L., Fu, Q., Sheng, L. and Sun, T.Y. (2016) 'Study on the Prediction of Cotton Yield within Field Scale with Time Series Hyperspectral Imagery', *Spectroscopy and Spectral Analysis*, 36(8), pp. 2585-2589.

Liu, L., Liang, L., Schwartz, M.D., Donnelly, A., Wang, Z., Schaaf, C.B. and Liu, L. (2015) 'Evaluating the potential of MODIS satellite data to track temporal dynamics of autumn phenology in a temperate mixed forest', *Remote Sensing of Environment*, 160(0), pp. 156-165.

Liu, Y., Hill, M.J., Zhang, X., Wang, Z., Richardson, A.D., Hufkens, K., Filippa, G., Baldocchi, D.D., Ma, S., Verfaillie, J. and Schaaf, C.B. (2017) 'Using data from Landsat, MODIS, VIIRS and PhenoCams to monitor the phenology of California oak/grass savanna and open grassland across spatial scales', *Agricultural and Forest Meteorology*, 237–238, pp. 311-325.

Lopez-Sanchez, J.M., Ballester-Berman, J.D. and Hajnsek, I. (2011) 'First Results of Rice Monitoring Practices in Spain by Means of Time Series of TerraSAR-X Dual-Pol Images', *IEEE Journal of Selected Topics in Applied Earth Observations and Remote Sensing*, 4(2), pp. 412-422.

Lu, L., Guo, H., Wang, C. and Li, Q. (2013a) 'Assessment of the SeaWinds scatterometer for vegetation phenology monitoring across China', *International Journal of Remote Sensing*, 34(15), pp. 5551-5568.

Lu, L.L., Guo, H.D., Wang, C.Z. and Li, Q.T. (2013b) 'Assessment of the SeaWinds scatterometer for vegetation phenology monitoring across China', *International Journal of Remote Sensing*, 34(15), pp. 5551-5568.

Lucas, R., Bunting, P., Paterson, M. and Chisholm, L. (2008) 'Classification of Australian forest communities using aerial photography, CASI and HyMap data', *Remote Sensing of Environment*, 112(5), pp. 2088-2103.

Malenovský, Z., Lucieer, A., King, D.H., Turnbull, J.D. and Robinson, S.A. (2017) 'Unmanned aircraft system advances health mapping of fragile polar vegetation', *Methods in Ecology and Evolution*, 8(12), pp. 1842-1857.

Mascolo, L., Lopez-Sanchez, J.M., Vicente-Guijalba, F., Mazzarella, G., Nunziata, F. and Migliaccio, M. (2015) 'Retrieval of phenological stages of onion fields during the first year of growth by means of C-band polarimetric SAR measurements', *International Journal of Remote Sensing*, 36(12), pp. 3077-3096.

Matese, A., Toscano, P., Di Gennaro, S.F., Genesio, L., Vaccari, F.P., Primicerio, J., Belli, C., Zaldei, A., Bianconi, R. and Gioli, B. (2015) 'Intercomparison of UAV, Aircraft and Satellite Remote Sensing Platforms for Precision Viticulture', *Remote Sensing*, 7(3), pp. 2971-2990.

Mathews, A.J. (2014) *Assessing Grapevine Canopy Health in the Texas Hill Country with Remote Sensing and GIS Techniques*. Texas State University [Online]. Available at: https://digital.library.txstate.edu/handle/10877/4945.

Mathews, A.J. (2015) 'A Practical UAV Remote Sensing Methodology to Generate Multispectral Orthophotos for Vineyards: Estimation of Spectral Reflectance Using Compact Digital Cameras', *International Journal of Applied Geospatial Research (IJAGR)*, 6(4), pp. 65-87.

Matsushita, B., Yang, W., Chen, J., Onda, Y. and Qiu, G. (2007) 'Sensitivity of the Enhanced Vegetation Index (EVI) and Normalized Difference Vegetation Index (NDVI) to Topographic Effects: A Case Study in High-Density Cypress Forest', *Sensors*, 7(11), pp. 2636-2651.

McGwire, K.C., Weltz, M.A., Finzel, J.A., Morris, C.E., Fenstermaker, L.F. and McGraw, D.S. (2013) 'Multiscale assessment of green leaf cover in a semi-arid rangeland with a small unmanned aerial vehicle', *International Journal of Remote Sensing*, 34(5), pp. 1615-1632.

McNairn, H., Kross, A., Lapen, D., Caves, R. and Shang, J. (2014) 'Early season monitoring of corn and soybeans with TerraSAR-X and RADARSAT-2', *International Journal of Applied Earth Observation and Geoinformation*, 28, pp. 252-259.

Mehdipoor, H., Zurita-Milla, R., Rosemartin, A., Gerst, K.L. and Weltzin, J.F. (2015) 'Developing a Workflow to Identify Inconsistencies in Volunteered Geographic Information: A Phenological Case Study', *PLoS ONE*, 10(10), p. e0140811.

Mei, C. and Durrieu, S. (2004) 'Tree crown delineation from digital elevation models and high resolution imagery', *Proc. IAPRS*, 36, pp. 218-223.

Melaas, E.K., Friedl, M.A. and Zhu, Z. (2013) 'Detecting interannual variation in deciduous broadleaf forest phenology using Landsat TM/ETM plus data', *Remote Sensing of Environment*, 132, pp. 176-185.

Melaas, E.K., Sulla-Menashe, D., Gray, J.M., Black, T.A., Morin, T.H., Richardson, A.D. and Friedl, M.A. (2016) 'Multisite analysis of land surface phenology in North American temperate and boreal deciduous forests from Landsat', *Remote Sensing of Environment*, 186, pp. 452-464.

Menzel, A. (2002) 'Phenology: its importance to the global change community', *Climatic change*, 54(4), pp. 379-385.

Menzel, A., Sparks, T.H., Estrella, N., Koch, E., Aasa, A., Ahas, R., Alm-KÜBler, K., Bissolli, P., Braslavská, O.g. and Briede, A. (2006) 'European phenological response to climate change matches the warming pattern', *Global Change Biology*, 12(10), pp. 1969-1976.

Meyer, F. and Beucher, S. (1990) 'Morphological segmentation', *Journal of Visual Communication and Image Representation*, 1(1), pp. 21-46.

Miao, L., Luan, Y., Luo, X., Liu, Q., Moore, J.C., Nath, R., He, B., Zhu, F. and Cui, X. (2013) 'Analysis of the Phenology in the Mongolian Plateau by Inter-Comparison of Global Vegetation Datasets', *Remote Sensing*, 5(10), pp. 5193-5208.

Michez, A., Piégay, H., Lisein, J., Claessens, H. and Lejeune, P. (2016) 'Classification of riparian forest species and health condition using multi-temporal and hyperspatial imagery from unmanned aerial system', *Environmental Monitoring and Assessment*, 188(3), pp. 1-19.

Migliavacca, M., Sonnentag, O., Keenan, T.F., Cescatti, A., O'Keefe, J. and Richardson, A.D. (2012) 'On the uncertainty of phenological responses to climate change, and implications for a terrestrial biosphere model', *Biogeosciences*, 9(6), pp. 2063-2083.

Miller-Rushing, A.J., Lloyd-Evans, T.L., Primack, R.B. and Satzinger, P. (2008) 'Bird migration times, climate change, and changing population sizes', *Global Change Biology*, 14(9), pp. 1959-1972.

Mizunuma, T., Mencuccini, M., Wingate, L., Ogée, J., Nichol, C. and Grace, J. (2014) 'Sensitivity of colour indices for discriminating leaf colours from digital photographs', *Methods in Ecology and Evolution*, 5(10), pp. 1078-1085.

Mizunuma, T., Wilkinson, M., L Eaton, E., Mencuccini, M., Il Morison, J. and Grace, J. (2013) 'The relationship between carbon dioxide uptake and canopy colour from two camera systems in a deciduous forest in southern England', *Functional Ecology*, 27(1), pp. 196-207.

Monte, M.A., Reis, M.d.G.F., dos Reis, G.G., Leite, H.G. and Stocks, J.J. (2007) 'Métodos indiretos de estimação da cobertura de dossel em povoamentos de clone de eucalipto', *Pesquisa Agropecuária Brasileira*, 42(6), pp. 769-775.

Montes-Hugo, M.A., Barrado, C. and Pastor, E. (2015) 'A NEW TECHNIQUE BASED ON MINI-UAS FOR ESTIMATING WATER AND BOTTOM RADIANCE CONTRIBUTIONS IN OPTICALLY SHALLOW WATERS', *Int. Arch. Photogramm. Remote Sens. Spatial Inf. Sci.*, XL-1/W4, pp. 375-379.

Moore, C.E., Brown, T., Keenan, T.F., Duursma, R.A., van Dijk, A., Beringer, J., Culvenor, D., Evans, B., Huete, A., Hutley, L.B., Maier, S., Restrepo-Coupe, N., Sonnentag, O., Specht, A., Taylor, J.R., van Gorsel, E. and Liddell, M.J. (2016) 'Reviews and syntheses: Australian vegetation phenology: new insights from satellite remote sensing and digital repeat photography', *Biogeosciences*, 13(17), pp. 5085-5102.

Morellato, L.P.C., Camargo, M.G.G., D'Eça Neves, F.F., Luize, B.G., Mantovani, A. and Hudson, I.L. (2010) 'The Influence of Sampling Method, Sample Size, and Frequency of Observations on Plant Phenological Patterns and Interpretation in Tropical Forest Trees', in Hudson, I.L. and Keatley, M.R. (eds.) *Phenological Research: Methods for Environmental and Climate Change Analysis*. Dordrecht: Springer Netherlands, pp. 99-121.

Morin, X., Roy, J., Sonie, L. and Chuine, I. (2010) 'Changes in leaf phenology of three European oak species in response to experimental climate change', *New Phytologist*, 186(4), pp. 900-910.

Morin, X., Viner, D. and Chuine, I. (2008) 'Tree species range shifts at a continental scale: new predictive insights from a process-based model', *Journal of Ecology*, 96(4), pp. 784-794.

Morisette, J.T., Jarnevich, C.S., Ullah, A., Cai, W.J., Pedelty, J.A., Gentle, J.E., Stohlgren, T.J. and Schnase, J.L. (2006) 'A tamarisk habitat suitability map for the continental United States', *Frontiers in Ecology and the Environment*, 4(1), pp. 11-17.

Morisette, J.T., Privette, J.L. and Justice, C.O. (2002) 'A framework for the validation of MODIS Land products', *Remote Sensing of Environment*, 83(1–2), pp. 77-96.

Morisette, J.T., Richardson, A.D., Knapp, A.K., Fisher, J.I., Graham, E.A., Abatzoglou, J., Wilson, B.E., Breshears, D.D., Henebry, G.M., Hanes, J.M. and Liang, L. (2009) 'Tracking the rhythm of the seasons in the face of global change: phenological research in the 21st century', *Frontiers in Ecology and the Environment*, 7(5), pp. 253-260.

Morris, D.E., Boyd, D.S., Crowe, J.A., Johnson, C.S. and Smith, K.L. (2013) 'Exploring the Potential for Automatic Extraction of Vegetation Phenological Metrics from Traffic Webcams', *Remote Sensing*, 5(5), pp. 2200-2218.

Mulder, C.P.H., Iles, D.T. and Rockwell, R.F. (2017) 'Increased variance in temperature and lag effects alter phenological responses to rapid warming in a subarctic plant community', *Global Change Biology*, 23(2), pp. 801-814.

Müllerová, J., Bartaloš, T., Brůna, J., Dvořák, P. and Vítková, M. (2017a) 'Unmanned aircraft in nature conservation: an example from plant invasions', *International Journal of Remote Sensing*, pp. 1-22.

Müllerová, J., Brůna, J., Bartaloš, T., Dvořák, P., Vítková, M. and Pyšek, P. (2017b) 'Timing Is Important: Unmanned Aircraft vs. Satellite Imagery in Plant Invasion Monitoring', *Frontiers in Plant Science*, 8(887).

Muralikrishna, P., Prakash, S. and Subbaraya, B.H. (1982) 'Digital processing of spacelab imagery', *Advances in Space Research*, 2(7), pp. 107-110.

Myneni, R.B. and Asrar, G. (1994) 'ATMOSPHERIC EFFECTS AND SPECTRAL VEGETATION INDEXES', *Remote Sensing of Environment*, 47(3), pp. 390-402.

Myneni, R.B., Hoffman, S., Knyazikhin, Y., Privette, J.L., Glassy, J., Tian, Y., Wang, Y., Song, X., Zhang, Y., Smith, G.R., Lotsch, A., Friedl, M., Morisette, J.T., Votava, P., Nemani, R.R. and Running, S.W. (2002) 'Global products of vegetation leaf area and fraction absorbed PAR from year one of MODIS data', *Remote Sensing of Environment*, 83(1–2), pp. 214-231.

Nagai, S., Inoue, T., Ohtsuka, T., Kobayashi, H., Kurumado, K., Muraoka, H. and Nasahara, K.N. (2014) 'Relationship between spatio-temporal characteristics of leaf-fall phenology and seasonal variations in near surface- and satellite-observed vegetation indices in a cool-temperate deciduous broad-leaved forest in Japan', *International Journal of Remote Sensing*, 35(10), pp. 3520-3536.

Nagai, S., Nasahara, K., Inoue, T., Saitoh, T. and Suzuki, R. (2015) 'Review: advances in in situ and satellite phenological observations in Japan', *International Journal of Biometeorology*, pp. 1-13.

Nagai, S., Saitoh, T.M., Kobayashi, H., Ishihara, M., Suzuki, R., Motohka, T., Nasahara, K.N. and Muraoka, H. (2012) 'In situ examination of the relationship between various vegetation indices and canopy phenology in an evergreen coniferous forest, Japan', *International Journal of Remote Sensing*, 33(19), pp. 6202-6214.

Nagai, S., Saitoh, T.M., Noh, N.J., Yoon, T.K., Kobayashi, H., Suzuki, R., Nasahara, K.N., Son, Y. and Muraoka, H. (2013) 'Utility of information in photographs taken upwards from the floor of closed-canopy deciduous broadleaved and closed-canopy evergreen coniferous forests for continuous observation of canopy phenology', *Ecological Informatics*.

Nagol, J.R., Vermote, E.F. and Prince, S.D. (2009) 'Effects of atmospheric variation on AVHRR NDVI data', *Remote Sensing of Environment*, 113(2), pp. 392-397.

Nagy, G. (1985) 'Image database', *Image and Vision Computing*, 3(3), pp. 111-117.

Nasahara, K. and Nagai, S. (2015) 'Review: Development of an in situ observation network for terrestrial ecological remote sensing: the Phenological Eyes Network (PEN)', *Ecological Research*, 30(2), pp. 211-223.

National Science Foundation (2016) *Season Spotter*. Available at: http://seasonspotter.org/ (Accessed: 18/08/2016).

Nevalainen, O., Honkavaara, E., Tuominen, S., Viljanen, N., Hakala, T., Yu, X., Hyyppä, J., Saari, H., Pölönen, I., Imai, N. and Tommaselli, A. (2017) 'Individual Tree Detection and Classification with UAV-Based Photogrammetric Point Clouds and Hyperspectral Imaging', *Remote Sensing*, 9(3), p. 185.

Newcastle University (2015) *Cockle Park Weather Station monthly records*. Available at: https://www.ncl.ac.uk/library/nclonly/cockle_park_data/ (Accessed: 14/01/2017).

Ni, J., Yao, L.L., Zhang, J.C., Cao, W.X., Zhu, Y. and Tai, X.X. (2017) 'Development of an Unmanned Aerial Vehicle-Borne Crop-Growth Monitoring System', *Sensors*, 17(3).

Niethammer, U., James, M.R., Rothmund, S., Travelletti, J. and Joswig, M. (2012) 'UAV-based remote sensing of the Super-Sauze landslide: Evaluation and results', *Engineering Geology*, 128, pp. 2-11.

Nijland, W., de Jong, R., de Jong, S.M., Wulder, M.A., Bater, C.W. and Coops, N.C. (2014) 'Monitoring plant condition and phenology using infrared sensitive consumer grade digital cameras', *Agricultural and Forest Meteorology*, 184, pp. 98-106.

Norby, R.J., Hartz-Rubin, J.S. and Verbrugge, M.J. (2003) 'Phenological responses in maple to experimental atmospheric warming and CO2 enrichment', *Global Change Biology*, 9(12), pp. 1792-1801.

Oliveira, G., Correia, O., Martins-Loução, M.A. and Catarino, F.M. (1994) 'Phenological and growth patterns of the Mediterranean oak Quercus suber L', *Trees*, 9(1), pp. 41-46.

Optronic (2002) *OL Series 750 Automated Spectroradiometric Measurement System* (M000215).

Panagiotidis, D., Abdollahnejad, A., Surový, P. and Chiteculo, V. (2016) 'Determining tree height and crown diameter from high-resolution UAV imagery', *International Journal of Remote Sensing*, pp. 1-19.

Parulski, K.A. (1985) 'COLOR FILTERS AND PROCESSING ALTERNATIVES FOR ONE-CHIP CAMERAS', *Ieee Transactions on Electron Devices*, 32(8), pp. 1381-1389.

Peddle, D.R., Hall, F.G. and LeDrew, E.F. (1999) 'Spectral Mixture Analysis and Geometric-Optical Reflectance Modeling of Boreal Forest Biophysical Structure', *Remote Sensing of Environment*, 67(3), pp. 288-297.

Phillimore, A.B., Proios, K., O'Mahony, N., Bernard, R., Lord, A.M., Atkinson, S. and Smithers, R.J. (2013) 'Inferring local processes from macro-scale phenological pattern: a comparison of two methods', *Journal of Ecology*, 101(3), pp. 774-783.

Piao, S., Fang, J., Zhou, L., Ciais, P. and Zhu, B. (2006) 'Variations in satellite-derived phenology in China's temperate vegetation', *Global Change Biology*, 12(4), pp. 672-685.

Pisek, J., Rautiainen, M., Nikopensius, M. and Raabe, K. (2015) 'Estimation of seasonal dynamics of understory NDVI in northern forests using MODIS BRDF data: Semi-empirical versus physically-based approach', *Remote Sensing of Environment*, 163, pp. 42-47.

Polgar, C., Primack, R., Dukes, J., Schaaf, C., Wang, Z. and Hoeppner, S. (2013) 'Tree leaf out response to temperature: comparing field observations, remote sensing, and a warming experiment', *International Journal of Biometeorology*, pp. 1-7.

Polgar, C.A. and Primack, R.B. (2011) 'Leaf-out phenology of temperate woody plants: from trees to ecosystems', *New Phytologist*, 191(4), pp. 926-941.

Polgar, C.A. and Primack, R.B. (2013) 'Leaf out phenology in temperate forests', *Biodiversity Science*, 21(1), pp. 111-116.

Pölönen, I., Saari, H., Kaivosoja, J., Honkavaara, E. and Pesonen, L. (2013) 'Hyperspectral imaging based biomass and nitrogen content estimations from light-weight UAV', *SPIE Remote Sensing*. SPIE.

Pouliot, D.A., King, D.J., Bell, F.W. and Pitt, D.G. (2002) 'Automated tree crown detection and delineation in high-resolution digital camera imagery of coniferous forest regeneration', *Remote Sensing of Environment*, 82(2-3), pp. 322-334.

Proisy, C., Mougin, E., Dufrene, E. and Le Dantec, V. (2000) 'Monitoring seasonal changes of a mixed temperate forest using ERS SAR observations', *Ieee Transactions on Geoscience and Remote Sensing*, 38(1), pp. 540-552.

Puliti, S., Orka, H.O., Gobakken, T. and Naesset, E. (2015) 'Inventory of Small Forest Areas Using an Unmanned Aerial System', *Remote Sensing*, 7(8), pp. 9632-9654.

PwC (2016) *Clarity from above. PwC global report on the commercial applications of drone technology.* Available at: http://pwc.blogs.com/files/clarity-from-above-pwc.pdf (Accessed: 17/01/2018).

Qi, J., Kerr, Y. and Chehbouni, A. (1994) 'External factor consideration in vegetation index development', *Sixth International Colloquium on Physical Measurements and Signatures in Remote Sensing*. Val d'Isère, France pp. 723-730.

Rabatel, G., Gorretta, N. and Labbe, S. (2014) 'Getting simultaneous red and near-infrared band data from a single digital camera for plant monitoring applications: Theoretical and practical study', *Biosystems Engineering*, 117, pp. 2-14.

Rasmussen, J., Ntakos, G., Nielsen, J., Svensgaard, J., Poulsen, R.N. and Christensen, S. (2016) 'Are vegetation indices derived from consumer-grade cameras mounted on UAVs sufficiently reliable for assessing experimental plots?', *European Journal of Agronomy*, 74, pp. 75-92.

Rautiainen, M., Mõttus, M., Heiskanen, J., Akujärvi, A., Majasalmi, T. and Stenberg, P. (2011) 'Seasonal reflectance dynamics of common understory types in a northern European boreal forest', *Remote Sensing of Environment*, 115(12), pp. 3020-3028.

Ray, D., Morison, J. and Broadmeadow, M. (2010) 'Climate change: impacts and adaptation in England's woodlands', *Research Note-Forestry Commission*, (201).

Reed, B.C., Brown, J.F., VanderZee, D., Loveland, T.R., Merchant, J.W. and Ohlen, D.O. (1994) 'Measuring phenological variability from satellite imagery', *Journal of Vegetation Science*, 5(5), pp. 703-714.

Reed, B.C., Schwartz, M.D. and Xiao, X. (2009) 'Remote Sensing Phenology: Status and the way forward', in *Phenology of ecosystem processes*. Springer, pp. 231-246.

Ricciuto, D.M., Butler, M.P., Davis, K.J., Cook, B.D., Bakwin, P.S., Andrews, A. and Teclaw, R.M. (2008) 'Causes of interannual variability in ecosystem-atmosphere CO2 exchange in a northern Wisconsin forest using a Bayesian model calibration', *Agricultural and Forest Meteorology*, 148(2), pp. 309-327.

Richardson, A. and O'Keefe, J. (2009) 'Phenological Differences Between Understory and Overstory', in Noormets, A. (ed.) *Phenology of Ecosystem Processes*. Springer New York, pp. 87-117.

Richardson, A.D., Anderson, R.S., Arain, M.A., Barr, A.G., Bohrer, G., Chen, G.S., Chen, J.M., Ciais, P., Davis, K.J., Desai, A.R., Dietze, M.C., Dragoni, D., Garrity, S.R., Gough, C.M., Grant, R., Hollinger, D.Y., Margolis, H.A., McCaughey, H., Migliavacca, M., Monson, R.K., Munger, J.W., Poulter, B., Raczka, B.M., Ricciuto, D.M., Sahoo, A.K., Schaefer, K., Tian, H.Q., Vargas, R., Verbeeck, H., Xiao, J.F. and Xue, Y.K. (2012) 'Terrestrial biosphere models need better representation of vegetation phenology: results from the North American Carbon Program Site Synthesis', *Global Change Biology*, 18(2), pp. 566-584.

Richardson, A.D., Braswell, B.H., Hollinger, D.Y., Jenkins, J.P. and Ollinger, S.V. (2009) 'Near-surface remote sensing of spatial and temporal variation in canopy phenology', *Ecological Applications*, 19(6), pp. 1417-1428.

Richardson, A.D., Jenkins, J.P., Braswell, B.H., Hollinger, D.Y., Ollinger, S.V. and Smith, M.-L. (2007) 'Use of digital webcam images to track spring green-up in a deciduous broadleaf forest', *Oecologia*, 152(2), pp. 323-334.

Richardson, A.D., Keenan, T.F., Migliavacca, M., Ryu, Y., Sonnentag, O. and Toomey, M. (2013a) 'Climate change, phenology, and phenological control of vegetation feedbacks to the climate system', *Agricultural and Forest Meteorology*, 169, pp. 156-173.

Richardson, A.D., Klosterman, S. and Toomey, M. (2013b) 'Near-Surface Sensor-Derived Phenology', in *Phenology: An Integrative Environmental Science*. Springer, pp. 413-430.

Ritchie, G.L., Sullivan, D.G., Perry, C.D., Hook, J.E. and Bednarz, C.W. (2008) 'Preparation of a low-cost digital camera system for remote sensing', *Applied engineering in agriculture*, 24(6), p. 885.

Robinson, I. and MacArthur, A. (2011) 'The Field Spectroscopy Facility Post Processing Toolbox User Guide' *Post processing spectral data in MATLAB* [Other contribution]. Edinburgh, UK: Field Spectroscopy Facility, Natural Environment Research Council, p. 27. Available at: http://www.mathworks.com/matlabcentral/fileexchange/31547-field-spectroscopy-facility-post-processing-toolbox.

Rodriguez-Galiano, V.F., Dash, J. and Atkinson, P.M. (2015) 'Intercomparison of satellite sensor land surface phenology and ground phenology in Europe', *Geophysical Research Letters*, 42(7), pp. 2253-2260.

Roerink, G.J., Menenti, M. and Verhoef, W. (2000) 'Reconstructing cloudfree NDVI composites using Fourier analysis of time series', *International Journal of Remote Sensing*, 21(9), pp. 1911-1917.

Rogers, B.M., Jantz, P. and Goetz, S.J. (2017) 'Vulnerability of eastern US tree species to climate change', *Global Change Biology*, 23(8), pp. 3302-3320.

Rondeaux, G., Steven, M. and Baret, F. (1996) 'Optimization of soil-adjusted vegetation indices', *Remote Sensing of Environment*, 55(2), pp. 95-107.

Rötzer, T., Grote, R. and Pretzsch, H. (2004) 'The timing of bud burst and its effect on tree growth', *International Journal of Biometeorology*, 48(3), pp. 109-118.

Rouse, J.W., Haas, R.H., Schell, J.A. and Deering, D.W. (1973) 'Monitoring vegetation systems in the Great Plains with ERTS', *Third ERTS Symposium*. Washington. D.C. NASA SP, pp. 309-317. Available at: http://ntrs.nasa.gov/archive/nasa/casi.ntrs.nasa.gov/19740022592.pdf.

Rüetschi, M., Schaepman, M. and Small, D. (2018) 'Using Multitemporal Sentinel-1 C-band Backscatter to Monitor Phenology and Classify Deciduous and Coniferous Forests in Northern Switzerland', *Remote Sensing*, 10(1), p. 55.

Ryan, C.M., Williams, M., Hill, T.C., Grace, J. and Woodhouse, I.H. (2012) 'Assessing the Phenology of Southern Tropical Africa: A Comparison of Hemispherical Photography, Scatterometry, and Optical/NIR Remote Sensing'.

Rychkov, I., Brasington, J. and Vericat, D. (2012) 'Computational and methodological aspects of terrestrial surface analysis based on point clouds', *Computers & Geosciences*, 42, pp. 64-70.

Ryu, Y., Verfaillie, J., Macfarlane, C., Kobayashi, H., Sonnentag, O., Vargas, R., Ma, S. and Baldocchi, D.D. (2012) 'Continuous observation of tree leaf area index at ecosystem scale using upward-pointing digital cameras', *Remote Sensing of Environment*, 126, pp. 116-125.

Said, A. and Pearlman, W.A. (1996) 'An image multiresolution representation for lossless and lossy compression', *IEEE Transactions on image processing*, 5(9), pp. 1303-1310.

Samiappan, S., Turnage, G., Hathcock, L.A. and Moorhead, R. (2017) 'Mapping of invasive phragmites (common reed) in Gulf of Mexico coastal wetlands using multispectral imagery and small unmanned aerial systems', *International Journal of Remote Sensing*, 38(8-10), pp. 2861-2882.

Samseemoung, G., Soni, P., Jayasuriya, H.P.W. and Salokhe, V.M. (2012) 'Application of low altitude remote sensing (LARS) platform for monitoring crop growth and weed infestation in a soybean plantation', *Precision Agriculture*, 13(6), pp. 611-627.

Sandmeier, S.R. and Itten, K.I. (1999) 'A field goniometer system (FIGOS) for acquisition of hyperspectral BRDF data', *IEEE Transactions on Geoscience and Remote Sensing*, 37(2), pp. 978-986.

Sankey, T., Donager, J., McVay, J. and Sankey, J.B. (2017) 'UAV lidar and hyperspectral fusion for forest monitoring in the southwestern USA', *Remote Sensing of Environment*, 195, pp. 30-43.

Santesteban, L.G., Di Gennaro, S.F., Herrero-Langreo, A., Miranda, C., Royo, J.B. and Matese, A. (2017) 'High-resolution UAV-based thermal imaging to estimate the instantaneous and seasonal variability of plant water status within a vineyard', *Agricultural Water Management*, 183, pp. 49-59.

Sawchuk, A.A. (1977) 'REAL-TIME CORRECTION OF INTENSITY NONLINEARITIES IN IMAGING-SYSTEMS', *Ieee Transactions on Computers*, 26(1), pp. 34-39.

Schaber, D.S.-W.J. (2002) *Phenology in Germany in the 20th century: methods, analyses and models*. UNIVERSITY of POTSDAM, GERMANY.

Schaber, J. and Badeck, F.-W. (2003) 'Physiology-based phenology models for forest tree species in Germany', *International Journal of Biometeorology*, 47(4), pp. 193-201.

Schofield, L.A. (2016) *QUANTIFYING STRUCTURAL CHANGE IN UK WOODLAND CANOPIES WITH A DUAL-WAVELENGTH FULL WAVEFORM TERRESTRIAL LASER SCANNER.* University of Salford [Online]. Available at: http://usir.salford.ac.uk/38743/1/Schofield_thesis_final.pdf.

Schwartz, M.D. (2013) 'Introduction', in *Phenology: An Integrative Environmental Science.* Springer, pp. 1-4.

Schwartz, M.D., Hanes, J.M. and Liang, L. (2013) 'Comparing carbon flux and high-resolution spring phenological measurements in a northern mixed forest', *Agricultural and Forest Meteorology*, 169(0), pp. 136-147.

Schwartz, M.D., Reed, B.C. and White, M.A. (2002) 'Assessing satellite-derived start-of-season measures in the conterminous USA', *International Journal of Climatology*, 22(14), pp. 1793-1805.

Seidel, D., Fleck, S. and Leuschner, C. (2012) 'Analyzing forest canopies with ground-based laser scanning: A comparison with hemispherical photography', *Agricultural and Forest Meteorology*, 154-155(Supplement C), pp. 1-8.

Shahtahmassebi, A., Yang, N., Wang, K., Moore, N. and Shen, Z. (2013) 'Review of shadow detection and de-shadowing methods in remote sensing', *Chinese Geographical Science*, 23(4), pp. 403-420.

Sharma, R.C., Kajiwara, K. and Honda, Y. (2013) 'Automated extraction of canopy shadow fraction using unmanned helicopter-based color vegetation indices', *Trees-Structure and Function*, 27(3), pp. 675-684.

Silva, C.A., Hudak, A.T., Vierling, L.A., Loudermilk, E.L., O'Brien, J.J., Hiers, J.K., Jack, S.B., Gonzalez-Benecke, C., Lee, H., Falkowski, M.J. and Khosravipour, A. (2016) 'Imputation of Individual Longleaf Pine (Pinus palustris Mill.) Tree Attributes from Field and LiDAR Data', *Canadian Journal of Remote Sensing*, 42(5), pp. 554-573.

Smigaj, M., Gaulton, R., Barr, S.L. and Suarez, J.C. (2015) 'UAV-BORNE THERMAL IMAGING FOR FOREST HEALTH MONITORING: DETECTION OF DISEASE-INDUCED CANOPY TEMPERATURE INCREASE', in Mallet, C., Paparoditis, N., Dowman, I., Elberink, S.O., Raimond, A.M., Sithole, G., Rabatel, G., Rottensteiner, F., Briottet, X., Christophe, S., Coltekin, A. and Patane, G. (eds.) *Isprs Geospatial Week 2015.* Gottingen: Copernicus Gesellschaft Mbh, pp. 349-354.

Smith, G.M. and Milton, E.J. (1999) 'The use of the empirical line method to calibrate remotely sensed data to reflectance', *International Journal of Remote Sensing*, 20(13), pp. 2653-2662.

Snavely, N., Seitz, S.M. and Szeliski, R. (2008) 'Modeling the world from Internet photo collections', *International Journal of Computer Vision*, 80(2), pp. 189-210.

Sonnentag, O., Hufkens, K., Teshera-Sterne, C., Young, A.M., Friedl, M., Braswell, B.H., Milliman, T., O'Keefe, J. and Richardson, A.D. (2012) 'Digital repeat photography for phenological research in forest ecosystems', *Agricultural and Forest Meteorology*, 152, pp. 159-177.

Soudani, K., Hmimina, G., Delpierre, N., Pontailler, J.Y., Aubinet, M., Bonal, D., Caquet, B., de Grandcourt, A., Burban, B., Flechard, C., Guyon, D., Granier, A., Gross, P., Heinesh, B., Longdoz, B., Loustau, D., Moureaux, C., Ourcival, J.M., Rambal, S., Saint Andre, L. and Dufrene, E. (2012) 'Ground-based Network of NDVI measurements for tracking temporal dynamics of canopy structure and vegetation phenology in different biomes', *Remote Sensing of Environment*, 123, pp. 234-245.

Soudani, K., le Maire, G., Dufrêne, E., François, C., Delpierre, N., Ulrich, E. and Cecchini, S. (2008) 'Evaluation of the onset of green-up in temperate deciduous broadleaf forests derived from Moderate Resolution Imaging Spectroradiometer (MODIS) data', *Remote Sensing of Environment*, 112(5), pp. 2643-2655.

Sparks, T.H. (2014) 'Local-scale adaptation to climate change: the village flower festival', *Climate Research*, 60(1), pp. 87-89.

Spetsakis, M. and Aloimonos, J.Y. (1991) 'A multi-frame approach to visual motion perception', *International Journal of Computer Vision*, 6(3), pp. 245-255.

St-Onge, B., Audet, F.A. and Begin, J. (2015) 'Characterizing the Height Structure and Composition of a Boreal Forest Using an Individual Tree Crown Approach Applied to Photogrammetric Point Clouds', *Forests*, 6(11), pp. 3899-3922.

Steele-Dunne, S.C., McNairn, H., Monsivais-Huertero, A., Judge, J., Liu, P.W. and Papathanassiou, K. (2017) 'Radar Remote Sensing of Agricultural Canopies: A Review', *IEEE Journal of Selected Topics in Applied Earth Observations and Remote Sensing*, 10(5), pp. 2249-2273.

Storey, J., Choate, M. and Lee, K. (2014) 'Landsat 8 Operational Land Imager On-Orbit Geometric Calibration and Performance', *Remote Sensing*, 6(11), pp. 11127-11152.

Stow, D., Hope, A., Nguyen, A.T., Phinn, S. and Benkelman, C.A. (1996) 'Monitoring detailed land surface changes using an airborne multispectral digital camera system', *Geoscience and Remote Sensing, IEEE Transactions on*, 34(5), pp. 1191-1203.

Studer, S., Stöckli, R., Appenzeller, C. and Vidale, P.L. (2007) 'A comparative study of satellite and ground-based phenology', *International Journal of Biometeorology*, 51(5), pp. 405-414.

Sugiura, R., Noguchi, N. and Ishii, K. (2005) 'Remote-sensing Technology for Vegetation Monitoring using an Unmanned Helicopter', *Biosystems Engineering*, 90(4), pp. 369-379.

Suomalainen, J., Anders, N., Iqbal, S., Roerink, G., Franke, J., Wenting, P., Hünniger, D., Bartholomeus, H., Becker, R. and Kooistra, L. (2014) 'A Lightweight Hyperspectral Mapping System and Photogrammetric Processing Chain for Unmanned Aerial Vehicles', *Remote Sensing*, 6(11), p. 11013.

Suzuki, T., Amano, Y., Takiguchi, J., Hashizume, T., Suzuki, S. and Yamaba, A. (2009) 'Development of low-cost and flexible vegetation monitoring system using small unmanned aerial vehicle', *ICCAS-SICE, 2009*. 18-21 Aug. 2009.

Tagle Casapia, M.X. (2017) 'Study of radiometric variations in Unmanned Aerial Vehicle remote sensing imagery for vegetation mapping', *Lund University GEM thesis series*.

Tang, J.W., Korner, C., Muraoka, H., Piao, S.L., Shen, M.G., Thackeray, S.J. and Yang, X. (2016) 'Emerging opportunities and challenges in phenology: a review', *Ecosphere*, 7(8).

Thackeray, S.J., Sparks, T.H., Frederiksen, M., Burthe, S., Bacon, P.J., Bell, J.R., Botham, M.S., Brereton, T.M., Bright, P.W., Carvalho, L., Clutton-Brock, T.I.M., Dawson, A., Edwards, M., Elliott, J.M., Harrington, R., Johns, D., Jones, I.D., Jones, J.T., Leech, D.I., Roy, D.B., Scott, W.A., Smith, M., Smithers, R.J., Winfield, I.J. and Wanless, S. (2010) 'Trophic level asynchrony in rates of phenological change for marine, freshwater and terrestrial environments', *Global Change Biology*, 16(12), pp. 3304-3313.

Theuwissen, A.J.P. (1995) *Solid State Imaging with Charge Coupled Devices* Kluwer Academic Publishers.

Thiel, C. and Schmullius, C. (2016) 'DERIVATION OF FOREST PARAMETERS FROM STEREOGRAPHIC UAV DATA–AComparison WITH AIRBORNE LIDAR DATA', *Living Planet Symposium*. Prague, Czech Republic, 9-13 May 2016. ESA-SP. Available at: http://lps16.esa.int/posterfiles/paper0158/158thiel.pdf.

Thompson, R. and Clark, R.M. (2008) 'Is spring starting earlier?', *The Holocene*, 18(1), pp. 95-104.

Toneli, C.A.Z., Vieira, S., Fillho, A. and Brito, A. (2007) 'Análise da relação entre a estrutura do dossel a partir de fotografias hemisféricas e Eucalyptus grandis', *SIMPÓSIO BRASILEIRO DE SENSORIAMENTO REMOTO*. pp. 1891-1898.

Toomey, M., Friedl, M.A., Frolking, S., Hufkens, K., Klosterman, S., Sonnentag, O., Baldocchi, D.D., Bernacchi, C.J., Biraud, S.C., Bohrer, G., Brzostek, E., Burns, S.P., Coursolle, C., Hollinger, D.Y., Margolis, H.A., McCaughey, H., Monson, R.K., Munger, J.W., Pallardy, S., Phillips, R.P., Torn, M.S., Wharton, S., Zeri, M. and Richardson, A.D. (2015) 'Greenness indices from digital cameras predict the timing and seasonal dynamics of canopy-scale photosynthesis', *Ecological Applications*, 25(1), pp. 99-115.

Torres-Sanchez, J., Lopez-Granados, F., De Castro, A.I. and Pena-Barragan, J.M. (2013) 'Configuration and specifications of an Unmanned Aerial Vehicle (UAV) for early site specific weed management', *PloS one*, 8(3), pp. e58210-e58210.

Torresan, C., Andrea Berton and Federico Carotenuto, S.F.D.G., Beniamino Gioli, Alessandro Matese, Franco Miglietta, Carolina Vagnoli, Alessandro Zaldei & Luke Wallace (2017) 'Forestry applications of UAVs in Europe: a review', *International Journal of Remote Sensing*, 38(8-10), pp. 2427-2447.

Tsingas, V. (1992) *Automatisierung der Punktubertragung in der Aerotriangulation durch mehrfache digitale Bildzuordnung*. Munchen.

Tuanmu, M.-N., Vina, A., Bearer, S., Xu, W., Ouyang, Z., Zhang, H. and Liu, J. (2010) 'Mapping understory vegetation using phenological characteristics derived from remotely sensed data', *Remote Sensing of Environment*, 114(8), pp. 1833-1844.

Tucker, C.J. (1979) 'RED AND PHOTOGRAPHIC INFRARED LINEAR COMBINATIONS FOR MONITORING VEGETATION', *Remote Sensing of Environment*, 8(2), pp. 127-150.

Turner, D., Lucieer, A. and Wallace, L. (2014) 'Direct georeferencing of ultrahigh-resolution UAV imagery', *IEEE Transactions on Geoscience and Remote Sensing*, 52(5), pp. 2738-2745.

Turner, I.L., Harley, M.D. and Drummond, C.D. (2016) 'UAVs for coastal surveying', *Coastal Engineering*, 114, pp. 19-24.

Universität Bern (2016) *Open Nature*. Available at: http://www.opennature.ch (Accessed: 18/08/2016).

USGS 6.6 (2016a) 'Landsat 4-7 climate data record (CDR) surface reflectance' *Product guide*. July 2016. U.S. Geological Survey, p. 42. Available at: https://landsat.usgs.gov/sites/default/files/documents/ledaps_product_guide.pdf.

USGS 3.1 (2016b) 'Provisional landsat 8 surface reflectance code (LaSRC) product' *Product guide*. July 2016. U.S. Geological Survey, p. 27. Available at: https://landsat.usgs.gov/sites/default/files/documents/Landsat8DataUsersHandbook.pdf.

Vallet, J., Panissod, F., Strecha, C. and Tracol, M. (2011) 'PHOTOGRAMMETRIC PERFORMANCE OF AN ULTRA LIGHT WEIGHT SWINGLET "UAV"', in Eisenbeiss, H., Kunz, M. and Ingensand, H. (eds.) *International Conference on Unmanned Aerial Vehicle in Geomatics*. pp. 253-258.

Van Blyenburgh, P. (2013) '2013-2014 RPAS Year book: Remotely piloted aircraft systems: The global perspective 2013/2014', *UVS International: Paris, France*.

van Iersel, W.K., Straatsma, M.W., Addink, E.A. and Middelkoop, H. (2016) 'MONITORING PHENOLOGY OF FLOODPLAIN GRASSLAND AND HERBACEOUS VEGETATION WITH UAV IMAGERY', in Halounova, L., Sunar, F., Potuckova, M., Patkova, L., Yoshimura, M., Soergel, U., BenDor, E., Smit, J., Bareth, G., Zhang, J., Kaasalainen, S., Sorgel, U., Osmanoglu, B., Crespi, M., Crosetto, M., Blaschke, T., Brovelli, M.A. and Zagajewski, B. (eds.) *Xxiii Isprs Congress, Commission Vii*. pp. 569-571.

Vega, F.A., Ramírez, F.C., Saiz, M.P. and Rosúa, F.O. (2015) 'Multi-temporal imaging using an unmanned aerial vehicle for monitoring a sunflower crop', *Biosystems Engineering*, 132, pp. 19-27.

Verhoeven, G., Doneus, M., Briese, C. and Vermeulen, F. (2012) 'Mapping by matching: a computer vision-based approach to fast and accurate georeferencing of archaeological aerial photographs', *Journal of Archaeological Science*, 39(7), pp. 2060-2070.

Verhoeven, G.J. (2012) 'Near-Infrared Aerial Crop Mark Archaeology: From its Historical Use to Current Digital Implementations', *Journal of Archaeological Method and Theory*, 19(1), pp. 132-160.

Verhoeven, G.J., Smet, P.F., Poelman, D. and Vermeulen, F. (2009) 'Spectral Characterization of a Digital Still Camera's NIR Modification to Enhance Archaeological Observation', *IEEE Transactions on Geoscience and Remote Sensing*, 47(10), pp. 3456-3468.

Verhoeven, G.J.J. (2010) 'It's all about the format-unleashing the power of RAW aerial photography', *Int. J. Remote Sens.*, 31(8), pp. 2009-2042.

Vina, A., Bearer, S., Zhang, H.M., Ouyang, Z.Y. and Liu, J.G. (2008) 'Evaluating MODIS data for mapping wildlife habitat distribution', *Remote Sensing of Environment*, 112(5), pp. 2160-2169.

Vitasse, Y., Delzon, S., Dufrêne, E., Pontailler, J.-Y., Louvet, J.-M., Kremer, A. and Michalet, R. (2009) 'Leaf phenology sensitivity to temperature in European trees: Do within-species populations exhibit similar responses?', *Agricultural and Forest Meteorology*, 149(5), pp. 735-744.

Vitasse, Y., François, C., Delpierre, N., Dufrêne, E., Kremer, A., Chuine, I. and Delzon, S. (2011) 'Assessing the effects of climate change on the phenology of European temperate trees', *Agricultural and Forest Meteorology*, 151(7), pp. 969-980.

von Bueren, S.K., Burkart, A., Hueni, A., Rascher, U., Tuohy, M.P. and Yule, I.J. (2015) 'Deploying four optical UAV-based sensors over grassland: challenges and limitations', *Biogeosciences*, 12(1), pp. 163-175.

Walker, J.J., de Beurs, K.M. and Wynne, R.H. (2014) 'Dryland vegetation phenology across an elevation gradient in Arizona, USA, investigated with fused MODIS and Landsat data', *Remote Sensing of Environment*, 144, pp. 85-97.

Walker, J.J., De Beurs, K.M., Wynne, R.H. and Gao, F. (2012) 'Evaluation of Landsat and MODIS data fusion products for analysis of dryland forest phenology', *Remote Sensing of Environment*, 117, pp. 381-393.

Wallace, L., Lucieer, A., Watson, C. and Turner, D. (2012) 'Development of a UAV-LiDAR System with Application to Forest Inventory', *Remote Sensing*, 4(6), pp. 1519-1543.

Walther, G.-R., Post, E., Convey, P., Menzel, A., Parmesan, C., Beebee, T.J.C., Fromentin, J.-M., Hoegh-Guldberg, O. and Bairlein, F. (2002) 'Ecological responses to recent climate change', *Nature*, 416(6879), pp. 389-395.

Wang, C. and Myint, S.W. (2015) 'A Simplified Empirical Line Method of Radiometric Calibration for Small Unmanned Aircraft Systems-Based Remote Sensing', *IEEE Journal of Selected Topics in Applied Earth Observations and Remote Sensing*, 8(5), pp. 1876-1885.

Wang, H., Dai, J. and Ge, Q. (2014) 'Comparison of Satellite and Ground-Based Phenology in China's Temperate Monsoon Area', *Advances in Meteorology*, 2014.

Wang, H., Jia, G., Zhang, A. and Miao, C. (2016a) 'Assessment of Spatial Representativeness of Eddy Covariance Flux Data from Flux Tower to Regional Grid', *Remote Sensing*, 8(9), p. 742.

Wang, Q.M., Blackburn, G.A., Onojeghuo, A.O., Dash, J., Zhou, L.Q., Zhang, Y.H. and Atkinson, P.M. (2017) 'Fusion of Landsat 8 OLI and Sentinel-2 MSI Data', *Ieee Transactions on Geoscience and Remote Sensing*, 55(7), pp. 3885-3899.

Wang, R., Gamon, J., Emmerton, C., Li, H., Nestola, E., Pastorello, G. and Menzer, O. (2016b) 'Integrated Analysis of Productivity and Biodiversity in a Southern Alberta Prairie', *Remote Sensing*, 8(3), p. 214.

Weiss, M. and Baret, F. (2014) *CAN-EYE V6. 313 User Manual*. Available at: http://www6.paca.inra.fr/can-eye/Documentation-Publications/Documentation (Accessed: 18/01/2017).

Welles, J.M. and Cohen, S. (1996) 'Canopy structure measurement by gap fraction analysis using commercial instrumentation', *Journal of Experimental Botany*, 47(9), pp. 1335-1342.

West, N.E. and Wein, R.W. (1971) 'A Plant Phenological Index Technique', *BioScience*, 21(3), pp. 116-117.

Westoby, M.J., Brasington, J., Glasser, N.F., Hambrey, M.J. and Reynolds, J.M. (2012) ''Structure-from-Motion'photogrammetry: A low-cost, effective tool for geoscience applications', *Geomorphology*, 179, pp. 300-314.

White, K., Pontius, J. and Schaberg, P. (2014) 'Remote sensing of spring phenology in northeastern forests: A comparison of methods, field metrics and sources of uncertainty', *Remote Sensing of Environment*, 148, pp. 97-107.

White, M.A., de Beurs, K.M., Didan, K., Inouye, D.W., Richardson, A.D., Jensen, O.P., O'Keefe, J., Zhang, G., Nemani, R.R., van Leeuwen, W.J.D., Brown, J.F., de Wit, A., Schaepman, M., Lin, X., Dettinger, M., Bailey, A.S., Kimball, J., Schwartz, M.D., Baldocchi, D.D., Lee, J.T. and Lauenroth, W.K. (2009) 'Intercomparison, interpretation, and assessment of spring phenology in North America estimated from remote sensing for 1982-2006', *Global Change Biology*, 15(10), pp. 2335-2359.

White, M.A. and Nemani, R.R. (2006) 'Real-time monitoring and short-term forecasting of land surface phenology', *Remote Sensing of Environment*, 104(1), pp. 43-49.

White, M.A., Thornton, P.E. and Running, S.W. (1997) 'A continental phenology model for monitoring vegetation responses to interannual climatic variability', *Global biogeochemical cycles*, 11(2), pp. 217-234.

Wilkinson, M., Eaton, E.L., Broadmeadow, M.S.J. and Morison, J.I.L. (2012) 'Inter-annual variation of carbon uptake by a plantation oak woodland in south-eastern England', *Biogeosciences*, 9(12), pp. 5373-5389.

Willis, C.G., Ruhfel, B.R., Primack, R.B., Miller-Rushing, A.J., Losos, J.B. and Davis, C.C. (2010) 'Favorable Climate Change Response Explains Non-Native Species' Success in Thoreau's Woods', *Plos One*, 5(1).

Woebbecke, D.M., Meyer, G.E., Von Bargen, K. and Mortensen, D.A. (1995) 'Color indices for weed identification under various soil, residue, and lighting conditions', *Transactions of the ASAE*, 38(1), pp. 259-269.

Woodget, A.S., Austrums, R., Maddock, I.P. and Habit, E. (2017) 'Drones and digital photogrammetry: from classifications to continuums for monitoring river habitat and hydromorphology', *Wiley Interdisciplinary Reviews: Water*, pp. e1222-n/a.

Woodland Trust (2016) *Nature's Calendar*. Available at: https://naturescalendar.woodlandtrust.org.uk/ (Accessed: 18/08/2016).

Wu, C.Y., Peng, D.L., Soudani, K., Siebicke, L., Gough, C.M., Arain, M.A., Bohrer, G., Lafleur, P.M., Peichl, M., Gonsamo, A., Xu, S.G., Fang, B. and Ge, Q.S. (2017) 'Land surface phenology derived from normalized difference vegetation index (NDVI) at global FLUXNET sites', *Agricultural and Forest Meteorology*, 233, pp. 171-182.

Wu, J., He, Z.L., Wei, W.X., O'Donnell, A.G. and Syers, J.K. (2000) 'Quantifying microbial biomass phosphorus in acid soils', *Biology and Fertility of Soils*, 32(6), pp. 500-507.

Xiao, Z., Wang, T., Liang, S. and Sun, R. (2016) 'Estimating the fractional vegetation cover from glass leaf area index product', *Remote Sensing*, 8(4).

Xin, Q.C., Olofsson, P., Zhu, Z., Tan, B. and Woodcock, C.E. (2013) 'Toward near real-time monitoring of forest disturbance by fusion of MODIS and Landsat data', *Remote Sensing of Environment*, 135, pp. 234-247.

Yamamoto, N., Saito, T., Ogawa, S. and Ishimaru, I. (2016) 'Middle infrared (wavelength range: 8 mu m -14 mu m) 2-dimensional spectroscopy (total weight with electrical

controller: 1.7 kg , total cost: less than 10,000 USD) so called hyperspectral camera for unmanned air vehicles like drones', in VelezReyes, M. and Messinger, D.W. (eds.) *Algorithms and Technologies for Multispectral, Hyperspectral, and Ultraspectral Imagery Xxii*.

Yang, C., Westbrook, J., Suh, C., Martin, D., Hoffmann, W., Lan, Y., Fritz, B. and Goolsby, J. (2014a) 'An Airborne Multispectral Imaging System Based on Two Consumer-Grade Cameras for Agricultural Remote Sensing', *Remote Sensing*, 6(6), pp. 5257-5278.

Yang, X., Tang, J.W. and Mustard, J.F. (2014b) 'Beyond leaf color: Comparing camera-based phenological metrics with leaf biochemical, biophysical, and spectral properties throughout the growing season of a temperate deciduous forest', *Journal of Geophysical Research-Biogeosciences*, 119(3), pp. 181-191.

Yates, H., Strong, A., McGinnis, D. and Tarpley, D. (1986) 'Terrestrial observations from NOAA operational satellites', *Science*, 231(4737), pp. 463-470.

Yu, W. (2004) 'Practical anti-vignetting methods for digital cameras', *IEEE Transactions on Consumer Electronics*, 50(4), pp. 975-983.

Yuan, C., Zhang, Y.M. and Liu, Z.X. (2015) 'A survey on technologies for automatic forest fire monitoring, detection, and fighting using unmanned aerial vehicles and remote sensing techniques', *Canadian Journal of Forest Research*, 45(7), pp. 783-792.

Yuanjie, Z., Lin, S., Kambhamettu, C., Jingyi, Y. and Sing Bing, K. (2009) 'Single-Image Vignetting Correction', *Pattern Analysis and Machine Intelligence, IEEE Transactions on*, 31(12), pp. 2243-2256.

Yun, H.S., Park, S.H., Kim, H.-J., Lee, W.D., Lee, K.D., Hong, S.Y. and Jung, G.H. (2016) 'Use of Unmanned Aerial Vehicle for Multi-temporal Monitoring of Soybean Vegetation Fraction', *Journal of Biosystems Engineering*, 41(2), pp. 126-137.

Yuzugullu, O., Erten, E. and Hajnsek, I. (2015) 'Rice Growth Monitoring by Means of X-Band Co-polar SAR: Feature Clustering and BBCH Scale', *IEEE Geoscience and Remote Sensing Letters*, 12(6), pp. 1218-1222.

Zaki, N.A.M., Latif, Z.A., Zainal, M.Z. and Zainuddin, K. (2015) 'Individual tree crown (ITC) delineation using watershed transformation algorithm for tropical lowland dipterocarp', *2015 International Conference on Space Science and Communication (IconSpace)*. 10-12 Aug. 2015.

Zaman, B., Jensen, A., Clemens, S.R. and McKee, M. (2014) 'Retrieval of Spectral Reflectance of High Resolution Multispectral Imagery Acquired with an Autonomous Unmanned Aerial Vehicle: AggieAir™', *Photogrammetric Engineering & Remote Sensing*, 80(12), pp. 1139-1150.

Zhang, X. (2015) 'Reconstruction of a complete global time series of daily vegetation index trajectory from long-term AVHRR data', *Remote Sensing of Environment*, 156, pp. 457-472.

Zhang, X., Friedl, M. and Schaaf, C. (2009) 'Sensitivity of vegetation phenology detection to the temporal resolution of satellite data', *International Journal of Remote Sensing*, 30(8), pp. 2061-2074.

Zhang, X., Friedl, M.A. and Schaaf, C.B. (2006) 'Global vegetation phenology from Moderate Resolution Imaging Spectroradiometer (MODIS): Evaluation of global patterns and comparison with in situ measurements', *Journal of Geophysical Research: Biogeosciences (2005–2012)*, 111(G4).

Zhang, X., Friedl, M.A., Schaaf, C.B., Strahler, A.H., Hodges, J.C.F., Gao, F., Reed, B.C. and Huete, A. (2003) 'Monitoring vegetation phenology using MODIS', *Remote sensing of environment*, 84(3), pp. 471-475.

Zhang, X.Y., Wang, J.M., Gao, F., Liu, Y., Schaaf, C., Friedl, M., Yu, Y.Y., Jayavelu, S., Gray, J., Liu, L.L., Yan, D. and Henebry, G.M. (2017) 'Exploration of scaling effects

on coarse resolution land surface phenology', *Remote Sensing of Environment*, 190, pp. 318-330.

Zhao, J., Zhang, Y., Tan, Z., Song, Q., Liang, N., Yu, L. and Zhao, J. (2012) 'Using digital cameras for comparative phenological monitoring in an evergreen broad-leaved forest and a seasonal rain forest', *Ecological Informatics*, 10, pp. 65-72.

Zhen, Z., Quackenbush, L.J. and Zhang, L. (2016) 'Trends in automatic individual tree crown detection and delineation—Evolution of LiDAR data', *Remote Sensing*, 8(4), p. 333.

Zhou, G. and Liu, S. (2015) 'Estimating ground fractional vegetation cover using the double-exposure method', *International Journal of Remote Sensing*, 36(24), pp. 6085-6100.

Zhu, W., Tian, H., Xu, X., Pan, Y., Chen, G. and Lin, W. (2012) 'Extension of the growing season due to delayed autumn over mid and high latitudes in North America during 1982–2006', *Global Ecology and Biogeography*, 21(2), pp. 260-271.